

**Electroanalysis in the Nanodomain : Quinone Monolayers and
Nanometer Dimensioned Electrodes**

Mary M. Farrell, B.Sc. (Hons)

**A Thesis presented at Dublin City University for the degree of
Doctor of Philosophy**

**Supervisor : Prof. Robert J. Forster,
School of Chemical Sciences,
Dublin City University.**

April 2003

I hereby certify that the material, which I now submit for assessment on the programme of study leading to the award of Doctor of Philosophy is entirely of my own work and has not been taken from the work of others save and to the extent that such works has been cited and acknowledged within the text of my work.

Signed: Mary Farrell

ID No.: 95635653

Date: 16th April 2003

Acknowledgements

First and foremost I would like to express my most sincere gratitude to my supervisor, Professor Robert Forster. Thank you for the time and effort you have invested to further my understanding of electrochemistry, which has enabled me to present the work in this thesis to the best of my ability. Thank you also for the encouragement and endless enthusiasm you have shown over the last few years and for our many “disagreements”, which got me thinking! To the technical staff in the School of Chemical Sciences, Mick, Maurice, Damien, Veronica, Ann, Mary, Vinny, Ambrose and John, thank you for all your help during my time in DCU. Thanks also to all the secretarial, faculty office and lecturing staff that I was in contact with during my postgrad years.

To the past members of the RFRG – Dominic, Conor, Egbert, Edna and Jenni, and present members – Lorraine, Johan, Andrea, Darren, Lynn, Darragh, Tommy, Sonia, Michael and Richard, I would like to thank you all. A special word of thanks to Dominic for the wonderful introduction to electrochemistry in my fourth year undergraduate project, which led to me starting my postgrad; also to Jenni with whom I had the pleasure of sharing a lab throughout most of my experimental work. To Johan and Lorraine for your friendship and support over the years, it is very much appreciated. Lastly, to the entire group for the most memorable nights out, especially at Christmas time!

Thanks to all the chemistry postgrads and postdocs in DCU I’ve met over the past few years, to name a few – Carol, Mairead, Helen, Davnat, Marco (many thanks for showing me the sights in Amsterdam!), Scott, Adrian, Dec, Wesley, Stephania, Sabine, Ger, Ian, Karl, Ray, Johnnie, John, Shane, Noel, Clare, Maire, Aoife, Kathleen, Emer, Clodagh, Dave, Andrea and Neil and Brendan in biology. Thanks also to the members of the Paul Cahill research group in the biotechnology department and to the BRS for all the great nights out and the trip to Budapest – a special word of thanks to Catherine!

Lastly I would like to thank the good friends I’ve made while in DCU; Mary, Sandra, Mairead, Lorraine and Lisa, thanks girls for everything! - and finally to the people that provide me with constant support and advice, and most importantly always encourage me to do what I want, my family – to my mother, Marcella, father, Luke and brother and sisters, Edward, Anita and Elizabeth – thank you.

This Thesis is dedicated to my parents.

TABLE OF CONTENTS

Chapter 1	Theoretical Framework and Literature Survey	1
1	Introduction.....	2
1.1	Electrochemical Double Layer.....	4
1.2	Heterogeneous Electron Transfer Kinetics.....	6
1.2.1	Elementary Steps of Heterogeneous Electron Transfer.....	7
1.2.2	Butler Volmer Model.....	9
1.2.3	Marcus Theory of Heterogeneous Electron Transfer.....	13
1.2.3.1	The Reorganisation Energy.....	16
1.2.3.2	Adiabatic vs. Non-Adiabatic Electron Transfer.....	17
1.3	Electron Transfer Kinetics of Adsorbed Monolayers.....	18
1.3.1	Alkanethiol Monolayers.....	19
1.3.2	Osmium and Ruthenium Monolayers.....	22
1.4	Proton Coupled Electron Transfer.....	27
1.4.1	Evaluation of the Reaction Sequence.....	29
1.4.2	Electrochemical Studies of Anthraquinone Derivatives.....	32
1.4.2.1	Adsorption Isotherms.....	36
1.4.2.2	Two Component Anthraquinone Monolayers.....	38
1.5	Surface Characterisation of Monomolecular Films.....	41
1.5.1	Raman Spectroscopy Studies.....	43
1.5.2	Infrared Spectroscopy.....	50
1.5.3	Scanning Probe Microscopy.....	53
1.6	Electrochemical Techniques and Instrumentation.....	57
1.6.1	Cyclic Voltammetry.....	57
1.6.1.1	Solution Phase Electrochemistry.....	60
1.6.1.2	Electrochemistry of Surface Confined Species.....	61
1.6.2	Chronoamperometry.....	63
1.7	Microelectrodes.....	64
1.7.1	Ultramicroelectrode Geometries.....	66
1.7.2	Electrochemistry at Ultramicroelectrodes.....	66

1.7.2.1	Mass Transport	67
1.7.2.2	Double Layer Charging	70
1.7.2.3	Ohmic Drop Effects.....	71
1.7.3	Microelectrode to Nanode Dimensions	72
1.7.4	Microelectrode Fabrication Procedures.....	74
1.7.4.1	Mercury Microelectrodes	77
1.7.5	Shapes of Ultramicroelectrodes.....	78
1.7.6	Characterisation of Ultramicroelectrodes.....	80
1.8	Conclusions	82
1.9	References	84

Chapter 2 Characterisation of Anthraquinones..... 90

2	Introduction.....	91
2.1	Characterisation of Anthraquinones.....	93
2.1.1	HPLC	94
2.1.2	UV-Visible Spectroscopy.....	95
2.1.3	NMR Spectroscopy	96
2.1.4	Raman Spectroscopy	98
2.1.5	IR Spectroscopy	101
2.1.6	Solution Phase Electrochemistry.....	103
2.2	Conclusions	105
2.3	References	106

Chapter 3	Impact of Hydrogen Bonding on the Redox Properties of Anthraquinone Monolayers	108
3	Introduction	109
3.1	Experimental Setup	110
3.1.1	Materials and Procedures	110
3.2	Results and Discussion.....	111
3.2.1	General Electrochemical Properties.....	111
3.2.2	Scan Rate Dependence.....	113
3.2.3	Raman Spectroscopy	115
3.2.4	Concentration Dependence	119
3.2.5	Adsorption Thermodynamics.....	124
3.2.5.1	Langmuir Isotherm.....	124
3.2.5.2	Frumkin Isotherm.....	131
3.2.6	Potential Dependent Adsorption Thermodynamics	137
3.2.7	Origin of the Current Spike.....	141
3.3	Conclusions	144
3.4	References	146

Chapter 4	Thermodynamics and Kinetics of Adsorption in Single and Two Component Anthraquinone Monolayers	148
4	Introduction	149
4.1	Experimental	150
4.1.1	Materials and Procedures	150
4.2	Results and Discussion.....	152
4.2.1	General EC Properties of Single Component Monolayers	152
4.2.2	Scan Rate Dependence.....	154
4.2.3	Adsorption Isotherms	155
4.2.4	Interfacial Capacitance.....	160

4.2.5	1,5-DMAQ Adsorption Kinetics.....	163
4.2.5.1	Initial Growth Kinetics – Process 1	167
4.2.5.2	Interconversion Kinetics – Process 2A	171
4.2.5.3	Growth Kinetics – Process 2B	173
4.2.5.4	Mechanism of 1,5-DMAQ Adsorption	176
4.2.6	Two Component Monolayers.....	178
4.2.7	General EC Properties of Two Component Monolayers	179
4.2.8	Competitive Adsorption.....	180
4.2.9	Adsorption Dynamics in Two Component System.....	187
4.2.9.1	Mechanism of Monolayer Formation.....	191
4.3	Conclusions.....	193
4.4	References	195

Chapter 5	Coupled Proton and Electron Transfer in 1-amino-2-sulphonic-4-hydroxyanthraquinone Monolayers	197
5	Introduction	198
5.1	pH Dependence of the CV Response	199
5.1.1	Relative Rates of Proton and Electron Transfer	201
5.2	Rapid Scan Rate CV of 1,2,4-AQASH	203
5.2.1	Simplex Algorithm Method.....	207
5.2.2	Laviron Method	215
5.3	Chronoamperometric Measurements.....	218
5.3.1	Potential Dependence of Reduction / Oxidation Rates	221
5.4	pH Dependence of the Reaction Rates	226
5.4.1	Surface Reaction Kinetics	231
5.5	Conclusions	234
5.6	References	235

<u>Chapter 6</u>	Nanodes – New Dimensions of Space and Time in Electroanalysis	237
6	Introduction	238
6.1	Fabrication of Mercury Microelectrodes.....	239
6.1.1	Microelectrode Preparation	241
6.1.2	Mercury Deposition and Determination of Electrode Area	244
6.2	Construction of Nanoelectrodes	247
6.2.1	Fabrication Process	250
6.2.2	Polishing Procedure.....	252
6.3	Characterisation of Nanoelectrodes.....	253
6.3.1	Optical Microscopy	254
6.3.2	Scanning Electron Microscopy.....	256
6.3.3	Cyclic Voltammetry	260
6.3.3.1	Determination of the Electrochemical Area.....	260
6.3.3.2	Determination of the Geometric Area	261
6.4	Ultramicroelectrode Geometries	264
6.5	Mercury Nanoelectrodes	267
6.6	Conclusions	271
6.7	References	272
<u>Chapter 7</u>	Conclusions and Future Work.....	274
<u>Appendix 1</u>	Abbreviations and Symbols.....	279
	Standard Abbreviations	280
	Symbols	281
	Greek Symbols	282
<u>Appendix 2</u>	Publications.....	283

Abstract

“Electroanalysis in the Nanodomain: Quinone Monolayers and Nanometer Dimensioned Electrodes”

Mary M. Farrell, B.Sc.

Spontaneously adsorbed monolayers, which are formed by the immersion of an electrode into a dilute solution of surface-active molecules have been studied extensively in recent years. The work presented in this thesis deals with the modification of mercury electrode surfaces with 9,10-anthraquinone and two anthraquinone derivatives, 1-amino,2-sulphonic,4-hydroxyanthraquinone (1,2,4-AQASH), and 1,5-dimethoxyanthraquinone (1,5-DMAQ). These adsorbates form a π interaction with the electrode surface. The thermodynamics of adsorption has been modeled using the Langmuir and Frumkin adsorption isotherms. Binary monolayers formed by the coadsorption of 1,2,4-AQASH and 1,5-DMAQ have been investigated to probe the extent of interaction between adsorbed moieties. The kinetics of single component 1,5-DMAQ adsorption has been modeled over a wide concentration range to probe the mode of adsorption of these molecules. It has been concluded from the CV and kinetic fits of this data that 1,5-DMAQ molecules undergo a reorientation on the electrode surface as adsorption proceeds.

Quinonoid monolayers form tightly bound adsorbate layers on mercury, which are stable in both redox forms. These monomolecular films undergo coupled proton and electron transfer reactions and are important in areas such as catalysis, molecular electronics and biological applications. The heterogeneous electron transfer rate of 1,2,4-AQASH has been investigated and was modeled using the Butler-Volmer and Marcus theories of electron transfer. Platinum electrodes of micrometer to nanometer dimensions have been fabricated using a laser based micropipette puller. Mercury has been electrodeposited on the platinum surface to produce micrometer sized mercury electrodes of hemispherical geometry. These electrodes exhibit faster response times than macroelectrodes and thus enable the measurement of fast heterogeneous electron transfer rates. A mechanism for the sequence of proton and electron transfer in monomolecular films of 1,2,4-AQASH in both oxidation and reduction directions was postulated from the experimental data in solutions of high and low pH.

Chapter 1

Theoretical Framework and Literature Survey

“Let him who would enjoy a good future waste none of his present.”

- *Roger Babson*

1. Introduction

The electrode/solution interface is an important area of study for electrochemists. Events which occur at this interface include the adsorption of molecules and ions from solution, electron transfer reactions and the diffusion of atoms and molecules into and out of the interfacial region.¹ Modification of the electrode interface with self assembled monolayers and spontaneously adsorbed layers provides model systems for the study of heterogeneous electron transfer dynamics. This work deals with the modification of an electrode surface with anthraquinone and anthraquinone derivatives, which spontaneously adsorb on mercury. The orientation of these species on the electrode surface is investigated briefly and high-speed electrochemical measurements are implemented to gain an insight into the mechanism of electron and proton transfer in these monomolecular films.

Interest in this area of research started with the pioneering work of Sagiv and coworkers in the early 1970s² who looked at the modification of electrode surfaces with self-assembled monolayers of organic compounds. These organic thin films play an important role in areas of technological importance, including adhesion, electrochemical catalysis³ and corrosion inhibition.^{4,5,6,7,8} The self assembly technique is based upon spontaneous adsorption of amphi-functional molecules from organic solutions onto solid surfaces. These films are in the thickness range from a few nanometers (a monolayer) to several hundred nanometers.⁹ The spontaneity of monolayer formation implies that such systems are thermodynamically stable, i.e., binding to the surface occurs by strong chemical bonds.^{9,10,11} Alkane thiol monolayers adsorbed on gold are the most intensively studied self assembled monolayers, mainly due to their stability, organisation, and potential applications in areas such as corrosion protection.

Quinonoid molecules, although less extensively studied form tightly bound adsorbate layers on mercury, are stable in both redox forms and exhibit nearly ideal electrochemical responses in low pH electrolyte solutions. They offer ideal systems to study the thermodynamics and kinetics of adsorption. These monomolecular films also undergo coupled proton and electron transfer reactions and are important in areas such as catalysis, molecular electronics¹² and especially biological systems.^{13,14}

This thesis is arranged as follows; Chapter 1 gives an introduction to electron transfer theory and reviews the most relevant literature dealing with the construction and characterization of monolayers formed on electrode surfaces. The electrochemical techniques implemented in the subsequent experimental chapters are explained and literature relating to the fabrication and characterization of microelectrodes is summarized.

Chapter 2 reports on the characterisation of the anthraquinone species in the experimental work, the techniques are high performance liquid chromatography, uv-visible, nuclear magnetic resonance, infrared and raman spectroscopy.

Chapter 3 presents the electrochemical properties of an anthraquinone derivative; 1-amino,2-sulphonic,4-hydroxyanthraquinone (1,2,4-AQASH) within single component monolayers on a mercury electrode surface. The thermodynamics of adsorption are modeled using the Langmuir and Frumkin isotherms to probe the extent to which the adsorbates interact. An unusual spike appears in the voltammetry at relatively high coverages and the origin of this unusual behaviour is probed and compared with the behaviour of the parent anthraquinone compound.

Chapter 4 reports the electrochemical properties of two component monolayers formed from 1,2,4-AQASH and 1,5-dimethoxyanthraquinone (1,5-DMAQ). The dynamics of monolayer formation of single component monolayers is also considered. 1,5-DMAQ molecules undergo a reorientation on the electrode surface as time proceeds and the time dependent kinetic data is modeled at varying concentration.

Chapter 5 focuses on fast electrochemical measurements to determine heterogeneous electron transfer rate constants for 1,2,4-AQASH adsorbed on mercury microelectrodes. Fast scan cyclic voltammograms obtained in low pH media are modeled using a previously reported model based on the Marcus theory of electron transfer. Chronoamperometric measurements are carried out on a high-speed potentiostat and this data is fit to the Butler-Volmer model, a comparison of the results from both models is made.

Chapter 6 summarizes the procedure used to fabricate platinum microelectrodes and nanoelectrodes. The platinum nanoelectrodes are constructed using a microelectrode puller and these are characterized using a number of techniques. The geometry of the resulting nanodes is estimated from the cyclic voltammetry behaviour. Mercury is then deposited on the platinum substrate to form hemispherical drop electrodes. These ultrasmall probes are necessary for the measurement of fast heterogeneous electron transfer rates of the adsorbed anthraquinone molecules.

Finally, Chapter 7 draws some conclusions from the study and suggestions for future work are proposed.

1.1 Electrochemical Double Layer

At the interface between an electrode and the electrolyte solution an electrochemical double layer is built up. As this work deals with the deliberate modification of the electrode surface it is important to have an understanding of the structure of the electrochemical interface. Most of the knowledge of the double layer comes from studies carried out on mercury due to its high degree of purity and atomically smooth surface.

A number of theories have been proposed to characterize the electrode/solution interface, the earliest of which by Helmholtz^{15,16} in 1879. This simplified model suggests that the structure of the double layer is equivalent to a parallel-plate capacitor, in that all excess charge resides strictly at the surface. Gouy¹⁷ (1910) and Chapman¹⁸ (1913) improved on this model by introducing the idea of a diffuse layer where the highest concentration of excess charge resides at the electrode surface and extends out into the surrounding electrolytic solution. Stern¹⁹ and Graham proposed the most recent model of the electrode/electrolyte double layer in 1947. The interface is split into three regions as illustrated in Figure 1, the metal layer, the inner layer and the diffuse layer. The inner layer is also known as the Helmholtz, Stern or compact layer and comprises the Inner and Outer Helmholtz planes. The layer nearest to the electrode surface contains solvent molecules and specifically adsorbed ions. Solvated ions reside in and outside the Outer Helmholtz plane and only interact with the surface through long-range electrostatic interactions; these ions are said to be non-specifically adsorbed. The

diffuse layer extends from the Outer Helmholtz plane into the bulk solution. The thickness of this diffuse layer depends on the total ionic strength of the solution. In dilute solutions the diffuse layer may extend more than 10 nm, but for concentrations of 0.1 M, the thickness of the double layer decreases to values not much greater than that of the Helmholtz layer itself. Therefore, it follows that for higher ionic strengths the diffuse layer becomes sufficiently small that it can be neglected.

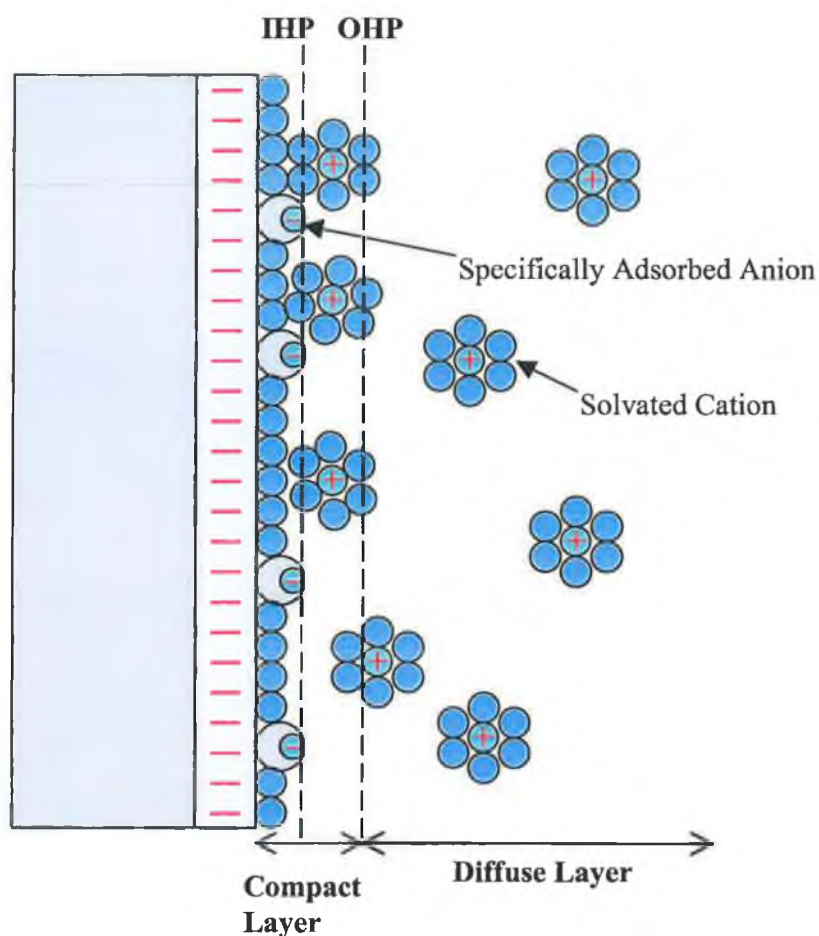


Figure 1. The electrode/electrolyte double layer region; \oplus and \ominus represent cations and anions respectively, and \bullet represents solvent molecules, IHP is the inner helmholtz plane and OHP is the outer helmholtz plane.

The structure of the electrode/electrolyte interface discussed above refers to an unmodified surface, i.e., unmodified in the sense that there are no electroactive species specifically adsorbed on the electrode surface. Adsorption of species onto the electrode

surface causes specifically adsorbed ions and solvent molecules to be displaced from the interface and results in a change in the double layer capacitance from that observed at a clean unmodified surface. In the case of an electrode coated with a monolayer the total double layer capacitance, C_{dl} is given by the sum of contributions from the film, C_f and the diffuse layer, C_{diff} , as stated in Equation (1):

$$\frac{1}{C_{dl}} = \frac{1}{C_f} + \frac{1}{C_{diff}} \quad (1)$$

The absolute value of C_{dl} is governed by the magnitude of the film and diffuse layer capacitances, the smaller of the two determining the observed behaviour. In high electrolyte concentration the double layer is compressed and C_{diff} becomes so large that it no longer contributes to C_{dl} . The total double layer capacitance is then controlled by the monolayer capacitance. This change in capacitance between a modified and unmodified interface can be measured using cyclic voltammetry by analysing the background current at potentials where the monolayer is fully oxidized and reduced. Results presented in Chapter 3 and Chapter 4, respectively look at the effect of increasing the surface coverage of 1,2,4-AQASH and 1,5-DMAQ on the measured double layer capacitance.

1.2 Heterogeneous Electron Transfer Kinetics

Self assembled and spontaneously adsorbed monolayers have been used extensively in recent years to study heterogeneous electron transfer kinetics. These assemblies are attractive model systems for the study of heterogeneous dynamics due to their well-defined structure and the ability to change the distance between the electrode and redox centre, for example in the case of alkanethiol systems. The increased popularity of micro- and nanoelectrodes in electrochemical measurements allows for the investigation of electron transfer rates of rapid redox reactions such as those presented in Chapter 5 of this document. In this chapter, the heterogeneous electron transfer rates of 1,2,4-AQASH is investigated. These molecules are adsorbed approximately 4-5 Å from the electrode surface and the electron transfer rates are rapid, as the rate of electron transfer is not limited by diffusion. The purpose of this section is to present a description of the

elementary steps of heterogeneous electron transfer and outline theories proposed by Butler and Volmer as well as Marcus to describe this simple process.

Most of the theoretical and experimental work on which the understanding of the electron transfer process is based is a result of investigations into homogeneous electron transfer reactions. Electron transfer occurring at a metal electrode surface shares many of the characteristics of homogeneous electron transfer reactions and with certain constraints the same theories can be applied to the examination of both processes. The fundamental difference between homogeneous and heterogeneous electron transfer lies primarily in the driving force, which can be controlled externally in the case of the heterogeneous process by varying the applied potential relative to the formal potential of the reactant. This capability contrasts sharply with homogeneous electron transfer reactions where the temperature or chemical structure of the reactant must be altered in order to change the driving force.

1.2.1 Elementary Steps of Heterogeneous Electron Transfer

An electron transfer reaction occurring at an electrode surface involves a series of steps which are depicted in Figure 2. When an electrode is immersed into an electrolytic solution and an electrical potential is applied, redox active species are transported to the electrode surface via diffusion. Depending on the identity of the electroactive species in solution, and the type of electrode used, specific chemical and electrostatic interactions may cause the redox molecule to be attracted to the electrode surface and adsorbed as illustrated in Figure 2A. In order for an electron to transfer between the redox molecule and the electrode a number of conditions have to be fulfilled.

First the electron transfer step requires thermal activation of the redox molecule. Random thermal fluctuations cause the energy of the donor or acceptor states in the molecule to vary continuously and its only when the redox molecule comes into resonance with the appropriate electronic states in the metal (filled electronic states for reductions, vacant for oxidations) that electron transfer is possible. Second, electronic coupling between the donor or acceptor orbitals of the molecule with the electrode must occur. The extent to which this coupling occurs typically increases exponentially with decreasing separation between the reactant and the electrode surface.²⁰ If the molecule

is in close enough proximity to the electrode surface electrons can tunnel between the electrode and redox couple as illustrated in Figure 2C. Following electron transfer the product relaxes to its equilibrium structure and if its not specifically adsorbed on the electrode will be transported away from the electrode surface again via diffusion.

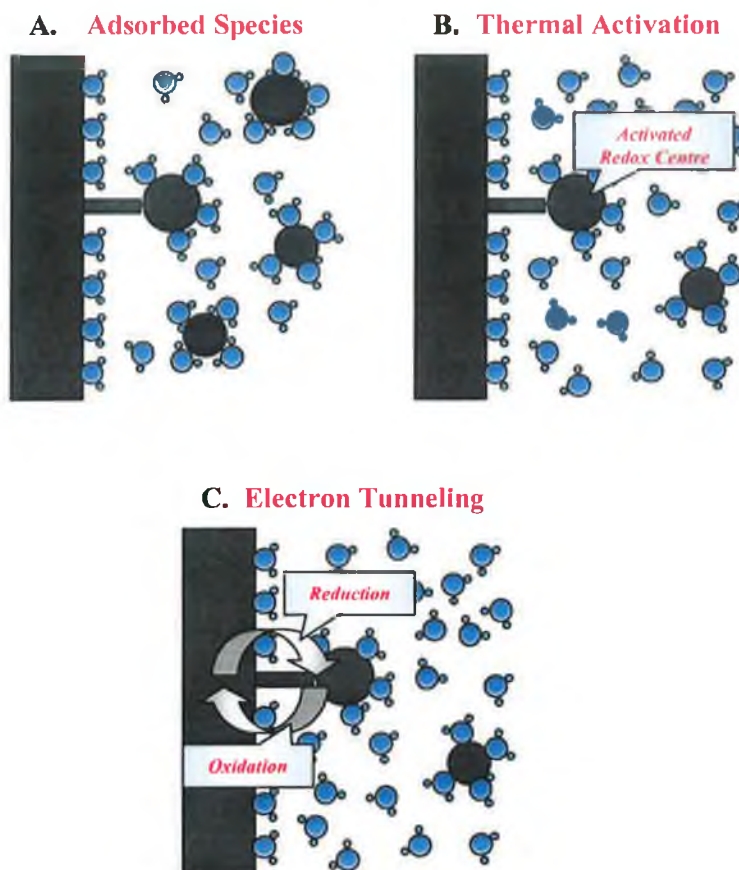
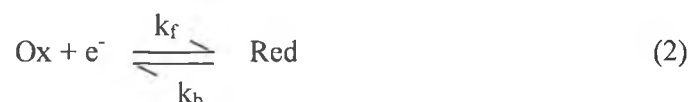


Figure 2. Elementary steps involved in a heterogeneous electron transfer reaction, adsorption of redox molecule, thermal activation and electron tunneling.

The first model presented in this section to explain the heterogeneous electron transfer process is the Butler-Volmer model, which is a macroscopic model containing a minimum number of parameters. The second model is the classical Marcus Theory of electron transfer developed from 1956 to 1965 by Professor Rudolph A. Marcus. This theory is used extensively to describe both homogeneous and heterogeneous electron transfer reactions and forms the basis of more complicated theories of electron transfer.

1.2.2 Butler Volmer Model

The Butler Volmer model^{21,22} of electrode kinetics is the oldest and least complicated theory available to describe heterogeneous electron transfer. A simple electron exchange between a redox species in an electrolytic solution and an electrode can be written as,



where k_f and k_b are the electrochemical rate constants for the forward and reverse reactions respectively. In accordance with transition state theory, a reaction coordinate diagram²³ is illustrated in Figure 3 to explain the change in free energy of the system as the reactant is reduced to the product-state. For electron transfer to occur, the oxidized molecule, moves from its equilibrium structure, position A along the reaction coordinate to position B, the transition state. It is here that electron transfer occurs as the internal and solvent structure of the reactant molecule becomes more like that of the product state. Thus, the Frank Condon principal is fulfilled, which states that electron transfer is an instantaneous process, i.e. reactants and products share a common nuclear configuration at the moment of electron transfer.²⁴ The rate at which an electron transfers will therefore depend on the magnitude of the structural difference between the reactant and product states. Accounting for these structural differences is beyond the scope of this theory but is dealt with more fully in the Marcus Theory of electron transfer presented later.

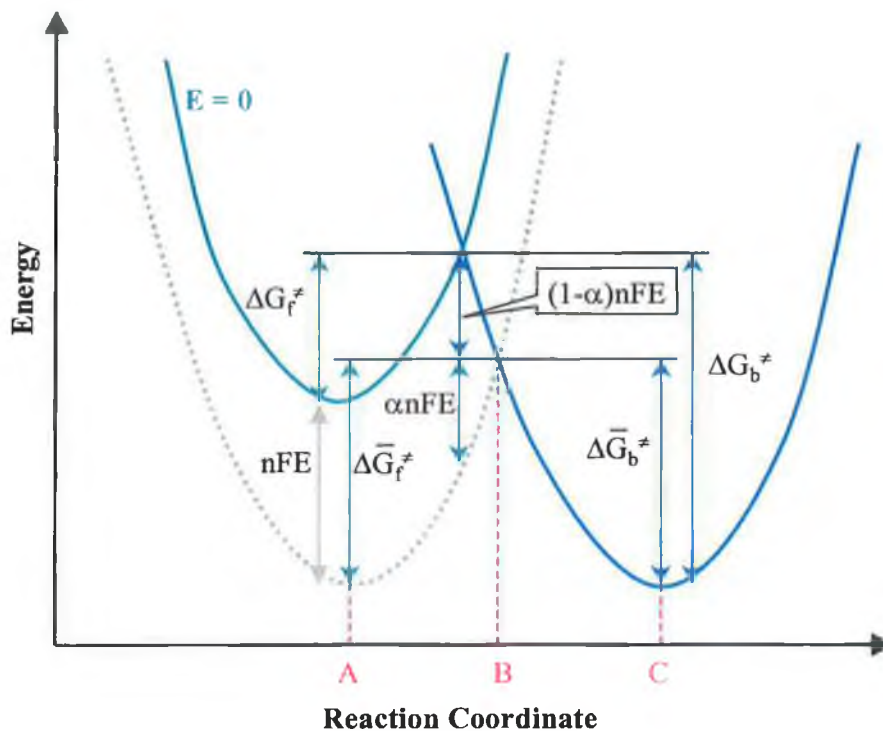


Figure 3. Reaction coordinate diagram illustrating the effect of potential on the free energy of activation for oxidation and reduction processes, according to the Butler Volmer model of electron transfer. (—) represents the equilibrium state of the reactant at $E=0$, this equilibrium shifts to (---) when a potential is applied, and (---) represents the equilibrium state of the product. A, and C denote the equilibrium structure of reactant, (oxidized) and product, (reduced) states, and B is the transition state where electron transfer occurs.

Considering Equation (2) as a chemical as opposed to an electrochemical reaction; simplified activation complex theory assumes an Arrhenius type dependence of the forward rate constant, k_f on the chemical free energy of activation, ΔG^\ddagger , Equation (3).

$$k_f = \frac{k_B T}{h} \exp\left(\frac{-\Delta G^\ddagger}{RT}\right) \quad (3)$$

where k , h and R are the Boltzmann, Planck and gas constants, respectively, and T is the absolute temperature. However, in electrochemical measurements the driving force for a reaction can be controlled instrumentally by changing the electrical driving force, i.e.,

the applied potential relative to the formal potential for the redox species. Therefore, in studying heterogeneous electron transfer the free energy of the reaction is controlled by the electrical driving force and the chemical free energy, ΔG^\ddagger is replaced by the electrochemical free energy, $\Delta \bar{G}_f^\ddagger$.

The electrochemical rate constant for the forward reaction, i.e., reduction, is given by Equation (4):

$$k_f = \frac{kT}{h} \exp\left(\frac{-\Delta \bar{G}_f^\ddagger}{RT}\right) \quad (4)$$

The potential energy profiles for reactant (green) and product (blue) states are illustrated in Figure 3. The grey dashed line shows that a shift in the potential of the electrode to a value E changes the energy of the electrons within the electrode by an amount nFE . As a result the barrier for the oxidation process, ΔG_b^\ddagger is less than ΔG_b by a fraction of the total free energy. This fraction is equal to $(1-\alpha)$, where α is the transfer coefficient. It takes on values from 0 to 1 depending on the shape of the free energy curves in the intersection region. Thus, the electrochemical free energies of activation can be described as follows,

$$\Delta \bar{G}_f^\ddagger = \Delta G_f^\ddagger + \alpha nFE \quad (5)$$

$$\Delta \bar{G}_b^\ddagger = \Delta G_b^\ddagger - (1-\alpha)nFE \quad (6)$$

Substitution of these expressions into Equation (4) yields Equations (7) and (8), which describe the potential dependence of the reduction and oxidation reactions, respectively.

$$k_f = \frac{kT}{h} \exp\left(\frac{-\Delta G_f^\ddagger}{RT}\right) \exp\left(\frac{-\alpha nFE}{RT}\right) \quad (7)$$

$$k_b = \frac{kT}{h} \exp\left(\frac{-\Delta G_b^\ddagger}{RT}\right) \exp\left(\frac{(1-\alpha)nFE}{RT}\right) \quad (8)$$

The first exponential term in both equations is independent of the applied potential and is designated as k_f^0 and k_b^0 for the reductive and oxidative reactions, respectively. They represent the rate constants for a reaction at equilibrium, i.e., for a solution, which contains an equal concentration of oxidized and reduced species. However, the system is at equilibrium at the formal potential, E^0 , and the product of the rate constant and the concentration are equal for the forward and backward reactions, i.e., k_f^0 equals k_b^0 . Therefore, the standard rate constant is written as k^0 . Substitution into equations (7) and (8) yields the Butler Volmer equations (9) and (10).

$$k_f = k^0 \exp\left(\frac{-\alpha nF(E - E^0)}{RT}\right) \quad (9)$$

$$k_b = k^0 \exp\left(\frac{(1 - \alpha)nF(E - E^0)}{RT}\right) \quad (10)$$

Hence, k^0 is a measure of the rate of heterogeneous electron transfer at zero driving force, i.e., at the formal potential, E^0 and its units are s^{-1} for an adsorbed reactant. The Butler Volmer formulation provides a theoretical description of electrode kinetics, which can be verified through experiment. The overpotential is the difference between the applied electrode potential, E and the formal potential of the redox couple, E^0 . Equations (9) and (10) predict that a plot of the logarithm of the measured heterogeneous rate constant versus the formal overpotential, η , yields values for α and k^0 from the slope and intercept, respectively.

However, as mentioned previously, the Butler Volmer analysis is a simplified model containing a minimum number of parameters. It does not take into consideration many of the molecular factors that influence the rate of electron transfer. For example, the rate at which an electron transfers from the reactant to the product state depends greatly on the structural difference of these two forms. The Marcus theory contains parameters, which take into consideration changes in the redox molecules structure upon conversion from the reactant to product state and the effect of solvent in determining the electron transfer rate. Also the distance dependence of electron transfer is accounted for in the Marcus model through a probability factor depending on whether the reactant and electrode are strongly or weakly coupled. Finally, the assumption that the rate constant

of electron transfer scales exponentially with increasing overpotential is not complete since at high overpotentials a deviation from linearity appears. This behaviour is predicted by the Marcus model.

1.2.3 Marcus Theory of Heterogeneous Electron Transfer

The Marcus theory^{25,26,27,28} provides a more complete description of the factors that affect both homogeneous and heterogeneous electron transfer. Here it is applied solely to a heterogeneous process such as that illustrated in Figure 2 above. Similar to the Butler Volmer model described previously, transition state theory focuses on the intersection point of the free energy curves for the oxidised and reduced forms (designated as reactant, (R) and product, (P) in Figure 4). In the Marcus theory the curvature of the reactant and product surfaces is assumed to be equal, hence parabolic energy surfaces^{29,30} as a function of reaction coordinate are used to describe a number of conditions outlined below. In order for electron transfer to occur in either direction the system has to surmount an energy barrier, ΔG^* , the Gibbs energy of activation. ΔG^0 represents the difference in Gibbs energy between the equilibrium configurations of the reactant and product states.

According to the Marcus theory of electron transfer, the rate of heterogeneous electron transfer can be determined from Equation (11).

$$k^{\circ} = \nu \sigma \exp\left(\frac{-\Delta G^{\circ}}{RT}\right) \quad (11)$$

where R is the gas constant, T is the absolute temperature, ν is the frequency factor, which describes the rate of reactive crossings of the transition state, σ is an equivalent reaction layer thickness and ΔG^* is the free energy of activation.

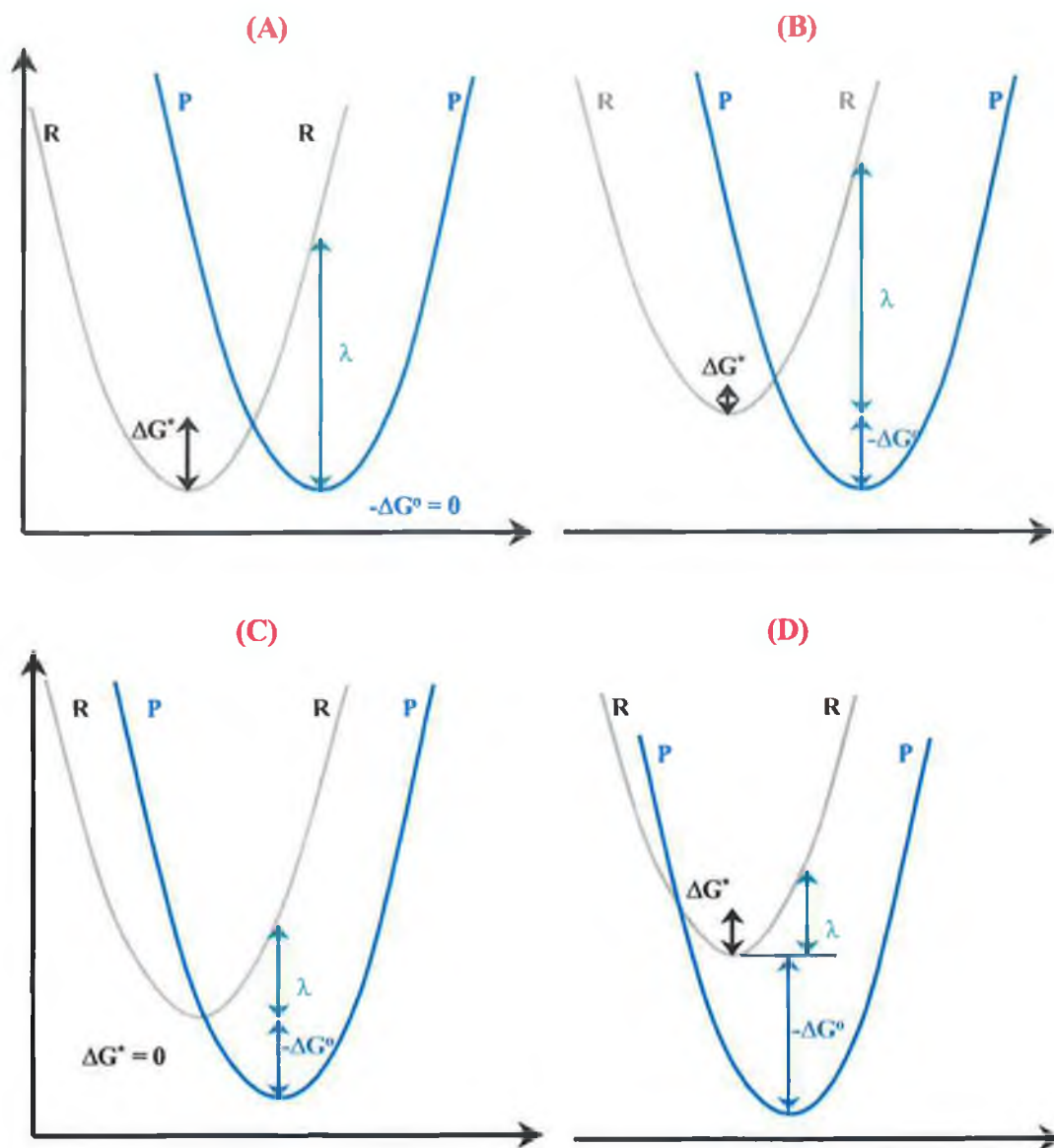


Figure 4. Reaction coordinate diagrams illustrating the Gibbs free energy curves for reactant (R) and product (P) states : (A) reactant and product surfaces have same energy, $\Delta G^\circ = 0$, (B) the normal region where $0 \leq -\Delta G^\circ \leq \lambda$, (C) maximum rate constant region where $-\Delta G^\circ = \lambda$, (D) the inverted region where $-\Delta G^\circ > \lambda$.

Figure 4 displays four different situations where the free energy of the reactant and product curves vary, thus having an effect on the electron transfer rate measured. Figure 4(A) represents the situation where the energy of the equilibrium reactant and product states is equal. However, the activation energy is significant for the reaction to occur. Another parameter, which is significant in the Marcus model is the reorganisation energy, which can be defined as the energy required to convert the reactant geometry and surrounding media to the equilibrium product state without transfer of the electron.^{23,30} As evident from Figure 4(A) the free energy of activation is a quarter of the reorganisation energy,

$$\Delta G^{\ddagger} = \frac{\lambda}{4} \quad (12)$$

If we consider the situation where the energy of the product state shifts vertically by an amount ΔG° with respect to the reactant state as illustrated in Figure 4(B) it follows that,

$$\Delta G^{\ddagger} = \frac{(\lambda + \Delta G^{\circ})^2}{4\lambda} \quad (13)$$

By substitution of Equation (13) into Equation (11) we obtain the classical Marcus Equation (14).

$$k^{\circ} = \nu \sigma \exp\left(-\frac{(\lambda + \Delta G^{\circ})^2}{4\lambda RT}\right) \quad (14)$$

Thus, the effect of increasing the difference in Gibbs energy between the equilibrium reactant and product states, ΔG° on the electron transfer rate can be easily investigated. As ΔG° decreases, the rate of electron transfer increases until $\Delta G^{\circ} = \lambda$. At this point the activation energy, ΔG^{\ddagger} decreases to zero as there is no energy barrier to surmount for electron transfer to proceed, Figure 4(C). The electron transfer rate reaches its maximum value as $k^{\circ} = \nu$; from Equation (14). However, as ΔG° becomes more negative, the intersection point of reactant and product curves moves more to the left of the center of the reactant curve, as illustrated in Figure 4(D). Now the activation energy increases again and the difference in free energy between the reactant and product

states, ΔG° will become greater than the reorganisation energy, λ . Hence, from Equation (14) it follows that the rate of electron transfer will decrease with increasing ΔG° . This phenomenon is known as the *Marcus Inverted Region* and was treated with much skepticism in the 1960s, as this prediction was completely counter to chemist's expectations. Experimental work carried out in the 1980s verified the existence of such a region and some of this work will be presented briefly in Section 1.3.1 of this chapter.

1.2.3.1 The Reorganisation Energy

The reorganisation energy defined above consists of two contributions, an inner sphere and outer sphere component, $\lambda = \lambda_{is} + \lambda_{os}$. The solvent reorganisation energy is denoted λ_{os} and it involves changes in the polarisation and orientation of solvent molecules around the reactant and product states. The expression for the outer sphere reorganisation energy is derived from the dielectric continuum theory and is given by:

$$\lambda_{out} = \frac{(\Delta e^2)}{4\pi\epsilon_0} \left[\frac{1}{2R_D} + \frac{1}{2R_A} - \frac{1}{r_{DA}} \right] \left[\frac{1}{\epsilon_{op}} - \frac{1}{\epsilon_s} \right] \quad (15)$$

where Δe is the electronic charge transferred in the reaction, ϵ_0 is the permittivity of free space, R_D and R_A are the radii of the donor and acceptor moieties respectively, r_{DA} , is the distance between the donor and acceptor, ϵ_{op} and ϵ_s are the optical and static dielectric constants of the surrounding solvent medium. By varying the dielectric constant of the solvent medium used in the experiment, the outer sphere component of the reorganization energy and therefore the total reorganization energy of a given system may be changed.

λ_{is} is a solvent independent term and is defined as the energy required to reorganise the inner shell of atoms close to the redox centre as the reactant is converted to the product state.²³ As the structure of the reactive molecule adsorbed on the electrode surface is frequently not known it is difficult to calculate the inner sphere contribution to the total reorganisation energy. The inner sphere component is given in Equation (16).

$$\lambda_{in} = \sum_j \frac{f_j^r f_j^p}{f_j^r + f_j^p} (\Delta q_j)^2 \quad (16)$$

where f_j^r is the j^{th} normal mode force constant in the reactant species and f_j^p is the j^{th} normal mode force constant in the product species, and Δq_j is the equilibrium displacement of the j^{th} normal coordinate.

1.2.3.2 Adiabatic vs. Non-Adiabatic Electron Transfer

The pre-factor in Equation (11) comprises two factors, ν , the vibrational frequency and κ_{el} , the transmission coefficient. These two factors control respectively the rate of promotion of an electron from the reactant to the product state and the probability of transferring from one state to the other, once the transition state has been reached.

$$\nu = \nu \kappa_{el} \quad (17)$$

Two types of electron transfer are possible, depending on the strength of electronic coupling between the redox species and the electrode.³¹ If the redox molecule is adsorbed strongly on the electrode surface, the reaction can be termed adiabatic, as there is significant overlap between the molecular orbitals and the electrode. The transmission coefficient approaches unity and there is significant flattening of the reaction hypersurface, as illustrated in Figure 5(A). In this case the rate of crossing over the transition state is decreased, but the probability of electron transfer occurring once the transition state is reached is increased. Heterogeneous electron transfer reactions are often assumed to be adiabatic as it simplifies the analysis. This assumption is only reasonable if the distance between the redox center and electrode is very small. For instance anthraquinone molecules are adsorbed approximately 4 Å from the surface and adiabatic electron transfer is likely. However, the redox center in alkanethiol monolayers and osmium and ruthenium redox centers are adsorbed in the range 10-30 Å from the electrode surface and experimental studies, which are discussed in the following sections of this review show that non-adiabatic electron transfer results.

The second classification to be considered is non-adiabatic, also known as diabatic electron transfer. In this case, the reactant and product curves have no significant

interaction and the probability of crossing over the transition state to the product is greatly reduced. The electronic transmission factor is less than 1. As illustrated in Figure 5(B) when we proceed along the reaction coordinate, the system often returns to the equilibrium state of the reactant when it reaches the intersection region. Occasionally the reaction proceeds to the product state resulting in an electron transfer occurring.

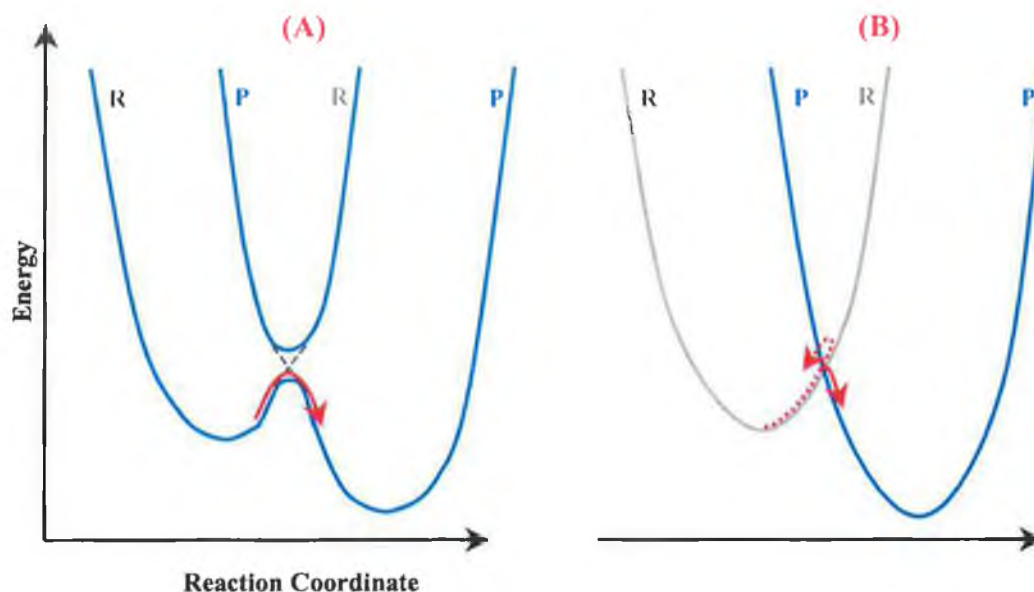


Figure 5. Reaction coordinate diagrams for (A) adiabatic and (B) diabatic electron transfer showing the splitting of the energy curves in the intersection region. (A) A strong interaction exists between the adsorbate and the electrode, if the reactant reaches the transition state the probability is high that it will proceed to the product state, as indicated by the curved arrow. (B) A weak interaction exists, thus when the reactant reaches the transition state it has a tendency to remain on the reactant curve, the crossover probability is small.

1.3 Electron Transfer Kinetics of Adsorbed Monolayers

After describing the principal electron transfer models used in the study of heterogeneous electron transfer processes some of the experimental studies carried out recently to probe these theories are now reviewed. Much of this research concentrates on self-assembled alkanethiol monolayers adsorbed on gold surfaces and spontaneously

adsorbed osmium and ruthenium complexes on platinum. Anthraquinone derivatives are the focus of the experimental work presented in this thesis so the mechanism of coupled proton and electron transfer reactions is looked at in more detail in Section 1.4. The principal difference in the three aforementioned classes of adsorbed moieties is the distance of the electroactive redox centre from the electrode surface. In the case of alkanethiols the redox active center is held approximately 20-30Å from the surface, while osmium and ruthenium complexes are adsorbed approximately 10Å from the electrode surface.^{32,33} As explained in section 1.5 of this chapter anthraquinones are adsorbed closer to the electrode surface (~4 Å). This will affect both the mechanism and rate of electron transfer for these molecules and this forms the basis of the experimental work presented in Chapter 5 of this document.

1.3.1 Alkanethiol Monolayers

Alkanethiol monolayers with attached redox active centers are useful model systems for the investigation of electron transfer rates due to their ability to adsorb onto metal surfaces in an ordered and close packed arrangement.

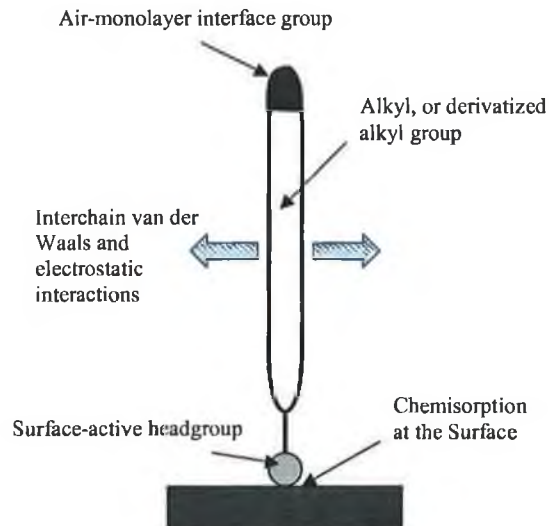


Figure 6. A schematic view of the forces in a self assembled alkanethiol monolayer with an attached redox active group held at a fixed distance from the electrode surface.

Chidsey and coworkers^{34,35} published two papers in the early 1990s probing electron transfer rates between a gold electrode and an electroactive ferrocene group held at a fixed distance from the electrode by an alkanethiol chain. The ferrocene-terminated

thiols were coadsorbed with unsubstituted alkanethiols, thus keeping the electroactive ferrocene groups well separated from each other. The length of the alkanethiol chains were varied to investigate the distance dependence of the electron transfer rate. This study showed that the rate of electron transfer falls off exponentially with increasing distance from the electrode surface and agrees with earlier work carried out by Li and Weaver.³⁶

In Chidsey's study rate constants were measured using chronoamperometry, a potential step technique described in more detail in section 1.6.2 of this chapter. Briefly it consists of stepping from an initial potential to a final potential to drive the oxidation or reduction of the redox centre and measuring the current decay, which can be analysed to obtain a value for the rate constant. Rate constants were measured at a number of overpotentials and the results fitted to the Butler Volmer and Marcus theories of electron transfer. The dashed line in Figure 7 shows the Butler Volmer fit, which does not provide an adequate fit to the experimental data far from the formal potential. The curvature in the data at high overpotentials is better described by the Marcus theory of electron transfer (Marcus inverted region). The other various dashed and solid lines in Figure 7 are model Marcus fits, predicted using different values for the reorganization energy, λ and the electronic coupling factor, κ_{el} . The curve with $\lambda = 0.85$ eV and coupling of 10^{-6} approximates the experimental data quite well. Hence, the interaction between the redox center and the electrode surface is weak and the electron transfer process is classed as non-adiabatic.

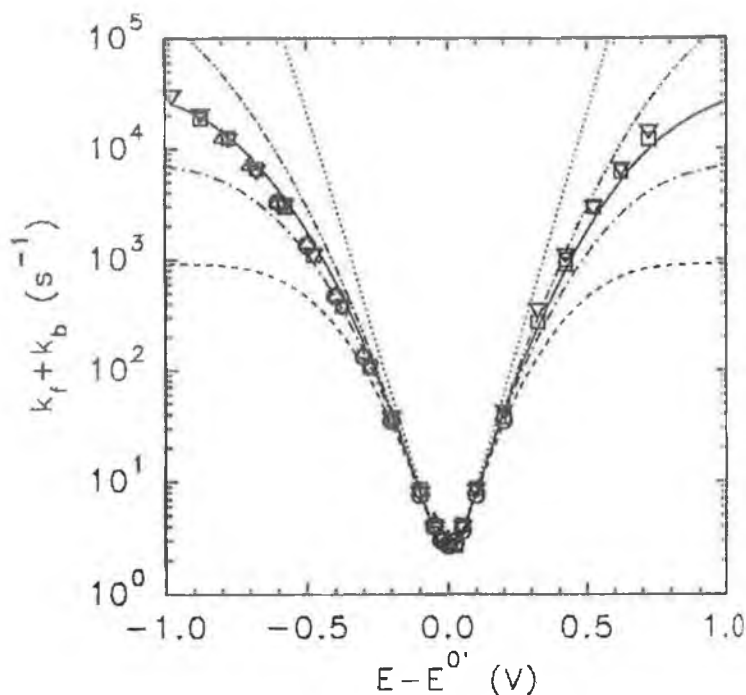


Figure 7. Semi-log plot of the measured decay rate constants at 25°C (symbols) for mixed monolayers of ferrocene terminated alkanethiol and unsubstituted alkanethiol adsorbed on gold, and calculated decay constants from the Butler Volmer model with $k^0 = 1.25 \text{ s}^{-1}$, $\alpha = 0.5$ (dotted); and the Marcus model with : $\lambda = 1.1 \text{ eV}$, $\nu = 7.48 \times 10^5 \text{ s}^{-1} \text{ eV}^{-1}$ (dot-dot-dashed); $\lambda = 0.85 \text{ eV}$, $\nu = 6.73 \times 10^4 \text{ s}^{-1} \text{ eV}^{-1}$ (solid); $\lambda = 0.7 \text{ eV}$, $\nu = 1.55 \times 10^4 \text{ s}^{-1} \text{ eV}^{-1}$ (dot-dashed) and $\lambda = 0.5 \text{ eV}$, $\nu = 2.29 \times 10^3 \text{ s}^{-1} \text{ eV}^{-1}$ (dashed).

Further work on substituted alkanethiol systems has been carried out by Finklea and coworkers.^{37,38} In these two papers, the kinetics of electron transfer were examined as a function of electrolyte concentration and temperature. The monolayers were formed on gold electrodes by coadsorption of an alkanethiol with a pendent $\text{pyRu}(\text{NH}_3)_5$ redox center with an alkanethiol with a terminal carboxylic acid group. These studies compare the electron transfer rates obtained from two experimental methods, cyclic voltammetry and chronoamperometry. In potential sweep experiments, when the timescale of the experiment becomes comparable to the rate of heterogeneous electron transfer peak splitting between the cathodic and anodic branches occurs. This peak-to-peak splitting can be converted into a standard rate constant using Laviron's formulation,³⁹ which is based on the Butler Volmer Theory of electron transfer. This method for the estimation of the standard heterogeneous electron transfer rate is less accurate than the chronoamperometric method presented in Chidsey's work above due

to a number of factors. Firstly, the peak splitting observed may be due to ohmic drop effects if the electrode is not sufficiently small. Secondly, and more importantly, Laviron's theory assumes that the transfer coefficient is equal for cathodic and anodic branches ($\alpha = 0.5$) and is independent of the applied potential. It is evident from Tafel plots that this is not the case, the transfer coefficient changes markedly with the applied potential. However, Finklea reports that the rate constants determined from CV measurements generally agree with chronoamperometric measurements within a factor of two. Hence, the peak splitting observed in CV provides a rapid and qualitative method for estimation of the rate constant.

1.3.2 Osmium and Ruthenium Monolayers

Osmium and Ruthenium polypyridyl complexes have also been studied extensively to elucidate the rate and mechanism of heterogeneous electron transfer.^{32,40,41,42,43,44,45,46,47} In two extensive papers published by Forster and Faulkner^{32,42} in 1994 the dependence of the electron transfer rate on solvent, temperature and electrolyte concentration was examined. The heterogeneous electron transfer dynamics of spontaneously adsorbed osmium monolayers, $[\text{Os}(\text{bpy})_2\text{Cl}(\text{pNp})]^+$, where bpy is 2,2'-bipyridyl and pNp is either 4,4'-bipyridyl, 1,2-bis(4-pyridyl)-ethene, or 4,4'-trimethylenedipyridine were reported. As the bridging ligand between the redox centre and the electrode contain zero, two or three methylene spacer groups an investigation of the distance dependence of electron transfer was possible.

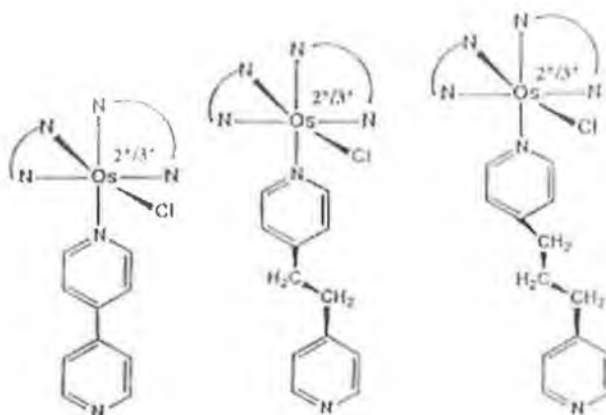


Figure 8. Schematic illustrating the structures of three osmium complexes, $[\text{Os}(\text{bpy})_2\text{Cl}(\text{pNp})]^+$, where bpy is 2,2'-bipyridyl and pNp is either 4,4'-bipyridyl, 1,2-bis(4-pyridyl)-ethene, or 4,4'-trimethylenedipyridine.

The complexes illustrated above are adsorbed 9-10Å from the electrode surface resulting in weak interactions. This result is in accordance with Chidsey's³⁵ work on the ferrocene alkanethiol system presented above. Both systems are classed as non-adiabatic. This is reasonable when the distance of the electroactive center from the electrode is taken into consideration. It is thought that a system is more likely to couple strongly with the electrode surface if adsorbed closer to the electrode and an adiabatic electron transfer would result. Forster and Faulkner's papers conclude that the Marcus theory of electron transfer provides a superior fit to the Butler Volmer formulation when the experimentally measured rate constants for the osmium complexes were analysed.

As the overpotential was increased in chronoamperometry measurements the rate of electron transfer increased. However at high overpotentials the rate became independent of overpotential and a curvature was observed in the Tafel plots. This curvature was not predicted by the Butler Volmer approach, as this is only a low driving force limiting case of the Marcus theory. The rate constant data obtained at overpotentials of over 200 mV has been fit to the Marcus theory and values for the reorganization energy have been elucidated. Best fits of the experimental data yield reorganization energies of 27.7 and 26.4 kJ mol⁻¹ for p2p and p3p monolayers, respectively. These values compare well with a value of 25.5 kJ mol⁻¹ when the theoretical value for outer sphere reorganization was calculated from the Marcus theory

of electron transfer. Hence it has been concluded that the total reorganization in this system was due to solvent reorganization.

A later paper by Forster and Faulkner⁴³ deals with the electrochemical properties of binary monolayers formed by the coadsorption of $[\text{Os}(\text{bpy})_2\text{Cl}(\text{p2p})]^+$ and $[\text{Ru}(\text{bpy})_2\text{Cl}(\text{p2p})]^+$, where bpy is 2,2'-dipyridyl and p2p is 1,2-bis(4-pyridyl)ethane. These two redox species have the same formal potential and so the surface coverage of the two adsorbates cannot be determined by conventional cyclic voltammetry measurements. However, as shown in the previous papers, the rate of heterogeneous electron transfer depends on the distance of the redox centre from the electrode surface and this is used to determine surface coverages of the two adsorbates within two component monolayers. Chronoamperometry reveals three single exponential decays following a potential step, which changes the redox states of the adsorbates. These exponential decays correspond to double layer charging of the electrode and heterogeneous electron transfer to the two redox centers. RC cell time constants were in the range 50–500 ns, depending on the electrode radius and the electrolyte concentration used. The heterogeneous electron transfer rate constants measured at an overpotential of 50 mV for the osmium and ruthenium centers within the monolayer were $8.7 \pm 0.3 \times 10^5$ and $1.1 \pm 0.2 \times 10^4 \text{ s}^{-1}$, respectively. In this work the heterogeneous electron transfer rates have been measured as the solution concentration ratio of the two complexes used to form the monolayers was varied from 0.1 to 0.9. The electron transfer rates were seen to vary very little as the solution concentrations were changed and this implies that lateral interactions between the two redox centers was not important in this system even at high surface coverages. In conclusion this paper presented an alternative way to determine the surface coverages in a two component assembly, not on the basis of different thermodynamic properties, but on the basis of different heterogeneous rate constants.

In a more recent paper Forster and O'Kelly⁴⁵ looked at the pH dependence of the heterogeneous electron transfer rate. For an $[\text{Os}(\text{bpy})_2(\text{p3p})_2]^{2+}$ monolayer, where bpy is 2,2'-bipyridyl and p3p is 4,4'-trimethylenedipyridine. This complex adsorbs to the platinum electrode surface through a free pyridine ring while the other pyridine ring of the p3p ligand is free for protonation. The extent of protonation of this ligand has a varying effect on the measured rate of electron transfer across the monolayer-electrode

interface and this was investigated by fitting experimental data to a Marcus model proposed by Finklea and Hanshew. Best fits of the experimental data to the Marcus model at varying pH's are presented in Figure 9.

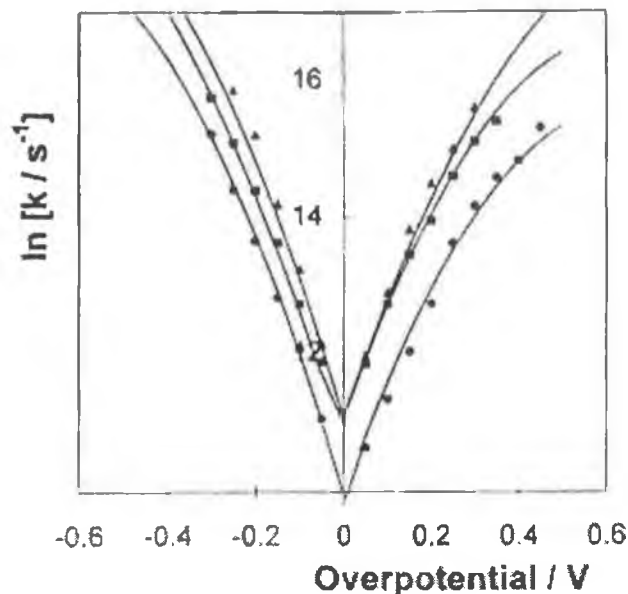


Figure 9. Tafel plots for $[\text{Os}(\text{bpy})_2(\text{p3p})_2]^{2+}$ monolayers, where bpy is 2,2'-bipyridyl and p3p is 4,4'-trimethylenedipyridine adsorbed on a platinum electrode surface as a function of the supporting electrolyte pH. The data (top to bottom, right hand side) represent electrolyte pH's of 5.05, 3.10, and 1.07, respectively. The solid lines denote theoretical fits obtained from a through space tunneling model where $\lambda = 100, 68,$ and 56 kJ mol^{-1} from top to bottom respectively.

The significant feature of these results is that the reorganisation energy varies with pH in the range 5.05 to 1.07. At low pH the reorganisation energy is predominantly due to outer sphere reorganization, λ_{os} as Finklea and Hanshew's model provides a value of 56 kJ mol^{-1} for the solvent reorganisation, which is in good agreement with the value of 56.9 kJ mol^{-1} calculated from the theoretical Marcus equation. However, at high pH values, the experimental reorganisation energy reported for non-protonated monolayers was significantly larger (100 kJmol^{-1}) than that predicted for solvent reorganization. Hence, the inner sphere component, λ_{is} must contribute to the reorganisation energy, possibly due to reorientation of the adsorbate on the electrode surface.

The final paper to be reviewed in this section shows how rate constants are determined from cyclic voltammetry data.⁴⁷ The study centers around dense monolayers of $[\text{Os}(\text{OMe-bpy})_2(\text{p3p})\text{Cl}]^{1+}$, where OMe-bpy is 4,4'-dimethoxy-2,2'-bipyridyl and p3p is 4,4'-trimethylenedipyridine adsorbed on platinum, mercury, gold, silver, carbon, and copper microelectrodes. The objective of the paper was to see if the nature of the electrode material had an effect on the rate and mechanism of electron transfer. The fast scan rate CV data (2000 Vs^{-1}) was fit to a model, again based on Finklea and Hanshew's non-adiabatic Marcus model for heterogeneous electron transfer. Figure 10 shows high scan rate cyclic voltammetric behaviour for monolayers immobilized on carbon and platinum microelectrodes. The peak-to-peak separations at high scan rates are significantly larger than those observed at low scan rates. Slow heterogeneous electron transfer could explain this increased peak separation as discussed earlier in this chapter. The two adjustable parameters in the fitting model used were the standard rate constant, k^0 and the free energy of activation, ΔG^\ddagger . The rate constants measured were in the range 10^3 to 10^4 s^{-1} depending on the electrode material used. One of the conclusions from this work is that cyclic voltammetry can provide a convenient approach for determining the electron transfer rate, however, it is not particularly sensitive to changes in the free energy. When the free energy of activation was changed by 25 % the residual sum of squares between the predicted and experimental peak currents increased by less than 10 %. A comparison of the cyclic voltammetry and chronoamperometry methods for the elucidation of heterogeneous rate constants is presented in Chapter 5 of this report also.

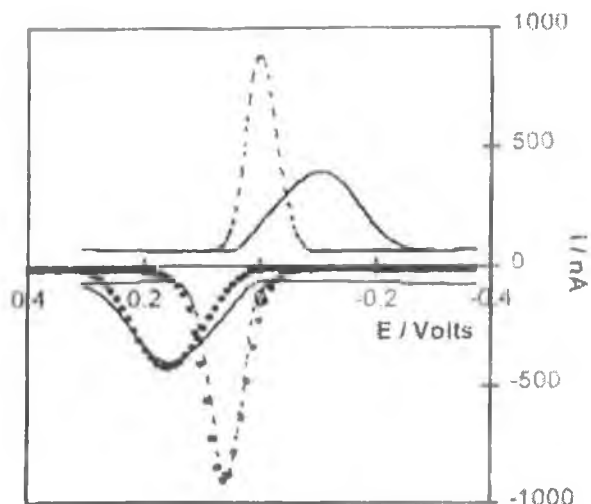
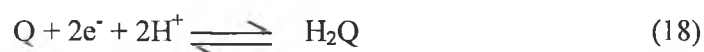


Figure 10. Experimental voltammetric responses for 5 μm radius carbon (—) and platinum (---) microelectrodes modified with $[\text{Os}(\text{OMe-bpy})_2(\text{p3p})\text{Cl}]^{1+}$ monolayers. The scan rate is 2000 Vs^{-1} for both CV's, and the supporting electrolyte is 1 M aqueous NaClO_4 . The data points represent optimized fits to a non-adiabatic electron transfer model in which k^0 is 4×10^3 and $6 \times 10^4 \text{ s}^{-1}$ for carbon and platinum, respectively. The free energy of activation, ΔG^\ddagger , is 6.8 kJ mol^{-1} for both electrode materials.

1.4 Proton Coupled Electron Transfer

Proton coupled electron transfer reactions occur frequently in biological systems and are also significant in areas of research relating to corrosion and sensors. Quinone couples have been used extensively as model systems for this study and have been the subject of reviews by Chambers,¹³ more recently by Goldsby and coworkers⁴⁸ and Okamura and coworkers.¹⁴ The reduction of a quinone, Q to a hydroquinone, H_2Q species involves the transfer of two electrons coupled to the uptake of two protons from solution,⁴⁹ the reaction mechanism in low pH solution can be summarised as follows:



The mechanism of proton and electron transfer is not yet fully understood, although many papers by authors such as Vetter,^{50,51} Laviron^{52,53,54,55} and Wightman^{56,57,58} have focused on this topic. Vetter's early work in the 1950s, looked at the redox chemistry

of p-benzoquinone/hydroquinone adsorbed on a platinum electrode. The proposition from these papers that the mechanism of proton and electron transfer varies with pH is widely accepted. Laviron's theoretical work in the early 1980s is the most informative and conclusive to date. The analysis considers all of the possible intermediates involved, the rates of electron transfer in the system, the pK_a s of all reactants, intermediates and products and the formal potentials for the single electron transfers. Laviron's analysis is based around a scheme of squares, known as the "nine-member box scheme" illustrated in Figure 11.

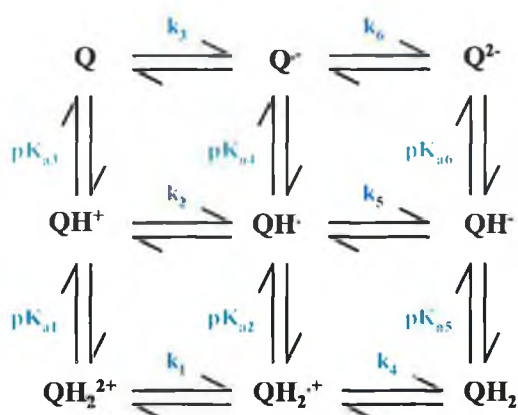


Figure 11. 9-member box scheme.

Quinones are most suitable for probing coupled proton and electron transfer reactions due to the binding of protons by quinone molecules in many different redox states, quinone (Q), semiquinone ($\text{Q}^{\cdot-}$) and hydroquinone (H_2Q). The extent to which each of these states binds protons varies and is reflected in the pK_a values, which can be measured experimentally for the different redox states with varying degrees of success. Values of the acid-base dissociation constants have been published extensively. These show conclusively that binding of the protons by the semiquinone is relatively weak, pK_a values of approximately 4 (pK_{a4} in Figure 11). The binding of protons by the reduced hydroquinone form is relatively stronger, pK_a values are reported to be in the range 9.85 to 11.40 for QH_2/QH^- and QH/Q^{2-} respectively^{55,56} (pK_{a5} and pK_{a6} in Figure 11).

1.4.1 Evaluation of the Reaction Sequence

In order to elucidate what the reaction sequence is in the oxidation or reduction direction, a first step is to determine whether proton or electron transfer steps are rate limiting. A number of cases have been considered in literature, mechanisms in which proton transfer precedes electron transfer, eH , electron transfer precedes proton transfer, eH , and the case where electron and proton transfer occur in a concerted fashion. The mechanism by which the coupled proton electron reaction proceeds depends on the pH of the system. This is demonstrated in the electrochemical investigation of anthraquinone-2,7-disulphonic acid (2,7-AQDS) carried out by Forster and O'Kelly.^{59,60} In this study the pH dependence of the rate of heterogeneous electron transfer is probed, both in solution and when 2,7-AQDS is adsorbed on a mercury surface. The rate of electron transfer and hence the reaction mechanism is seen to be dependent on the solution pH, in agreement with Laviron's and Vetter's predictions.

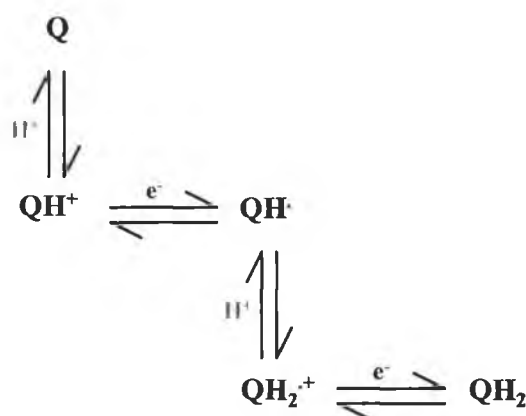


Figure 12. Simplified 9-member box scheme.

In low pH electrolyte solution the scheme of squares can be simplified if the unlikely intermediates of Q^{2-} and QH_2^{2+} are ignored, due to their extreme pK_a values.⁵⁷ The most likely intermediates are thus presented in Figure 12, leading to a mechanism, which involves a $H^+e^-H^+e^-$ transfer process in the reduction step and the opposite for the oxidation step. This has been probed experimentally by Forster and O'Kelly by looking at the pH dependence of the formal potential. The Nernst equation⁶¹ presented below

predicts that the formal potential will shift in a negative potential direction with an increase in the solution pH.

$$E = E^0 - \frac{0.0592}{n} \log \frac{[H_2Q]}{[Q]} - 0.0592(m/n)pH \quad (19)$$

The cyclic voltammograms recorded for 2,7-AQDS in the pH range 2.8 to 6.1 show a negative shift in potential with increasing pH as illustrated in Figure 13. The inset of this figure shows that the potential varies with pH, with a slope of 78 mV per pH unit up to a pH of 3.9. This slope can be used to predict the number of electrons involved in the redox reaction. Equation (19) predicts a slope of 59mV for a n-electron/m-proton reaction. The slope determined experimentally is closest to that predicted for the transfer of an equal number of protons and electrons and hence we can conclude that the quinone/hydroquinone reaction involves the transfer of 2 protons and 2 electrons as predicted.

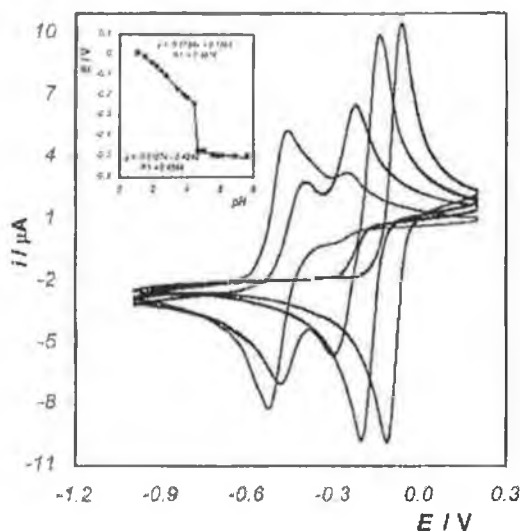


Figure 13. Cyclic voltammograms for a mercury electrode immersed in a 5mM solution of 2,7-AQDS as the pH of the unbuffered contacting electrolyte solution, 0.1 M LiClO₄ is varied using either HClO₄ or NaOH. The pH values from left to right are 2.8, 3.5, 4.8 and 6.1. The scan rate is 0.1 Vs⁻¹. Cathodic currents are up and anodic currents are down. The initial potential is -1.000 V. The inset shows the dependence of the formal potential on the solution pH.

Also evident from the inset of Figure 13 is the independence of the formal potential on proton concentration in the pH range 4.1 to 13.7. This would indicate that proton transfer is possibly not involved in the redox reaction over this pH range. Electron transfer is essentially independent of proton transfer at pH values greater than 4. The proposed mechanism in this pH region is one that involves the transfer of two electrons and one proton, thus converting the quinone to a deprotonated hydroquinone form. Protonations are unimportant at high pH and the electron transfer reactions would only be affected by electron transfer kinetics. The change in mechanism may be due to the fact that protons are less readily available in solution for protonation of the monolayer at high pH values.

Another feature of the inset of Figure 13 is the dramatic shift in potential at pH 4. The formal potential shifts from -185 to -509 mV. This shift is consistent with that observed in work carried out by Bailey and Ritchie⁶² investigating the electrochemistry of solution phase quinones. These studies agree with the theoretical work of Laviron and Vetter and propose that this potential shift represents the pK_a of the semiquinone moiety, QH^\bullet . The value for pK_{a4} is not easily measured but has been reported to be in the region of 4 by Laviron.⁵⁵ Also, in the intermediate pH region, the mechanism of proton and electron transfer has not been determined absolutely but the process has been approximated as $e^-H^+H^+e^-$ by Laviron and Vetter. In contrast to this Hale and Parsons⁶³ suggest that the redox reaction at pH 4 proceeds with either $H^+e^-e^-H^+$ or $e^-H^+e^-H^+$.

Another comprehensive study of the pH dependent voltammetric behaviour of an anthraquinone monolayer has been presented by Uosaki et al.⁶⁴ The redox properties of an adsorbed mercaptohydroquinone (H_2QSH) on gold are investigated in the pH range 0-12.7 in both buffered and unbuffered solutions. In unbuffered solutions the peak potential shows a linear relationship with pH up to a value of approximately 4. The slope of the potential-pH graph is 60 mV/pH unit, which is indicative of a Nernstian two electron two proton transfer mechanism as described previously. At pH 4 a second reduction peak and corresponding oxidation peak appear in the CV in addition to the original peaks observed at lower pH values. This is similar to the behaviour observed by Forster and O'Kelly⁵⁹ for 2,7-AQDS monolayers and also for related anthraquinone derivatives, 2,6-AQDS^{65,66} and 1,2,4-AQASH.⁶⁷ In related reviews by Eggins and Chambers^{68,69} and Parker⁷⁰ dealing with the redox behaviour of Q- H_2Q systems the

same phenomenon is observed in the voltammetric response. The overall conclusion from these works is that the mechanism of the redox reaction is different at pH 4. In all of these related studies it is also evident that the sum of the charges under the redox peaks at pH 4 is identical to that found under a single redox peak at any other pH value. This suggests that over the entire pH range the redox reaction involves the transfer of two electrons but for pH values in the region of 4 two chemically distinct species cause two 1-electron transfers. These two chemically distinct species are most probably semiquinone and hydroquinone, as outlined above.

1.4.2 Electrochemical Studies of Anthraquinone Derivatives

Quinone couples have occupied an important position in the efforts to modify electrode surfaces with electroactive groups due to their well-defined and characterised electrochemical responses. Work carried out by Bailey and Ritchie⁶² described in detail the electrochemistry of various quinones in aqueous solution primarily by means of cyclic voltammetry. The nine quinones studied were chosen to represent a variety of structural types. Many of the structures, including anthraquinone-2-sulphonate, which is most relevant to this study were sulphonated in order to ensure high solubility in entirely aqueous solutions.

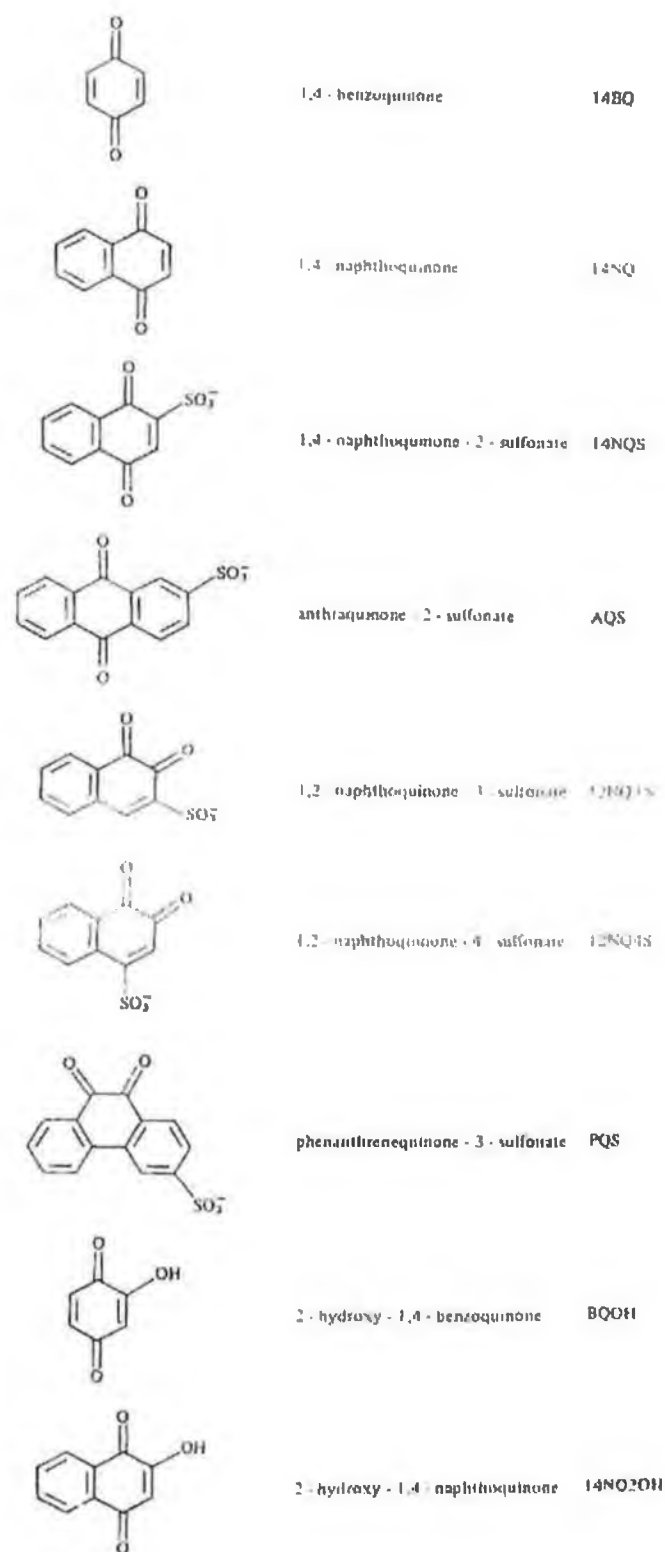


Figure 14. Structures of Anthraquinone Derivatives used in Bailey and Ritchie's studies.

The electrochemistry of sulphonated anthraquinone derivatives have been studied extensively by a number of research teams. Faulkner, Crooks and He⁶⁵ discussed the behaviour of three anthraquinonesulphonates, namely 2,6-anthraquinonedisulphonate (2,6-AQDS), 1,5-anthraquinonedisulphonate (1,5-AQDS), and 2-anthraquinonemonosulphonate (2-AQMS). They noted that 2,6-AQDS forms extremely tightly bound adsorbate layers on a mercury surface, which are stable in both redox states. This work, in common with other recent experimental investigations of 2,6-AQDS adsorbing on mercury and pyrolytic graphite electrodes^{66,71,72,73,74} reports interesting voltammetry. A spike is seen to appear in the cyclic voltammogram when high surface coverages are reached. This phenomenon has also been observed in this work⁶⁷ for 1-amino,2-sulphonic,4-hydroxyanthraquinone (1,2,4-AQASH) monolayers and will be discussed in more detail in Chapter 3.

Faulkner and coworkers⁶⁵ and Zhang and Anson⁶⁶ propose that intermolecular hydrogen bonding is responsible for the sharp voltammetric feature. When cyclic voltammograms are run from solutions containing low concentrations of the electroactive species no spike is observed in the voltammetric waves and a Langmuir response is obtained. The adsorbates are well separated at low surface coverages, hence preventing intermolecular interactions. At higher solution concentrations the adsorbates are closer on the electrode surface, thus allowing hydrogen bonding interactions between the hydroxy group on one molecule and the sulphonic group on a adjacent molecule to occur. It has also been observed in these studies that the prominence and sharpness of the spike in voltammograms strongly depends on the pH of the deposition solution. As shown in Figure 15 the spike diminishes in size and is ultimately eliminated as the pH of the supporting electrolyte is increased. It has been suggested in Faulkner's study that protonation of the sulphonate groups does not occur at high pH values, and this results in a breakdown in the hydrogen bonded network. This would account for the disappearance of the sharp spikes in cyclic voltammograms at high pH. McDermott and coworkers⁷⁴ have structurally characterised 2,6-AQDS films adsorbed on a graphite surface by means of scanning force microscopy. These results further investigate the theory of interacting adsorbates on the electrode surface and are presented in Section 1.5.2 of this chapter.

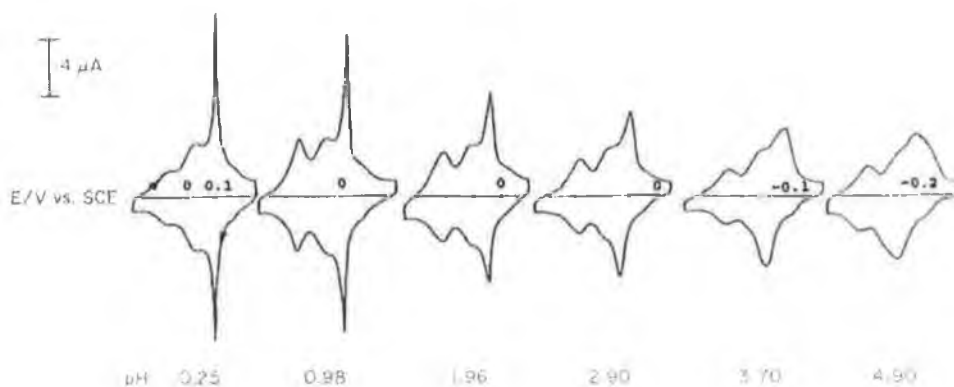


Figure 15. pH dependence of the cyclic voltammetry of 2,6-AQDS adsorbed on graphite electrodes. The electrode surfaces were saturated with 2,6-AQDS by exposure to 10^{-3} M solutions in 0.05 M H_2SO_4 for 10 min. The resulting electrodes were washed and transferred to 1 M sulphate supporting electrolytes adjusted to the indicated pH values. Scan rate is 20 mV s^{-1} .

The cyclic voltammetric response for 1,5-AQDS is significantly different from that observed for 2,6-AQDS monolayers. No spikes are seen in the voltammetry of 1,5-AQDS. Faulkner and coworkers have attributed this difference to the structural difference between 1,5-AQDS and 2,6-AQDS molecules. It is assumed in this publication that 1,5-AQDS undergoes intramolecular hydrogen bonding between the hydroxy groups in the 9 and 10 positions and the sulphonic groups in positions 1 and 5, Figure 16(B). This is not the case for 2,6-AQDS monolayers as the phenolic protons and sulphonate group are too far apart in the structure, Figure 16(A). This structural analysis by Faulkner, Crooks and He⁶⁵ presented in Figure 16 was based on cyclic voltammetry and was not otherwise experimentally proven in this publication.

The structural differences in 1,5-AQDS and 2,6-AQDS have a significant effect on the heterogeneous electron transfer rates measured for the two molecules when adsorbed on mercury and this has been shown in experimental investigations by Xu,⁷⁵ Forster,⁷⁶ He et al,⁶⁵ and Berg.⁷⁷ The heterogeneous electron transfer rate for 1,5-AQDS monolayers is about 50 times smaller than that found for 2,6-AQDS systems. This difference in kinetics is attributed in all cases to differences in the film structure and existence of internal hydrogen bonding in 1,5-AQDS films.

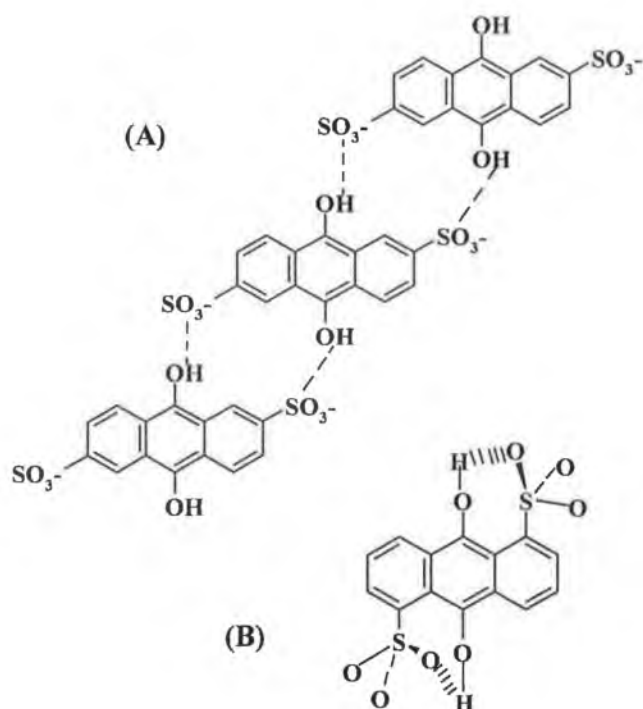


Figure 16. (A) Proposed extended hydrogen bonded structure for reduced, adsorbed 2,6-AQDS. (B) Proposed intramolecular hydrogen bonding in 1,5-AQDS.

1.4.2.1 Adsorption Isotherms

The formation of a bond between an adsorbate and an electrode surface is called adsorption. The extent of adsorption is usually expressed as a surface coverage, Γ , i.e., the fraction of the surface covered by adsorbate. Adsorption may be considered as a competition between all species in the system for sites on the electrode surface. Hence Γ will depend on the nature of the electrode material, solvent, electrolyte composition, adsorbate structure and concentration. The extent to which a surface is covered by specifically adsorbed ions or molecules can be described by adsorption isotherms that relate the amount of substrate adsorbed on the electrode per unit area, Γ , to the bulk concentration in solution.

The main isotherms are the Langmuir, Frumkin and Temkin isotherms. The Langmuir isotherm assumes no interactions between adsorbed species on the electrode surface and

at high bulk concentration saturation coverage, Γ_s is dictated simply by the size of the adsorbate. The orientation adopted by the adsorbates is that which minimises the local interfacial energy. Moreover, it is assumed that the equilibrium coverage is attained rapidly and reversibly. The Langmuir isotherm is described by the following expression:

$$\frac{\Gamma_i}{(\Gamma_s - \Gamma_i)} = \beta_i C_i \quad (20)$$

where Γ_i is the surface excess of an adsorbed species i , Γ_s is the surface excess of species i at saturation, β_i is the adsorption coefficient and C_i is the bulk concentration.

In experimental studies carried out on a number of anthraquinones outlined in chapters 3 and 4 we see that these molecules generally adsorb rapidly and reversibly to a mercury electrode surface. However in the case of single component monolayers of 1,5-dimethoxyanthraquinone (1,5-DMAQ) a period of time is required to achieve equilibrium surface coverage, this will be discussed in detail in chapter 4. If attractive or repulsive adsorbate-adsorbate interactions are present among adsorbates, then an exponential term is added to the Langmuir isotherm to account for these interactions. These forces could arise due to electrostatic interactions between charged adsorbates, e.g. hydrogen bonding. One of the simpler isotherms that considers these lateral interactions is proposed by Frumkin and is described by:

$$\beta_i C_i = \frac{\theta_i}{1 - \theta_i} \exp(g\theta_i) \quad (21)$$

where $\theta_i = \Gamma_i / \Gamma_{sat}$, Γ_i is the saturation coverage of species i in mol cm⁻² at a bulk concentration C_i , Γ_{sat} is the saturation coverage obtained at high bulk concentrations and β_i the adsorption coefficient.

The interaction parameter, g in Equation (21) expresses the way in which increased surface coverage changes the adsorption energy. If g is positive, the interactions between two adsorbates are repulsive. If g is negative, the interactions are attractive. This isotherm generally provides a better fit to experimental data, when investigating

the electrochemistry of anthraquinone species. As outlined previously in section 1.4.2, anthraquinones can hydrogen bond intra- or intermolecularly. The experimental results presented in chapter 3 for monolayers of 1-amino, 2-sulphonic, 4-hydroxyanthraquinone (1,2,4-AQASH) and 9,10-anthraquinone (9,10-AQ) probe the existence and extent of H-bonding interactions in adsorbed films in more detail.

1.4.2.2 Two Component Anthraquinone Monolayers

To conclude this section, a brief summary of work carried out on two component anthraquinone monolayers is presented. Recent studies have been reported by Forster and coworkers^{76,78} and Willner and Katz.⁷⁹ The coadsorption of surfactants at the solid liquid interface represents a significantly more powerful approach to probing the nature and strength of lateral interactions between adsorbates since both the intersite separation and the identity of the adsorbates can be systematically varied. In an early publication by Forster, adriamycin and quinizarin were studied.

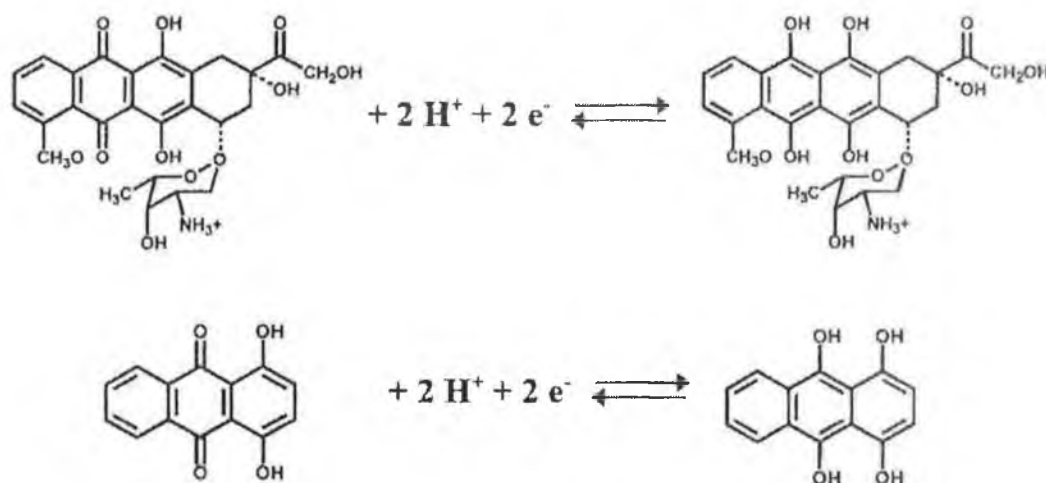


Figure 17. Structures of adriamycin and quinizarin.

The cyclic voltammetric data for adriamycin suggests that heterogeneous electron transfer is a relatively fast process, compared with that of quinizarin. This can be seen from a scan rate dependent study from 5 to 50 Vs⁻¹. In adriamycin films the integrated charges under the cathodic and anodic peaks are identical up to 50 Vs⁻¹ and ΔE_p is less than 10 mV. However, for quinizarin films, ΔE_p is not negligible for scan rates above 5

Vs^{-1} and the magnitude of the peak separation increases with increasing scan rate. Cyclic voltammetry also shows that the formal potential of these two species overlap on the potential axis, hence chronoamperometry was used to determine the surface coverages of both adriamycin and quinizarin when they are coadsorbed on the electrode surface. The ultimate objective of this work was to compare the rate constants obtained for single component systems with those obtained for mixed structures.

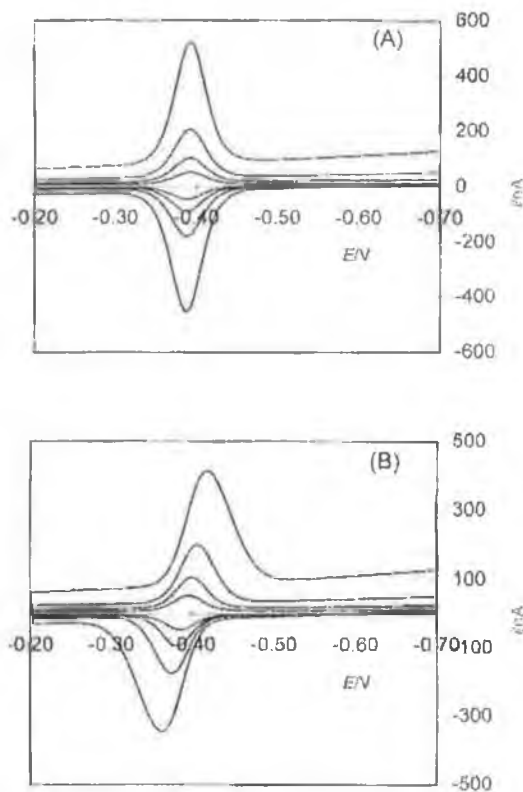


Figure 18. Cyclic voltammogram for 30 μm radius mercury microelectrodes immersed in (A) a 5 μM solution of adriamycin and (B) a 5 μM solution of quinizarin. Scan rates from top to bottom: 50, 20, 10 and 5 Vs^{-1} . The supporting electrolyte is 1 M $HClO_4$. Cathodic currents are up and anodic currents are down. The initial potential is -0.7 V.

In chronoamperometry experiments a potential step is applied, which oxidises both the adriamycin and quinizarin redox centres within the monolayer. Three exponential decays result as illustrated in Figure 19, which correspond to double layer charging of the electrode and oxidation of the two anthraquinone molecules. The mercury microelectrode used in these measurements is 30 μm radius and has a response time of

450 ns. When an identical potential step is applied to an electrode coated with a monolayer of a single redox species the rate constants observed from the exponential decay is within 10% of that found for the binary monolayers. Observation of the same heterogeneous electron transfer rate constants for single and binary monolayers indicates that lateral interactions between adjacent adriamycin and quinizarin molecules does not occur to any great extent. It was also found that modelling the experimental data using the Frumkin isotherm,²⁰ which considers adsorbate-adsorbate interactions gave interaction parameters that were close to zero.

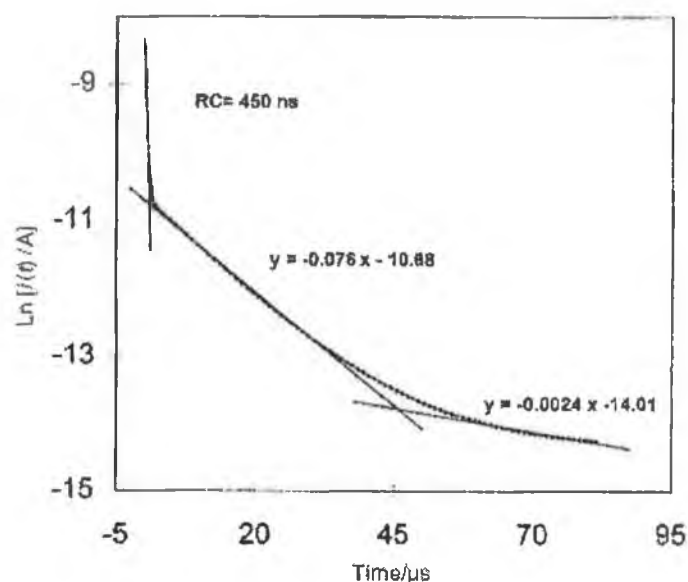


Figure 19. Log (current) versus time response for a 30 μm radius mercury microelectrode immersed in a solution containing 10 μM adriamycin and 10 μM quinizarin following a potential step where the overpotential was 0.050 V. The supporting electrolyte is 1.0 M HClO_4 . The time axis is referenced with respect to the leading edge of the potential step.

In a more recent publication by Forster and O'Hanlon⁸⁰ detailing the electrochemical behaviour of 2,7-AQDS and 1,4-AQClOH in a binary system, the lateral interactions between unlike molecules were significant. The goal of this work was to probe the extent to which these quinones interact as both the intersite separation and the composition of the monolayer was systematically varied. Voltammetric results show that the formal potential of 2,7-AQDS shifts to more negative potentials when it is part

of a two component system indicating that its easier to oxidise and the electron density on the adsorbate is higher. In contrast, the potential of 1,4-AQClOH shifts to a relatively more positive potential indicating lower electron density. Also, the peak-to-peak separation, ΔE_p for 1,4-AQClOH is slightly larger in a two component assembly. These observations suggest that the adsorbates interact laterally through intermolecular hydrogen bonds in which 2,7-AQDS and 1,4-AQClOH act as electron donors and acceptors, respectively. In conclusion the data was satisfactorily fit to a competitive Frumkin isotherm, thus confirming the theory that the species interact when coadsorbed. In chapter 4 of this work, the electrochemical behaviour of two different anthraquinone derivatives, 1,5-dimethoxyanthraquinone (1,5-DMAQ), and 1-amino,2-sulphonic,4-hydroxyanthraquinone (1,2,4-AQASH) is investigated when coadsorbed on a mercury surface. The results show interesting similarities and contrasts to Forster and O'Hanlon's earlier work presented above. When coadsorbed the two anthraquinone molecules are seen to interact on the electrode surface. The competitive Frumkin isotherm provides a good fit to the experimental data, however the interaction parameter predicted is positive. This indicates that there are repulsive interactions between 1,2,4-AQASH and 1,5-DMAQ adsorbates at high surface coverages.

1.5 Surface Characterisation of Monomolecular Films

The monomolecular films presented in the previous sections can be characterised by a number of methods to determine the mode and orientation of adsorbates on the electrode surface and the extent of interaction between adsorbed species. Raman and infrared spectroscopy and surface probe microscopies are the principal techniques reviewed in this section.

A number of publications by Soriaga and coworkers^{81,82,83,84,85,86} in the early 1980s concentrate on the adsorption and orientation of aromatic/quinonoid compounds adsorbed on platinum surfaces. The compounds employed in all of these studies were chosen because they display comparatively uncomplicated electrochemical reactivity, and represent a range of structures and chemical properties. The experimental method used throughout these studies employs a thin layer electrochemical technique. In cells of this design a thin layer of electrolyte is contained between a cylindrical platinum electrode and surrounding glass tubing. The data obtained in these studies was from a

10^{-4} M solution of the adsorbing aromatic compound. This ensured that saturation coverage determined from voltammetric data was reached for each possible orientation. With this setup an accurate measure of the amount of adsorbed species was obtained and from this a measure of the average area adsorbed per molecule, σ can be calculated using Equation (22).

$$\sigma = \frac{10^{16}}{6.023 \times 10^{23} \Gamma} \quad (22)$$

where σ has units of \AA^2 and Γ is the surface coverage on the electrode and has units of mol cm^{-2} . In order to go from coverage data to conclusions about how the aromatic moiety is oriented on the electrode surface it is necessary to calculate the theoretical surface area for a number of possible orientations and compare these with experimental results. Soriaga and coworkers have used molecular models, which take into consideration the covalent and van der Waals radii tabulated by Pauling.⁸⁷ Each molecule studied was considered to be surrounded by an envelope, as illustrated in Figure 20, which represented the probable distance of closest approach between molecules.

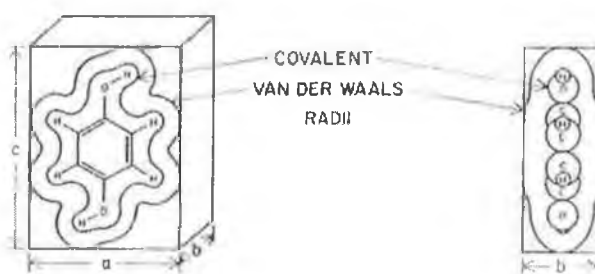


Figure 20. Molecular unit cell assumed in theoretical estimates of the average area adsorbed per molecule, σ .

The three possible orientations proposed in Soriaga's studies are where the aromatic ring is adsorbed parallel to the electrode surface or perpendicular to the electrode surface, either in an edgewise or endwise orientation. Nomenclature proposed by Cotton⁸⁸ is used to refer to these orientations as η^6 (parallel), η^2 (edgewise) and η^1 (endwise) respectively. The orientation of a molecule of the surface is potentially

dependent on a number of different variables. These include the molecular structure, solute concentration, electrolyte, potential, temperature, pH, electrode material and possibly others. These are the focus of the series of papers presented by Soriaga and coworkers but will not be discussed in detail here. It is sufficient to comment on the results of sulphonated anthraquinones, 1,5-AQDS and 2,6-AQDS, which formed part of these studies and are most relevant to the experimental work in this report. The experimental σ values for 1,5-AQDS and 2,6-AQDS adsorbing on a platinum electrode surface are 140.7 ± 1.4 and $130.7 \pm 7.1 \text{ \AA}^2$ respectively, and the theoretical values calculated by the method described earlier are 138.0 and 126.3 \AA^2 for a flat orientation on the electrode surface.⁸² Theoretical values for an edgewise, and endwise, orientation are 75.5 and 74.2 \AA^2 for 1,5-AQDS and 102.4 and 98.6 \AA^2 for 2,6-AQDS respectively. Hence, the experimental values agree with those predicted for a flat orientation, η^6 , on the electrode surface. The resistance of these molecules to reorientation could be due to an entropy effect. When the adsorbates are adsorbed parallel to the surface the three fused rings can interact with the surface, where an edgewise or endwise orientation would only allow for limited interaction.

1.5.1 Raman Spectroscopy

Surface enhanced Raman spectroscopy (SERS) has been used extensively since it was discovered in 1974 and is therefore emerging as a valuable surface characterization technique for the systems reviewed here. The overall spectral intensity provides an approximate measure of the surface coverage of the redox species. The relative intensity of the individual bands can be used to determine an average orientation of the adsorbate molecules on the surface. A comprehensive review written by Garrell⁸⁹ in 1989 presents a description of the SERS technique and presents some of the broader fields in which it is applied. SERS has a number of advantages to the conventional Raman spectroscopy technique. When characterizing monomolecular films such as anthraquinones on mercury the weak intensity of Raman scattering makes this impossible to probe using conventional methods. Using SERS it is possible to study molecules adsorbed on a metal surface even at sub-monolayer coverages. The surface can provide up to 10^7 -fold enhancement of the Raman scattering of the adsorbed species while scattering from the solvent remains relatively weak. The most obvious requirement for the investigation of a species by SERS is that the analyte in solution

interacts strongly with a SERS metal. Metals, which give good surface enhancement using a visible wavelength Raman excitation source are silver, gold, mercury and copper, while gallium and platinum are often used with an infrared source.⁸⁹

Surface enhanced Raman scattering studies of various anthraquinone derivatives have been carried out by Ramakrishnan since 1990.^{90,91,92,93,94} These publications provide useful information on the orientation of these molecules on a silver surface, which show interesting contrasts to the conclusions drawn by Soriaga in the previous section. In all of Ramakrishnan's studies the anthraquinone derivatives were adsorbed on a silver sol. This sol was prepared by adding 100 mls of AgNO_3 ($6 \times 10^{-4} \text{ mol l}^{-1}$) solution drop wise to 300 mls of NaBH_4 ($1 \times 10^{-3} \text{ mol l}^{-1}$) while stirring slowly. The mixed solution was then cooled to ice temperature and the resultant silver sol was yellow in colour, which showed a single adsorption band in the Raman spectrum at 390 nm.

Much of the Raman spectroscopy studies detailing the structure of anthraquinone derivatives focus on disubstituted hydroxyanthraquinones. Marasinghe and Gillispie⁹⁵ report on the geometry of 1,4-, 1,5- and 1,8-dihydroxyanthraquinone and 1-aminoanthraquinone. The principal conclusion from this work is that substitution of the anthraquinone ring causes distortion of the molecule from planarity. More recent work by Margetic and Maksic⁹⁶ and Smulevich and coworkers⁹⁷ examine similarly substituted anthraquinones to determine the optimal geometry of the molecules. Figure 21 illustrates the Raman spectra obtained for four substituted anthraquinones and shows clearly that the position and intensity of the spectral peaks is determined by the mode of substitution on the anthraquinone rings. The principal peaks in the high frequency spectral region, i.e., from 980 to 1700 cm^{-1} are listed in Table 1. These studies however do not consider the changes in the structure of the anthraquinones when they are adsorbed on an electrode surface.

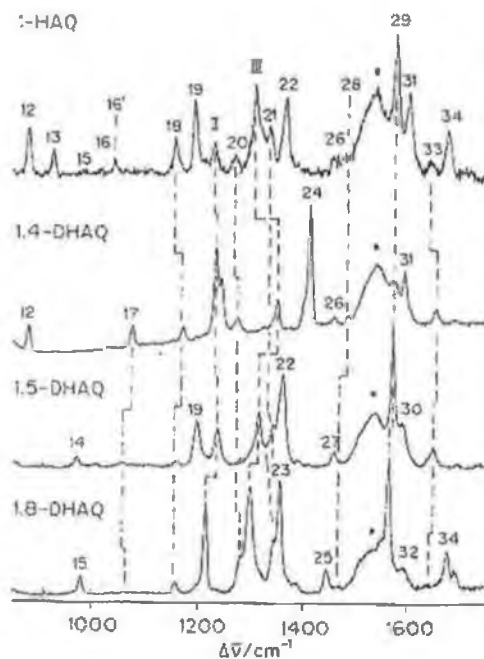


Figure 21. High frequency resonance Raman spectra of 1-hydroxyanthraquinone and 1,4-, 1,5- and 1,8-dihydroxyanthraquinone, in CCl_4 , recorded with 406.7 nm excitation. Experimental conditions were as follows: 5 cm^{-1} resolution, 4 s/cm^{-1} collection interval and 20 mW laser power at the sample. The numbered bands are assigned in Table 1 below.

Table 1. Assignment of the principal Raman spectra bands for hydroxyanthraquinones. The frequencies are in cm^{-1} and the intensity of the bands are assigned as follows; s-strong, m-medium, w-weak, sh-shoulder.

<i>n</i>	<i>Assignment 1-HAQ</i>	<i>Assignment 1,4-DHAQ</i>	<i>Assignment 1,5-DHAQ</i>	<i>Assignment 1,8-DHAQ</i>	<i>Mode</i>
12	880m	877s			sk def
13	926w				sk def
18	1154m	1162m	1157w	1156w	δ_{CH}
19	1189s		1194m		δ_{CH}
II	1226s	1225s	1234m	1213s	δ_{OH}
20	1268m	1265m	1315w	1279sh	δ_{CH}
III	1304m	1341m	1311m	1296m	ν_{COH}
21	1331m	1331w	1339m	1341m	ring st
22	1361s		1357s		ring st, δ_{CH}
23				1354s	ring st, δ_{CH}
24		1403s			ring st, δ_{CH}
29	1577s	1570w	1571s	1566s	ring st
30			1591sh		ring st
31	1601m	1589m			ring st
32				1597w	ring st
34	1678			1680w	$\nu_{\text{C=O}}$

Two of Ramakrishnan's papers^{91,93} concentrate solely on the adsorption of 1,4-dihydroxyanthraquinone and conclude that this molecule adsorbs on a silver surface in a flat orientation. This is due to intramolecular hydrogen bonding between the C=O groups in the 9 and 10 positions and the O-H groups in the 1 and 4 positions, making them unavailable for adsorption. Thus, the π orbital system is most available for surface interaction and a parallel orientation results. Figure 22 illustrates the normal Raman spectrum and surface enhanced Raman spectrum of 1,4-DHAQ. It is obvious from this illustration that SERS is much more sensitive than the normal Raman spectroscopy, with 8 weak bands appearing in the normal spectrum in comparison to 16 stronger bands in the SERS. Although the reason for the enhancement is still not fully understood it is thought to be due to two principal mechanisms, electromagnetic and chemical.^{91,98} In the case of the electromagnetic mechanism, the enhancement relative to the normal Raman spectrum arises because of increased electromagnetic fields on the surface that is used as the SERS substrate. In the case of the chemical mechanism the enhancement may be due to some short-range interaction between the adsorbate and the surface.

The bands in the Raman spectra are labeled and have been assigned as follows; the bands at 1594, 1537 and 1469 cm^{-1} (a, b, c) are seen in the SERS spectrum only and are all assigned to ring stretching vibration. The intense band at 961 cm^{-1} (d) in the SERS spectrum is due to the ring breathing mode. However, the ring breathing mode is very weak in the normal Raman spectrum. The band at 1042 cm^{-1} in the normal Raman spectrum is due to C-H in plane bending mode, however this is shifted to 1059 cm^{-1} in the SERS and is of greater intensity than in the normal Raman spectrum. The weak band in the SERS at 2900 cm^{-1} (f) has been assigned to a C-H stretching vibration, which occurs only when the anthraquinone is adsorbed on an electrode surface. The bands at 912, 866 and 697 cm^{-1} (g, h, i) are due to out of plane C-H bending modes. These bands are not observed in the normal Raman spectrum. The ring deformation vibrational modes appear as medium intensity bands at 617 and 651 cm^{-1} (j, k) in the SERS but only one band is seen in the normal Raman spectrum at 651 cm^{-1} . A weak and broad band at 3011 cm^{-1} (l) is due to a O-H stretching mode, which is characteristic in hydrogen bonded molecules. The intense band at 1354 cm^{-1} (m) corresponds to a C-OH stretching mode whose intensity is much greater than that in the normal Raman spectrum. Carbonyl stretching occurs at 1674 cm^{-1} in the normal Raman spectrum and

in the SERS (n). This band is of relatively low intensity and Ramakrishnan attributes this to hydrogen bond formation in 1,4-DHAQ when it is adsorbed on the silver sol surface.

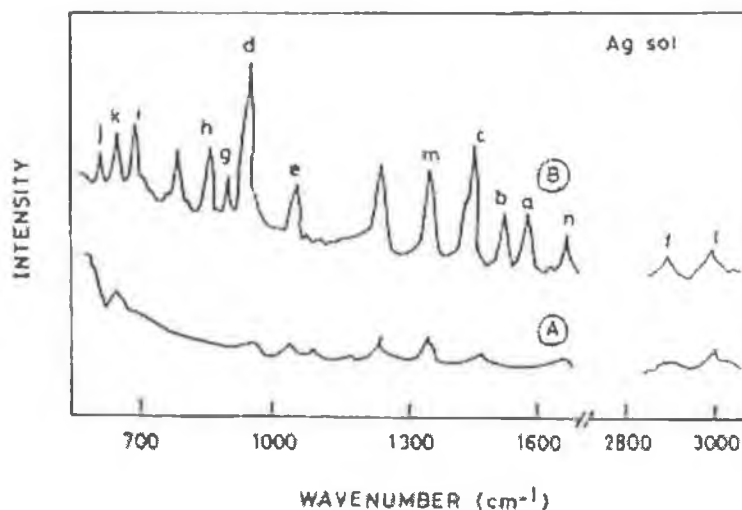


Figure 22. (A) Normal solution Raman spectrum of 1,4-DHAQ and (B) Surface Enhanced Raman spectrum of 0.1×10^{-3} M 1,4-DHAQ in silver sol.

Another hydroxyanthraquinone studied in this series of papers is 1,5-dihydroxyanthraquinone (1,5-DHAQ).⁹² Figure 23 illustrates the normal Raman spectra of 1,5-DHAQ and the SERS when adsorbed on a silver substrate. In the normal Raman spectrum the spectral bands are swamped by the fluorescence background. The SERS spectrum however shows well-resolved bands and this is due to the fact that the fluorescence is quenched when the molecule is adsorbed on the metal surface. The SERS spectrum shows four strong bands (818, 1259, 1679 and 1734 cm^{-1}), five medium intensity bands (478, 1278, 1642, 2834 and 3044 cm^{-1}) and three weak bands (741, 999 and 1159 cm^{-1}). According to surface selection rules, the vibrational modes involving atoms that are closer to the metal surface attain greater enhancement in comparison with other vibrations. The spectral bands are assigned as for 1,4-DHAQ as outlined above, but most notable is the band attributed to the C=O stretching mode. This band is of strong intensity and indicates that 1,5-DHAQ is adsorbed perpendicular to the electrode surface in a “stand-on” orientation through the C=O group, as illustrated in Figure 23 below.

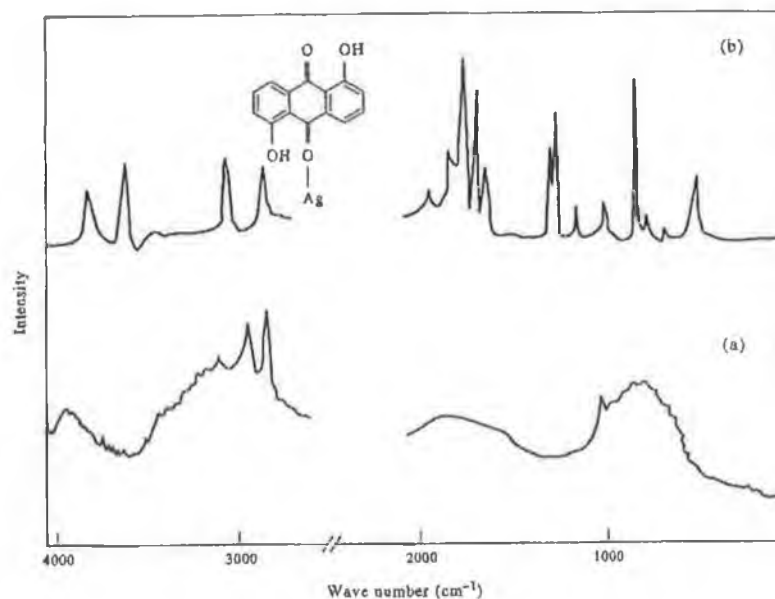


Figure 23. (a) Normal Raman Spectrum of 1,5-DHAQ and (b) SERS spectrum when 1,5-DHAQ is adsorbed on silver sol.

The spectral analysis of 1,4-DHAQ and 1,5-DHAQ in Ramakrishnan's two publications outlined in this section draws unlikely conclusions if the structure of the two adsorbates is considered. 1,4-DHAQ and 1,5-DHAQ have the same structure except that one of the -OH groups is attached at the 4 position and the other is attached at the 5 position. However in both cases the -OH group is adjacent to a C=O, Figure 24. Therefore, if 1,4-DHAQ intramolecularly hydrogen bonds and adsorbs in a parallel orientation as a result, it would seem logical that 1,5-DHAQ would undergo the same interaction. One possible reason for the difference in orientation could be explained if the roughness of the electrode surface is considered. All of Ramakrishnan's studies involves adsorption of AQs onto silver sol. This surface consists of large aggregates of silver spheres or randomly spaced individual silver spheres and is therefore not atomically smooth and may influence the mode of adsorption of the adsorbates.

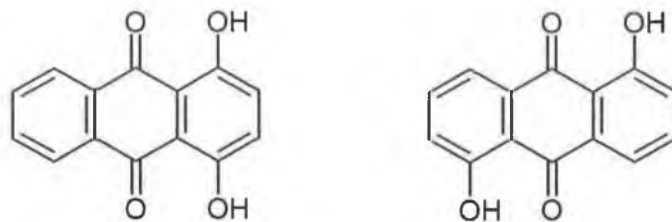


Figure 24. Structure of 1,4-dihydroxyanthraquinone and 1,5-dihydroxyanthraquinone.

One other notable contribution in this area is a publication by Taniguchi and coworkers⁹⁹ in 1999. Cyclic voltammetry and Raman spectroscopy were the techniques employed in this study to probe two anthraquinone derivatives, namely, 1-anthraquinonylbutylsulfide, 1-AQS and 2-anthraquinonylbutylsulfide, 2-AQS. These adsorbates were investigated when adsorbed on silver and gold surfaces. The frequency shifts and relative intensities of C-H bands to ring breathing bands in the Raman spectrum are used to elucidate the orientation on the surface. This will be discussed in more detail in Chapter 3 of this work, as it bears relevance to the experimental results presented therein.

1.5.2 Infrared Spectroscopy

One of the earlier studies probing the electrochemistry and surface characterization of 1,5- and 1,6-anthraquinone disulphonate films is that presented by Zhang and Anson⁶⁶ in 1992. Further to the cyclic voltammetry results presented in section 1.4.2 of this review, IR spectroscopy provided an additional insight into the factors which effect the electrochemical response of these adsorbates as the solution concentration and the deposition time increases. When adsorption is carried out from a dilute solution of 2,6-AQDS (10^{-5} M) on a graphite electrode for times less than 60 seconds the IR spectrum shows no significant difference from that obtained from a bare graphite electrode, Figure 25 (a) and (b).

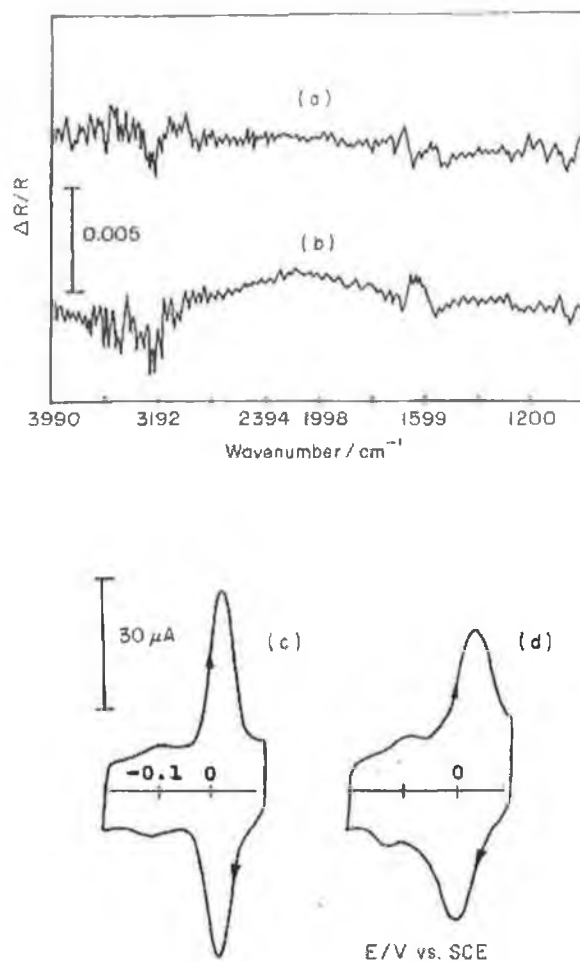


Figure 25. Spectrum (a) IR spectrum from a polished basal plane pyrolytic graphite electrode in 0.05 M H_2SO_4 . The electrode was stepped from 0.1 V to -0.2 V to obtain the spectrum shown. Spectrum (b), IR spectrum for the same electrode after it had been exposed to a 10^{-5} M solution of 2,6-AQDS for 1-2 min and then transferred to a thin layer IR cell to record the spectrum. Curve (c), cyclic voltammogram recorded in 10^{-5} M 2,6-AQDS in 0.05 M H_2SO_4 before the electrode was washed and transferred to the thin layer IR cell to record spectrum (b). Curve (d), cyclic voltammogram recorded with the same electrode after recording spectrum (b).

However, when the solution concentration is increased to 10^{-3} M and the time allowed for adsorption is increased to 10 minutes the IR spectrum shows features due to the adsorbed 2,6-AQDS moieties, Figure 26. The authors conclude that the IR spectra recorded at low and high surface coverage provides information about the orientation of the adsorbates on the graphite surface. In IR spectroscopy only species adsorbed with

their dipole moments perpendicular to the electrode surface can be detected. Thus, it can be concluded that 2,6-AQDS and 1,5-AQDS are adsorbed parallel to the electrode surface at low surface coverages, as the adsorbed spectra show no difference from the spectrum of bare graphite. At high concentrations the appearance of additional bands in the IR spectrum would suggest that the adsorbates are arranged in a more perpendicular or tilted orientation. This interpretation of the CV and IR results is reasonable assuming that IR spectroscopy measurements are sensitive enough to measure a small amount of adsorbate on the electrode surface. After 60 seconds of adsorption it is clear from the CV data, illustrated in Figure 25 (c), that adsorption has occurred, however it has not been proven that IR spectroscopy is capable of detecting such small amounts on the surface. Cyclic voltammetry is a sensitive technique and is capable of measuring down to a small fraction of monolayer coverage. This is illustrated in this study and repeatedly in the experimental chapters of this work.

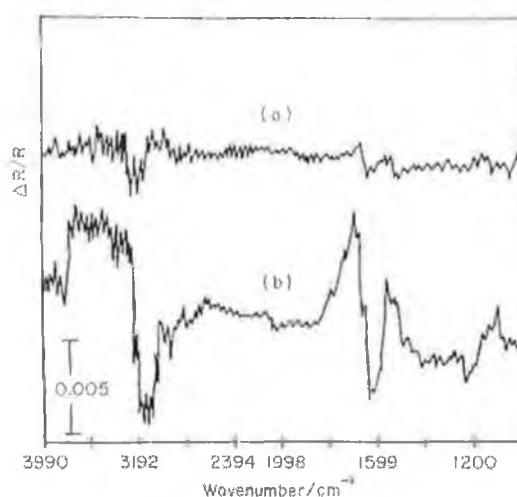


Figure 26. (a) IR spectrum of a polished basal plane pyrolytic graphite electrode in 0.05 M H₂SO₄ and (b) IR spectrum of the same electrode after it is exposed to a 10⁻³ M solution of 2,6-AQDS for 10 min and then transferred to a thin layer IR cell. The potential was stepped from 0.1 to -0.2 V to obtain both spectra.

1.5.3 Scanning Probe Microscopy

A number of papers have focused on the characterization of monolayers using scanning probe microscopy. This section will focus mainly on the limited number of publications concerning anthraquinone derivatives. Ta, Kanda and McDermott⁷⁴ have published a combined voltammetric and scanning force microscopy investigation of 2,6-AQDS films adsorbed on an ordered graphite surface. Consistent with the results presented in Zhang and Anson's combined IR and cyclic voltammetry study, the structure of 2,6-AQDS films varies as a function of concentration. Images collected from two solution concentrations, 10 μM and 1 mM are presented in Figure 27. At low surface coverages the adsorbed layer appears to be discontinuous with a high density of pinhole defects. The darker regions of the images in Figure 27 (A) and (B) represent the unmodified graphite surface, this has been determined by recording SFM images of an unmodified HOPG surface in 1 M HClO_4 . The defect sites range in size from 100 to 250 nm.

When the electrode was exposed to a higher concentration of the anthraquinone images such as those displayed in Figure 27 (C) and (D) were obtained. The topographic image shows a pattern of intersecting elongated domains that are 0.3 to 0.7 nm higher than the surrounding background. The domains range in length from 100 to 700 nm and in width from 35 to 100 nm. Further experiments have shown that application of a higher imaging force causes the top layer to be swept away leaving the disordered layer. These results imply that when the solution concentration is increased a relatively more ordered layer is formed on top of the initial disordered layer.

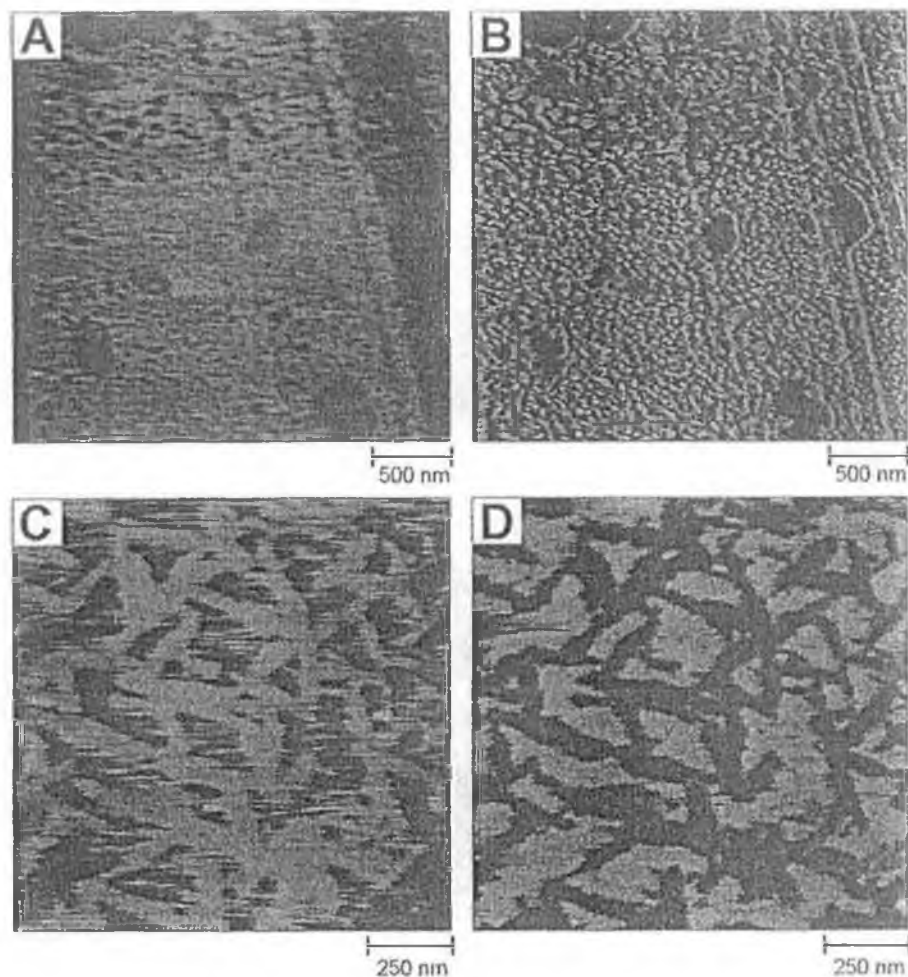


Figure 27. (A) and (B) are respectively $2.7 \mu\text{m} \times 2.7 \mu\text{m}$ topographic (Z -scale = 10 nm) and lateral force (Z -scale = 0.2 V) SFM images of an equilibrated 2,6-AQDS film on HOPG. Images were collected in $10 \mu\text{M}$ AQDS (1M HClO_4). (C) and (D) are respectively $1.6 \mu\text{m} \times 1.6 \mu\text{m}$ topographic (Z -scale = 2 nm) and lateral force (Z -scale = 0.5 V) SFM images collected in 1mM 2,6-AQDS (1M HClO_4) solution.

Kim and coworkers¹⁰⁰ have more recently probed the adsorption of anthraquinone-2-carboxylic acid on silver. This study encompasses a number of techniques including IR Spectroscopy, Quartz Crystal Microbalance, and Atomic Force Microscopy. The primary goal of this work is to determine if the two surface probing techniques produce consistent results in the characterization of this self-assembly process. The infrared measurements conclude that AQ-2-COOH is chemisorbed on the silver surface through the carboxylate group after deprotonation. This has been concluded from the IR

spectrum recorded when AQ-2-COOH is adsorbed on a silver surface, which shows an intense peak at 1394 due to symmetric stretching of a COO^- group. The relative intensity of the spectral bands in IR indicate that the molecular plane of the adsorbed AQ-2-COO⁻ is neither perpendicular nor flat with respect to the silver surface. Hence, it has been concluded from this study that the anthraquinone adopts a tilted orientation to the surface normal, Figure 28:

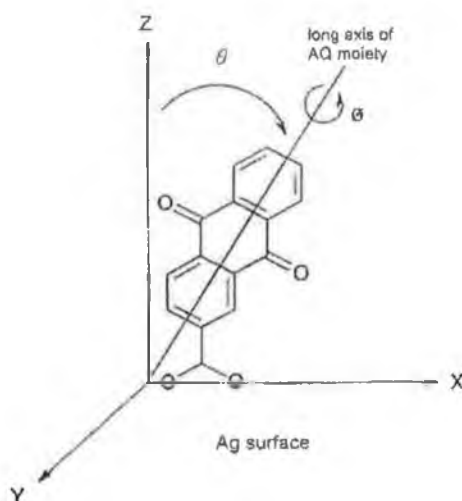


Figure 28. Mode of adsorption of AQ-2-COOH on a silver surface.

The peak positions and intensities in IR spectroscopy show no notable difference after 5 minutes of self-assembly to those observed after two hours. Therefore, it was concluded that AQ-2-COOH forms maximum surface coverage in a short time. This result is confirmed through QCM measurements. In these experiments the silver coated quartz was placed in contact with a 0.5mM AQ-2-COOH ethanol solution. When the anthraquinone solution was injected, the resonant frequency of the quartz abruptly decreased by approximately 15 Hz and stabilized within two minutes, regardless of the concentration used (concentrations in the range 0.02-2mM were used in these measurements). This implies that the monolayers are formed rapidly and are stable over long periods of time.

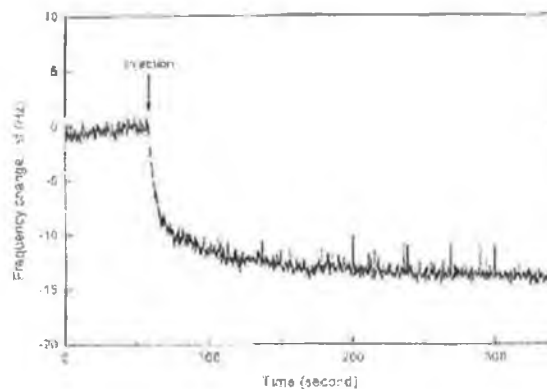


Figure 29. Frequency change of QCM in a 0.5 mM AQ-2-COOH solution in ethanol. The arrow indicates the time at which a AQ-2-COOH stock solution was injected into the cell.

The results obtained from IR and QCM are also in agreement with AFM measurements. Figure 30 shows an AFM image covering an area 3.0 nm x 3.0 nm of a self assembled monolayer of AQ-2-COOH on a silver substrate. The lighter areas denote higher regions and the darker areas represent lower areas. From this image its evident that the adsorbed moieties are arranged parallel to one another and form a close packed structure. This study shows that AFM can produce molecularly resolved images of layers adsorbed on a surface, providing there is some order in the adsorption pattern. An area of occupation by one adsorbate of AQ-2-COOH was estimated to be $62 \pm 5 \text{ \AA}$ from the AFM image.



Figure 30. AFM image (3.0 nm x 3.0 nm) of a self assembled monolayer of AQ-2-COOH on silver. Image was FT-filtered to remove noise.

1.6 Electrochemical Techniques and Instrumentation

1.6.1 Cyclic Voltammetry

Numerous methods in electroanalytical chemistry have been developed in recent decades, among the most popular of these is cyclic voltammetry. In 1941 Laitinen and Kolthoff introduced the term voltammetry to describe steady-state current-voltage curves.¹⁰¹ The data available from this technique refers not only to the thermodynamic parameters such as e.g., the redox potential, but also gives direct insights into the kinetics of electrode reactions, which include both heterogeneous and homogeneous electron transfer steps.^{102,103,104} Cyclic voltammetry consists of scanning a chosen potential region and measuring the current response arising from the electron transfer and associated reactions that occur at the electrode surface.^{102,105} It is implemented in the experimental section of this thesis to characterise various anthraquinone monolayers. In addition to indicating the number of different oxidation states in a complex, the peak height of a voltammogram is related to both the concentration and reversibility of a reaction. Cyclic voltammograms run at varying scan rates can be analysed to determine if a species is adsorbed on an electrode surface or diffusing to the electrode. As seen from results in chapters 3 and 4 anthraquinones adsorb on a mercury electrode surface and cyclic voltammetry can then be used to give an insight into the packing density and orientation of these surface-confined species.

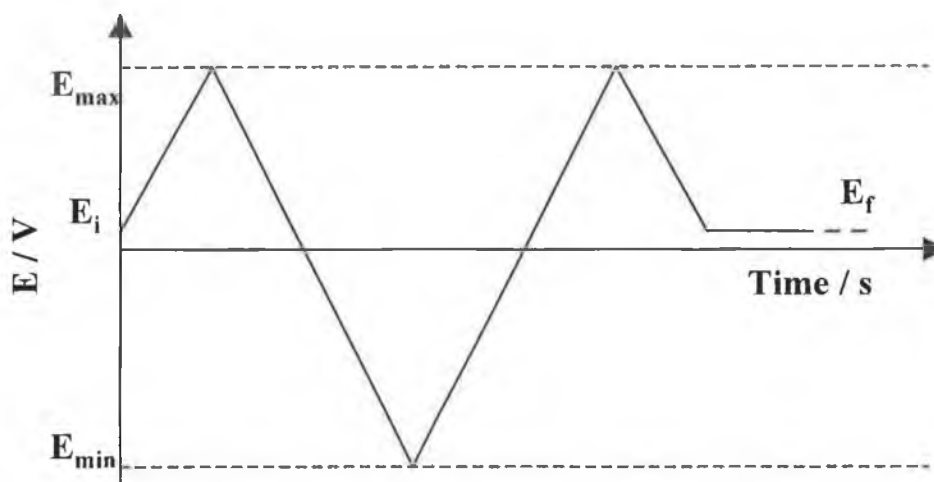


Figure 31. Potential waveform for cyclic voltammetry. E_i is the initial potential, E_f the final potential, E_{max} , the maximum and E_{min} the minimum potentials.

Normally, voltammetric experiments are performed using a stationary working electrode in a quiescent solution. The voltage is scanned in a triangular fashion, Figure 31, and the resulting current measured. Most cyclic voltammograms have a peak shaped current-voltage curve. Starting with an initial potential, E_i , a linear potential sweep is applied to the electrode. The initial potential is chosen where no redox reaction occurs. As the potential is scanned in either a positive or negative direction, the half wave potential for the species in solution is reached and the current starts to increase. This reaction creates a concentration gradient, which sucks in more electroactive species until depletion effects set in and the current begins to fall back towards the baseline.¹⁰² After reaching a switching potential, the sweep is reversed and the potential is returned to its initial value, which explains the term cyclic voltammetry.¹⁰⁶ The potential scan can be terminated after the first cycle but is usually scanned for a number of cycles. Scan rates vary from a few millivolts per second to thousands of volts per second. Typically the scan rate is from 50 mVs^{-1} to 1 Vs^{-1} at macroscopic electrodes but much higher scan rates may be applied at ultramicroelectrodes.¹⁰⁵

Bard and Faulkner use energy level diagrams to explain the reduction/oxidation process of an electroactive species at the electrode surface. The system described could represent an anthraquinone moiety in an electrolytic solution at a mercury electrode. In an electrochemical experiment the energy of an electron can be changed at will. For

reduction to occur a negative potential is applied to the working electrode in the electrochemical cell. The energy of the electrons in the electrode increases with increasing negative potential as illustrated in Figure 32(A). When they reach a level high enough to transfer to vacant electronic states in the electroactive species an electron transfers into solution and a reduction current flows. Similarly, if the energy of the electrons in the electrode are lowered by applying a positive potential to the electrode, electrons can transfer from the electroactive species in solution to the electrode. This flow of electrons results in an oxidation current and is depicted in Figure 32(B) below.

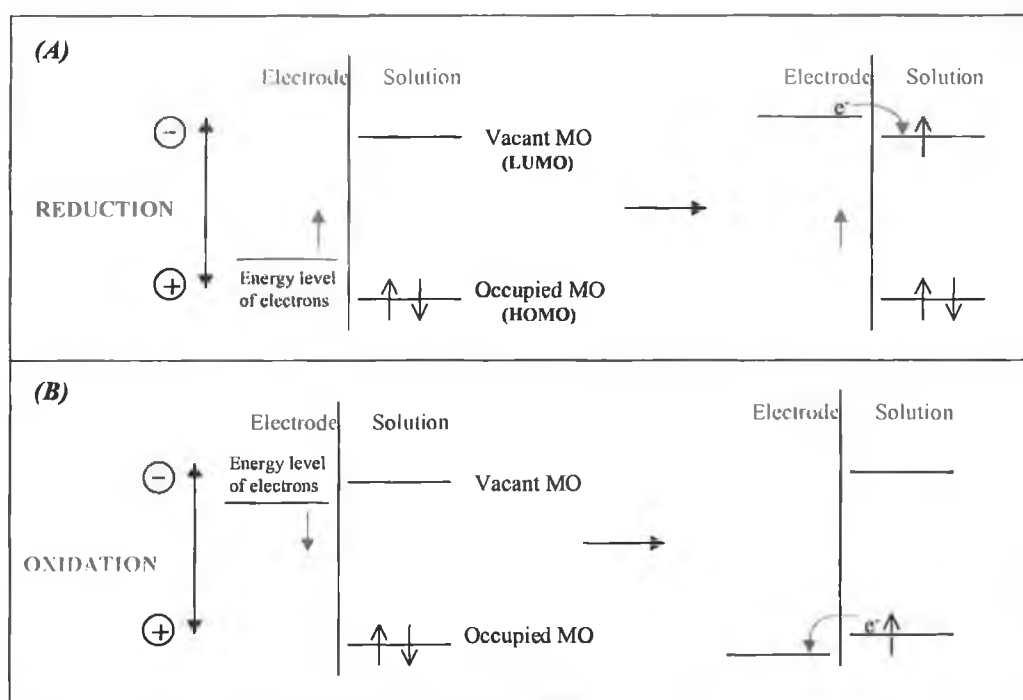


Figure 32. Reduction (A) and oxidation (B) of an electroactive species in solution, molecular orbitals shown are those of the highest occupied MO and lowest vacant MO.

1.6.1.1 Solution Phase Electrochemistry

Figure 33 shows the response expected for a species, which freely diffuses to and from the electrode surface to undergo a redox reaction. The most important features in the cyclic voltammogram are the two peak potentials, the cathodic peak potential, E_{pc} and anodic peak potential, E_{pa} and corresponding peak currents, i_{pc} and i_{pa} . The current that flows across the electrode/solution interface is a sum of the contribution from the faradaic reaction and capacitive current.¹⁰⁷ In electrochemical measurements the faradaic current is of most importance since this results from the oxidation and reduction of the electroactive species and is therefore a means of measuring the rate of a redox reaction. However, once a potential is applied to the electrode surface double layer charging occurs by electrostatic attraction and repulsion of cations and anions near the electrode surface. This serves to balance the charge on the electrode, and is shown as an approximately constant value at the foot of the voltammetric wave in the cyclic voltammogram. One of the ways to reduce this capacitive effect is to use ultramicroelectrodes, as the double layer capacitance is proportional to the electrode area. Thus, shrinking the size of the electrode causes the interfacial capacitance to decrease with decreasing r^2 . This is discussed further in Section 1.7.2.2 of this chapter.

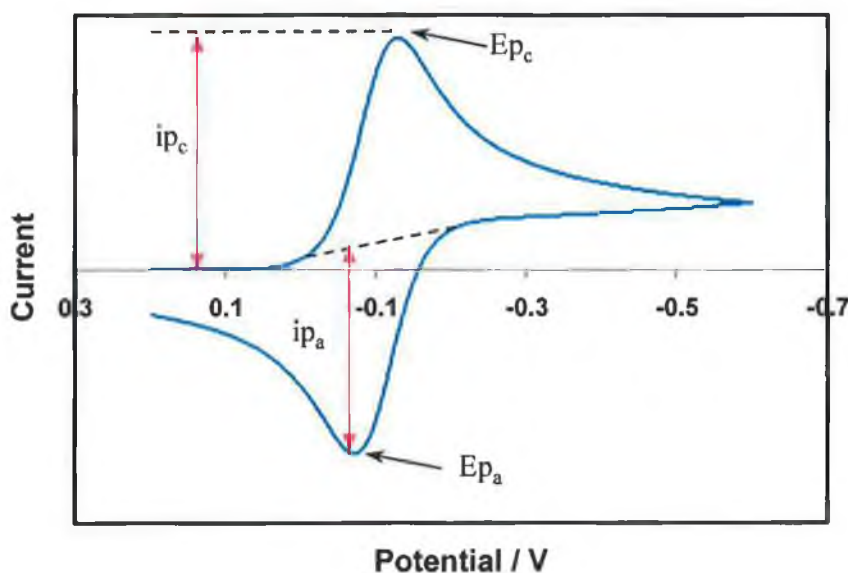


Figure 33. Cyclic voltammetric response for a fully reversible reaction in solution.

In practice, under standard measuring conditions reversible and quasi-reversible cases occur most frequently.¹⁰² A reversible response means that the rate of the redox reaction is fast enough to maintain equilibrium concentrations of reactant and product at the electrode surface as the applied potential is varied. For a reversible wave the potential, E_p is independent of scan rate¹⁰⁸ and the peak current, i_p is proportional to $v^{1/2}$, as given by the Randles-Sevcik Equation,

$$i_p = (2.69 \times 10^5) n^{3/2} A D^{1/2} v^{1/2} C \quad (23)$$

where n is the number of electrons transferred in the reaction, A is the area of the electrode, v is the scan rate employed and C is the concentration of the electroactive species in solution. The Randles-Sevcik Equation applies only when the current is diffusion controlled and hemispherical diffusion is unimportant. Under semi-infinite diffusion conditions, in the absence of ohmic effects and slow electron transfer processes the following conditions also hold in the cyclic voltammetric response,

$$\Delta E_p = \frac{0.059}{n} V @ 25^\circ C \quad (24)$$

$$\frac{i_{pa}}{i_{pc}} = 1 \quad (25)$$

1.6.1.2 Electrochemistry of Surface Confined Species

When species adsorb on the electrode surface this leads to changes in the shape of the cyclic voltammogram. This change in shape occurs because the electroactive species no longer has to diffuse to the electrode surface. The adsorption energy of the oxidised and reduced species are equal, $E_{pa} = E_{pc}$, and the cyclic voltammogram is symmetrical with oxidation and reduction peaks coincident, as illustrated in Figure 34. The surface concentrations of species involved in the faradaic process can be related to the current in a cyclic voltammetry experiment. The following conditions hold under finite diffusion control, this is a condition where the redox composition of the layer is in thermodynamic equilibrium with the electrode potential, i.e. the Nernst condition.

$$i_p = \frac{n^2 F^2 \nu A \Gamma}{4RT} \quad (26)$$

$$E_{pa} = E_{pc} \quad (27)$$

$$(\text{FWHM}) = \frac{3.53RT}{nF} = \frac{90.6}{n} \text{ mV} @ 25^\circ \text{C} \quad (28)$$

where n is the number of electrons transferred, F is Faradays constant (96485.4C), ν is the scan rate in Vs^{-1} , A is the area of the electrode in cm^2 , Γ is the surface coverage in mol cm^{-2} .

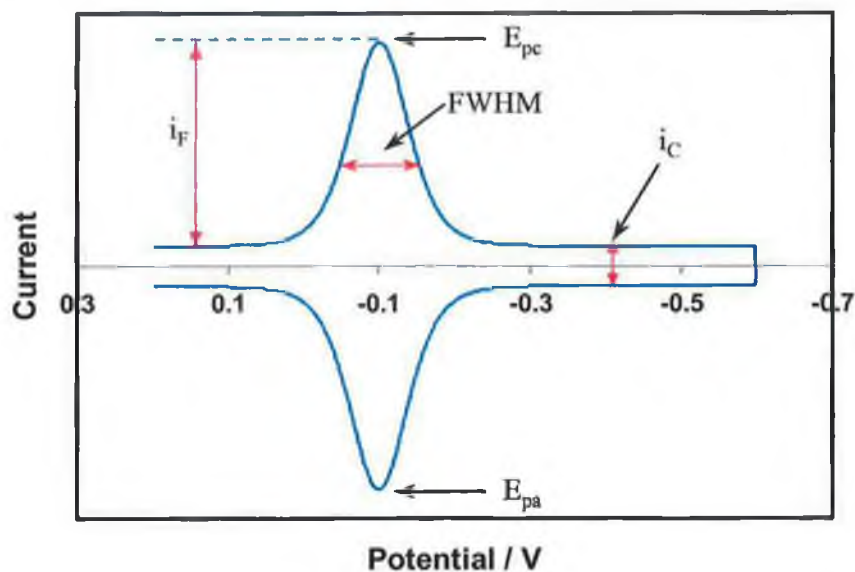


Figure 34. Cyclic voltammetric response for a reversible reaction of an adsorbed species. The potential limits are +0.2 and -0.6 V and the formal potential is -0.1 V. The scan rate is 5 Vs^{-1} .

1.6.2 Chronoamperometry

Chronoamperometry is a potential step technique, in which the potential of the working electrode is changed rapidly from an initial potential E_1 to a final potential E_2 . The capacitive current associated with the charging of the electrode interface decays over a time according to Equation (29).¹⁰⁶

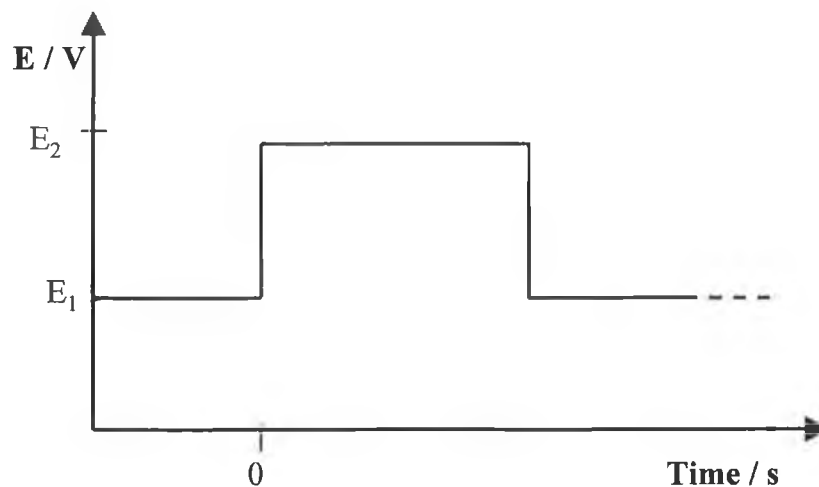


Figure 35. Potential waveform for chronoamperometry. E_1 is the initial potential, E_2 the final potential.

$$i_c(t) = \left(\frac{\Delta E}{R} \right) \exp\left(\frac{-t}{RC_{dl}} \right) \quad (29)$$

The resistance, R and double layer capacitance, C_{dl} may be calculated from the above equation where ΔE is the potential step amplitude. If the potential is stepped in a region where a surface bound species is electroactive a double exponential decay is observed. The two current decays correspond to double layer charging and faradaic current flow. The two processes are time resolved because the time required to charge the double layer is much smaller than that for the faradaic reaction¹⁰⁶ when microelectrodes are used.

The rate constant for heterogeneous electron transfer may be calculated from Equation (30)^{35,76}

$$i_F(t) = kQ\exp(-kt) \quad (30)$$

where k is the apparent rate constant, Q is the total charge passed in the reaction, n is the number of electrons transferred, F is Faraday's constant, and A is the electrode area.

1.7 Microelectrodes

Historically, our understanding of dynamics in electrochemical systems has been limited by the lack of experimental tools with adequate sensitivity, range of timescale or chemical sensitivity. Only at the end of the 1970s did Fleishmann and coworkers at the University of Southampton establish beyond question that diminishing the size has not only quantitative effects, but also unusual qualitative effects.¹⁰⁹ In 1981 Wightman provided the first comprehensive survey of the special properties of ultramicroelectrodes (UMEs).¹⁰¹ These discoveries have encouraged numerous research groups to study the properties and applications of UMEs in theory and practice. Hence, further reports have been published by Pons and Fleischmann,¹¹⁰ Heinze¹⁰² and Forster,¹¹¹ dealing primarily with electrochemistry at these ultrasmall probes.

Ultramicroelectrodes may be defined as electrodes with a tip diameter smaller than or equal to 20 μm . The term nanode is used for electrodes with a diameter less than 1 μm . Steady improvements in the construction of UMEs have reduced their characteristic dimensions. The construction of platinum and gold ultramicrodisk electrodes with radii as small as 0.1 μm has become routine in electrochemical laboratories and dimensions in the angstrom range have been reported. These small voltammetric probes have greatly extended the range of sample environments and experimental timescales that are useful in electrochemical measurements. One focus of this thesis is the determination of fast electron transfer rate constants, and the unique attributes which enable microelectrodes to be used in this area are explained in more detail in section 1.7.2.

The ultrasmall size of these electrodes allows for their application in other areas of science, especially in biology. Interest in this area arose in the 1940s and 1950s. Bond

and Oldham¹¹² refer to studies, which focused on the determination of oxygen concentrations in living organisms for application in medical and biological research. For such measurements, biologically inert platinum electrodes of micrometer size were inserted in muscles and tissues of animals. The small size of the electrodes ensured easy placement within a living cell and minimal damage due to the small currents produced. The implementation of ultramicroelectrodes is necessary in such applications as the cell membrane must seal around the electrode following implantation. Information concerning drug induced changes in the concentration of chemical compounds in the mammalian brain can be obtained by using microvoltammetric probes.

Work carried out by Adams and coworkers^{113,114} in the 1970s involved the use of microelectrodes to stimulate and monitor psychological processes. Obviously ultrasmall probes are necessary for these *in-vivo* measurements so that no harm comes to the region of the brain where the measurements are being made; nerve terminals have diameters as small as 1 μ m. These early studies have led to more developments in the area. A number of recent publications^{115,116,117,118,119} are concerned solely with the detection of a class of compounds referred to as neurotransmitters. Neurotransmitters have a very important function in the brain since they are the key link to communication between neurons. The ability to detect these species inside the brain but external to neurons would provide a direct method of understanding this mode of chemical communication. The ongoing interest in this area of research is not surprising when one considers the advances it provides in medical care. The detection of one neurotransmitter, dopamine within the mammalian brain can provide quantitative information about brain chemistry, Parkinsons disease and the action of anti-psychotic drugs.¹¹¹ The coupling of microelectrodes and fast scan cyclic voltammetry provide a unique means of detecting trace amounts of species in biological systems.

1.7.1 Ultramicroelectrode Geometries

Microelectrodes have many different forms, some of which are illustrated as cross sections in Figure 36. This diagram also illustrates the corresponding diffusion fields. The most popular geometry is the microdisk and is employed in approximately 50% of all investigations.¹¹¹ This particular geometry shows considerable advantage over the others displayed due to the ease of construction and the fact that the sensing surface can be mechanically polished. A wide range of materials are used to construct electrodes, the most popular of which are platinum, carbon fibers and gold, although mercury, iridium, nickel, silver, and superconducting ceramics have also been used.

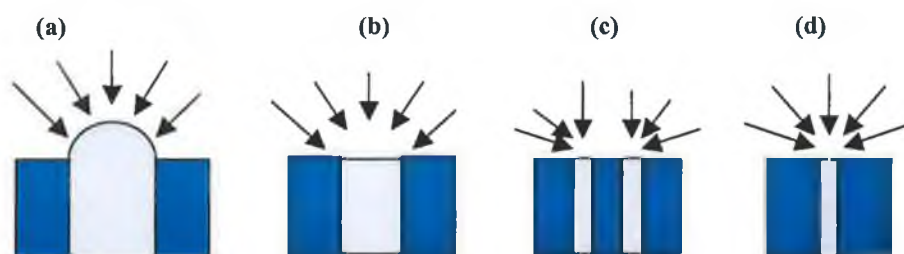


Figure 36. Microelectrode geometries and their associated diffusion fields, (a) hemisphere, (b) disk, (c) ring and (d) band.

1.7.2 Electrochemistry at Ultramicroelectrodes

Electrochemistry at electrodes with microscopic dimensions constitutes one of the most important frontiers in modern electrochemical science.¹²⁰ The advance in the fabrication of microelectrodes provides some significant advantages in electrochemical measurements. These are due to three primary characteristics; the mode of mass transport of the electroactive species to the electrode surface, the reduced capacitance in the electrochemical response, and significantly reduced ohmic drop effects. These three characteristics will be explained in more detail in the following section.

1.7.2.1 Mass Transport

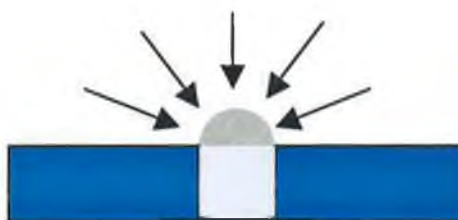
In electrochemical systems three types of mass transport need to be considered, these are diffusion, migration and convection. Migration is the movement of charged species due to a potential gradient. In the experiments presented in this work conditions have been chosen so that migration effects can be neglected. These conditions correspond to the presence of a large quantity of supporting electrolyte (>0.1 M), which does not interfere with the electrode reaction. The electrolyte transports all current in the cell and also decreases the cell resistance. Diffusion is the movement of species from an area of high to low concentration. For example, in the case of a reduction reaction ($O \rightarrow R$) at an electrode surface a depletion layer will form in which the concentrations of O and R are a function of distance from the electrode surface. The concentration of O will be lower at the surface than in the bulk solution, the opposite case will exist for R. Hence, the oxidised species will diffuse towards the electrode surface and the reduced species will diffuse away from the surface.

Shrinking the size of an electrode has a significant and measurable effect on the diffusion process to the electrode surface. Steady state currents may be measured at microelectrodes as the time taken to achieve a steady state depends on the square root of the smallest dimension of an electrode.¹²¹ Therefore, an ultra-small electrode is required to reach a steady state response in a brief period of time. The timescale of an experiment may be changed by varying the scan rate in cyclic voltammetry. The consequences on the voltammetric response at different scan rates are outlined in this section.

- At low scan rates (long experimental timescales) the spherical character of the electrode becomes important, and mass transport is dominated by radial or spherical diffusion as seen in Figure 37(A). The efficient mass transport to the electrode surface allows one to observe a steady state response, i.e., the electrolysis rate is equal to the rate at which molecules diffuse to the electrode surface, Figure 37(B).^{101,111,121} The current response is described by Equation (31) for a disk shaped electrode.

$$i_{(ss)} = 4nFDcR \quad (31)$$

(A) Spherical Diffusion Field



(B)

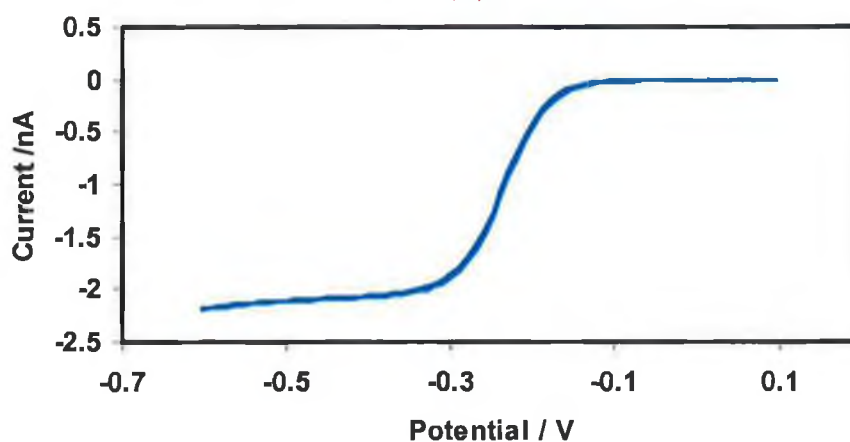


Figure 37. (A) Radial diffusion at long experimental timescales with the associated CV response, (B), the potential limits are +0.1 and -0.6 V and the scan rate is 0.1 Vs⁻¹. The electroactive species is 5 mM [Ru(NH₃)₆]³⁺ containing 0.1 M KCl as the supporting electrolyte.

- Gradually raising the scan rate causes a change to a semi-infinite planar diffusion field, as seen in Figure 38(A). The CV response changes from the sigmoidal response illustrated above to a classic CV response with potential separated anodic and cathodic peaks, Figure 38(B). At these short experimental timescales the current response is described by Equation (32).

$$i_p = (2.69 \times 10^5) n^{3/2} A D^{1/2} v^{1/2} C \quad (32)$$

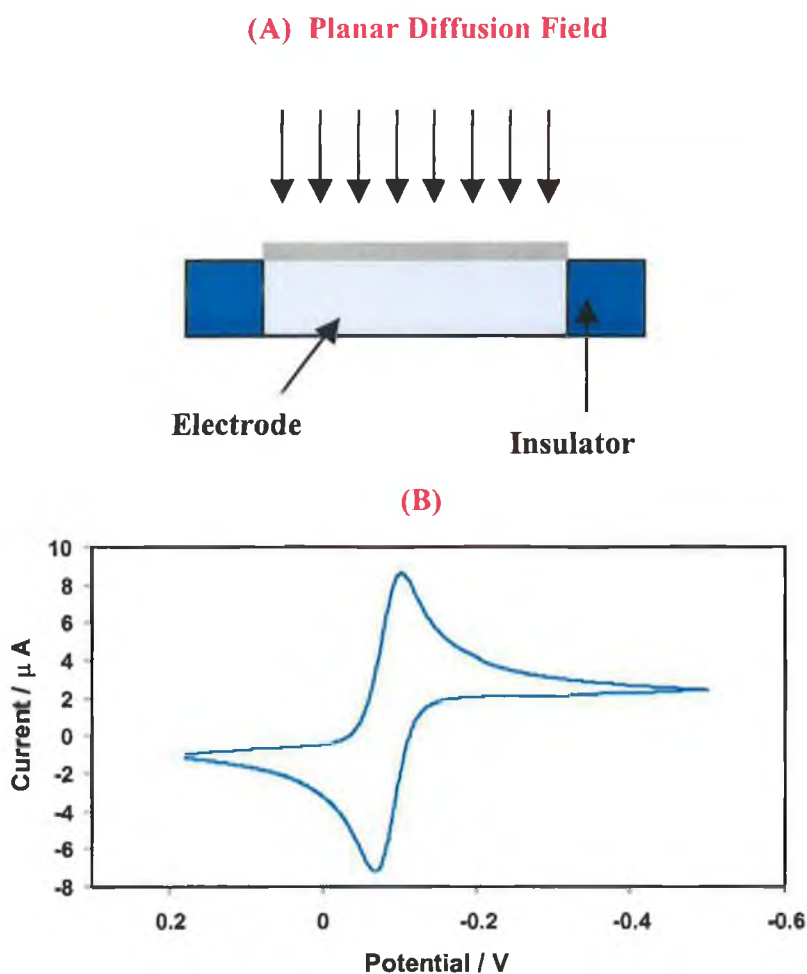


Figure 38. (A) Linear diffusion at short experimental timescales with the associated CV response, (B), the potential limits are +0.2 and -0.6 V and the scan rate is 10 Vs^{-1} . The initial potential is +0.2 V. The electroactive species is 5 mM $[\text{Ru}(\text{NH}_3)_6]^{3+}$ containing 0.1 M KCl as the supporting electrolyte.

1.7.2.2 Double Layer Charging

When an electrode comes into contact with an electrolytic solution, a double layer is formed at the interface, in which the charge present on the metal electrode is compensated for by a layer of oppositely charged ions in solution. This electrochemical double layer behaves like a capacitor.¹¹¹ When the applied potential is changed, a current flows to change the double layer capacitance. The potential at the interface does not attain the applied potential until this charging process is complete. Hence, it is desirable to minimize both the magnitude of the charging current and the time it takes to charge the double layer. The time constant for the charging process is given by Equation (33):

$$RC = \frac{\pi r C_0}{4\kappa} \quad (33)$$

where C_0 is the specific capacitance of an electrode, κ is the conductivity of the solution and r is the radius of a microdisk electrode.

The decreased times for charging current observed at microelectrodes are important since this parameter determines the shortest time at which meaningful measurements of faradaic current can be made.¹⁰¹ The current required to change the double layer capacitance, C , must flow through a resistance, R , corresponding to the total cell resistance. The product RC represents the *cell time constant*, and it is only at times longer than about 5 to 10 RC that useful analytical information is obtained. The small double layer capacitance at ultramicroelectrodes facilitates rapid changes in the electrode potential (fast response times), as seen in Figure 39. As the electrode radius decreases from 25 to 1 μm , the cell time constant decreases linearly from approximately 2 μs to 80 ns. The slope of the best-fit line is consistent with Equation (32), where the double layer capacitance is about 40 $\mu\text{F cm}^{-2}$. The intercept in this graph is approximately 4.3 ns, indicating that the stray capacitance of these microelectrodes is very small. Stray capacitance is explained in section 1.7.3 of this chapter, which details the electrochemical responses observed at nanometer sized electrodes.

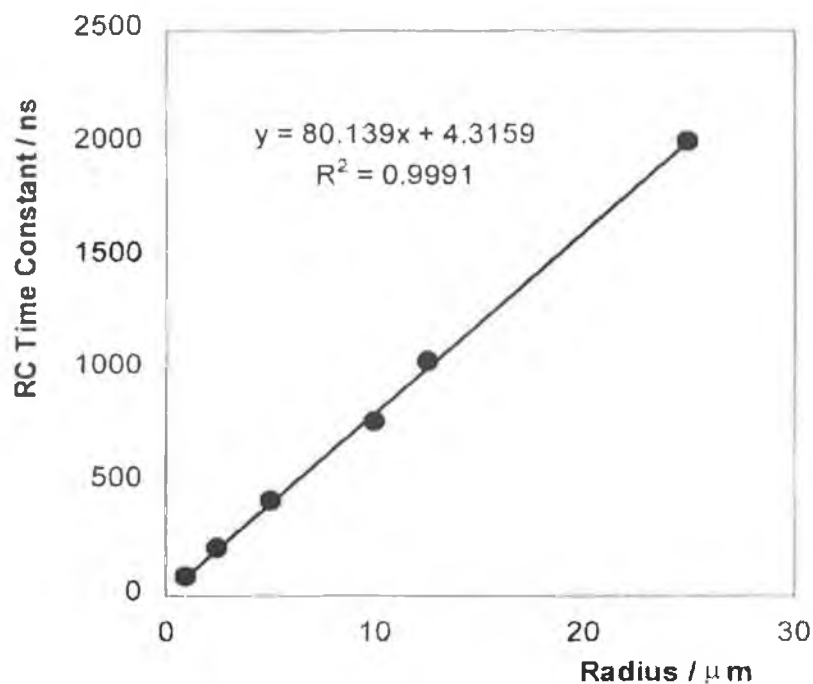


Figure 39. Relationship between the RC cell time constant and the radius of platinum microdisks where the supporting electrolyte is 0.1 M HCl. Cell time constants were measured using chronoamperometry conducted on a microsecond to submicrosecond timescale by stepping the potential from 0.200 to 0.250 vs Ag/AgCl.

1.7.2.3 Ohmic Drop Effects

When charging and discharging currents flow through a solution, they generate a potential that acts to weaken the applied potential by an amount iR , where i is the total current and R is the cell resistance. As the radius of an electrode decreases the solution resistance increases as described by Equation (34):

$$R = \frac{1}{4\kappa r} \quad (34)$$

where κ is the conductivity of the solution and r is the radius of a microdisk electrode. However, the faradaic currents observed at microelectrodes are typically 5-6 orders of magnitude smaller than those observed at macroelectrodes.^{111,122} These small currents lead to a significant decrease in ohmic drop effects. It is important to minimise iR drop

as it can cause separation of the peak potentials and inaccurate results could be obtained in evaluation of kinetic parameters.¹²³

A reduction in iR drop at ultramicroelectrodes allows one to perform amperometric experiments in previously inaccessible samples such as non-polar solvents with diminished amounts of electrolytic solutions. Bond et al.^{124,125,126} measured the same diffusion limited currents with 50 μm disk electrodes for the oxidation of ferrocene in electrolyte-free acetonitrile and in electrolytic solution. The only precondition for experiments in non-polar solvents such as benzene and toluene is that the electrolytes are soluble in these media and that they dissociate to some degree to provide an acceptable level of conductivity in the solution.¹²⁷

1.7.3 Microelectrode to Nanode Dimensions

As fabrication procedures become more advanced, electrodes with nanometer dimensions and below are now available. When an electrode approaches molecular dimensions, approximately 10-100Å, the electrochemical properties change as the diffuse layer becomes equal to or greater than the dimension of the electrode. Although the theory in this area has not been investigated in great detail some characteristics of the electrochemical properties are discussed here.

As the radius of an electrode is decreased to nanometer dimensions, as presented in Chapter 6 of this work, the double layer capacitance no longer decreases but reaches a limiting value. This is due to a number of problems associated with the sealing of such small electrodes and also due to what is known as stray capacitance. Stray capacitance arises from the leads and electrical connections and results in an increase in the cell RC time constant as follows,

$$RC = \frac{1}{4\kappa r} (\pi r^2 C_o + C_{\text{stray}}) \quad (35)$$

where RC is the cell time constant, κ is the conductivity of the solution, r is the radius of the electrode, C_o is the specific double layer capacitance of an electrode and C_{stray} is the stray capacitance. Depending on the quality of the electrode used and experimental

setup, the stray capacitance is typically between a few pF and several tens of pF.¹²⁸ At a normal size electrode, this stray capacitance is negligible compared to the double layer capacitance, and therefore, does not affect the observed cell time constant. However, the magnitude of the double layer capacitance is reduced, typically by six orders of magnitude by shrinking the size of the electrode. Hence, the stray and double layer capacitances become comparable at nanometer-sized tips and an increased cell time constant relative to that measured at a micrometer sized electrode results. This increased cell time constant could cause faradaic responses to be obscured by charging/discharging processes. Therefore, it is very important when fabricating nanodes that the seal between the insulation and electrode material is good, thus preventing any solution leakage. Methods used to determine the quality of the microelectrode seal are discussed in Section 1.7.6.

Amatore²³ considered the effect of decreasing the electrode size to nanode dimensions on the cell time constant and ohmic drop parameters. The predicted responses are illustrated in Figure 40. As discussed above RC and iR are proportional to the electrode radius at micrometer size electrodes. However, when the radius is of nanode dimension edge effects and non-planar diffusion control the transport of molecules to the electrode surface, with the result that the current becomes proportional to the radius of the electrode rather than to its surface area. Under these conditions iR becomes independent of the electrode dimension, i.e. decreasing the size further yields no further improvement in the electrochemical response.

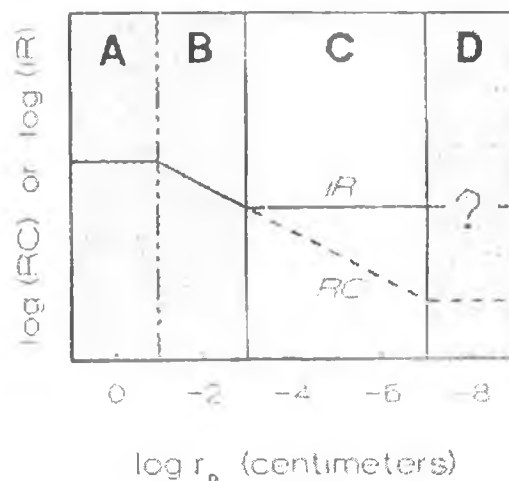


Figure 40. Schematic representation of ohmic drop and cell time constant of an electrochemical cell as a function of the radius of the working electrode. The various zones may be defined as A, macroelectrodes, B, microelectrodes, C, ultramicroelectrodes and D, nanoelectrodes or smaller. The scales are arbitrary.

1.7.4 Microelectrode Fabrication Procedures

The manufacture and use of electrodes with characteristic dimensions in the submicrometer to nanometer range is becoming more widespread and common. The survey of literature presented here deals with procedures, which have been published for the construction of platinum, iridium, carbon fiber,^{115,119,129} and mercury electrodes.^{130,131,132,133,134,135} Since the early 1980s Pt^{136,137,138,139,140,141,142,143,144,145} and Pt-Ir¹⁴⁶ microdisk electrodes are among the most popular due to the mechanical stability of these electrodes. However, as outlined in a previous section, mercury electrodes have a central role in developments in electroanalytical chemistry due to the reproducibility of the mercury surface.

One of the more recent publications dealing with the fabrication and characterisation of nanometer-sized platinum electrodes was made by Katemann and Schuhmann.¹³⁶ The pipette-wire assembly was placed in a Sutter P-2000 laser pipette puller which allowed varying of five parameters; temperature of heating, the length of the segment heated, delay time between turning the heat on and beginning of the pull, the velocity of the

pull, and the strength of the pull. The instrument allows pipettes to be pulled to a fine point in the nanometer length scale. The use of a microelectrode puller offers a few significant advantages. First, it is quick and easy to fabricate electrodes. Secondly, it allows for the construction of very small microelectrodes with smooth tapers. However this technique also has a number of notable disadvantages. The wire is sealed in glass after the pulling procedure and requires polishing to make a connection to a contacting solution. The geometry of the microelectrode after polishing is unknown and can be hard to evaluate. Methods by which this can be determined are scanning electron microscopy and cyclic voltammetry measurements. These methods of characterisation are discussed in more detail in the experimental results section presented in chapter 6 of this work.

Other research groups which have implemented this procedure for the fabrication of nanoelectrodes are Unwin et al.,¹³⁹ Wong and Xu,¹²⁹ Shao and Mirkin,¹⁴⁰ Lewis et al.,¹⁴³ Kim, Scarnlis and Ewing,¹¹⁵ and Wightman and Kelly.¹¹⁹ Wong and Xu reported a success rate of 85% for the construction of carbon disk electrodes with total structural diameters between 500 and 1000 nm using a horizontal micropipette puller. However, the success rate dropped to lower than 70% when the structural diameters decreased to between 500 and 100 nm. Pendley and Abruna¹⁴⁴ make an interesting observation when fabricating micron-sized platinum electrodes using the microelectrode puller technique. They note that to ensure success in the electrode preparation it is essential that the platinum wire used is annealed and not hard-drawn. Hard drawn wire did not decrease in diameter when pulled. They attribute this to the fact that the annealed platinum wire is more ductile and can be drawn to much smaller diameters. This result contrasts with the results presented by Katemann and Schuhmann¹³⁶ and the experimental work presented in chapter 6 of this document. These results suggest that platinum wire of different grades can be used in these experiments but it is imperative that all five pulling parameters outlined previously are optimised to produce a nanometer-sized electrode.

Exposing the metal electrode once the pulling procedure has been executed may be done by a number of methods. One way of doing this is electrochemical etching of the wire. This is done by submerging the wire in an etching bath comprising for example saturated sodium nitrate¹³⁹ or 40 % hydrogen fluoride.¹⁴⁰ Lewis et al.¹⁴⁶ used a solution of 2 M NaOH and 6 M KCN. The hemispherical tip produced from this method was

observed to be smooth to the limiting resolution of the scanning electron microscope (SEM). This indicates that the metal undergoes an effective electro-polishing process during etching. For this reason further polishing of the electrode surface was not necessary. The etching procedure has a number of significant features: (1) no mechanical pretreatment, i.e., polishing of the ultramicroelectrode is not required because the etched metal surface is microscopically smooth and (2) the metal insulator seals of the electrodes are reproducible. However a possible disadvantage of this design is the fact that the metal surface of the ultramicroelectrodes cannot be renewed or polished.

Another method of exposing the metal wire is micropolishing. This procedure can be carried out using a BV-10 micropipette beveller available from Sutter. The tip of the microelectrode is lowered using the control of a micromanipulator¹¹⁹ until it is just above the surface of the polishing material, using diamond or alumina particles. The size of the prepared tip increases with the length of polishing. Only a fraction of a complete turn of the polishing wheel is required to produce a nanometer-sized electrode. Once polished the tip of the electrode should be smooth and free from cracks. This procedure is similar to the one used by Katemann and Schuhmann to polish nanometer sized platinum tips. A custom built polishing machine was developed by these researchers, which consisted of a cylindrical brass holder, the motor from a rotating disk electrode and a computer hard disk as the polishing wheel, Figure 41. For polishing the electrode is placed in a soft silicon tube and secured in the brass holder using a screw. The brass holder is then rotated using an elastic band and slowly lowered down onto the surface of the polishing plate using manual micropositioning elements. The polishing process determines the size of the electrode produced and so it has to be done very carefully.

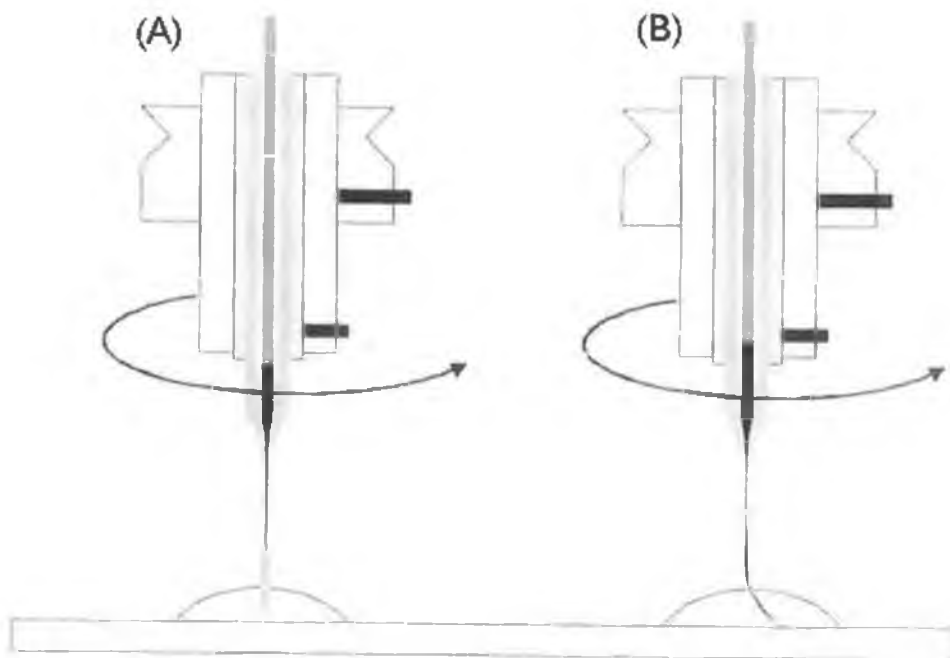


Figure 41. Schematic presentation of the set-up for nanoelectrode polishing, (A) the nanode is rotated on a polishing plate in a water-alumina suspension, and (B) rotation of the fragile electrode tip as the electrode approaches the polishing surface.

1.7.4.1 Mercury Microelectrodes

The development of mercury microelectrodes has been the subject of numerous papers^{130,131,132,133,134,135} over the past 15 years. Mercury microelectrodes are usually prepared by electrodeposition of mercury on metal substrates. A support material for mercury films should be easily wetted by mercury, but on the other hand its solubility in mercury should be very low. It is practically impossible to combine these two features. Films deposited on supports of platinum, silver, gold or iridium exhibit a reasonably uniform surface due to good wetting, but solubility of these metals in mercury is significant.^{132,133,135}

In a number of reports^{130,131,135} platinum microdisk electrodes serve as the substrate for mercury deposition. The electrodes were prepared by sealing a wire of micron radius in a glass capillary of 1 mm diameter or less.^{130,135} Carbon fiber electrodes were prepared in a similar manner.^{133,134} Electrodes were polished before use in each experiment. The

initial step in the deposition of a metallic phase onto a substrate involves the formation of nuclei of critical size from subcritical clusters of adatoms in a process referred to as nucleation. Following nucleation, the growth of the nuclei is potential driven. The drops coalesce to finally give a hemispherical mercury drop. In order to investigate the quality of the deposition process, Daniele et al.¹³⁰ performed experiments at different deposition potentials. Cyclic voltammetric experiments were controlled by a PAR 175 function generator, and a Keithley 428 picoammeter was used to measure the current. The aim of this was to attain complete coverage of the electrode surface with the smallest amount of mercury deposited in the shortest time. They concluded that the mercury electrodes formed on a platinum substrate were more stable if the deposition of mercury was carried out -0.4 V from 1 M HClO_4 with 10 - 50 mM Hg_2^{2+} . If the deposition potential was more negative than -0.5 V, strong hydrogen evolution could be seen, which increases as the acidity of the solution increases. Then hydrogen bubbles of size comparable with the electrode itself blocked the surface and further mercury deposition was inhibited. At potentials less than -0.4 V the mercury deposition was slow, increasing significantly the time required for total coverage of the surface.

Although it has been demonstrated that mercury can be relatively easily deposited on a platinum surface, the problem of mercury and platinum interdiffusion, especially at longer times remains. Despite this, it should be noted that a very small mercury electrode opens the possibility to study fundamental problems in electrochemistry, for which only mercury electrodes are suited and also broadens and strengthens practical analytical applications.¹³² An obvious application of microelectrode tips is in scanning tunneling microscopy (STM) and scanning electrochemical microscopy (SECM).^{147,148} These techniques require small geometrically well-defined tips fabricated from chemically inert conductors to obtain images of high resolution.

1.7.5 Shapes of Ultramicroelectrodes

The voltammetric response of an ultramicroelectrode does not provide sufficient information about the geometry of a microelectrode. Shao and Mirkin¹⁴⁰ present several different electrode shapes that can result from different preparation procedures. A perfect microdisk UME (Figure 42A) is very unlikely to be produced when the radius, is less than 2 μm . It is more likely that an irregularly shaped planar electrode (Figure

42B) will result. A tip with a conductor protruding from the insulating sheath (Figure 42C) may be shaped as a spherical cone. Convex UMEs require thorough characterisation and should be used cautiously. If the tip is recessed into the glass insulator (Figure 42D,E) its voltammetric behaviour depends on the relation between the radius of the conducting cone and that of the aperture in the insulating sheath. When the opening in the glass is significantly larger than the surface area of the metal exposed to solution (Figure 42D), the UME behaviour may not be very different from that of the regular inlaid electrode. In contrast, Figure 42E represents the most dangerous “lagooned” geometry, i.e., an electrode with the metal recessed into the solution filled microcavity inside the glass insulator. Such an electrode can mimic the behaviour of a much smaller UME, and the measured apparent rate constant may be orders of magnitude higher than the true value. A leaky UME (Figure 42F) can be easily identified from the relatively high double-layer charging current, i_c . The ratio of the i_c to the steady-state diffusion-limiting current is proportional to the sweep rate, v . For a well-sealed sub-micrometer-sized UME, this ratio should be small even at sweep rates of the order of several volts per second.

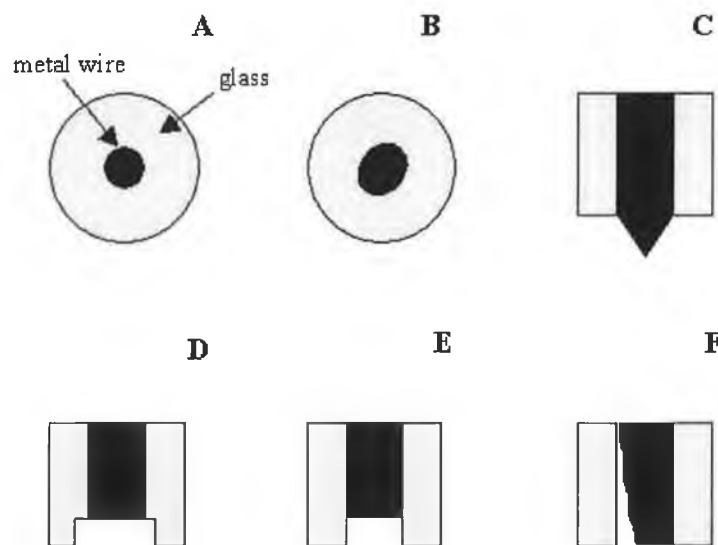


Figure 42. Different shapes of ultramicroelectrodes (A) a perfect microdisk, (B) an irregularly shaped disk-type planar UME, (C) a convex UME with metal protruding from the glass sheath, (D) a recessed electrode, (E) a lagooned electrode, (F) a leaky UME.

1.7.6 Characterisation of Ultramicroelectrodes

Ultramicroelectrodes may be characterized by a number of techniques to determine the geometry and size of the fabricated tip. The most common techniques used are cyclic voltammetry and scanning electron microscopy (SEM). The mass-transport-controlled limiting current, i_{lim} , measured from the plateau of the sigmoidal steady-state voltammogram can be related to the effective electrochemical radius of the exposed metal in a disk electrode by Equation (36):

$$i_{ss} = 4nFDcR \quad (36)$$

where D and C are the diffusion coefficient and concentration of the electroactive species present in solution, n is the number of electrons transferred per redox event, F is the Faraday's constant, and r is the radius of the exposed section of the tip. Penner, Heben and Lewis¹⁴⁹ have used this method to determine the radius of Pt-Ir ultramicroelectrodes with radii of 0.5-10 μ m. They subsequently compared the radii obtained from voltammetry measurements with those measured from SEM images and observed good correlation between both results. For example, the radius a polymer-coated electrode determined from the limiting current in cyclic voltammetry was 6 μ m. This compared to a value of 8.2 μ m when the radius was estimated from an SEM image.

Scanning electron microscopy (SEM) is an imaging technique, which enables one to look at microfabricated tips to measure the radius and obtain an estimate of the geometry of the tip. If the tip is of micron dimension it is also possible to determine the quality of the seal between the metal wire and the insulating material. Improper sealing of the microelectrode tip causes the faradaic current to be obscured by the capacitive current. Caruana and Bannister¹⁴¹ note that the main factors affecting the reproducibility of the seal between the wire and insulator are the cleanliness of the wire used and the method of sealing employed.

Wightman and Kelly¹¹⁹ have fabricated bevelled carbon fiber electrodes. The active area of the microelectrode, defined by the surface area of the exposed carbon fiber as seen from the SEM image in Figure 43 is elliptical rather than disk shaped. This geometry provides a major advantage because an increase in the working electrode area

is obtained that is confined virtually to the same space as a regular disk electrode. However, the increased surface area allows for the measurement of very low concentrations, due to the large voltammetric currents observed. Using this electrode current in the picoamp range may be measured. Figure 43 also gives an approximation of the integrity of the seal between the epoxy, glass and carbon fiber. The radius of the electrode displayed is approximately 10 μm .

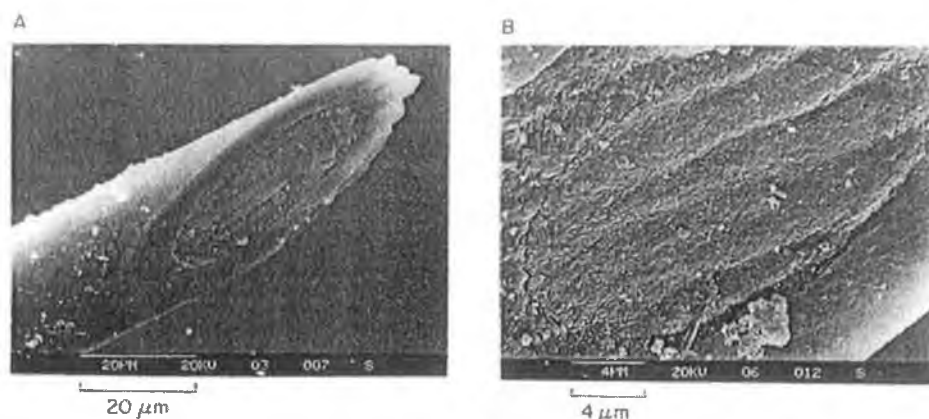


Figure 43. Electron micrographs of ultramicroelectrodes bevelled using 1 μm diamond polish: (A) electrode of approximately 10 μm tip radius with the extent and angle of bevel shown; (B) enlargement showing detail of the seal between the carbon fiber (at centre), epoxy, and the glass capillary.

SEMs of ultrasmall structures, i.e., tip diameters of about 1 μm or less are nondescript, as high-resolution imaging is no longer possible.¹¹⁵ Thus, it is impossible to detect the quality of a nanode by this technique and this has also been found when characterising the nanodes in chapter 6 of this work. Fabrication defects such as a very narrow gap (<0.1 μm) between the glass and the metal, a tiny crack or a glass bubble are negligible in the case of a 10 μm electrode, but it becomes more important as the diameter of the electrode decreases.¹⁵⁰ When the microprobe is of nanometer dimensions, such a gap can cause very severe distortions in the voltammetric response.¹²⁰ Hence, the only quantitative way of detecting such a gap is the observation of large capacitive current responses in voltammetry, as illustrated in Figure 44 below.

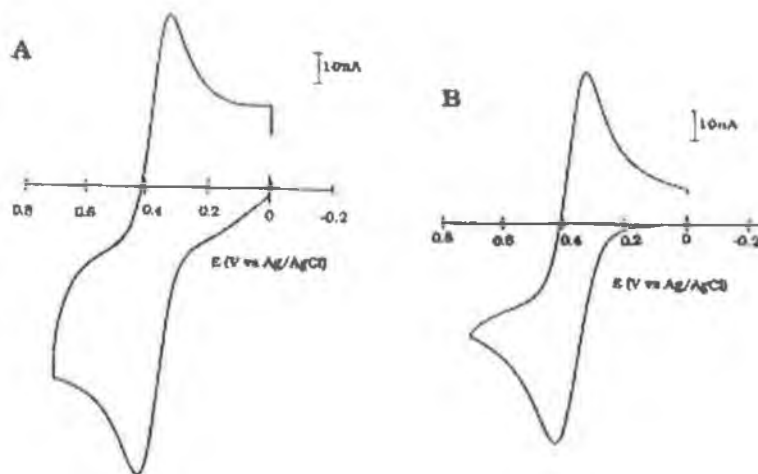


Figure 44. Cyclic voltammograms at 100 mV s^{-1} at a 10 nm gold disk electrode in $5 \text{ }\mu\text{M}$ aqueous TMAFc^+ and 1 mM NaNO_3 , (A) before thermal treatment and (B) after thermal treatment to seal the nanoelectrode tip.

1.8 Conclusions

This introductory chapter has given an insight into how an electroactive species can adsorb onto an electrode surface, the literature relating to anthraquinone molecules has been the main focus as these molecules form the basis of the experimental work in the remaining chapters of this report. The principal theories detailing heterogeneous electron transfer processes, the Butler-Volmer and Marcus theories have also been reviewed. Literature relating to the theory of proton coupled electron transfer are introduced to demonstrate the theoretical and experimental work carried out in this area to date.

This chapter also outlined the electrochemical techniques important to this work and explained some of the information, which can be extracted from cyclic voltammetry and chronoamperometry data. Spectroscopic techniques and some surface probe microscopy techniques are introduced also to highlight how these techniques have been used to characterise monomolecular films.

Finally the properties of microelectrodes have been discussed to show how microelectrodes can be implemented in electrochemical measurements and other areas of research. The small dimensions of these electrodes leads to properties, which are not exhibited by macroelectrodes and so more information can be accessed using these microprobes. However, as the dimensions of electrodes extend into the nanometer range the properties change again and this has an interesting consequence on the measurements, which are feasible with these electrodes. This has been reviewed briefly here and will be discussed further in the experimental chapters.

1.9 References

1. Bard, A.J., Abruna, H.D., Chidsey, C.E., Faulkner, L.R., Feldberg, S.W., Itaya, K., Majda, M., Melroy, O., Murray, R.W., Porter, M.D., Soriaga, M.P., White, H.S., *J. Phys. Chem.*, **1993**, 97, 7147.
2. Sagiv, J, *J. Am. Chem. Soc.*, **1980**, 102, 92.
3. Meyer, T.J., *J. Electrochem. Soc.*, **1984**, 131, 221C.
4. Slavcheva, E., Sokolova, E., Raicheva, S., *J. Electroanal. Chem.*, **1993**, 360, 271.
5. Aramaki, K., *Corrosion Science*, **1999**, 41, 1715.
6. Nozawa, K., Nishihara, H., Aramaki, K., *Corrosion Science*, **1997**, 39, 1625.
7. Nozawa, H., Nishihara, K., Aramaki, K., *Corrosion Science*, **1999**, 41, 57.
8. Haneda, R., Nishihara, K., Aramaki, K., *J. Electrochem. Soc.*, **1997**, 144, 1215.
9. Swalen, J.D., Allara, D.L., Andrade, J.D., Chandross, E.A., Garoff, S., Israelachvili, J., McCarthy, T.J., Murray, R., Pease, R.F., Rabolt, J.F., Wynne, K.J., Yu, H., *Langmuir*, **1987**, 3, 932.
10. Sabatani, E., Rubinstein, I, *J. Phys. Chem.*, **1987**, 91, 6663.
11. Muskal, N., Turyan, I, Mandler, D., *J. of Electroanal. Chem.*, **1996**, 131.
12. Blaho, J.K., Goldsby, K.A., *J. Am. Chem. Soc.*, **1990**, 112, 6132.
13. Chambers, J.Q., *Chemistry of Quinonoid Compounds, Vol.2*, **1988**, 719.
14. Okamura, M.Y., Paddock, M.L., Graige, M.S., Feher, G., **2000**, 1458, 148.
15. Von Helmholtz, H.L.F., *Ann. Physik*, **1853**, 89, 211.
16. Von Helmholtz, H.L.F., *Ann. Physik*, **1879**, 7, 337.
17. Gouy, G., *J. Phys. Chem.*, **1910**, 9, 457.
18. Chapman, D.L., *Phil. Mag.*, **1913**, 25, 475.
19. Stern, O., *Elektrochem.*, **1924**, 30, 508.
20. Forster, R.J., Keyes, T.E., Vos, J.G., *Interfacial Supramolecular Assemblies*, **2003**.
21. Butler, J.A., *Trans Faraday Soc.*, **1924**, 19, 729.
22. Erdey, Gruz, T., Volmer, M.Z., *Physik. Chem.*, **1930**, 150A, 203.
23. Rubenstein, I., *Physical Electrochemistry, Principles Methods and Applications*, *Dekker*, **1995**, 37.
24. Miller, R.J.D., McLendon, G.L., Nozik, A.J., Schmickler, W., Willig, F., *Surface Electron Transfer Processes*, **1995**, Chapter 3.

25. Marcus, R.A., *J. Chem. Phys.*, **1956**, 24, 4966.
26. Marcus, R.A., *J. Chem. Phys.*, **1965**, 43, 679.
27. Marcus, R.A., *Ann. Rev. Phys. Chem.*, **1964**, 15, 155.
28. Marcus, R.A., *Electrochim. Acta*, **1968**, 13, 955.
29. Sutin, N., *Acc. Chem. Res.*, **1982**, 15, 275.
30. Bolton, J.R., Archer, M.D., *Am. Chem. Soc.*, **1991**, 7.
31. Kuznetsov, A.M., Ulstrup, J., *Electrochim. Acta*, **2000**, 45, 2339.
32. Forster, R.J., Faulkner, L.R., *J. Am. Chem. Soc.*, **1994**, 116, 5444.
33. Forster, R.J., Figgemeier, E., Loughman, P., Lees, A., Hjelm, J., Vos, J.G., *Langmuir*, **2000**, 16, 7871.
34. Chidsey, C.E.D., Bertozzi, C.R., Putvinski, T.M., Mujisce, A.M., *J. Am. Chem. Soc.*, **1990**, 112, 4301.
35. Chidsey, C.E.D., *Science*, **1991**, 251, 919.
36. Li, T.T.-T., Weaver, M.J., *J. Am. Chem. Soc.*, **1984**, 106, 6107.
37. Finklea, H.O., Hanshew, D.D., *J. Am. Chem. Soc.*, **1992**, 114, 3173.
38. Finklea, H.O., Ravenscroft, M., Snider, D.A., *Langmuir*, **1993**, 9, 223.
39. Laviron, E., *J. of Electroanal. Chem.*, **1995**, 382, 111.
40. Acevedo, D., Abruna, H.D., *J. Phys. Chem.*, **1991**, 95, 9590.
41. Forster, R.J., Kelly, A.J., Vos, J.G., *J. Electroanal. Chem.*, **1989**, 270, 365.
42. Forster, R.J., Faulkner, L.R., *J. Am. Chem. Soc.*, **1994**, 116, 5453.
43. Forster, R.J., Faulkner, L.R., *Anal. Chem.*, **1995**, 67, 1232.
44. Forster, R.J., Faulkner, L.R., *Langmuir*, **1995**, 11, 1014.
45. Forster, R.J., O'Kelly, J.P., *J. Phys. Chem.*, **1996**, 100, 3695.
46. Forster, R.J., *Inorg. Chem.*, **1996**, 35, 3394.
47. Forster, R.J., Loughman, P., Keyes, T.E., *J. Am. Chem. Soc.*, **2000**.
48. Slattery, S.J., Blaho, J.K., Lehnes, J., Goldsby, K.A., *Coord. Chem. Reviews*, **1998**, 174, 391.
49. Thorp, H.H., *Journal of Chemical Education*, **1992**, 69, 250.
50. Vetter, K.J., *Z. Electrochem.*, **1952**, 56, 797.
51. Vetter, K.J., *Electrochemical Kinetics, Academic Press, New York*, **1967**.
52. Laviron, E., *J. Electroanal. Chem.*, **1981**, 124, 9.
53. Laviron, E., *J. Electroanal. Chem.*, **1981**, 130, 23.
54. Laviron, E., *J. Electroanal. Chem.*, **1983**, 146, 15.
55. Laviron, E., *J. Electroanal. Chem.*, **1984**, 164, 213.

56. Deakin, M.R., Wightman, R.M., *J. Electroanal. Chem.*, **1986**, 206, 167.
57. Deakin, M.R., Kovach, P.M., Stutts, K.J., Wightman, R.M., *Anal. Chem.*, **1986**, 58, 1474.
58. Wipf, D.O., Wehmeyer, K.R., Wightman, R.M., *J. Org. Chem.*, **1986**, 51, 4760.
59. O'Kelly, J.P., Forster, R.J., *The Analyst*, **1998**, 123, 1987.
60. Forster, R.J., O'Kelly, J.P., *J. of Electroanal. Chem.*, **2001**, 498, 127.
61. Walczak, M.M., Dryer, D.A., Jacobson, D.D., Foss, M.G., Flynn, N.T., *J. of Chem. Educ.*, **1997**, 74, 1195.
62. Bailey, S.I., Ritchie, I.M., *Electrochim. Acta*, **1985**, 30, 3.
63. Hale, J.M., Parsons, R., *Trans. Faraday Soc.*, **1963**, 59, 1429.
64. Sato, Y., Fujita, M., Mizutani, F., Uosaki, K., *J. of Electroanal. Chem.*, **1996**, 409, 145.
65. He, P., Crooks, R.M., Faulkner, L.R., *J. Phys. Chem.*, **1990**, 94, 1135.
66. Zhang, J., Anson, F.C., *J. Electroanal. Chem.*, **1992**, 331, 945.
67. Forster, R.J., Keyes, T.E., Farrell, M., O'Hanlon, D., *Langmuir*, **2000**, 16, 9871.
68. Eggins, B.R., Chambers, J.Q., *Chem. Commun.*, **1969**, 232.
69. Eggins, B.R., Chambers, J.Q., *J. Electrochem. Soc.*, **1970**, 117, 186.
70. Parker, V.D., *Chem. Commun.*, **1969**, 716.
71. Wipf, D.O., Wehmeyer, K.R., Wightman, R.M., *J. Org. Chem.*, **1986**, 51, 4760.
72. Sun, L., Johnson, B., Wade, T., Crooks, R.M., *J. Phys. Chem.*, **1990**, 94, 8869.
73. Xu, J., Chen, Q., Swain, G.M., *Anal. Chem.*, **1998**, 70, 3146.
74. Ta, T.C., Kanda, V., McDermott, M.T., *J. Phys. Chem.*, **1999**, 8, 1295.
75. Xu, C., *Thesis, University of Illinois at Urbana-Champaign*, **1992**, Chapter 5.
76. Forster, R.J., *Langmuir*, **1995**, 11, 2247.
77. Berg, H., *Naturwissenschaften*, **1961**, 48, 714.
78. Forster, R.J., *Analyst*, **1996**, 121, 733.
79. Katz, E., Willner, I., *Langmuir*, **1997**, 13, 3364.
80. O'Hanlon, D., Forster, R.J., *Langmuir*, **2000**, 16, 702.
81. Soriaga, M.P., Hubbard, A.T., *J. Am. Chem. Soc.*, **1982**, 104, 3937.
82. Soriaga, M.P., Hubbard, A.T., *J. Am. Chem. Soc.*, **1982**, 104, 2735.
83. Soriaga, M.P., Hubbard, A.T., *J. Am. Chem. Soc.*, **1982**, 104, 2742.
84. Soriaga, M.P., White, J.H., Hubbard, A.T., *J. Phys. Chem.*, **1983**, 87, 3048.
85. Soriaga, M.P., Hubbard, A.T., *J. Phys. Chem.*, **1984**, 88, 1089.

86. Soriaga, M.P., Soriaga, E.B., Hubbard, A.T., Benziger, J.B., Pang, K.-W.P., *Inorg. Chem.*, **1985**, 24, 65.
87. Pauling, L.C., *Nature of the Chemical Bond*, 3rd ed., Cornell University Press, New York, **1960**, pp221-264.
88. Cotton, F.A., *J. Am. Chem. Soc.*, **1968**, 90, 6230.
89. Garrell, R.L., *Anal. Chem.*, **1989**, 61, 401A.
90. Ramaakrishnan, V., Krishnamurthy, Gurunathan, M., Srivatsavoy, V.J.P., *Spectrochimica Acta*, **1990**, 46A, 1615.
91. Srikanth, V.G., Jayaraj, S.E., Ramakrishnan, V., *J. Phys.*, **1993**, 41, 467.
92. Jayaraj, S.E., Ramakrishnan, V., *Spectrochimica Acta*, **1995**, 51A, 979.
93. Benjamin, A.D., Jayaraj, S.E., Ramakrishnan, V., *Bulletin of Electrochemistry*, **2000**, 16, 512.
94. Umadevi, M., Ramakrishnan, V., *Spectrochimica Acta*, **2002**, in press.
95. Marasinghe, P.A.B., Gillispie, G.D., *Chem. Phys.*, **1989**, 136, 249.
96. Margetic, D., Eckert-Maksic, M. Maksic, Z.B., *J. of Molecular Structure (Theochem)*, **1992**, 277, 161
97. Marzocchi, M.P., Mantini, A.R., Casu, M., Smulevich, G., *J. Chem. Phys.*, **1998**, 108, 534.
98. Rivas, L., Sanchez-Cortes, S., Stanicova, J., Garcia, Ramos, J.V., Miskovsky, P., *Vibrational Spectroscopy*, **1999**, 20, 179.
99. Nishiyama, K., Tahara, S., Uchida, Y., Tanoue, S., Taniguchi, I., *J. of Electroanal. Chem.*, **1999**, 478, 83.
100. Han, S.W., Ha, T.H., Kim, C.H., Kim, K., *Langmuir*, **1998**, 14, 6113.
101. Wightman, R.M., *Anal. Chem.*, **1981**, 53, 1125A.
102. Heinze, H., *Angewandte Chemie*, **1984**, 23, 831
103. Nicholson, R.S., *Anal. Chem.*, **1965**, 37, 1351.
104. Andrieux, C.P., Hapiot, P., Saveant, J.M., **1990**, 90, 723.
105. Willard, H.H., Merritt, L.L., Dean, J.A., Settle, F.A., *Instrumental Methods of Analysis*, 698.
106. Bard, A.J., Faulkner, L.R., *Electrochemical Methods : Fundamentals and Applications, Second Edition*, Wiley, New York, **2001**, Chapter 1.
107. Brett, C.M.A., Brett, A.M.O., *Electroanalysis*, **1993**, 49.
108. Schreurs, J., Barendrecht, E., *J. of the Royal Netherlands Chem. Soc.*, **1984**, 103, 205.

109. Swan, P.N., Dissertation, University of Southampton, 1980.
110. Pons, S., Fleischmann, M., *Anal. Chem.*, **1993**, 32, 1268.
111. Forster, R. J., *Chemical Society Reviews*, **1994**, 289.
112. Bond, A.M., Oldham, K.B., Zoski, C.G., **1989**, 216, 177.
113. Adams, R.N., *Anal. Chem.*, **1976**, 48, 1126A.
114. Wightman, R.M., Strobe, E., Plotsky, P.M., Adams, R.N., *Nature*, **1976**, 262, 145.
115. Kim, Y.T., Scarnulis, D.M., Ewing, A.G., *Anal. Chem.*, **1986**, 58, 1782.
116. Baur, J.E., Kristensen, E.W., May, L.J., Wiedemann, D.J., Wightman, R.M., *Anal. Chem.*, **1988**, 60, 1268.
117. Kristensen, E.W., Kuhr, W.G., Wightman, R.M., *Anal. Chem.* **1987**, 59, 1752.
118. Mcricley, M.A., Linsenmeier, R.A., *J. of Electroanal. Chem.*, **1996**, 414, 235.
119. Kelly, R.S., Wightman, R.M., *Analytica Chimica Acta*, **1986**, 187, 79.
120. Menon, V.P., Martin, C.R., *Anal. Chem.*, **1995**, 67, 1920.
121. Moressi, M.B., Fernandez, H., *J. of Electroanal. Chem.*, **1993**, 153.
122. Pons, S., Fleischmann, M., *Anal. Chem.*, **1994**, 289.
123. Chen, X., Zhuang, J., He, P., *J. of Electroanal. Chem.*, **1989**, 271, 257.
124. Thormann, W., van den Bosch, P., Bond, A.M., *Anal. Chem.*, **1985**, 57, 2764.
125. Bond, A.M., Lay, P.A., *J. Electroanal. Chem.*, **1986**, 199, 285.
126. Cooper, J.B., Bond, A.M., *J. Electroanal. Chem.*, **1991**, 315, 143.
127. Heinze, J., *Angewandte Chemie*, **1993**, 32, 1268.
128. Tschuncky, P., Heinze, J., *Anal. Chem.*, **1995**, 67, 4020.
129. Wong, D.K.Y., Xu, L.Y.F., *Anal. Chem.*, **1995**, 67, 4086.
130. Daniele, S., Bragato, C., Argese, E., *Electrochem. Commun.*, **2000**, 2, 399.
131. Baldo, M.A., Daniele, S., Mazzocchin, G.A., *Electrochimica Acta*, **1996**, 41, 811.
132. Golas, J., Galus, Z., Osteryoung, J., *Anal. Chem.*, **1987**, 59, 389.
133. Golas, J., Osteryoung, J., *Anal. Chem. Acta*, **1986**, 181, 211.
134. Golas, J., Osteryoung, J., *Anal. Chem. Acta*, **1986**, 186, 1.
135. Wehmeyer, K.R., Wightman, R.M., *Anal. Chem.*, **1985**, 57, 1989.
136. Katemann, B.B., Schuhmann, W., *Electroanal.*, **2002**, 14, 22.
137. Robertson, R.T., Pendley, B.D., *J. of Electroanal. Chem.*, **1994**, 374, 173
138. Wipf, D.O., Michael, A.C., Wightman, R.M., *J. Electroanal. Chem.*, **1989**, 269, 15.

139. Slevin, C.J., Gray, N.J., Macpherson, J.V., Webb, M.A., Unwin, P.R., *Electrochem. Commun.*, **1999**, 1, 282.
140. Shao, Y., Mirkin, M.V., Fish, G., Kokotov, S., Palanker, D., Lewis, A., *Anal. Chem.*, **1997**, 69, 1627.
141. Caruana, D.J., Bannister, J.V., *J. of Electroanal. Chem.*, **1997**, 424, 197.
142. Zhang, C., Zhou, X., *J. of Electroanal. Chem.*, **1996**, 415, 65.
143. Fish, G., Bouevitch, O., Kokotov, S., Lieberman, K., Palanker, D., Turovets, I., Lewis, A., *Rev. Sci. Instrum.*, **1994**, 66, 3300.
144. Pendley, B.D., Abruna, H.D., *Anal. Chem.*, **1990**, 62, 782.
145. Morris, R.B., Franta, D.J., White, H.S., *J. Phys. Chem.*, **1987**, 91, 3559.
146. Penner, R.M., Heben, M.J., Longin, T.L., Lewis, N.S., *Science*, **1990**, 250, 1118.
147. Mirkin, M., *Anal. Chem. News & Features*, **1996**, 117A.
148. Mirkin, M.V., Fan, F., -R.F., Bard, A.J., *J. Electroanal. Chem.*, **1992**, 328, 47.
149. Penner, R.M., Heben, M.J., Lewis, N.S., *Anal. Chem.*, **1989**, 61, 1630.
150. Baranski, A.S., *J. Electroanal. Chem.*, **1991**, 307, 287.

Chapter 2

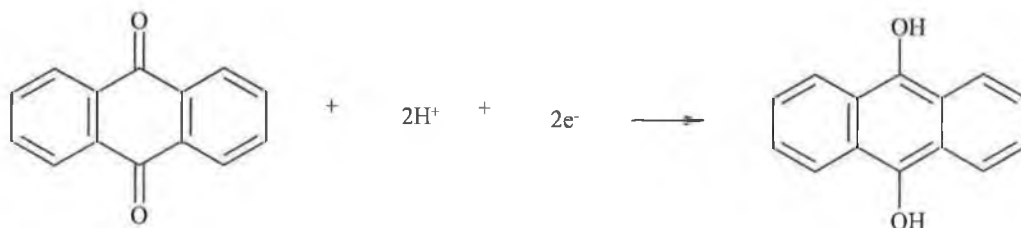
Characterisation of Anthraquinones

“Spoon feeding in the long run teaches you nothing but the shape of the spoon.”

- *E.M. Forster*

2. Introduction

Chapter 1 of this report gives a general overview of a number of adsorbed monolayer systems including alkanethiols, osmium and ruthenium complexes and anthraquinones, as well as an explanation of some of the techniques used to characterise these films. However, the experimental work that follows in Chapters 3 to 5 of this work deals only with anthraquinone species, hence some background information to the origin and use of these molecules will be discussed here. Anthraquinones belong to a group of compounds known as quinones, other variations are benzoquinones, naphthoquinones and polycyclic quinones.¹ Natural anthraquinones are distinguished by a large structural variety, wide range of biological activity and low toxicity.² Anthraquinone derivatives have been found in wild and cultured higher plants,³ mosses, lichens, fungi,⁴ as well as in sea animals and algae.² Anthraquinone, also called 9,10-anthraquinone is prepared commercially by oxidation of anthracene or condensation of benzene and phthalic anhydride, followed by dehydration of the condensation product. The three fused rings of anthraquinone make it a potential building block in supramolecular chemistry that has a planar span between the 2- and 6- positions of approximately 10 Å.⁵ It has two carbonyl groups directly opposite each other and it is reducible by 1- or 2-electron transfer to the radical anion or to the dianion respectively.



Scheme 1. Anthraquinone (oxidised form), left and hydroquinone (reduced form), right.

Anthraquinones have been used extensively in recent years in medicine, and are one of the most important classes of potential anti-cancer agents. Zogotto et al.⁶ carried out an extensive study using an aminofunctionalised 9,10-anthraquinone, which is now licensed for clinical use in a number of countries against breast cancer and acute leukemias. Similar studies carried out by Ali et al.⁷ and Perchellet et al.⁸ have focused on the anti-tumor activities of anthraquinone derivatives, which are capable of

preventing leukemic cells from growing. The extent of research published in recent years points to the importance of these complexes in anti-cancer laboratories throughout the world.^{9,10,11,12,13,14,15,16} Earlier work carried out by Clark et al.¹⁷ and Sydiskis et al.¹⁸ shows that 1,8-dihydroxy-3-methylantraquinone, which is extracted from the medicinal plant *Dianella longifolia* can be used for the treatment of the influenza virus. Traditionally, the fleshy roots of this plant have been used by Aboriginal people in southern Australia for the treatment of colds. Semple et al.¹⁹ also published a report on the anthraquinone abstract of *D. longifolia*, which is now used as an antipoliiovirus component. Zembower et al.²⁰ have studied a large series of variously substituted anthraquinones to investigate the inhibitory capacity against human leukocyte elastase (HLE) and cathepsin G (Cat G), two proteinases implicated in diseases characterised by the abnormal degradation of connective tissue such as pulmonary emphysema and rheumatoid arthritis.

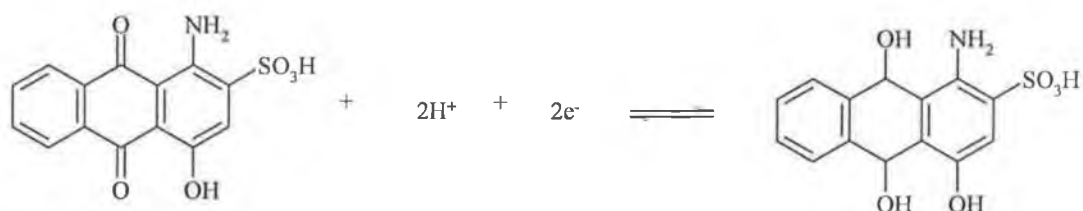
Besides medical applications, anthraquinones have found applications as diverse as dyes, pigments and as a chemical means for plant protection. The recognition of carbons tetravalency and the structure for benzene proposed by the German chemist Friedrich August Kekule, led to the structural elucidation of aromatic compounds and the development of the dyestuffs industry. The first example was the elucidation of the structure of alizarin by Graebe and Liebermann in 1868.^{1,4} Alizarin is derived from the madder plant and is red in colour. The anthraquinoid colourants form the basis of many of the synthetic dyes and after the azo class form the second most important group of organic colourants listed in the *Colour Index* today. Sulphonated anthraquinones provide a group of bright, fast dyes for wool, while unsulphonated analogues are disperse dyes for synthetic fibres.^{1,21} BASF Aktiengesellschaft, the leading manufacturer of vat dyes was founded in 1865. Its headquarters are in Ludwigshafen am Rhein, Germany, and this is where the anthraquinones used for the experimental work were obtained.

Finally, anthraquinone has been recognised for its effectiveness as a pesticide. It serves as a non-toxic seed treatment, which can be used to repel birds from crops.^{22,23,24,25,26,27} Anthraquinone was patented as a bird repellent on rice seed in the 1940s and was evaluated as a possible blackbird feeding deterrent on rice seed in the 1950s.²⁸ The

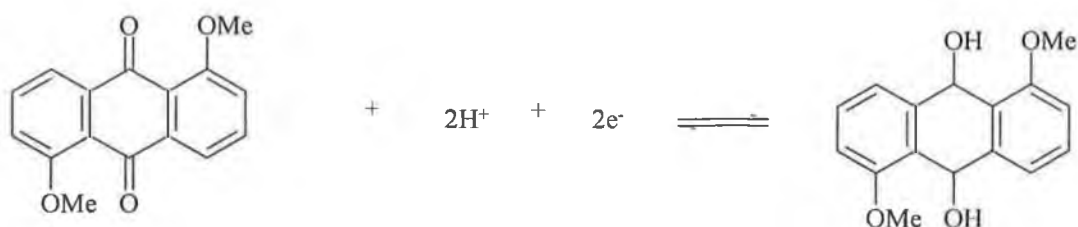
extent of recent investigations in this area confirms the utility of anthraquinones in this type of research also, however a review of these papers will not be considered here.

2.1 Characterisation of Anthraquinones

The parent anthraquinone, 9,10-anthraquinone was obtained from BDH Chemicals Ltd. Poole England and the anthraquinone derivatives implemented in this work; 1-amino, 2-sulphonic, 4-hydroxyanthraquinone (1,2,4-AQASH) and 1,5-dimethoxyanthraquinone (1,5-DMAQ) were obtained from BASF (Ludwigshafen, Germany). The purity of these compounds was analysed by a number of techniques, namely High Performance Liquid Chromotography (HPLC), UV-Visible Spectroscopy (UV-Vis), Nuclear Magnetic Resonance Spectroscopy (NMR), Raman Spectroscopy (Raman) and Infrared Spectroscopy (IR). Solution phase spectra of the three anthraquinones were run to confirm the purity of the complexes. The expected redox reactions of the two anthraquinone derivatives in low pH solution are displayed in Schemes 2 and 3 below.



Scheme 2. Redox reaction of 1-amino, 2-sulphonic, 4-hydroxyanthraquinone in low pH solution.

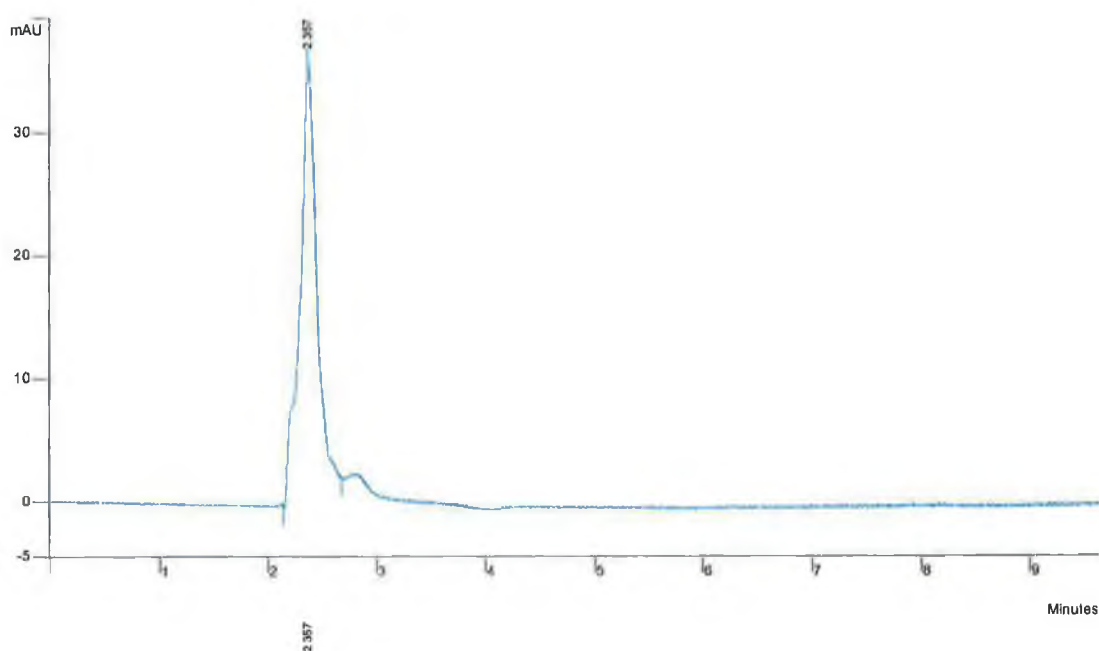


Scheme 3. Redox reaction of 1,5-dimethoxyanthraquinone in low pH solution.

2.1.1 HPLC

HPLC was carried out using a Varian Prostar Model 230 HPLC pump equipped with a 20 μ l injection loop. The column stationary phase was a partisil P10 SCX 3092 radical PAK cation exchange cartridge. A Varian Prostar photodiode array detector, interfaced with a personal computer with Varian Star Hichrom Cation Exchange software, Version 5.3 was used for detection and readout. A mobile phase of 80:20 (v/v) acetonitrile:water made up in 0.08 M LiClO₄ was used, which yielded optimum separation of the anthraquinone derivatives investigated. The HPLC chromatograms for 1,2,4-AQASH and 1,5-DMAQ are presented in Figure 1. The two anthraquinones are neutral species under the analysis conditions and exhibit single peaks at 2.36 and 2.28 minutes for 1,2,4-AQASH and 1,5-DMAQ, respectively. These elution times compare well with previous characterisation studies of analogous anthraquinones.^{29,30} The HPLC chromatograms run over a 10 minute period showed no other significant peaks, hence confirming the purity of these complexes.

(A)



(B)

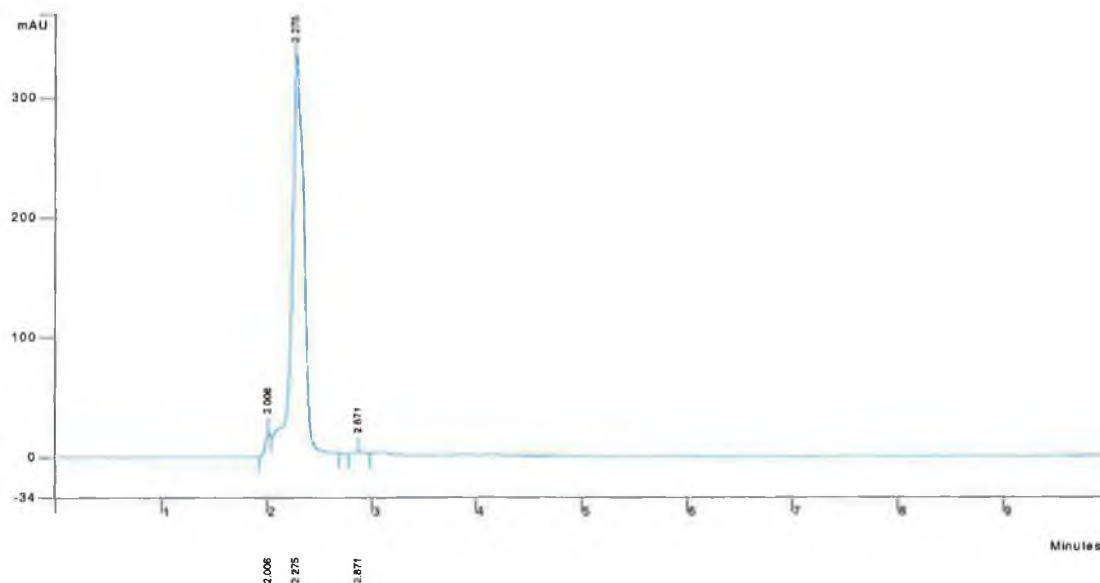


Figure 1. HPLC chromatograms of (A) 1,2,4-AQASH and (B) 1,5-DMAQ. The flow rate is 1.8 ml/min and the mobile phase is 80:20 Acetonitrile:Water, 0.08M LiClO₄.

2.1.2 UV-Visible Spectroscopy

UV-Vis spectra were obtained using a Shimadzu UV-3100 diode array spectrometer interfaced with a personal computer. Quartz cells of 1 cm path length were used, as these do not absorb in the UV region (200-380nm).³¹ The solvent used to run the UV-Vis spectra of the anthraquinones was spectroscopic grade acetonitrile. This solvent was chosen as it is transparent throughout the region investigated and dissolves a sufficient quantity of the sample to give well-defined peaks. The spectra were obtained at minimum slit width, 2 nm, to ensure maximum detail in the spectra.³² The main strong bands observed in Figure 2 are in the UV region below 300 nm, which correspond to π - π^* transitions in the molecules.

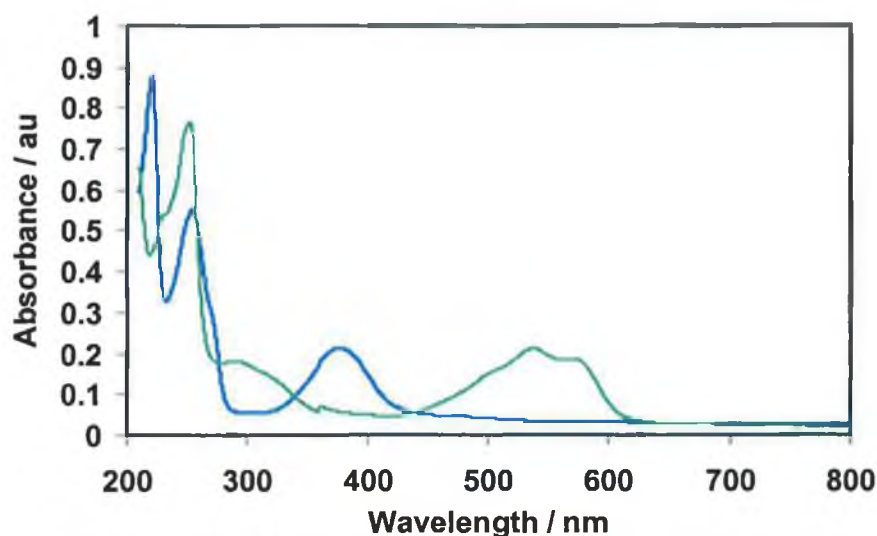


Figure 2. UV-Visible spectra of 1,2,4-AQASH (—) and 1,5-DMAQ (—) in spectroscopic grade acetonitrile.

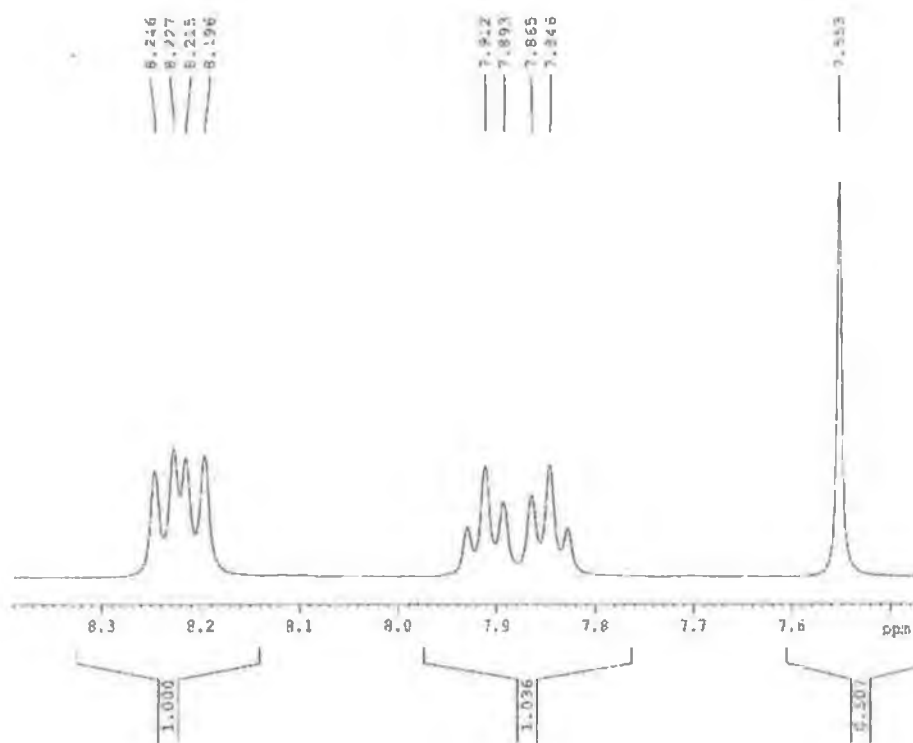
2.1.3 NMR Spectroscopy

Figure 3 represents the ^1H NMR spectrum for (A) 1,2,4-AQASH and (B) 1,5-DMAQ at room temperature. The spectra were run using a Bruker 400 MHz NMR spectrometer.

Integration of spectrum (A) gives a total of 5 protons, two triplets, two doublets and one singlet. The singlet at 7.55 ppm represents the proton in position 3. The protons in positions 5 and 8 are seen as doublets and appear further downfield due to the effect of the carbonyl atoms, which reside beside them in positions 9 and 10. The triplets at 7.85 and 7.89 ppm are due to the protons in positions 6 and 7.

Integration of spectrum (B) gives a total of 6 protons, one triplet, two doublets and one singlet. The singlet at 3.93 ppm corresponds to the proton in position 5. The doublets further downfield are due to the protons in positions 6 and 8. The triplet at 7.70 ppm represents the proton in position 7.

(A)



(B)

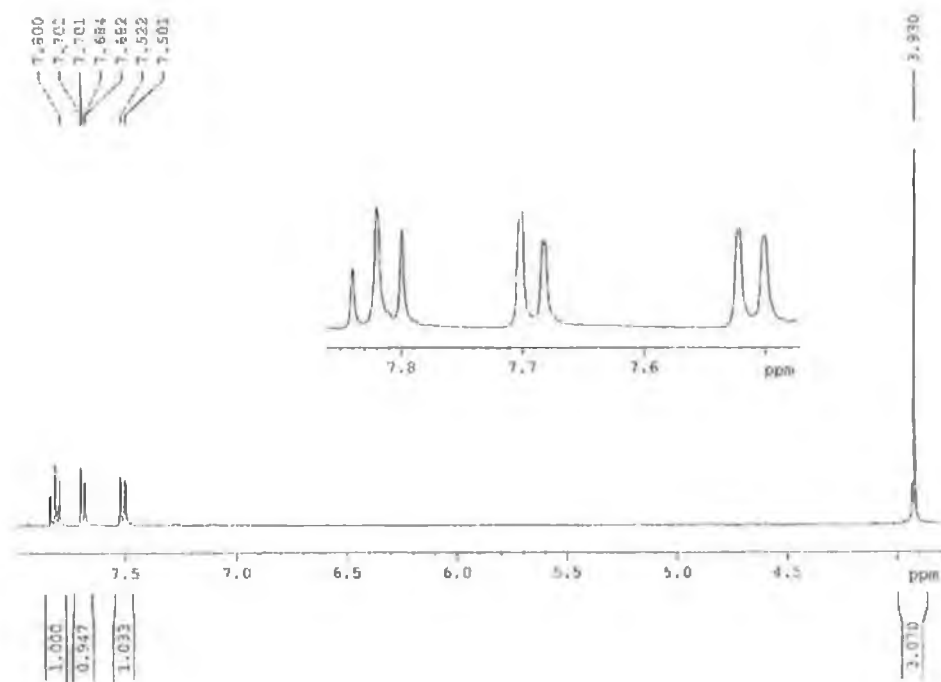


Figure 3. ^1H NMR of (A) 1,2,4-AQASH and (B) 1,5-DMAQ in d-DMSO

2.1.4 Raman Spectroscopy

Raman spectroscopy was conducted on a Dilor.Jobinyvon.Spex Labram. To obtain the solution Raman spectrum of 9,10-anthraquinone a 100 μM solution was made up in 1 M HClO_4 . In these experiments a 140 mW Argon ion laser (514.5nm), attenuated to 70 mW was used for excitation. The beam was focused through a purpose made electrochemical cell on the anthraquinone solution using a 10x objective lens. A spectral resolution of 1.5 cm^{-1} per pixel was achieved using a grating of 1800 lines/mm. Focusing was confirmed by using a CCD camera in imaging mode.

A Raman spectrum of the solution was run without applying a potential, i.e., the anthraquinone is in the oxidized form, Q. Bulk electrolysis of the solution was then carried out to convert the solution to the hydroquinone form, H_2Q and a spectrum was recorded. Both spectra are overlaid in Figure 4 for comparison. The spectra have been interpreted with reference to previous studies dealing with Raman spectra of anthraquinone derivatives^{33,34,35,36,37,38,39} and peaks have been assigned as shown in Table 2 below. Comparison of the solution spectra with those of the anthraquinone adsorbed on a mercury electrode surface will be presented in Chapter 3.

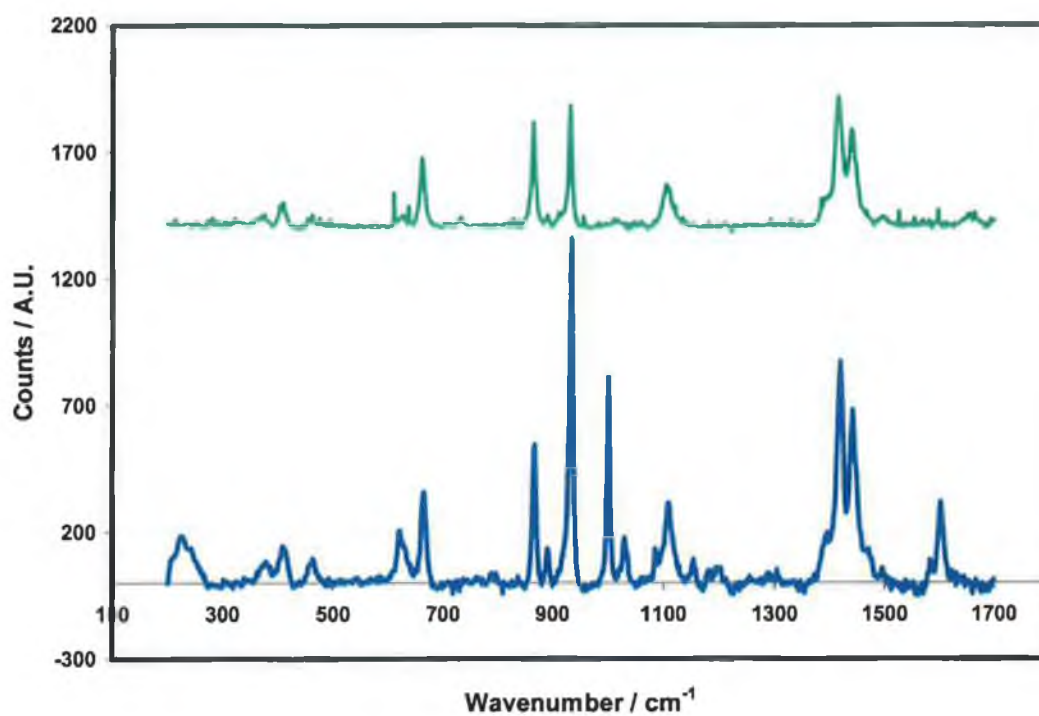


Figure 4. Raman spectra for a 100 μM solution of 9,10-AQ made up in 1.0 M HClO₄. (—) represents data for the oxidized, Q, form and (—) represents data for the reduced, H₂Q, form. In both cases an Ar⁺ laser (514.5 nm) was used for excitation.

Table 2. Assignment of Raman spectra peaks illustrated in Figure 4 above.

<i>Frequency</i>	<i>Assignment / Q</i>	<i>Frequency</i>	<i>Assignment / H₂Q</i>
220.7		362.5	
405.5		403.2	
622.9	Ring Deformation	637.1	
662.5	Ring Deformation	661.8	
865.5	CH Bend	863.2	CH Bend
889.5			
932.6	Peak due to solvent	931.9	Peak due to solvent
1002.3	Ring Breathing		
1027.5	Ring Breathing		
1107.4	CH Bend	1103.4	CH Bend
1150.8	CH Bend		
1183.3	CH Bend		
1418.8	Ring Stretching	1413.3	Ring Stretching
1439.7	Ring Stretching	1437.2	Ring Stretching
1600.6	Ring Stretching		
1646.1	C=O Stretch		

2.1.5 IR Spectroscopy

In IR spectroscopy the anthraquinone samples are exposed to IR light and the bonds within the molecules vibrate at characteristic frequencies. The infrared spectrum is formed as a consequence of the absorption of electromagnetic radiation at frequencies that correlate to the vibration of specific sets of chemical bonds from within a molecule. The IR spectra for 9,10-AQ, 1,2,4-AQASH and 1,5-DMAQ are illustrated in Figure 5. A 1:100 mixture of each anthraquinone:KBr was prepared and this mixture was pressed into the thin disk under high pressure. The disk was then placed in the Perkin Elmer 2000 FT-IR and spectra were recorded. The peaks observed in the IR spectra have been assigned and are summarised in Table 3 below.

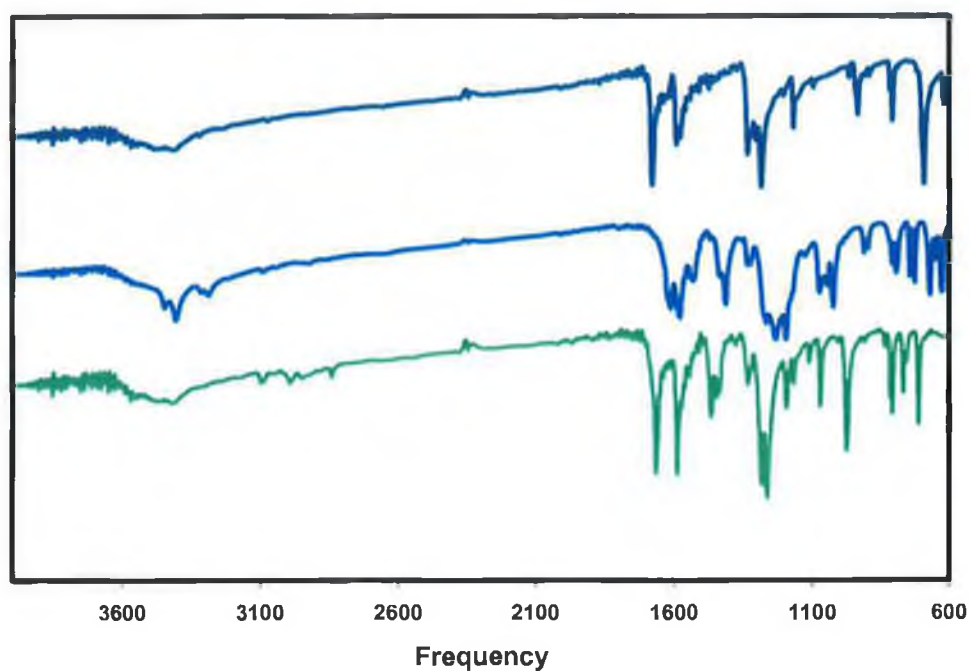


Figure 5. IR spectra of (–) 9,10-AQ, (–) 1,2,4-AQASH and (–) 1,5-DMAQ.

Table 3. Assignment of IR spectra peaks illustrated in Figure 5 above.

<i>Frequency</i>	<i>Assignment</i> <i>9,10-AQ</i>	<i>Frequency</i>	<i>Assignment</i> <i>1,2,4-AQASH</i>	<i>Frequency</i>	<i>Assignment</i> <i>1,5-DMAQ</i>
		3430	N-H stretch		
3400	O-H stretch	3401	O-H stretch	3399	O-H stretch
1676	C=O Stretch	1608	C=O Stretch	1662	C=O Stretch
1578	C=C aromatic stretch	1576	C=C aromatic stretch	1587	C=C aromatic stretch
1331	C-C skeletal vibrations	1523	C-C skeletal vibrations	1463, 1482	C-C skeletal vibrations
1282	C-C skeletal vibrations	1410	C-C skeletal vibrations	1329, 1267, 1260	C-C skeletal vibrations
1169	C-C skeletal vibrations	1226	C-N stretch	1069	C-C skeletal vibrations
935	C-C skeletal vibrations	1193, 1066, 1023, 897	C-C skeletal vibrations	974	C-C skeletal vibrations
808	C=C-H bend	790	C=C-H bend	807, 768	C=C-H bend
692	Ring in & out of plane bending	725, 669	Ring in & out of plane bending	712	Ring in & out of plane bending

2.1.6 Solution Phase Electrochemistry

Solution phase cyclic voltammograms of the three anthraquinones used in the experimental chapters are illustrated in Figures 6-8. Cyclic voltammetry was performed using a CH Instruments Model 600A Electrochemical Workstation and a conventional three electrode cell. Potentials were measured against a potassium chloride saturated silver/silver chloride (Ag/AgCl) reference electrode with a platinum wire used as the auxillary electrode. All anthraquinone solutions were deoxygenated by purging with nitrogen gas, and a blanket of nitrogen was maintained over the solution during measurements. The solution phase cyclic voltammograms of 9,10-AQ and 1,2,4-AQASH show the presence of a spike near the formal potentials of the electroactive species. This may be due to interactions between anthraquinone molecules. Similar voltammetric behaviour consisting of sharp spikes is seen when the anthraquinone species are adsorbed on a mercury surface and this has been attributed to hydrogen bonding interactions.⁴⁰ A detailed investigation of the electrochemical properties of 9,10-AQ and 1,2,4-AQASH monolayers is presented in Chapter 4 of this work.

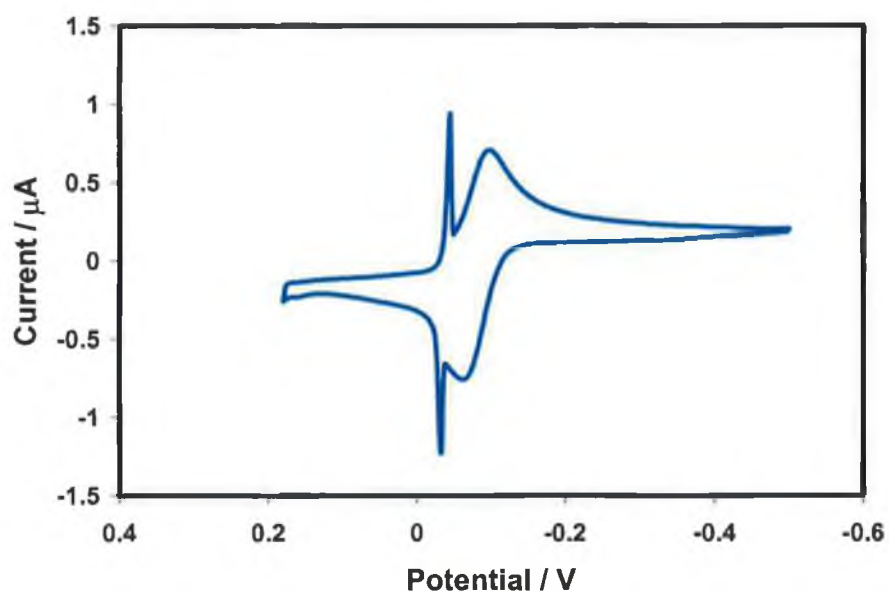


Figure 6. Solution phase cyclic voltammogram of a 3 mM solution of 9,10-AQ dissolved in 1M HClO₄. The scan rate is 0.05 Vs⁻¹ and the scan was initiated at the negative potential limit, cathodic currents are up and anodic currents are down.

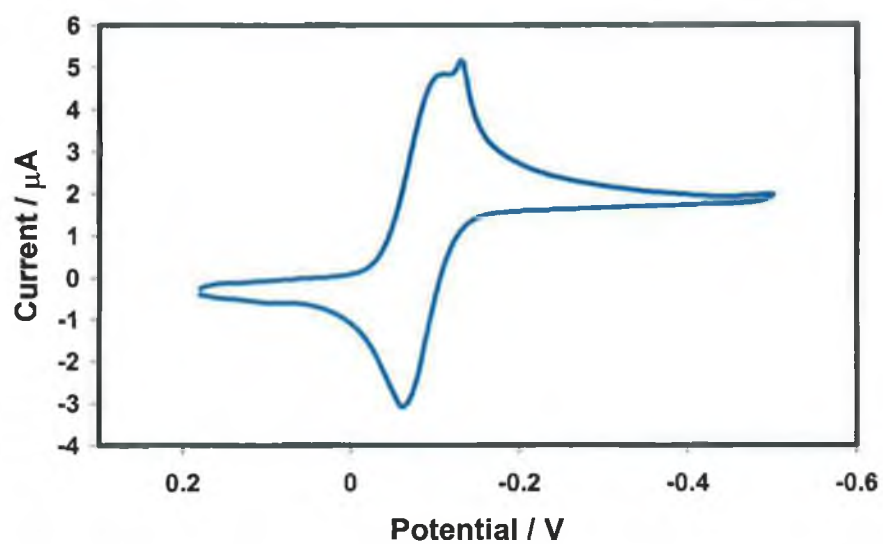


Figure 7. Solution phase cyclic voltammogram of a 5 mM solution of 1,2,4-AQASH dissolved in 1M HClO₄. The scan rate is 0.05 Vs⁻¹ and the scan was initiated at the negative potential limit, cathodic currents are up and anodic currents are down.

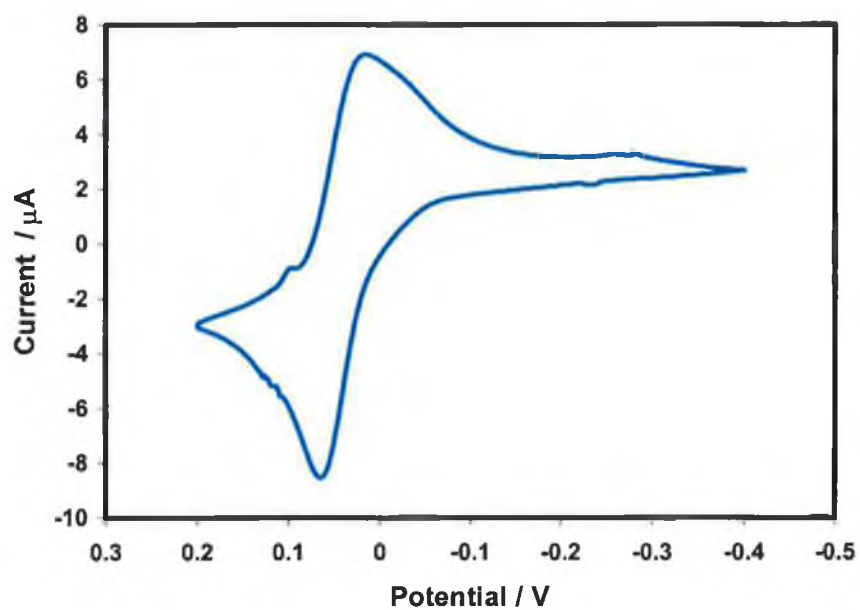


Figure 8. Solution phase cyclic voltammogram of a 5 mM solution of 1,5-DMAQ dissolved in 1M HClO₄. The scan rate is 0.1 Vs⁻¹ and the scan was initiated at the negative potential limit, cathodic currents are up and cathodic currents are down.

2.2 Conclusions

This chapter introduced the anthraquinones used throughout the experimental work of this thesis, as well as giving a general overview of the application of anthraquinone derivatives in different areas of research. The purity of the anthraquinone molecules, 9,10-AQ, 1,2,4-AQASH and 1,5-DMAQ was confirmed by using HPLC, UV-Vis, ¹H NMR, Raman and IR spectroscopy. The solution phase redox properties of the molecules were determined using electrochemistry.

2.3 References

1. Encyclopaedia Britannica, **2001**.
2. Natural Anthraquinones and physiochemical properties, Muzychkina, R.A., **1998**, Phasis.
3. Dagne, E., Bisrat, D., Viljoen, A., Van Wyk, B.-E., *Current Organic Chemistry*, **2000**, 10, 1055.
4. Hobson, D.K., Wales, D.S., *JSDC*, **1998**, 114, 42.
5. Chambers, J.Q., *Chemistry of Quinonoid Compounds, Vol.2*, **1988**, 719.
6. Zogotto, G., Supino, R., Favini, E., Moro, S., Palumbo, M., *Il Farmaco*, **2000**, 55, 1.
7. Ali, A.M., Ismail, N.H., Mackeen, M.M., Yazan, L.S., Mohamed, S.M., Ho, A.S.H., Lajis, N.H., *Pharmaceutical Biology*, **2000**, 4, 298.
8. Perchellet, E.M., Magill, M.J., Huang, X., Dalke, D.M., Hua, D.A., Perchellet, J.-P., *Anti-Cancer Drugs*, **2000**, 5, 339.
9. Gutierrez, P.L., *Free Radical Biology and Medicine*, **2000**, 314, 263.
10. Han, H., Hurley, L.H., *Trends in Pharmaceutical Sciences*, **2000**, 4, 136.
11. Kellard, L.R., *Anti-Cancer Drugs*, **2000**, 7, 503.
12. Tam, M.-N., Jin, G.-Z., Song, G.-Y., Ahn, B.-Z., *Archiv der Pharmazie*, **2000**, 6, 189.
13. Lee, A.E., Wilson, W.R., *Toxicology and Applied Pharmacology*, **2000**, 1, 50.
14. Swaine, D.J., Loadman, P.M., Bidy, M.C, Graham, M.A., Patterson, L.H., *J. of Chromatography B : Biomedical Sciences and Applications*, **2000**, 2, 239.
15. Perry, P.J., Read, M.A., Davies, R.T., Gowan, S.M., Reszka, A.P., Wood, A.A., Kelland, L.R., Neidle, S., *J. of Medical Chem.*, **1999**, 14, 2679.
16. Lin, D.-Y., Lin, S.-M., Liaw, Y.-F., *J. of Gastroenterology and Hepatology*, **1997**, 9-10, 5319.
17. Clarke, P.A., *J. Anth. Soc. S. Aust.*, **1987**, 25, 3.
18. Sysdiskis, R.J., Owen, D.G., Lohr, J.L., Rosler, K.H.A., Blomster, R.N., *Antimicrob. Agents. Chemother.*, **1991**, 35, 2463.
19. Semple, S.J., Pyke, S.M., Reynolds, G.D., Flower, R.L.P., *Antiviral Research*, **2001**, 49, 169.
20. Zembower, D.E., Kam, C.M., Powers, J.C., Zalkow, L.H., *J. of Medical Chem.*, **1992**, 9, 1597.

21. Sekar, N., *Colourage*, **2000**, 7, 48.
22. Blackwell, B.F., Helon, D.A., Dolbeer, R.A., *Crop Protection*, **2001**, 20, 65.
23. York, D.L., Cummings, J.L., Engeman, R.M., Davis, J.E., *Crop Protection*, **2000**, 19, 201.
24. Avery, M.L., Tillman, E.A., Humphrey, J.S., Cummings, J.L., York, D.L., Davis, J.E., *Crop Protection*, **2000**, 19, 225.
25. Hasan, H.A.H., *Microbiological Research*, **1999**, 1, 95.
26. Galadi, A., Julliard, M., *Chemosphere*, **1996**, 1, 1.
27. Ester, A., Nijënstein, J.H., *Crop Protection*, **1995**, 5, 409.
28. Neff, J.A., Meanley, B., *US Department of Interior Wildlife Research Lab., Denver, Colorado*, **1957**, unpublished report.
29. O'Hanlon, D.P., Ph.D. Thesis, *Spontaneously Adsorbed Monolayers : Anthraquinones and Osmium Polypyridyl Complexes as Molecular Building Blocks*, **1999**.
30. O'Kelly, J.P., Ph.D. Thesis, *Dynamics and Energetics of Electron Transfer across microelectrode/monolayer interfaces*, **1998**.
31. Harwood, L.M., Claridge, T.D.W., *Introduction to Organic Spectroscopy*, **1997**, Oxford Science Publications.
32. Skoog, D.A., West, D.M., Holler, F.J., *Fundamentals of Anal. Chem.*, **1996**, Saunders College Publishing, 7th Edition.
33. Ramaakrishnan, V., Krishnamurthy, Gurunathan, M., Srivatsavoy, V.J.P., *Spectrochimica Acta*, **1990**, 46A, 1615.
34. Srikanth, V.G., Jayaraj, S.E., Ramakrishnan, V., *J. Phys.*, **1993**, 41, 467.
35. Jayaraj, S.E., Ramakrishnan, V., *Spectrochimica Acta*, **1995**, 51A, 979.
36. Benjamin, A.D., Jayaraj, S.E., Ramakrishnan, V., *Bulletin of Electrochemistry*, **2000**, 16, 512.
37. Marasinghe, P.A.B., Gillispie, G.D., *Chem. Phys.*, **1989**, 136, 249.
38. Margetic, D., Eckert-Maksic, M. Maksic, Z.B., *J. of Molecular Structure (Theochem)*, **1992**, 277, 161.
39. Marzocchi, M.P., Mantini, A.R., Casu, M., Smulevich, G., *J. Chem. Phys.*, **1998**, 108, 534.
40. Forster, R.J., Keyes, T.E., Farrell, M., O'Hanlon, D., *Langmuir*, **2000**, 16, 9871.

Chapter 3

Impact of Hydrogen Bonding on the Redox Properties of Anthraquinone Monolayers

“I hear and I forget. I see and I remember. I do and I understand.”

- *Confucius*

3. Introduction

The review of electrode materials modified with various monolayers in Chapter 1 highlights the importance of this work in electrochemical research over the last 15 to 20 years. Much of the work has focused on alkanethiols^{1,2,3,4} as well as osmium and ruthenium polypyridyl complexes^{5,6,7,8,9}, however the electrochemical properties of anthraquinone derivatives^{10,11,12,13,14,15} have also been studied. Quinonoid monolayers are important model systems because of their unusually ideal electrochemical responses in low pH solution. In this chapter, the electrochemical properties of 1-amino, 2-sulphonic, 4-hydroxyanthraquinone, 1,2,4-AQASH, are studied in detail. This anthraquinone derivative adsorbs spontaneously onto the surface of a mercury electrode. This system reveals an interesting electrochemical response, in that when the surface coverage approaches saturation a spike appears in the anodic branch of the cyclic voltammogram. This occurs when the bulk concentration of 1,2,4-AQASH in solution is 1.5 μM or greater.

The electrochemical response of 9,10-anthraquinone, 9,10-AQ, is investigated in this chapter also to compare its electrochemistry with that of 1,2,4-AQASH. Spiked CVs are also recorded for 9,10-AQ when scanning in both the positive and negative potential directions, i.e., starting the voltammetric scan when the adsorbate is in the reduced, H_2Q and oxidized, Q, forms. Similar cyclic voltammetry behaviour has been reported by McDermott and coworkers,¹⁶ Anson and coworkers,¹⁷ and Faulkner and coworkers,¹⁸ when studying the electrochemistry of 2,6-anthraquinonedisulphonate, 2,6-AQDS. This molecule adsorbs on the electrode surface in a parallel orientation, as determined from calculations carried out by Soriaga and coworkers,¹⁹ which are detailed in Chapter 1 of this thesis. The spiked voltammetric response from 2,6-AQDS has been attributed to hydrogen bonding interactions between adsorbed AQ molecules, when the intersite separation between adsorbates decreases sufficiently to allow for such interactions. However, a detailed explanation of how the spike is formed in the course of the voltammetric scan has not been provided in these publications. This issue will be discussed in section 3.2.7 of this chapter.

The results presented in this chapter probe the concentration dependent cyclic voltammetric response of 1,2,4-AQASH and 9,10-AQ. The experimental data is fit to

the Langmuir and Frumkin adsorption isotherms to probe the presence and extent of interaction between adsorbates. Raman spectroscopy measurements are presented to determine the orientation of 9,10-AQ and 1,2,4-AQASH on mercury.

3.1 Experimental

Cyclic voltammetry was performed using a CH instruments Model 660 electrochemical workstation, a PAR EG&G Model 270 hanging mercury dropping electrode and a conventional three-electrode cell. Potentials were measured against a potassium chloride saturated silver/silver chloride (Ag/AgCl) reference electrode. A large area platinum wire was used as the auxiliary electrode. For temperature dependent experiments a Julabo F10-HC refrigerated circulating bath, thermostated within $\pm 0.2^\circ\text{C}$ was used. All solutions containing 1,2,4-AQASH were thoroughly deoxygenated by purging with nitrogen which was maintained over the solution during all measurements. The area of the mercury electrode was determined using the density of pure mercury (13.546 g cm^{-3}) by dispensing, collecting, and weighing 100 drops of mercury.²⁰ An electrochemical area of $0.0140 \pm 0.0007\text{ cm}^2$ was obtained. This area was also confirmed by recording cyclic voltammograms under steady state and linear diffusion conditions using $[\text{Ru}(\text{NH}_3)_6]^{2+}$ as a solution phase probe.

Raman spectroscopy was conducted on a Dilor.Jobinyvon.Spex Labram by Dr. Keyes in Dublin Institute of Technology. The exciting 140 mW argon ion laser (514.5 nm), attenuated to 70 mW was focused through a purpose made electrochemical cell onto either the solution or the mercury electrode surface using a 10x objective lens. The beam diameter when focused is approximately $3\text{ }\mu\text{m}$ producing approximately 10^8 W cm^{-2} at the sample. Focusing was confirmed by using a CCD camera in imaging mode. A spectral resolution of 1.5 cm^{-1} per pixel was achieved using a grating of 1800 lines/mm.

3.1.1 Materials and Procedures

The parent anthraquinone, 9,10-anthraquinone was obtained from BDH Chemicals Ltd. Poole England. The anthraquinone derivative, 1-amino-2-sulphonic-4-hydroxy-anthraquinone (1,2,4-AQASH) was obtained from BASF. Both anthraquinones were characterized as outlined in Chapter 2 to confirm their purity. Deposition solutions

were prepared using and Milli-Q purified water and unless otherwise stated, the supporting electrolyte was 1.0 M HClO₄. Spontaneously adsorbed monolayers were formed by allowing the anthraquinone at μM concentrations to adsorb onto the mercury electrode surface from electrolytic solutions. At high concentration, dense monolayers were typically formed within a few tens of milliseconds. At concentrations where sub-monolayer coverage was attained, repetitive cyclic voltammetry was performed until the peak current became independent of time. Transferring the modified surfaces into blank electrolyte caused the monolayer to rapidly desorb, i.e., adsorption is reversible in these systems. Therefore, all experiments were performed with micromolar concentrations of the anthraquinones in solution.

3.2 Results and Discussion

3.2.1 General Electrochemical Properties

Figure 1 shows the cyclic voltammetric response for a mercury electrode immersed in a 0.5 μM solution of 9,10-AQ and 1,2,4-AQASH. The supporting electrolyte is 1.0 M HClO₄. Both CVs were recorded within the potential limits +0.2 and -0.65 V, with both scans initiated at the positive potential limit. When a molecule is adsorbed on an electrode surface and there are no lateral interactions between adsorbates, the cathodic and anodic peak potentials should be the same. From Figure 1 a ΔE_p of 17 ± 2 mV and a full width at half maximum (FWHM) of 53.3 ± 3 mV and 63 ± 8 mV are observed for the cathodic and anodic branches of 1,2,4-AQASH, respectively. The peak-to-peak splitting in the cyclic voltammogram of 9,10-AQ is 9 ± 0.7 mV and the FWHM is 55.4 ± 2 mV for both cathodic and anodic branches. If the redox reaction involves the transfer of two electrons a FWHM of 45.3 mV is expected.^{21,22,23}

The values calculated for the peak separation and FWHM, while somewhat larger than the theoretical values, are within experimental error to those expected and suggest that the redox reaction involves the transfer of two electrons and two protons in low pH solution.²¹ The redox reactions for 9,10-AQ and 1,2,4-AQASH are depicted in Scheme 1.

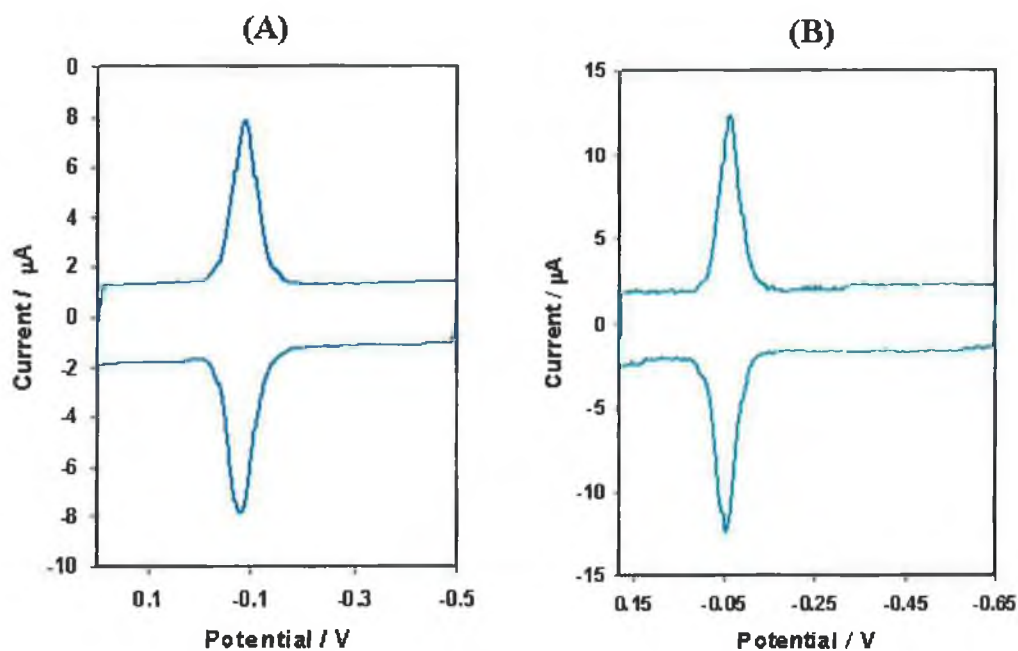
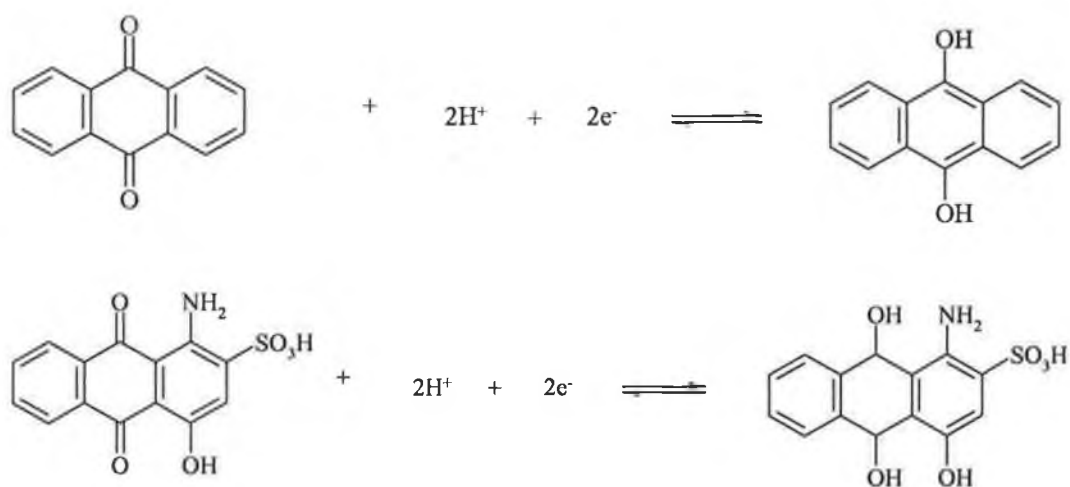


Figure 1. Cyclic voltammograms for a hanging mercury drop electrode (Area = 0.014 cm²) immersed in (A) a 0.5 μM solution of 9,10-AQ and, (B) a 0.5 μM solution of 1,2,4-AQASH. The supporting electrolyte is aqueous 1.0 M HClO₄ and the scan rate is 5 Vs⁻¹. The potential scan was started at the positive potential limit in both cases. Cathodic currents are up and anodic currents are down.

Scheme 1. Redox reaction of 9,10-AQ and 1,2,4-AQASH in low pH solution.



The surface coverage of the anthraquinones on the electrode surface can be calculated from the area under the voltammetric peaks after correction for the background charging current using Equation (1).²¹

$$\Gamma = \frac{Q}{nFA} \quad (1)$$

where Q is the total charge required to reduce or oxidise the electroactive species, n is the number of electrons transferred, F is Faraday's constant and A is the area of the electrode. The surface coverages of 9,10-AQ and 1,2,4-AQASH have been calculated as $3.04 \pm 0.06 \times 10^{-11}$ and $4.55 \pm 0.15 \times 10^{-11}$ mol cm⁻² respectively. Section 3.2.4 will investigate the effect of increasing the concentration of the anthraquinone in solution on the adsorbed CV response. Also, the effect of scanning in both positive and negative potential directions is investigated. The CV data is fit to a number of adsorption isotherms to determine the structure of the monolayers, and the extent of interaction between adsorbates in dense monolayers.

3.2.2 Scan Rate Dependence

The cyclic voltammograms presented in Figure 1 was recorded at a scan rate of 5 Vs⁻¹. Cyclic voltammograms were run at a number of different scan rates to probe the effect it would have on the electrochemical response. The voltammetric responses observed for both 9,10-AQ and 1,2,4-AQASH are consistent with that expected for a redox active species adsorbed on an electrode surface. The peak shapes are independent of scan rate, and the peak current scales linearly with scan rate, at least up to 50 Vs⁻¹. The non-ideal peak-to-peak separation, which increases as the scan rate is increased may be attributed to iR drop as these CVs were attained using a macroelectrode. The results shown in Figure 2 are for a monolayer of 1,2,4-AQASH, the same trend is observed in the scan rate dependent CVs of 9,10-AQ. This scan rate dependent behaviour contrasts with the diffusive tails and $v^{1/2}$ dependence of the peak current expected for a freely diffusing species.²⁴

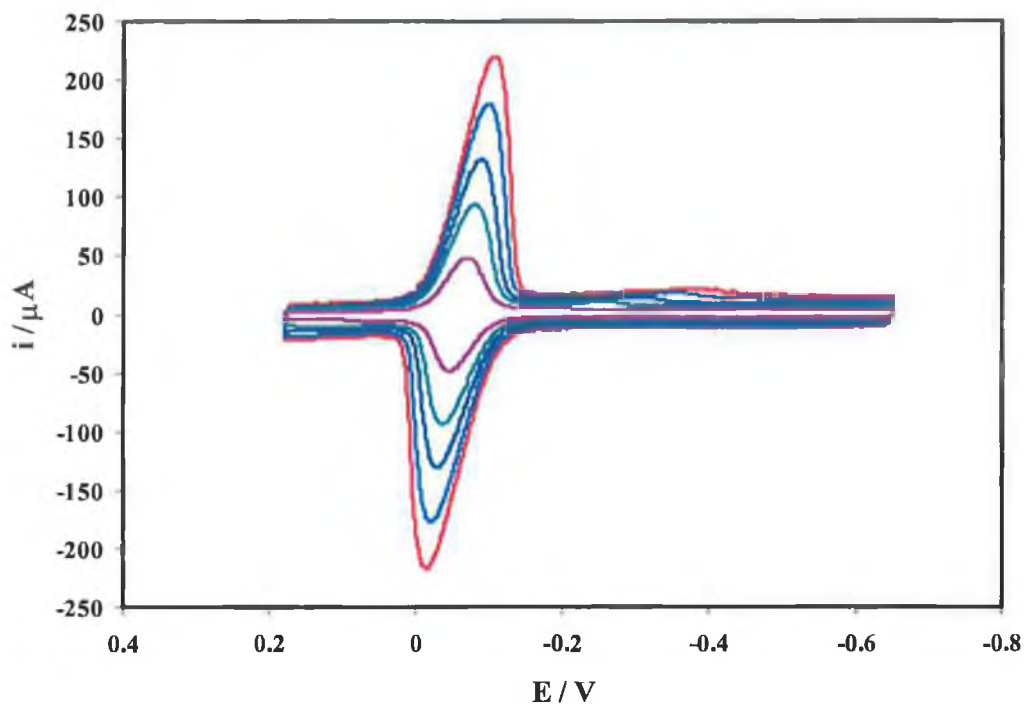


Figure 2. Cyclic voltammograms for a mercury electrode immersed in a 1 μM solution of 1,2,4-AQASH with 1.0 M HClO_4 as the supporting electrolyte. Scan rates are 50 (—), 40 (—), 30 (—), 20 (—) and 10 (—) Vs^{-1} . Cathodic currents are up and anodic currents are down. The initial potential is -0.65 V.

As the sweep rate is increased in cyclic voltammetry, the time scale of the experiment becomes smaller so that eventually redox equilibrium is not reached at the electrode surface and kinetic effects begin to appear.²⁵ When the time constants of the voltammetric experiments and electron transfer are comparable, it is expected that the rate of electron transfer across the metal/film interface will influence the voltammetric response. However, it can be seen from Figure 3 that the experimental i_p values increase linearly with increasing scan rate, thereby indicating that over this range, (5-50 Vs^{-1}), the experimental timescale is longer than that for electron transfer. In chapter 5, the sweep rates in cyclic voltammetry are increased to a few thousand volts per second. At these scan rates the rate of electron transfer becomes comparable to the timescale of the experiment. These cyclic voltammograms are fit to a number of electron transfer

models based on the Butler Volmer and Marcus theories of electron transfer to elucidate values for the heterogeneous electron transfer rate of 1,2,4-AQASH.

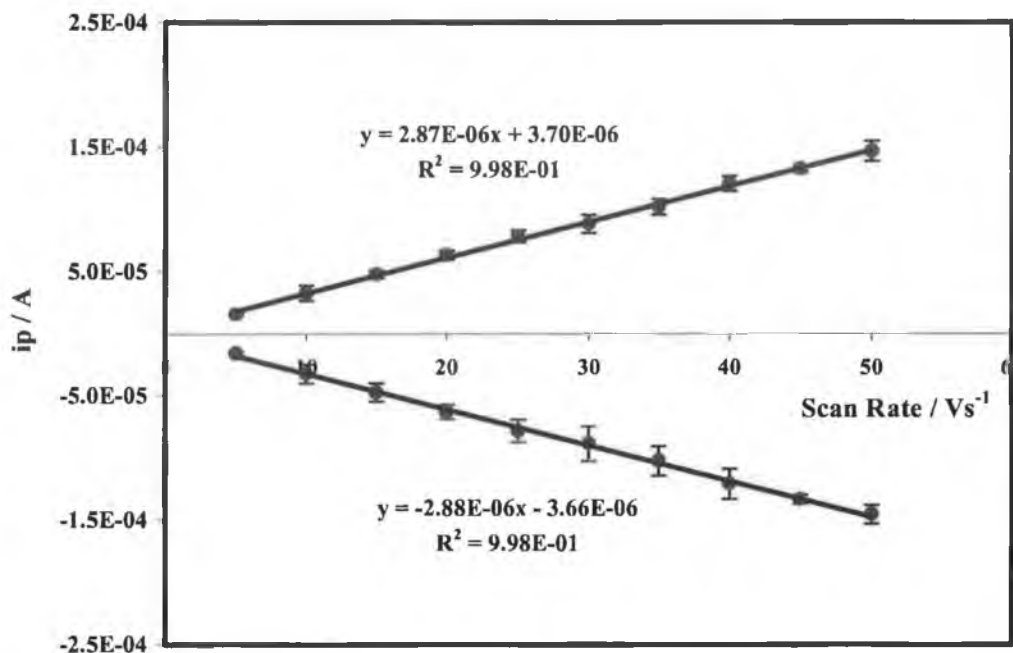


Figure 3. Scan rate dependence of the cyclic voltammetric peak current measured for 1,2,4-AQASH at scan rates of 5-50 Vs⁻¹. The concentration of 1,2,4-AQASH in solution is 1 μM with 1 M HClO₄ as the supporting electrolyte. Cathodic currents are up and anodic currents are down.

3.2.3 Raman Spectroscopy

Surface enhanced raman spectroscopy was used in this work to probe the orientation of 1,2,4-AQASH and 9,10-AQ on the mercury electrode surface. Figure 4 shows Raman spectra for 1,2,4-AQASH both as a monolayer on a mercury surface at an open circuit potential (+0.10±0.05 V), and a solution spectrum. The bulk concentration of 1,2,4-AQASH in solution is 100 μM, which is sufficiently high to form a dense monolayer. Given that the λ_{max} of 1,2,4-AQASH is 526 nm an Ar⁺ laser at 514.5 nm was used for excitation. It is evident that the spectrum for the monolayer is significantly different from that recorded for solution phase 1,2,4-AQASH. This difference is probably due to the fact that the adsorbed species

interacts with the surface altering the symmetry of the molecule, and hence the vibrational selection rules of the system. At the open circuit potential the monolayer is oxidised and a band at 1607 cm^{-1} corresponding to the C=O stretching is observed.²⁶ Upon adsorption, this band shifts to higher energy by approximately 30 cm^{-1} , indicating a stretching and strengthening of the C=O band.

Another feature of the spectrum of the solution species is the strong aromatic ring breathing mode at 1004 cm^{-1} , which decreases in intensity in the monolayer spectrum. The ratio of the intensity of the ring breathing mode relative to the C=O stretch is approximately 1.2 for the adsorbed spectrum, in comparison to approximately 7.7 for the solution phase spectrum. This ratio has been observed previously by Weaver and coworkers²⁷ when analysing the Surface Enhanced Raman Spectra of benzonitrile and toluene adsorbed on gold. In Weaver's study the sensitivity of certain vibrational modes, specifically C-H vibrations and out-of-plane and in-plane ring modes are analysed to determine adsorbate orientation. In the spectra of benzonitrile the intensity of the ring modes exhibit the same frequencies in the solution and adsorbed spectra. This would suggest that the aromatic ring does not interact strongly with the electrode surface and is consistent with benzonitrile adopting a tilted orientation. In contrast, the intensity of the ring modes is reduced in the adsorbed spectrum of toluene relative to the solution phase spectrum. Therefore, Weaver concluded that toluene adopts a flat orientation. For the adsorption of 1,2,4-AQASH, the observation that the ring breathing mode is suppressed relative to the C=O stretch suggests that the quinone is adsorbed coplanar to the electrode surface. This result however contrasts with Taniguchi's²⁸ work, which deals with the adsorption of 1-anthraquinonylbutylsulfide, 1-AQS, and 2-anthraquinonylbutylsulfide, 2-AQS, to silver and gold electrode surfaces. These adsorbates appear to be adsorbed perpendicular to the electrode surface, on the basis of a comparison of the relative intensities of the ring breathing modes to the C=O stretching mode. No study has been found in the literature which investigates the adsorption of an anthraquinone derivative molecule on mercury, therefore a direct comparison between the experimental results presented in this chapter and published work could not be made. However, it appears that the orientation of a molecule depends on a number of factors including the surface coverage of the

adsorbate on the electrode surface, the electrode material used and the surface roughness.

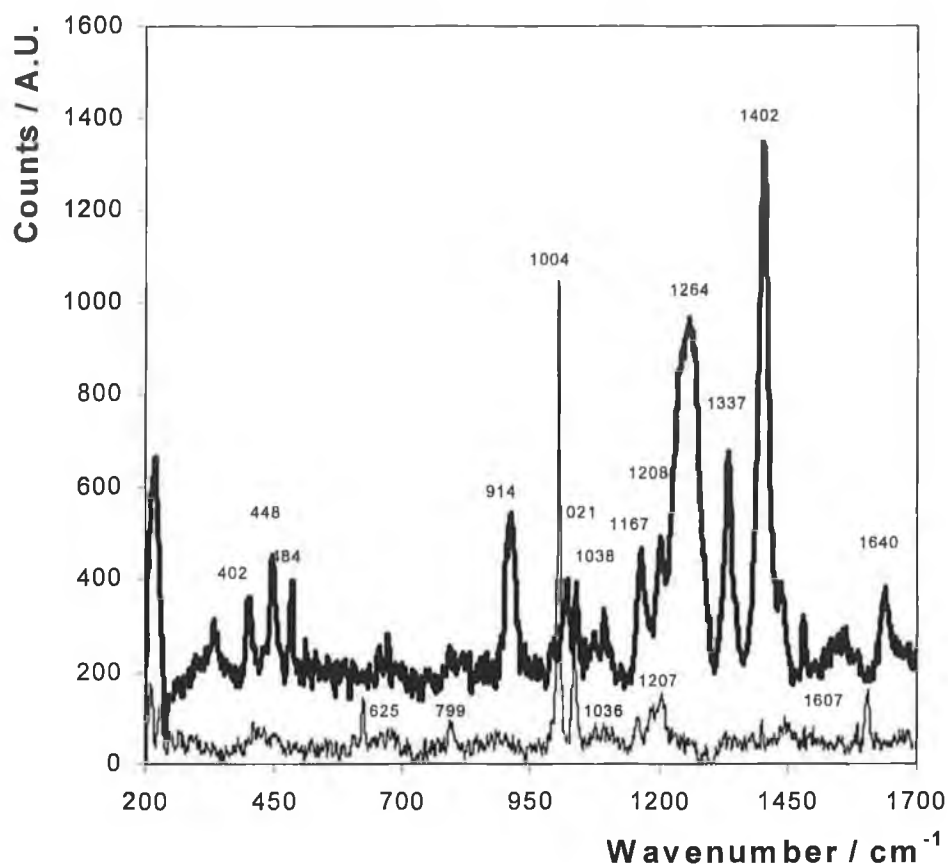


Figure 4. Resonance Raman spectrum for 1,2,4-AQASH where the bulk concentration is 100 μM (—), and for an adsorbed monolayer on a mercury electrode surface at an open circuit potential (---). In both cases an Ar^+ laser at a wavelength of 514.5 nm was used for excitation. Solutions were made up in Milli-Q purified water with 1M HClO_4 as the supporting electrolyte.

The solution and surface enhanced raman spectra of 9,10-AQ are illustrated in Figure 5. The principal difference in the solution and adsorbed Raman spectra is the presence of a band at 1000 cm^{-1} in the solution spectrum. This band, which is due to aromatic ring breathing is not visible in the adsorbed spectrum. The suppression of this peak in the adsorbed spectrum leads to the conclusion that 9,10-AQ adsorbates are adsorbed parallel to the electrode surface, as illustrated in Scheme 2.

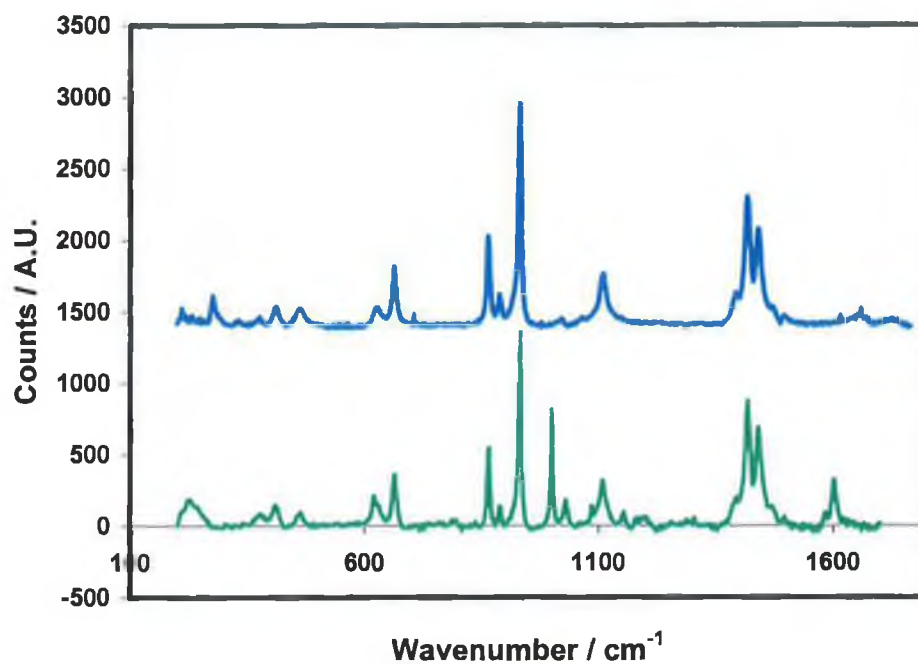
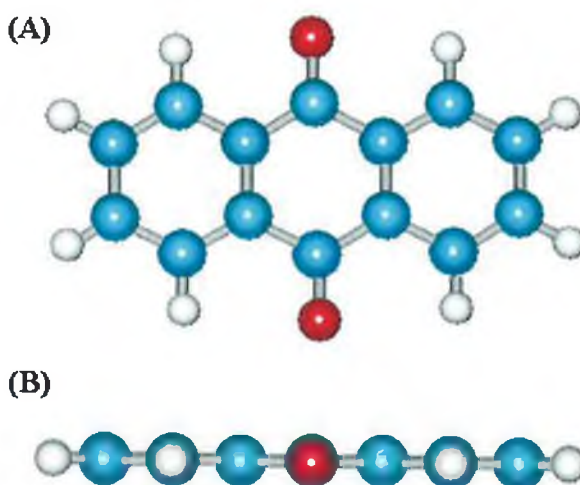


Figure 5. Resonance Raman spectrum for 9,10-AQ where the bulk concentration is 100 μM (—), and for an adsorbed monolayer on a mercury electrode surface at an open circuit potential (—). In both cases an Ar^+ laser at a wavelength of 514.5 nm was used for excitation.

Scheme 2. (A) Molecular Structure of the planar 9,10-AQ molecule, and, (B) an illustration of the parallel orientation adopted by the molecule on a mercury surface.



3.2.4 Concentration Dependence

An increase in the bulk concentration of the anthraquinones in solution causes the surface coverage to increase. Figure 6 illustrates the voltammetric responses as the bulk concentration of 1,2,4-AQASH is varied from 0.1 to 5.0 μM . Cyclic voltammograms are run in a negative potential direction from +0.18 to -0.65 V. The surface coverage increases from approximately 0.14 ± 0.10 to $1.60 \pm 0.05 \times 10^{-10}$ mol cm^{-2} over this concentration range. As the surface coverage increases there is a dramatic change in the voltammetric peak shapes and the cathodic and anodic peaks shift in a negative potential direction. The anodic branch of the voltammogram becomes distorted at high coverages with a spike being observed for surface coverages greater than about 1.2×10^{-10} mol cm^{-2} .

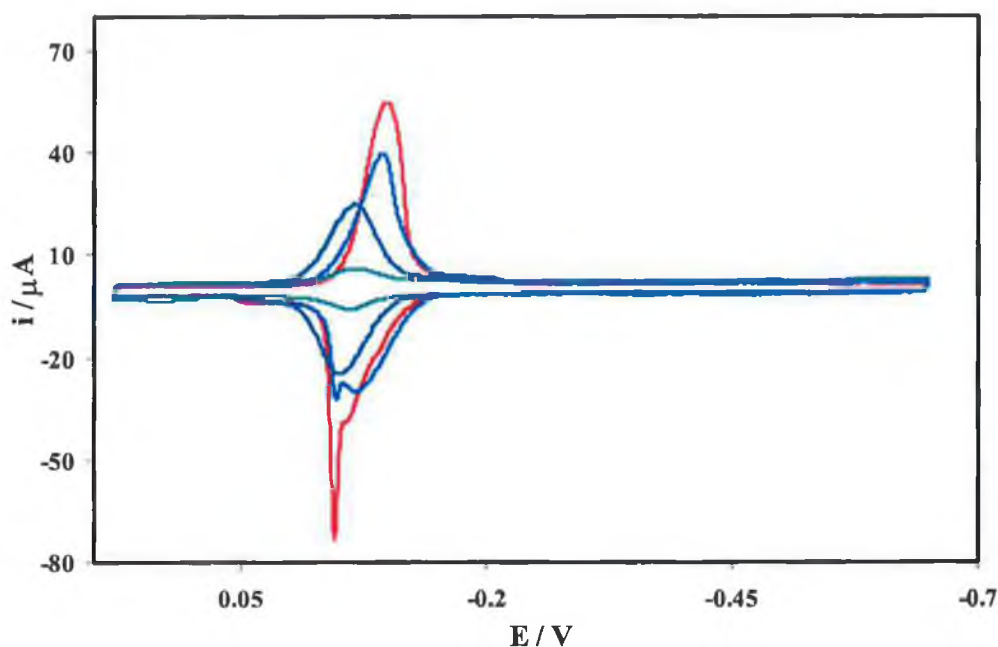


Figure 6. Dependence of the cyclic voltammetric response on the bulk concentration of 1,2,4-AQASH. The supporting electrolyte is aqueous 1 M HClO_4 and the anthraquinone concentrations are 5 ($-$), 1.5 ($-$), 1 ($-$) and 0.1 μM ($-$). The initial potential is 0.180 V and the scan rate is 5 Vs^{-1} . Cathodic currents are up and anodic currents are down.

It is possible that the voltammetric spike arises because electron and proton transfer are coupled in this system. For example, oxidation will trigger ejection of protons decreasing the interfacial pH. However, a decrease in the interfacial pH will cause E° to shift in a positive potential direction¹¹ and a current spike would not be expected. Moreover, the dynamics of proton transfer are unlikely to be responsible for the current spike. Under these low pH conditions, a layer less than 5 nm thick will be capable of providing the protons required during the two-electron, two-proton reduction of the monolayer to the doubly protonated hydroquinone, H₂Q. Under linear diffusion conditions this ultrasmall volume could be depleted of protons within nanoseconds, i.e., many orders of magnitude faster than the timescale on which the current spike is observed.

By looking at the surface coverage dependence of the cathodic and anodic peak potentials in Figure 7 we see that up to a surface coverage of approximately 1.2×10^{-10} mol cm⁻², the peak potentials are insensitive to the surface coverage. At surface coverages greater than 1.2×10^{-10} mol cm⁻² a spike appears in the anodic branch of the cyclic voltammogram, making an accurate measurement of E_{pa} more difficult. However, it is evident from the plot in Figure 7 that the anodic peak potential shifts in a positive potential direction at higher surface coverages. This is explained later through capacitive data, which reveals that 1,2,4-AQASH has a higher tendency to adsorb to the electrode surface in its reduced state. It is also evident from Figure 7 that the cathodic peak potential shifts to more negative potentials when the surface coverage exceeds approximately 1.2×10^{-10} mol cm⁻². Given that the formal potential of 1,2,4-AQASH is not dependent on the surface coverage at low surface coverages leads to the conclusion that the film exists as a random array of adsorbates on the electrode surface, rather than dense islands interspersed with regions of unmodified electrode. At higher surface coverages the cathodic and anodic peak potentials shift, consistent with interactions between adsorbates on the surface.

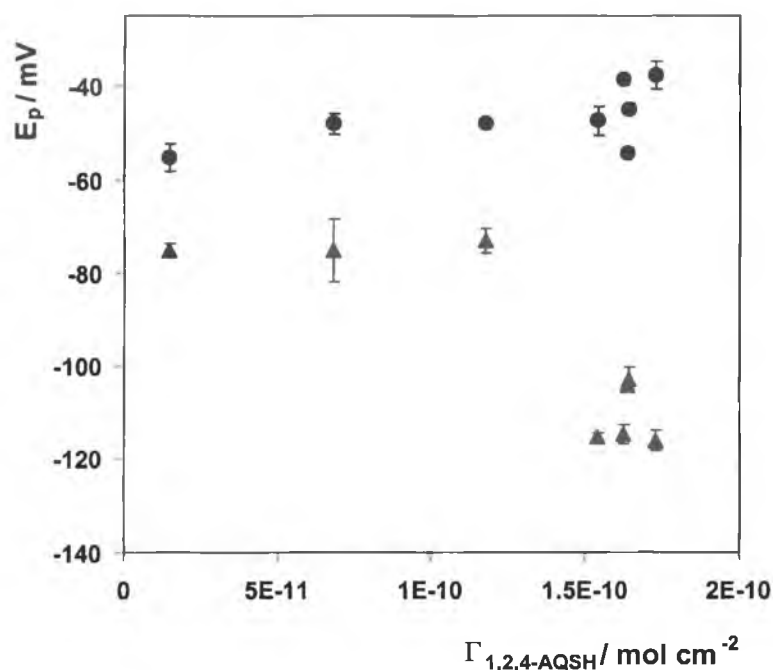


Figure 7. Dependence of the anodic (●) and cathodic (▲) peak potentials on the surface coverage of 1,2,4-AQASH. The monolayers were formed from the oxidised, quinone form of the compound at +0.18 V. The supporting electrolyte is 1.0 M HClO₄.

The concentration dependent response for 1,2,4-AQASH provides an unusual and interesting result in that the direction of the potential scan has a significant effect on the CV response. When scanning in a positive potential direction, i.e., initiating the scan at a potential of -0.65 V, when the anthraquinone is in the reduced, H₂Q form, no spike is present in the cathodic or anodic branches of the cyclic voltammogram. An overlay of the concentration dependent CVs up to a concentration of 5 μM is illustrated in Figure 8. The 5 μM solution yields a surface coverage of $1.2 \times 10^{-10} \text{ mol cm}^{-2}$, giving an intersite separation of approximately 4.4 Å. It was found that current spikes are observed for monolayers assembled from the hydroquinone form only for bulk concentrations in excess of 20 μM . It is possible that the anthraquinone molecules undergo repulsive interactions at low surface coverages and hydrogen bond when the surface coverage approaches saturation. The concentration dependent CV data is fit to the Langmuir and Frumkin adsorption isotherms in the following section of this chapter to model the thermodynamics of adsorption. This will allow a determination of the extent of interaction between adsorbates at different surface coverages.

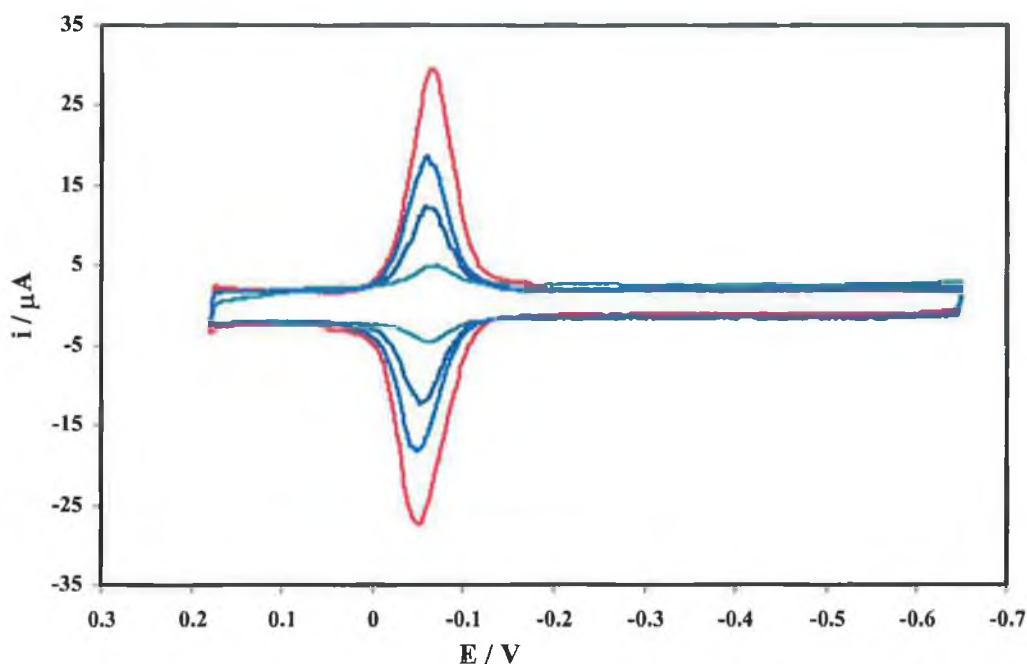


Figure 8. Dependence of the cyclic voltammetric response on the bulk concentration of 1,2,4-AQASH. The supporting electrolyte is 1 M HClO₄ and the anthraquinone concentrations are 5 (—), 3 (—), 1 (—), and 0.1 μM (—). The initial potential is -0.65 V and the scan rate is 5 Vs⁻¹ for all CVs. Cathodic currents are up and anodic currents are down.

The concentration dependent CV response of 9,10-AQ has similarities with that of 1,2,4-AQASH outlined above. Cyclic voltammograms were run using deposition solutions in the concentration range 0.1 to 4 μM. The surface coverage increases from $4.51 \pm 0.57 \times 10^{-12}$ to $1.15 \pm 0.01 \times 10^{-10}$ mol cm⁻² over this concentration range. In these experiments the CVs were run in both positive and negative potential direction. In deposition solutions where the bulk concentration is 0.85 μM and above a spike appears in the anodic branch of the cyclic voltammogram. This solution concentration yields a surface coverage of 8.74×10^{-11} mol cm⁻². The spike is seen to increase in intensity as the concentration of 9,10-AQ is increased. The full width at half maximum (FWHM) is 55.4 ± 2 mV in the CVs recorded from an anthraquinone solution of concentration 0.5 μM. This value is larger than the ideal value for the peak separation at half height of 45.3 mV for the CV response of a monolayer where there is no interaction between adsorbates. The FWHM decreases significantly in CVs obtained from a 4 μM 9,10-AQ

solution. The FWHM is 25.1 mV for the cathodic branch and 15.0 mV for the anodic branch. This change in peak shape as the surface coverage increases indicates that there is considerable attractive interaction between adsorbates at high surface coverages.²⁵ A detailed discussion of the origin of the spike in cyclic voltammograms is presented in section 3.2.7 of this chapter, based primarily on adsorption isotherm data.

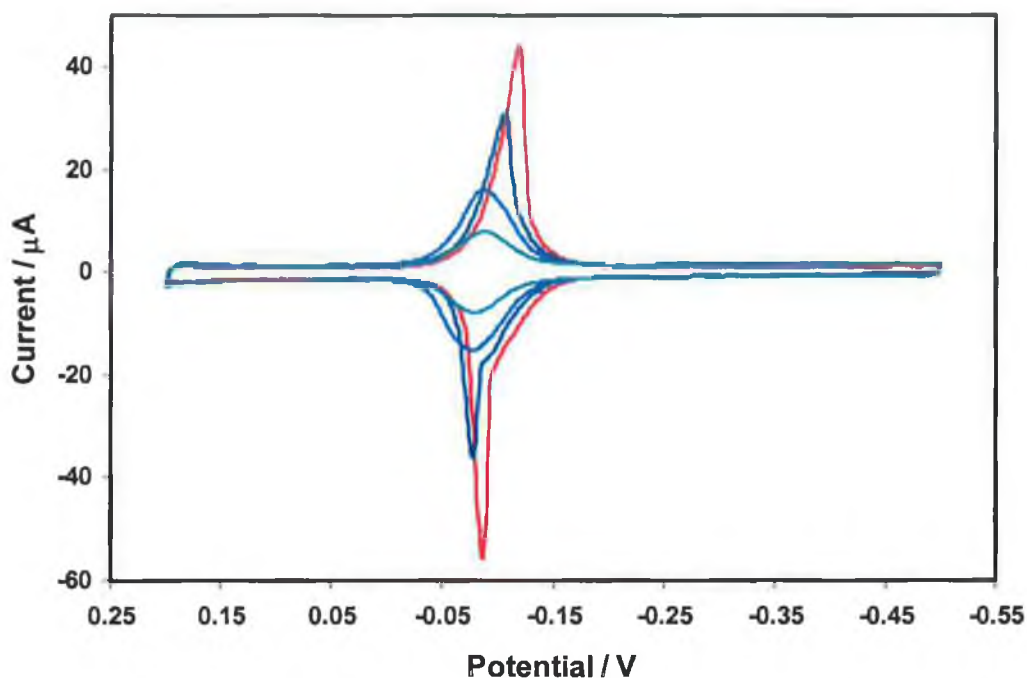


Figure 9. Dependence of the cyclic voltammetric response on the bulk concentration of 9,10-AQ. The supporting electrolyte is aqueous 1 M HClO₄ and the anthraquinone concentrations are 4 (—), 1 (—), 0.85 (—) and 0.5 μM (—). The initial potential is -0.5 V and the scan rate is 5 Vs⁻¹ for all CVs. Cathodic currents are up and anodic currents are down.

Current spikes have been reported previously by a number of research groups including McDermott and coworkers,¹⁶ Zhang and Anson¹⁷ and Faulkner and coworkers.¹⁸ These studies centered on the electrochemistry, spectroscopy and scanning probe microscopy investigations of sulphonated anthraquinone derivatives. The anthraquinones were adsorbed on mercury and graphite electrodes. All research groups propose that the spike is due to changes within the adsorbed monolayer through hydrogen bonding interactions as the surface coverage increases. Faulkner suggests the possibility of

condensation from a gas-like collection of isolated adsorbed species to a liquid or solid hydrogen bonded network. These publications propose that the spike is due to hydrogen bonding between adsorbates, however none of the papers describe why they come to this conclusion. A proposal as to why a hydrogen-bonded network would cause a “spike” to appear in a cyclic voltammogram is presented later in this chapter.

Given the structure of 9,10-AQ and 1,2,4-AQASH these molecules ought to be capable of both intra- and intermolecular hydrogen bonding. Therefore, these molecules are attractive model systems for investigating the distance dependence of hydrogen bonding in 2-dimensions, as the surface coverage can be systematically varied by controlling the bulk concentration of 9,10-AQ and 1,2,4-AQASH in solution.

3.2.5 Adsorption Thermodynamics

The equilibrium surface coverage depends on the bulk concentration of the anthraquinone in solution. To obtain the adsorption isotherms for 9,10-AQ and 1,2,4-AQASH the surface coverages at equilibrium were determined for each solution concentration by integrating the background corrected CVs. Surface coverages were determined using Equation (1), as outlined earlier in the text. The adsorption isotherms used to fit the experimental data throughout this chapter are the Langmuir and Frumkin isotherms. A more detailed description of these isotherms was presented in section 1.4.2.1 of Chapter 1. The primary difference between these isotherms is the ability of the Frumkin isotherm to probe the presence and extent of interactions between anthraquinone moieties when adsorbed on mercury.

3.2.5.1 Langmuir Isotherm

The Langmuir isotherm describes equilibrium adsorption where there are no lateral interactions between the adsorbed molecules and the limiting surface coverage is determined by the size of the adsorbate.^{13,14,24} It is assumed that adsorption takes place only at specific localised sites on the surface and that the saturation coverage corresponds to complete occupancy of these sites. It is also assumed that the maximum amount of adsorption is monolayer coverage. The Langmuir adsorption isotherm is described by the following expression:

$$\frac{\Gamma_i}{(\Gamma_s - \Gamma_i)} = \beta_i C_i \quad (2)$$

where β_i and C_i are the adsorption coefficient and the solution phase concentration of species i , respectively. Γ_i is the surface excess of an adsorbed species i , and Γ_s is the surface excess of species i at saturation. Equation (2) can be linearised to :

$$\frac{C_i}{\Gamma_i} = \frac{1}{\Gamma_s} C_i + \frac{1}{\Gamma_s} \beta_i \quad (3)$$

A plot of $\frac{C_i}{\Gamma_i}$ versus C_i is presented for all adsorption isotherms presented in this section and may be seen as insets in each respective isotherm plot. The saturation surface coverage and the energy parameter, β_i , which describes the strength of adsorption are obtained from the slope and intercept respectively. The free energy of adsorption values, ΔG_{ads} may be calculated from Equation (4):

$$-\Delta G_{\text{ads}} = RT \ln \beta \quad (4)$$

It is expected that the Langmuir isotherm will provide an inadequate fit to the experimental data, as the cyclic voltammetry results already presented indicate that both anthraquinones interact laterally when adsorbed on the electrode surface. The first set of data to be modelled was the concentration dependent response for 1,2,4-AQASH when *scanning in a negative potential direction*, i.e. the CV's where a spike was observed. This was followed by the concentration dependent data for 1,2,4-AQASH when *scanning in a positive potential direction*, and finally by the data for 9,10-AQ, again where a spike was observed in the CV's. The same sets of experimental data will be fit to the Frumkin adsorption isotherm in the following section of this chapter.

When scanning between potential limits of +0.18 and -0.65 V, i.e. *scanning in a negative potential direction*, the optimised fits to the Langmuir isotherm are displayed in Figures 10 and 11. In these cyclic voltammograms six sweep segments were typically enough to attain an equilibrium response. When plotting an adsorption isotherm the charge under the anodic and cathodic peaks is usually averaged, as these charges are equal in a symmetric CV response. However, as evident from Figure 6 the

areas under the cathodic and anodic peaks are different due to the presence of the spike from a concentration of 1.5 μM upwards. As a result the areas of the two peaks were measured separately and surface coverages determined. Two adsorption isotherms were plotted for the data obtained when scanning in the negative direction, i.e., starting at +0.18 V. At this potential the anthraquinone is in the oxidised, quinone form.

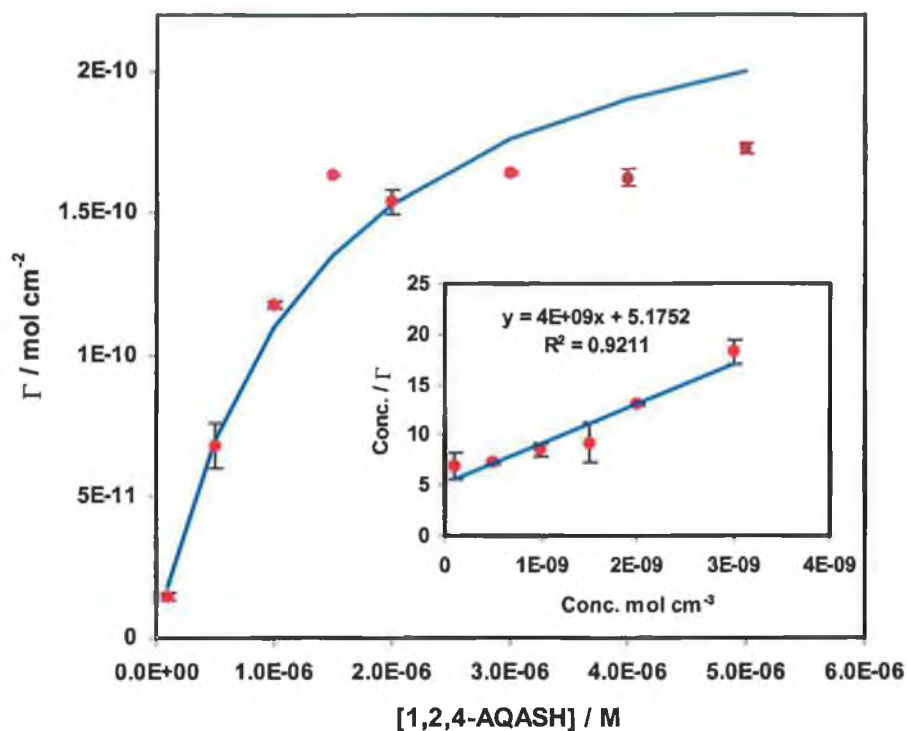


Figure 10. Dependence of the surface coverage on the bulk concentration of 1,2,4-AQASH. Surface coverages were determined from cathodic voltammetric peaks. The supporting electrolyte is 1 M HClO_4 . The data points are experimental results and the solid line represents the best fit of the experimental data to the Langmuir adsorption isotherm. The inset shows the optimum fit of the data to the linearised form of the Langmuir isotherm. Where error bars are not visible the error is comparable to the size of the symbol.

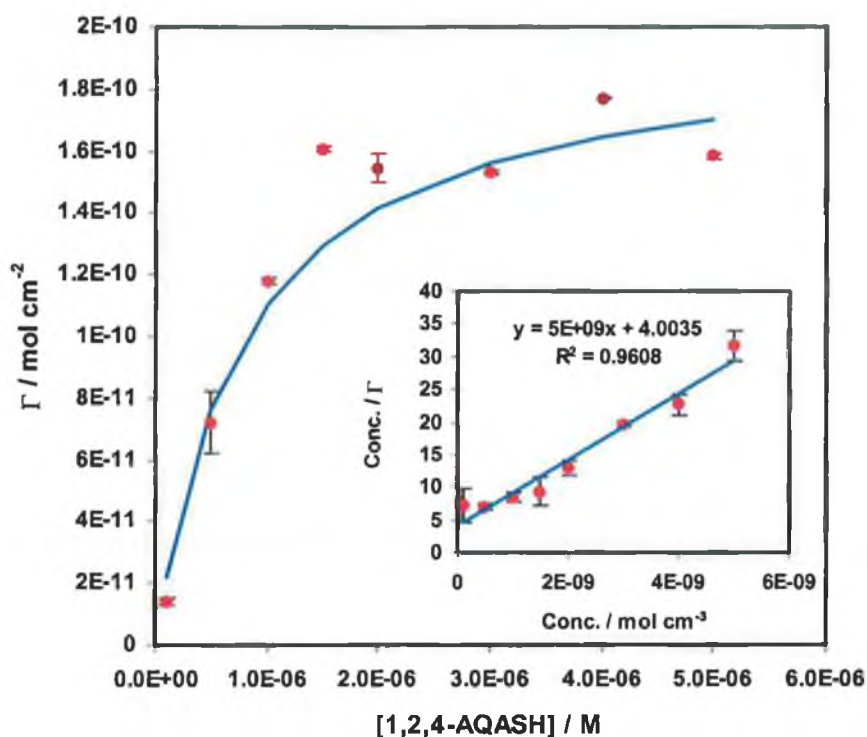


Figure 11. Dependence of the surface coverage on the bulk concentration of 1,2,4-AQASH. Surface coverages were determined from anodic voltammetric peaks. The supporting electrolyte is 1 M HClO_4 . The data points are experimental results and the solid line represents the best fit of the experimental data to the Langmuir adsorption isotherm. The inset shows the optimum fit of the data to the linearised form of the Langmuir isotherm. Where error bars are not visible the error is comparable to the size of the symbol.

In fitting the experimental data points to the Langmuir isotherm the data was first linearised, as displayed in the insets in Figures 10 and 11. Values for the saturation surface coverage and adsorption coefficient were obtained from the slope and intercept of this line, respectively. This data was then inputted into Equation (1) to calculate the theoretical surface coverages, according to the Langmuir isotherm. By looking at the graphs in Figure 10 and 11, it is evident that the experimental data deviates considerably from the ideal Langmuir response once the concentration of 1,2,4-AQASH in solution is above $1.5 \mu\text{M}$. This result is consistent with the CV data, which shows a current spike at concentrations above $1.5 \mu\text{M}$, and would suggest the onset of interactions between adsorbates at a concentration of $1.5 \mu\text{M}$. If this theory is correct

the Frumkin isotherm should approximate the experimental data accurately, as this isotherm contains an interaction parameter, thus modelling interaction between adsorbates.

When *scanning in a positive potential direction*, i.e. initiating the scan at a potential of -0.65 V the optimised fit to the Langmuir isotherm is displayed in Figure 12. It is evident from this Figure that the Langmuir isotherm provides an inadequate fit to the experimental data. This would imply that there is some interaction between adsorbates on the surface. These interactions could take the form of repulsive forces between adsorbates. This is supported by the CV data presented earlier, where the full width at half maximum was larger than the ideal value of 45.3 mV for a two electron transfer mechanism. This will be investigated further by fitting the data to the Frumkin isotherm, a positive interaction would be expected if repulsive interactions are present.

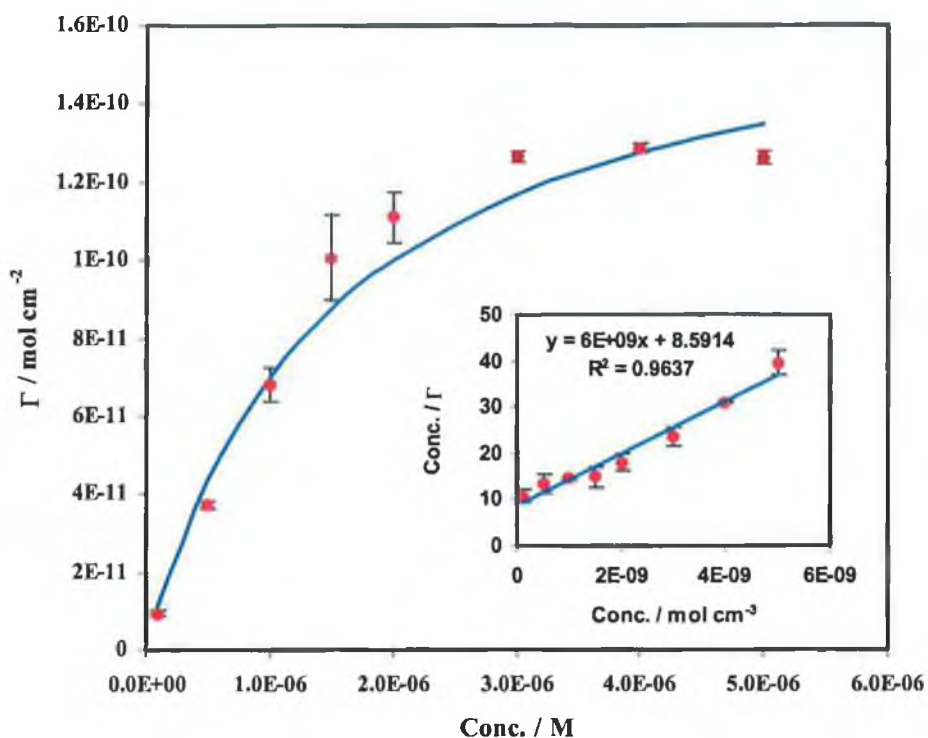


Figure 12. Dependence of the surface coverage on the bulk concentration of 1,2,4-AQASH. Surface coverages were determined from an average of cathodic and anodic peak currents. The supporting electrolyte is 1 M HClO_4 . The data points are experimental results and the solid line represents the best fit of the experimental data to the Langmuir adsorption isotherm. The inset shows the optimum fit of the data to the linearised form of the Langmuir isotherm. Where error bars are not visible the error is comparable to the size of the symbol.

To briefly compare the thermodynamics of 9,10-AQ with that of 1,2,4-AQASH the concentration dependent data for 9,10-AQ was fit to the Langmuir isotherm. However the Langmuir isotherm may provide an inadequate fit to the experimental data, as the cyclic voltammetry suggests there is interaction between adsorbates at surface coverages approaching saturation. Figure 13 confirms this theory, the theoretical linearised Langmuir isotherm provides a non-linear fit, which results in inaccurate results for Γ_{sat} and β . When these variables are substituted into Equation (3) the theoretical Langmuir data points are totally different from the experimental points. The Frumkin isotherm should provide a better fit to the experimental data.

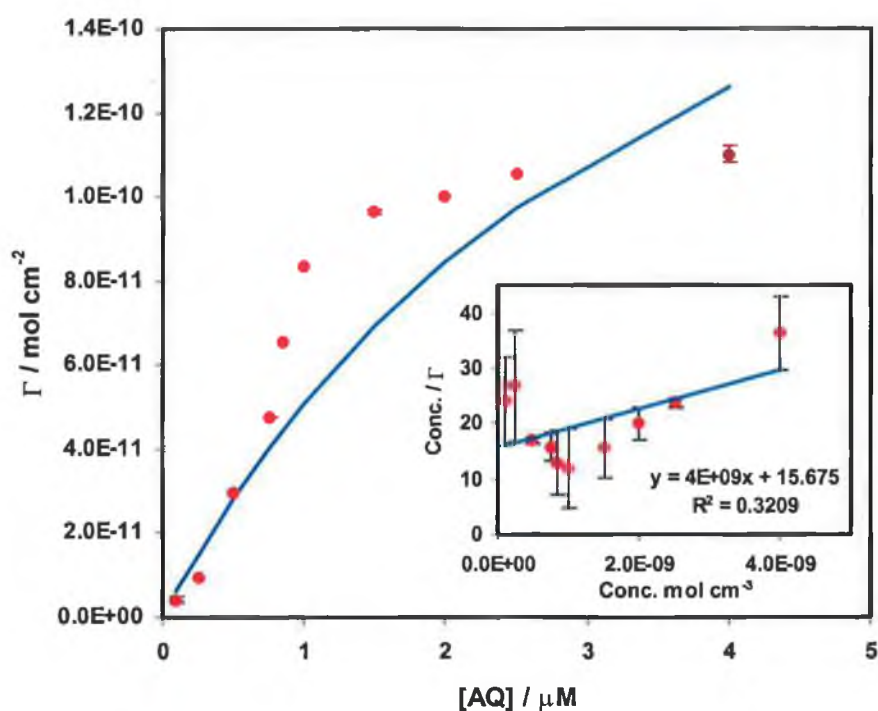


Figure 13. Dependence of the surface coverage on the bulk concentration of 9,10-AQ. Surface coverages were determined from an average of anodic and cathodic voltammetric peaks. The supporting electrolyte is 1 M HClO_4 . The data points are experimental results and the solid line represents the best fit of the experimental data to the Langmuir adsorption isotherm. The inset shows the optimum fit of the data to the linearised form of the Langmuir isotherm.

3.2.5.2 Frumkin Isotherm

The Frumkin adsorption isotherm accounts for lateral interactions by modelling the free energy of adsorption as an exponential function of the surface coverage:^{24,29,30}

$$\beta C_i = \frac{\theta_i}{1-\theta_i} \exp(g\theta_i) \quad (5)$$

where $\theta_i = \Gamma_i / \Gamma_{\text{sat}}$, Γ_i is the saturation coverage of the anthraquinone in mol cm⁻² at a bulk concentration C_i , Γ_{sat} is the saturation coverage obtained at high bulk concentrations and β the adsorption coefficient. The Frumkin isotherm differs from the Langmuir isotherm by containing an interaction parameter, g , which allows for coverage dependent adsorbate-adsorbate interactions. It is assumed that the electrochemical free energy of adsorption is linearly related to the surface coverage. Attractive interactions are indicated by $g < 0$ and repulsive interactions when $g > 0$.

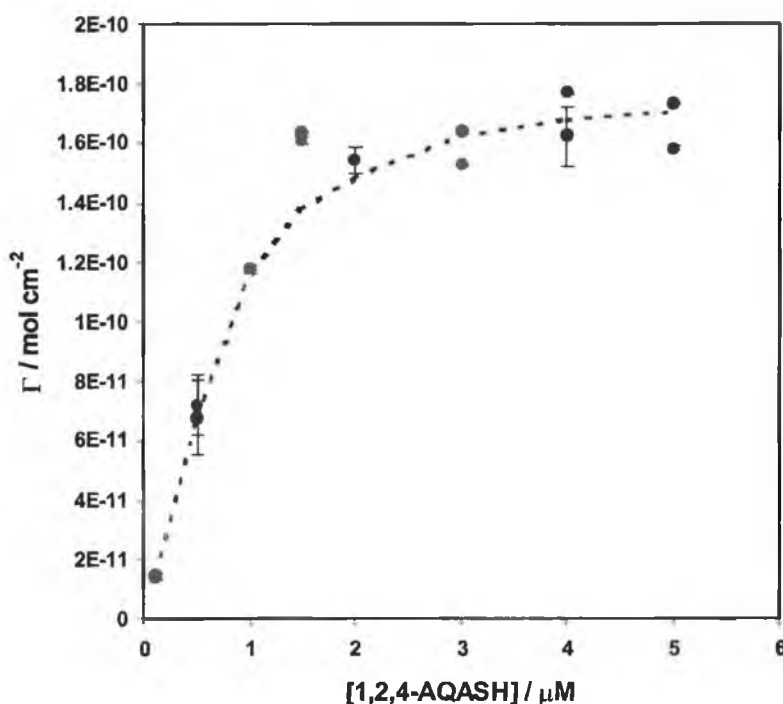


Figure 14. Dependence of the surface coverage on the bulk concentration of the quinone (● and • denote the areas under the anodic and cathodic peaks, respectively). The supporting electrolyte is 1.0 M HClO₄. The dashed line represents the best fit to the Frumkin adsorption isotherm.

Figure 14 illustrates the dependence of the surface coverage, Γ on the bulk concentration of 1,2,4-AQASH when monolayers were formed by *scanning the potential in a negative direction*. The Frumkin isotherm provides a significantly better fit to the experimental data than the Langmuir isotherm. The Frumkin model calculates the concentration of 1,2,4-AQASH and these values correlate well with experimental bulk concentrations in solution ($R^2 = 0.99$), Figure 15. The experimental data obtained when *scanning in a positive potential direction* was fit to the Frumkin isotherm also. In this way a limited insight into the effect of changing the redox state of the adsorbate on the thermodynamics of adsorption can be obtained. This isotherm fit is displayed in Figure 16.

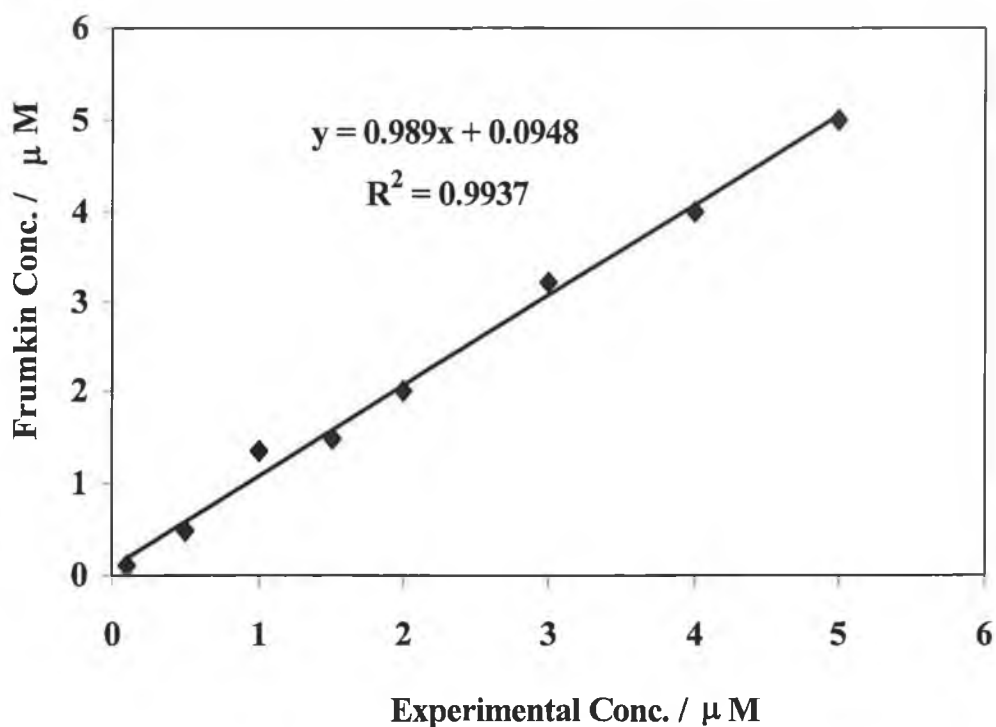


Figure 15. Correlation between the experimental concentrations of 1,2,4-AQASH and the optimized values predicted by the Frumkin adsorption isotherm.

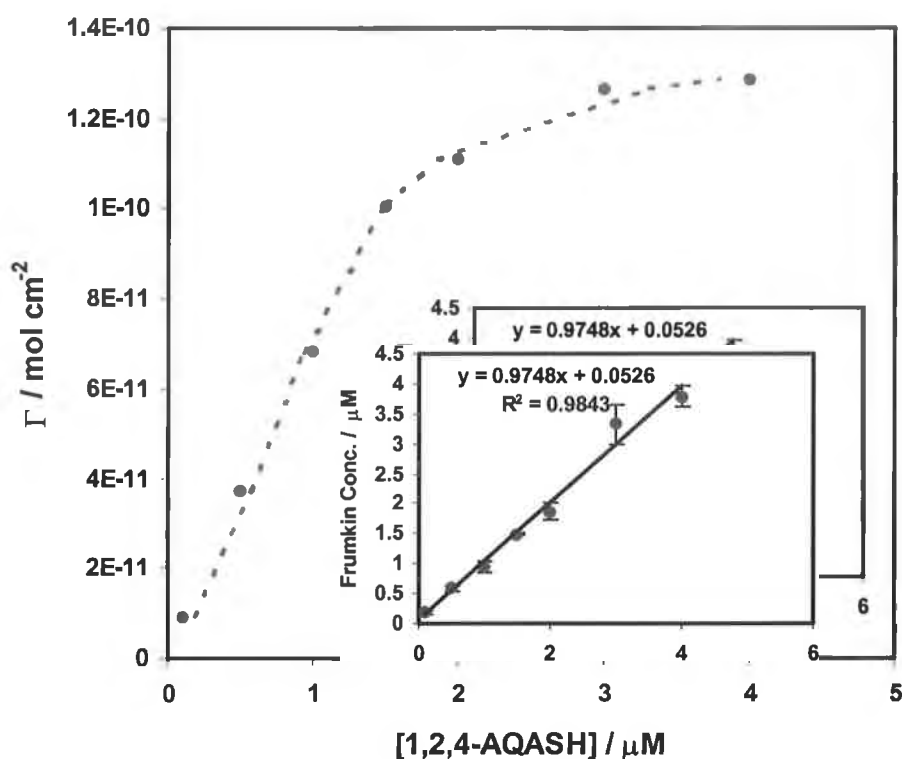


Figure 16. Dependence of the surface coverage on the bulk concentration of 1,2,4-AQASH. The supporting electrolyte is 1.0 M HClO_4 . The symbols represent experimental data points. The dashed line represents the best fit to the Frumkin adsorption isotherm. The inset shows the correlation between the experimental concentrations and the optimum concentration values calculated using the theoretical Frumkin isotherm. Where errors bars are not visible, errors determined from at least three independently formed monolayers are comparable to the size of the symbols.

Table 1 contains the best-fit parameters calculated from the Frumkin isotherm, when scanning in negative and positive potential directions, i.e. when monolayers are formed from the oxidised, Q and reduced, H_2Q forms. The interaction parameter when scanning negative is -0.29 ± 0.05 , indicating attractive stabilizing lateral interactions^{21,23} between adsorbates on the electrode surface. This stabilisation most likely involves hydrogen bonding between the carbonyl and hydroxy functionalities present in the oxidised and reduced forms of 1,2,4-AQASH. The interaction parameter when scanning positive is $+1.20 \pm 0.22$, which implies that repulsive interactions exist between adsorbates on the surface. This is reasonable if the CV data that was presented earlier is considered. When monolayers were formed when scanning in a positive

potential direction the surface coverage was below $1.2 \times 10^{-10} \text{ mol cm}^{-2}$. The FWHM of these CVs was larger than that expected for an ideal system, thus implying repulsive interactions between adsorbates. Therefore, for surface coverages up to $1.2 \times 10^{-10} \text{ mol cm}^{-2}$ repulsive interactions exist between adsorbates, above this coverage as saturation is approached, the available area on the surface decreases and adsorbates interact laterally through attractive hydrogen bonding interactions.

The free energies of adsorption were calculated from the values of the adsorption coefficients as before using Equation (4). The values were -34.8 ± 0.21 and -32.1 ± 1.6 kJ mol^{-1} for monolayers assembled from quinone and hydroquinone forms, respectively. These values indicate that both reduced and oxidised adsorbates are strongly bound to the electrode surface but monolayers formed using the quinone form are relatively more stable. In the following section of this chapter the potential dependent adsorption thermodynamics is probed. Experimental data at positive and negative potentials is fit to the Langmuir isotherm. This analysis will allow a determination of the origin of interactions in monolayers of 1,2,4-AQASH, i.e. in fully reduced monolayers, fully oxidised monolayers, or in monolayers where reduced and oxidised molecules are both present on the mercury surface.

Table 1. Saturation coverages, Adsorption Coefficients and Frumkin Interaction Parameters for 1,2,4-AQASH Monolayers assembled from both Oxidized, Q and Reduced, H₂Q, Species.

	Quinone	Hydroquinone
$10^{-10} \Gamma / \text{mol cm}^{-2}$	1.94±0.13	1.42±0.1
β / M^{-1}	1.27±0.11×10 ⁶	0.34±0.05×10 ⁶
$\Delta G / \text{kJ mol}^{-1}$	-34.8±0.8	-32.1±1.6
g	-0.29±0.05	+1.20±0.22

When the concentration dependent surface coverage for 9,10-AQ was fit to the Frumkin isotherm a good fit resulted, as illustrated in Figure 17 below. The charge under the cathodic and anodic peaks has been averaged, as both voltammetric branches were spiked at high surface coverages; this was displayed in Figure 9. A value for the equilibrium surface coverage at each concentration was determined using this charge. The experimental concentration values were accurately reproduced by the values obtained from the Frumkin isotherm. This result can be seen in the inset of Figure 17. The correlation coefficient of the graph is 0.9963. From this analysis it is reasonable to say that the Frumkin isotherm provides an accurate estimation of the saturation surface coverage, adsorption coefficient and most importantly interaction parameter for 9,10-AQ monolayers. Table 2 outlines these optimized parameters. The interaction parameter for these monolayers is negative, -2.67 ± 0.12 , indicating that there is attractive interactions between adsorbates on the electrode surface. Lateral hydrogen bonding interactions between adsorbed moieties, similar to those predicted for monolayers of 1,2,4-AQASH would account for these attractive forces. A schematic illustrating a possible hydrogen bonded network for 9,10-AQ and 1,2,4-AQASH is illustrated in Scheme 4 in section 3.2.7 of this chapter. The interaction parameter for 9,10-AQ is significantly greater than that calculated for 1,2,4-AQASH monolayers, suggesting that the strength of attractive interactions in these monomolecular films is quite large. Table 2 also contains a value for the free energy of adsorption, which in this case is negative, indicating that 9,10-AQ molecules are adsorbed strongly on the mercury electrode surface.

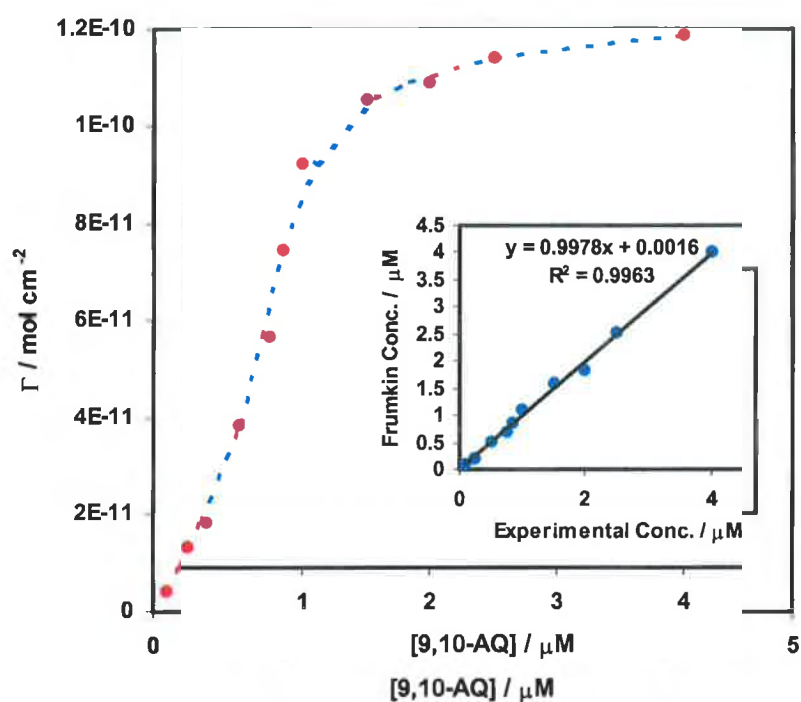


Figure 17. Dependence of the surface coverage on the bulk concentration of 9,10-AQ. The supporting electrolyte is 1.0 M HClO₄. The symbols represent experimental data points. The dashed line represents the best fit to the Frumkin adsorption isotherm. The inset shows the correlation between the experimental concentrations and the optimum concentration values calculated using the theoretical Frumkin isotherm. Where error bars are not visible, errors determined from at least three independently formed monolayers are comparable to the size of the symbols.

Table 2. Saturation coverage, Adsorption Coefficient and Frumkin Interaction Parameter for 9,10-AQ Monolayers.

	9,10-AQ
$10^{-10} \Gamma / \text{mol cm}^{-2}$	1.17 ± 0.11
β / M^{-1}	$0.33 \pm 0.07 \times 10^6$
$\Delta G / \text{kJ mol}^{-1}$	-30.9 ± 1.4
g	-2.67 ± 0.12

3.2.6 Potential Dependent Adsorption Thermodynamics

Determining the relationship between the surface coverage and double layer capacitance at potentials where the monolayer is fully oxidized and reduced allows the dependence of the adsorption thermodynamics on the oxidation state of the monolayer to be investigated. This method of analyzing the cyclic voltammetric data has a significant advantage over the methods presented thus far. In plotting the adsorption isotherms in section 3.2.5 of this chapter the measurements were taken at the formal potential, E^0 , where there exists approximately 50:50% ratio of oxidized and reduced species. The capacitance data, which were fit to the Langmuir isotherm in this section were measured at potentials where the monolayer was in the fully oxidized and reduced forms. Therefore, it is possible to determine the origin of the interactions in monomolecular films of 1,2,4-AQASH, i.e., from fully reduced, H_2Q layers, fully oxidized, Q layers, or at the formal potential where there is an equilibrium between oxidized and reduced species.

Figure 18 illustrates how the interfacial capacitance, as measured at + 0.1 and – 0.4 V, change as the bulk concentration of 1,2,4-AQASH is systematically varied from 0.1 to 5 μM , where the supporting electrolyte was 1.0 M HClO_4 . This change in capacitance is expected as the formation of a monolayer involves displacing adsorbed ions and solvent molecules from the interface, which would change the double layer capacitance from that observed at a clean, unmodified interface.²¹ Figure 18 shows that the double layer capacitance changed from $36.9 \pm 0.7 \mu\text{F cm}^{-2}$ for a clean mercury surface to a limiting value of $23.6 \pm 0.5 \mu\text{F cm}^{-2}$ in the case of oxidised monolayers and $19.7 \pm 0.5 \mu\text{F cm}^{-2}$ for reduced monolayers. The bulk concentration of 1,2,4-AQASH in solution was 5 μM . The dependence of the interfacial capacitance on the surface coverage can be described using a parallel plate capacitor model originally proposed by Delahey and coworkers.³¹ For this model, the total double layer capacitance, C_{dl} is given by Equation (6):

$$C_{dl} = C_{\text{mono}} + (C_{\text{bare}} - C_{\text{mono}})(1 - \theta) \quad (6)$$

where C_{bare} and C_{mono} are the double layer capacitances of a clean and modified electrode respectively and θ is the fractional monolayer coverage. This equation holds

for all potentials where C_{bare} is greater than C_{mono} . The parallel capacitor model predicts that the linearised Langmuir isotherm can be expressed as:

$$\frac{C_i}{(C_{\text{bare}} - C_{\text{dl}})} = \frac{1}{C_{\text{mono}}} C_i + \frac{1}{C_{\text{mono}} \beta_i} \quad (7)$$

where C_i is the bulk concentration of 1,2,4-AQASH in solution. Hence, the interfacial capacitance corresponding to a dense monolayer on the electrode surface, together with the adsorption coefficient can be determined from the slope and intercept of a plot of $C_i/(C_{\text{bare}} - C_{\text{dl}})$ vs. C_i . The inset of Figure 18 shows such a plot, constructed using capacitance data at -0.4 and $+0.1$ V, potentials where the film is fully reduced and oxidized. A good correlation results for both redox forms, indicating that the parallel capacitor model is an appropriate description of the adsorption in this system. That the dependence of the interfacial capacitance on the bulk concentration can be accurately modeled using the Langmuir isotherm indicates that lateral interactions are weak in fully oxidised and reduced films irrespective of the surface coverage.

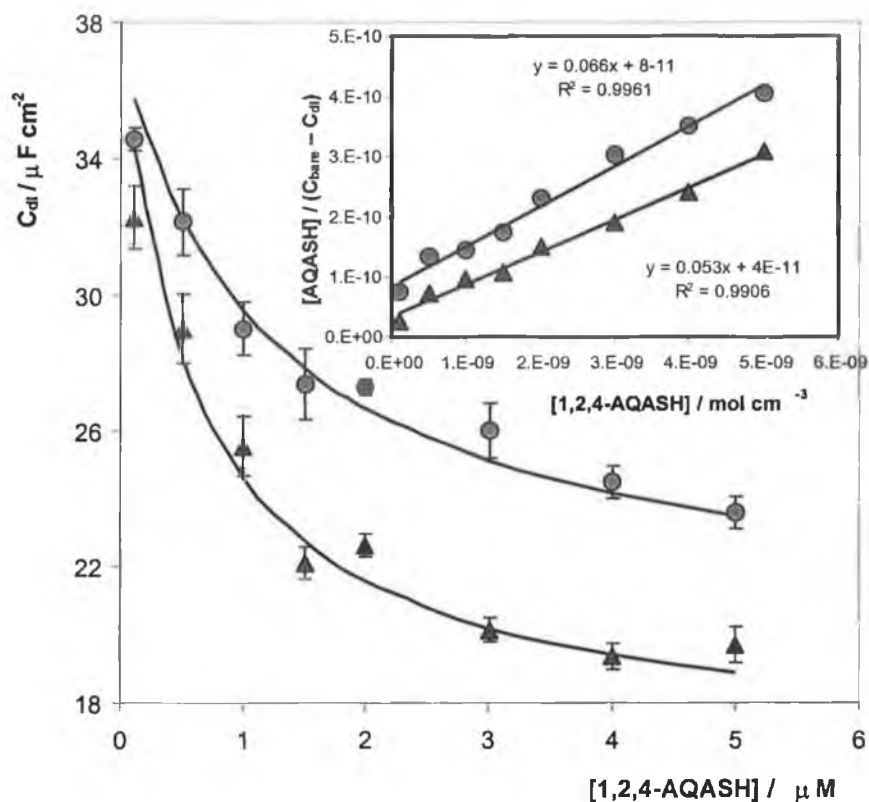


Figure 18. Dependence of the double layer capacitance on the bulk concentration of the quinone (●) and hydroquinone (▲) forms of 1,2,4-AQASH monolayers formed on hanging mercury electrodes. The interfacial capacitance was determined using scan rate dependent cyclic voltammetry at potentials of +0.180 and -0.400 V. The supporting electrolyte is 1.0 M HClO₄. The inset shows the best-fit linearized Langmuir isotherm.

Fitting the experimental data according to Equation (7) allowed the interfacial capacitance corresponding to the saturation surface coverage of 1,2,4-AQASH to be determined at potentials where the species was oxidized and reduced. Table 2 illustrates the results; C_{mono} was determined to be $18.9 \pm 0.9 \mu\text{F cm}^{-2}$ for the reduced state, which compares well with a value of $19.7 \pm 0.5 \mu\text{F cm}^{-2}$ obtained from cyclic voltammetry where the bulk concentration of 1,2,4-AQASH was $5 \mu\text{M}$ suggesting that a dense monolayer is formed when the bulk concentration is $5 \mu\text{M}$. However, C_{mono} calculated for the oxidised state was $15.0 \pm 1.1 \mu\text{F cm}^{-2}$, which was considerably lower than the value from cyclic voltammetry, i.e., $23.6 \pm 0.5 \mu\text{F cm}^{-2}$. Since a dense monolayer is associated with a lower interfacial capacitance,^{12,14} this data suggests that an incomplete oxidized monolayer is formed at $5 \mu\text{M}$, i.e. the $\Delta G_{\text{adsOx}} < \Delta G_{\text{adsRed}}$. This result is

consistent with capacitance data reported by Forster¹² investigating the concentration dependence of the interfacial capacitance of 2-AQCA monolayers in oxidized and reduced states. Forster's analysis showed that C_{mono} was constant at $17 \mu\text{F cm}^{-2}$ when the monolayer was in the reduced form but increases to $25 \mu\text{F cm}^{-2}$ when the monolayer was in the oxidized form. Therefore the packing density was higher in fully reduced monolayers of 2-AQCA, similar to the results observed for 1,2,4-AQASH in this work.

Table 3. Limiting Interfacial Capacitances and Adsorption Coefficients for 1,2,4-AQASH Monolayers assembled from both Oxidized, Q and Reduced, H₂Q, Species.

	Quinone	Hydroquinone
$C_{\text{mono}} / \mu\text{F cm}^{-2}$	15.0 ± 0.9	18.6 ± 1.1
β / M^{-1}	$0.77 \pm 0.07 \times 10^6$	$1.53 \pm 0.11 \times 10^6$
$\Delta G / \text{kJ mol}^{-1}$	-33.6 ± 0.3	-35.3 ± 0.2

A significant advantage of using capacitance data to probe monolayer formation is that adsorption coefficients can be determined for both oxidation states. The values obtained for the Q and H₂Q forms were $0.77 \pm 0.07 \times 10^6$ and $1.53 \pm 0.11 \text{ M}^{-1}$, respectively, indicating that the reduced form of 1,2,4-AQASH adsorbs relatively more strongly to the electrode surface. The difference in surface coverage and adsorption strength for oxidized and reduced monolayers of 1,2,4-AQASH may be due to the structural difference of these two molecules. The free energy of adsorption was calculated from Equation (4). This value changed from $-33.6 \pm 0.3 \text{ kJ mol}^{-1}$ when the monolayer was oxidized to $-35.3 \pm 0.2 \text{ kJ mol}^{-1}$, when the monolayer was in the reduced form. The free energy of adsorption calculated for 2-AQCA was $-26.0 \text{ kJ mol}^{-1}$ and $-42.8 \text{ kJ mol}^{-1}$, for oxidised and reduced monolayers, respectively. These values show that monolayers of 1,2,4-AQASH are stable on the electrode surface in both oxidized and reduced states.

3.2.7 Origin of the Current Spike

Much of the electrochemistry discussed in this chapter is dominated by the appearance of a sharp spike in the anodic branch of the cyclic voltammogram of 1,2,4-AQASH, when scanning in a negative potential direction. These monomolecular films are formed from the oxidized, quinone form. Spikes are also seen in anodic and cathodic branches of CVs of 9,10-AQ, when the bulk concentration of the anthraquinone in solution is 1 μM or greater. The spike in adsorbed monolayers of 1,2,4-AQASH occurs at surface coverages approaching saturation and above, where the supporting electrolyte is 1.0 M HClO_4 .



Here an analysis of the 1,2,4-AQASH adsorption data is carried out to determine the separation between adsorbed molecules on the surface as the solution concentration is increased. A possible mechanism, which would explain the presence of the spike in cyclic voltammograms is proposed. Repulsive interactions exist between adsorbates which would disfavour island formation or nucleation. Thus, it appears that for surface coverages up to $1.2 \times 10^{-10} \text{ mol cm}^{-2}$ the monolayers exist as weakly interacting, randomly dispersed adsorbates (Scheme 3A). Energy minimised molecular modelling determines that the area of the unsolvated molecule is approximately 70 \AA^2 ($6.6 \times 10.8 \text{ \AA}$). Hence, for surface coverages $< 1.2 \times 10^{-10} \text{ mol cm}^{-2}$ the average area occupied per molecule will be approximately 120 \AA^2 yielding an intersite separation greater than 3 \AA . This intersite separation is too large to allow efficient intermolecular hydrogen bonding. However, the abrupt shift in formal potential observed in Figure 7 and the current spike in Figure 6 occur when the surface coverage is greater than $1.6 \times 10^{-10} \text{ mol cm}^{-2}$. The intersite separation at increased surface coverage will be 2.4 \AA and less allowing hydrogen bonding interactions between the carbonyl oxygens of the quinone and the hydroxy groups on the adjacent hydroquinone (Scheme 3B). As the surface coverage increases further the extent of the hydrogen bonding interactions increases (Scheme 3C).

Scheme 3. Lateral interactions between 1,2,4-AQASH adsorbates as the bulk solution concentration increases.



(A) Non-interacting adsorbates at low surface coverage.



(B) Adsorbates undergo lateral hydrogen bonding between Q  and H₂Q  for intersite separations less than 3 Å.



(C) An increase in the bulk concentration of the anthraquinone solution causes the monolayer to compress causing an increase in intermolecular hydrogen bonding interactions.

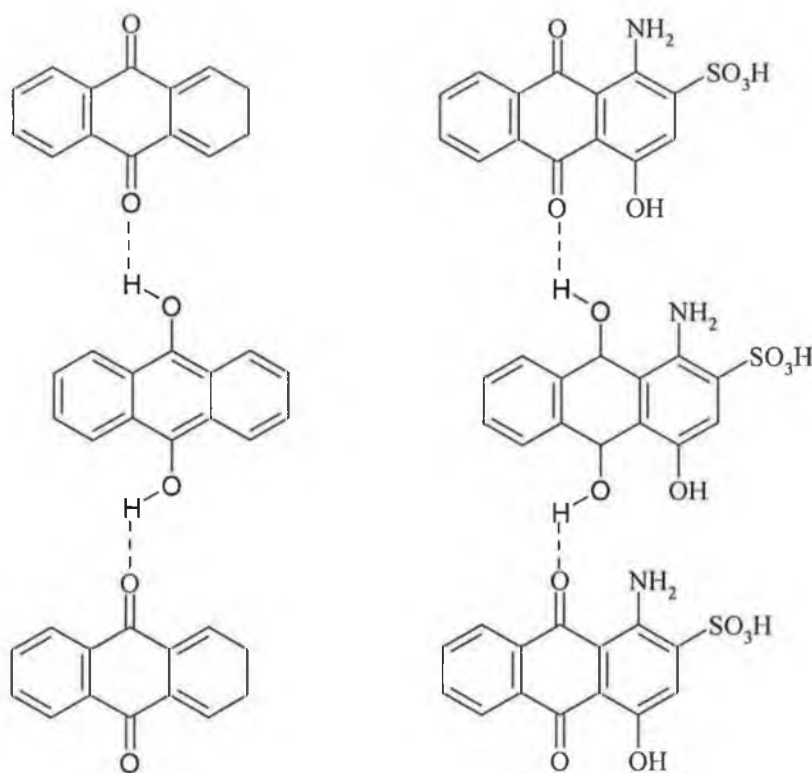
The sequence of events, which result in a spike being observed in the anodic branch of the cyclic voltammogram when scanning in the negative potential direction can be explained as follows:

- (1) The potential scan is initiated at a positive potential of +0.18 V, the anthraquinone exists in the oxidised form at this potential and spontaneously adsorbs on the mercury electrode surface.
- (2) As the potential is scanned in a negative direction the adsorbed Q molecules are reduced to the H₂Q form. This reduced form of the anthraquinone has a higher surface coverage (higher packing density) than the oxidised form, this has been confirmed through capacitance measurements.
- (3) The potential is then scanned from -0.65 V to +0.18 V and the oxidation reaction is driven. At the formal potential a nernstian redox equilibrium exists between the oxidised and reduced forms of 1,2,4-AQASH.
- (4) As the oxidation reaction proceeds and both redox forms exist on the mercury surface lateral interactions form between the reduced and oxidised adsorbates. The carbonyl oxygen groups in the quinone interact with the hydroxyl groups

in the adjacent hydroquinone. These two functional groups act as donors and acceptors in the hydrogen bonded network, as illustrated in Scheme 4.

- (5) Hydrogen bonding between the adsorbates causes the electron density to increase making it easier to oxidise the hydroquinone species causing the formal potential to shift in a negative potential direction.
- (6) The scan proceeds in the positive potential direction, however the nernstain equilibrium has been disturbed and an excess of H_2Q is present to be oxidised. This causes a spike in the anodic branch of the cyclic voltammogram to develop in the potential scan.

Scheme 4. Proposed intermolecular hydrogen bonded structure in mixed monolayers of 9,10-AQ and 1,2,4-AQASH.



The results presented thus far show that the current spike is only observed in voltammograms of 1,2,4-AQASH, when monolayers are assembled from the quinone form (scanning in a negative potential direction) for concentrations of anthraquinone solution up to $5 \mu\text{M}$. For the range of bulk concentrations investigated in the experimental section of this work (0.2 to $5 \mu\text{M}$) the surface coverage of hydroquinone

is always less than 1.2×10^{-10} mol cm⁻², the intersite separation is greater than 3 Å. A higher bulk concentration of hydroquinone is required to create films in which the intersite separation is small enough to allow hydrogen bonding interactions to occur. *However, current spikes are observed experimentally for monolayers formed from the hydroquinone species (scanning a positive potential direction) for bulk concentrations of approximately 20 μM and greater.*

3.3 Conclusions

This chapter presented a detailed investigation of the electrochemical properties of 9,10-AQ and 1,2,4-AQASH, which spontaneously adsorb to form monolayers on a mercury electrode surface. The effect of increasing the concentration of the electroactive species in solution was probed and the experimental data modeled thermodynamically. Both adsorbates interact laterally on the electrode surface at low and high surface coverages. In monolayers of 1,2,4-AQASH at low surface coverage where the intersite separation is greater than 4 Å repulsive interactions exist between adsorbates. At high surface coverage the intersite separation is 3 Å or less, thus hydrogen bonding interactions occur. The interaction parameters obtained from the Frumkin adsorption isotherm confirm this mechanism, a positive interaction parameter, (repulsive interactions) is obtained at low surface coverage, and a negative interaction parameter, (attractive interactions) results at high surface coverage.

The shape of the CVs recorded for 9,10-AQ and 1,2,4-AQASH from solutions of high bulk concentration exhibit spike shaped branches and this is also indicative of attractive interactions between adsorbates. When the interaction parameters for the two anthraquinones are compared it shows that 9,10-AQ adsorbates undergo stronger intermolecular interactions than 1,2,4-AQASH adsorbates. This is possibly due to the fact that 9,10-AQ has no substituents on the rings and so the molecules pack closer on the electrode surface, allowing for increased interactions.

It is evident from the results presented in this chapter that 1,2,4-AQASH adsorbates form stable monomolecular films on mercury. The redox reaction involves the transfer of two electrons coupled to the uptake of two protons from solution. Therefore, this system is ideal to study the kinetics of electron and proton transfer. This ideality forms the basis of the experimental work presented in Chapter 5 of this thesis. Chapter 4

probes the electrochemical properties of 1,2,4-AQASH further, as it is coadsorbed onto a mercury surface with a disubstituted anthraquinone derivative, 1,5-dimethoxyanthraquinone. The thermodynamics of competitive adsorption are investigated and compared to that of single component monolayers.

3.4 References

1. Finklea, H.O., Hanshew, D.D., *J. of Am. Chem. Soc.*, **1992**, 114, 3173.
2. Chidsey, C.E.D., *Science*, **1991**, 251, 919.
3. Chidsey, C.E.D., Bertozzi, C.R., Putvinski, T.M., Majsce, A.M., *J. Am. Chem. Soc.*, **1990**, 112, 4301.
4. Porter, M.D., Bright, T.B., Allara, D.L., Chidsey, C.E.D., *J. Am. Chem. Soc.*, **1987**, 109, 3559.
5. Forster, R.J., *Inorg. Chem.*, **1996**, 35, 3394.
6. Hudson, J.E., Abruna, H.D., *J Phys. Chem.*, **1996**, 100, 1036.
7. Forster, R.J., Faulkner, L.R., *Langmuir*, **1995**, 11, 1014.
8. Acevedo, D., Bretz, R.L., Tirado, J.D., Abruna, H.D., *Langmuir*, **1994**, 10, 1300.
9. Acevedo, D., Abruna, H.D., *J. Phys. Chem.*, **1991**, 95, 9590.
10. Forster, R.J., Keyes, T.E., Farrell, M., O'Hanlon, D., *Langmuir*, **2000**, 16, 9871.
11. O'Hanlon, D., Forster, R.J., *Langmuir*, **2000**, 16, 702.
12. Forster, R.J., *J. Electroanal. Chem.*, **1997**, 144, 1165.
13. Forster, R.J., *The Analyst*, **1996**, 121, 733.
14. Forster, R.J., *Anal. Chem*, **1996**, 68, 3143.
15. Forster, R.J., *Langmuir*, **1995**, 11, 2247.
16. Ta, T.C., Kanda, V., McDermott, M.T., *J. Phys. Chem.*, **1999**, 8, 1295.
17. Zhang, J., Anson, F.C., *J. Electroanal. Chem.*, **1992**, 331, 945.
18. He, P., Crooks, R.M., Faulkner, L.R., *J. Phys. Chem.*, **1990**, 94, 1135.
19. Soriaga, M.P., Hubbard, A.T., *J. Am. Chem. Soc.*, **1982**, 104, 2735.
20. O'Hanlon, D.P., Ph.D. Thesis, *Spontaneously Adsorbed Monolayers : Anthraquinones and Osmium Polypyridyl Complexes as Molecular Building Blocks*, **1999**.
21. Bard, A.J., Faulkner, L.R., *Electrochemical Methods : Fundamentals and Applications*, Wiley, New York, **1980**.
22. Brett, C.M.A.; Brett, A.M.O.; *Electroanalysis*; Oxford Science Publications.
23. Wopschall, R. H., Shain, I., *Anal. Chem.*, **1967**, 39, 1514.
24. Laviron, E., *J. Electroanal. Chem.*, **1974**, 52, 395.
25. Brown, A. P. Anson, F. C., *Anal. Chem.*, **1977**, 49, 1589.
26. Colthup, N. B. "Introduction to Infrared and Raman Spectroscopy" Academic Press, Boston, **1987**.

27. Gao, X., Davies, J.P., Weaver, M.J., *J. Phys. Chem.*, 1990, 94, 6864.
28. Nishiyama, K., Tahara, S., Uchida, Y., Tanoue, S., Taniguchi, I., *J. of Electroanal. Chem.*, 1999, 478, 83.
29. Ruthven, D., *Principles of Adsorption and Adsorption Processes*, John Wiley & Sons, 1984.
30. Adamson, A.W., Gast, A.P., *Physical Chemistry of Surfaces*, John Wiley & Sons, 1997.
31. Delahey, P., Trachtenberg, I., *J. Am. Chem. Soc.*, 1957, 79, 2355.

Chapter 4

Thermodynamics and Kinetics of Adsorption in Single and Two Component Anthraquinone Monolayers

“Hard work spotlights the character of people : some turn up their sleeves, some turn up their noses, and some don’t turn up at all.”

- *Sam Ewig*

4. Introduction

In the previous chapter the mechanism of monolayer formation was demonstrated to be uncomplicated, as 1,2,4-AQASH was seen to spontaneously adsorb on mercury. An equilibrium surface coverage was attained on a sub-second timescale. Scanning the potential between positive and negative potential limits did not alter the CV response. Calculations to determine the area per molecule were in agreement with literature values for a parallel-orientated molecule^{1,2,3,4,5} on the electrode surface. In this chapter the adsorption and desorption dynamics of 1,5-Dimethoxyanthraquinone (1,5-DMAQ) is reported in detail. Depending on the concentration of 1,5-DMAQ in the deposition solution the time taken for an equilibrium CV response to establish varies. A number of previous publications^{6,7,8,9,10,11,12} have focused on modeling the adsorption kinetics of electroactive species adsorbed on an electrode surface. In doing this an adsorption mechanism, which leads to an equilibrium surface coverage could be postulated for different systems. A kinetic model proposed by Hubbard, Silan and Plant¹³ was fit to the experimental data presented in this chapter. To the best of my knowledge this is the first work to deal with the adsorption and desorption dynamics of an anthraquinone derivative on a mercury surface, no other publications have been found in a thorough review of literature.

The second topic presented in this chapter is the electrochemical properties of two component anthraquinone monolayers. Chidsey and coworkers^{14,15} previously studied coadsorption of unsubstituted alkanethiols and ferrocene-terminated alkanethiols to investigate the distance dependence of electron transfer. Faulkner and Forster¹⁶ looked at binary monolayers of osmium containing complexes, which spontaneously adsorb onto platinum. These two complexes overlap on the potential axis in cyclic voltammetry. The magnitude of separation on the potential axis determines the selectivity of cyclic voltammetry and the potentials must be separated by at least 100 mV if the concentration of the individual species is to be determined accurately. The difference in electron transfer rates of the two adsorbates was used to determine their surface coverages in this two-component assembly. A similar investigation was carried out by Forster¹⁷ involving the coadsorption of two anthraquinone derivatives; 1,5-AQDS and 2,6-AQDS. In this investigation the concentrations of the two

anthraquinones in solution have been determined by combining information about heterogeneous kinetics and adsorption thermodynamics.

The molecules under investigation in this work are 1-amino, 2-sulphonic, 4-hydroxyanthraquinone (1,2,4-AQASH) and 1,5-dimethoxyanthraquinone (1,5-DMAQ). They are coadsorbed onto the surface of mercury from a deposition solution containing 70:30 % water:DMF. The formal potentials of the two molecules are well separated on the potential axis and so cyclic voltammetry has been used to investigate properties of these mixed monolayers. The thermodynamics and kinetics of adsorption are modeled to determine the mode of adsorption and structure of the mixed monolayer, when equilibrium surface coverage is reached.

4.1 Experimental

Cyclic voltammetry was performed using a CH Instruments Model 660 electrochemical workstation, a PAR EG&G model 270 dropping mercury electrode and a conventional three-electrode cell. Potentials were measured against a potassium chloride saturated silver/silver chloride (Ag/AgCl) reference electrode. The auxiliary electrode was a large area platinum wire. All solutions containing 1,2,4-AQASH and 1,5-DMAQ were thoroughly deoxygenated by purging with nitrogen and a blanket of nitrogen was maintained over the solution throughout the experiments. The area of the mercury electrode was determined using the density of pure mercury (13.546 g cm^{-3}) by dispensing, collecting and weighing 100 drops of mercury. An electrochemical area of $0.0140 \pm 0.0007 \text{ cm}^2$ was obtained. This area was also confirmed by recording cyclic voltammograms under steady state and linear diffusion conditions using $[\text{Ru}(\text{NH}_3)_6]^{2+/3+}$ as a solution phase electrochemical probe.

4.1.1 Materials and Procedures

The two anthraquinone derivatives used in the experimental; 1-amino, 2-sulphonic, 4-hydroxyanthraquinone (1,2,4-AQASH) and 1,5-dimethoxyanthraquinone (1,5-DMAQ) were obtained from BASF. Deposition solutions were prepared using 70:30% v/v mixture of water and DMF using 1.0 M HClO_4 as the supporting electrolyte. Spontaneously adsorbed monolayers were formed from electrolytic solutions of the anthraquinone at the desired concentration, typically in the micromolar range. A scan

rate of 5 Vs^{-1} was used in cyclic voltammetry, which is sufficiently fast to ensure that the current contribution from diffusion was less than 5% of the total current observed.^{18,19} For surface coverage experiments, repetitive cyclic voltammetry was performed until the peak currents observed in successive scans were identical, i.e., the equilibrium surface coverage was attained. For two component monolayers, the total surface coverage and the relative amounts of each species could be controlled by varying the solution phase concentration of the individual species. To determine the surface coverage, voltammograms were first corrected for double layer charging and then the charge under the faradaic peak was measured.

To probe the effect of coimmobilisation on both the formal potentials and the free energies of adsorption, a series of mixed anthraquinone solutions was prepared. In the two component system 1,5-DMAQ adsorbs more strongly to the electrode surface, hence the concentration of 1,2,4-AQASH was always in excess of 1,5-DMAQ when carrying out these experiments.

4.2 Results and Discussion

4.2.1 General EC Properties of Single Component Monolayers

Figure 1 illustrates the response obtained from 3 μM deposition solutions of the two anthraquinones under investigation here, 1,5-dimethoxyanthraquinone (1,5-DMAQ) and 1-amino,2-sulphonic,4-hydroxyanthraquinone (1,2,4-AQASH). As previously stated the solutions contained 30% DMF to ensure full solubility and 1 M HClO_4 was used as the supporting electrolyte.

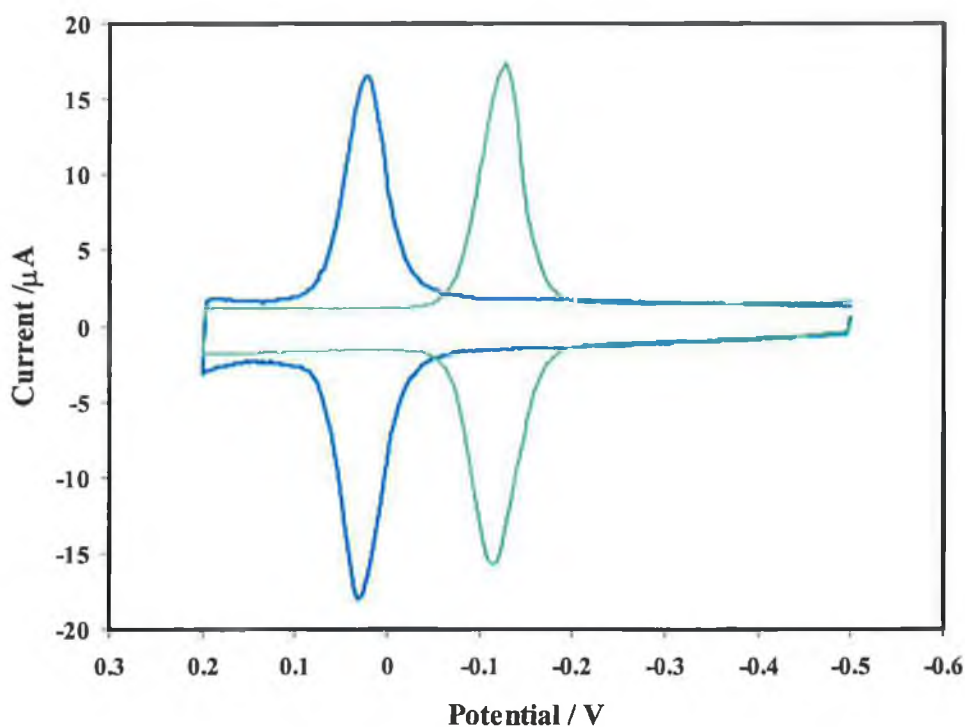
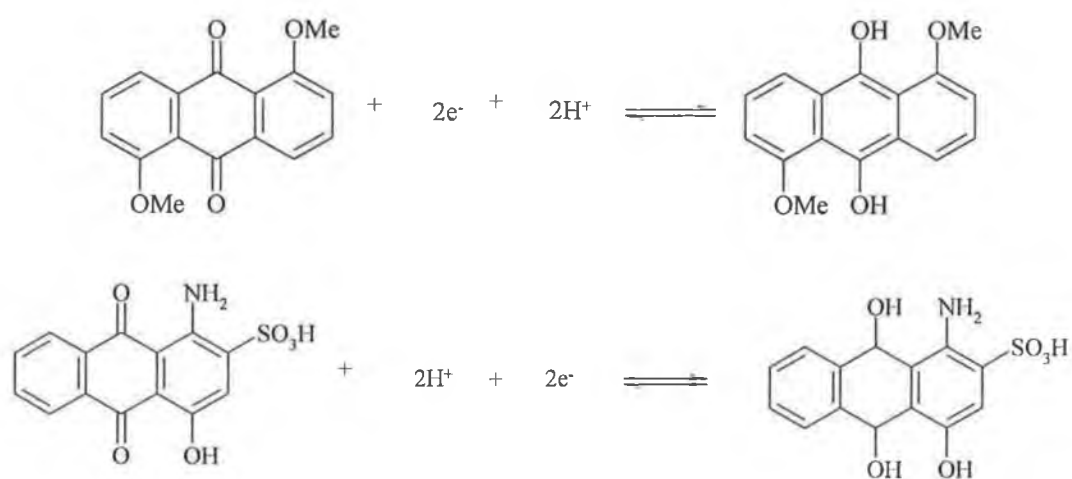


Figure 1. Cyclic voltammograms of a mercury electrode ($A = 0.014 \text{ cm}^2$) immersed in a 3 μM solution of 1,5-DMAQ (—) or 3 μM 1,2,4-AQASH (—). The solutions are 30:70 % v/v DMF:H₂O containing 1.0 M HClO_4 as the supporting electrolyte. The pH of the solutions is 0.16. The scan rate is 5 Vs^{-1} . Cathodic currents are up and anodic currents are down. The potential scan was started at the positive potential limit for both CVs.

Consistent with numerous previous reports concerning the adsorption of anthraquinone derivatives on mercury electrodes,^{20,21,22,23,24} it can be seen that these molecules adsorb to the electrode surface in an ideal manner. In theory when a substrate is adsorbed on

an electrode surface with no interactions between adsorbates and a rapid equilibrium is established between the applied potential and the redox composition of the film, a zero peak-to-peak splitting and a full width at half maximum (FWHM) of $90.6/n$ mV (n is the number of electrons transferred) are expected.^{18,19,25} The cathodic and anodic peak potentials for 1,5-DMAQ and 1,2,4-AQASH are separated by 9.0 ± 0.3 and 14.3 ± 0.5 mV respectively. Analysis of the cyclic voltammograms in Figure 1 shows that the FWHM values for 1,5-DMAQ and 1,2,4-AQASH are 45.8 ± 0.4 and 49.6 ± 0.7 mV, respectively. These values compare quite well with theory and suggest that the redox mechanisms for 1,5-DMAQ and 1,2,4-AQASH involve the transfer of two electrons and two protons in low pH media, as illustrated in Scheme 1 below. The small positive deviation between experimental FWHM values and theoretical FWHM for a two electron transfer mechanism may be indicative of slight repulsive interactions between adsorbates.¹⁸ Concentration dependent cyclic voltammetry data is fit to the Frumkin adsorption isotherm in section 4.2.3 of this chapter to investigate the possibility of such interactions.

Scheme 1. Redox reaction of 1,5-DMAQ and 1,2,4-AQASH in low pH solution.



4.2.2 Scan Rate Dependence

The effect of increasing the scan rate in cyclic voltammetry on the current response was investigated over the scan rate range 5-50Vs⁻¹. The results are presented in Figure 2 for a 6 μM solution of 1,5-DMAQ, which spontaneously adsorbs onto the mercury electrode surface as discussed previously. The inset of Figure 2 shows that the peak current scales linearly with scan rate, at least up to a scan rate of 50 Vs⁻¹. This is the response expected for an adsorbed moiety, the peak current would have a square root dependence on scan rate if the molecule was freely diffusing to the electrode surface.²⁶ As the scan rate increases from 5 to 50 Vs⁻¹ the peak-to-peak separation increases from 0.03 ± 0.001 mV to 0.06 ± 0.001 mV. This increase in separation between the cathodic and anodic peaks may be attributed to iR drop at the mercury macroelectrode. As the scan rate increases the resistance of the solution remains constant but the current response increases, thus the iR drop will increase with an increase in scan rate.

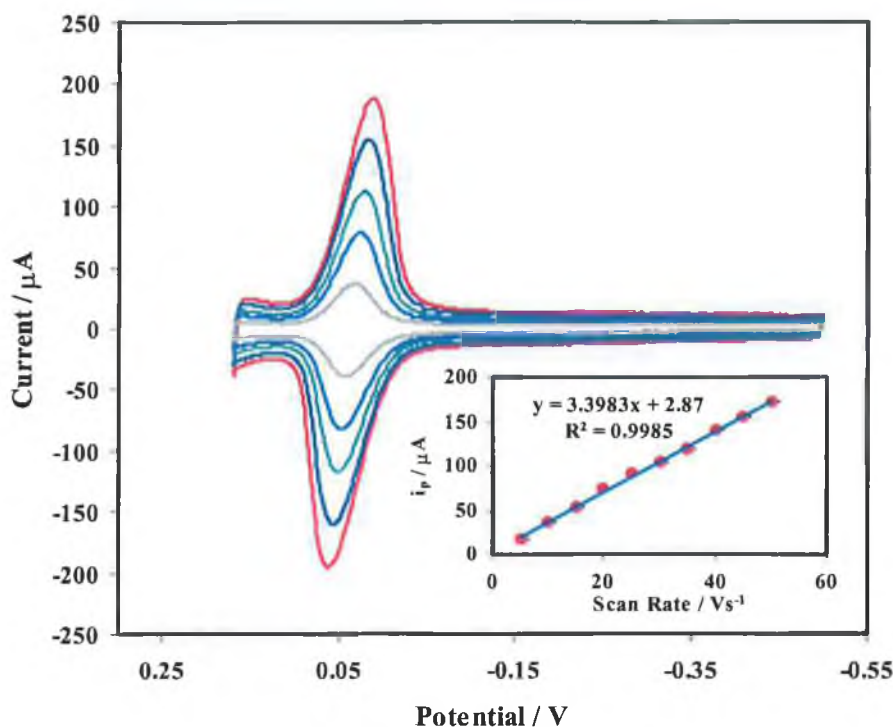


Figure 2. Cyclic voltammograms for a mercury electrode immersed in a 6 μM solution of 1,5-DMAQ with 1.0 M HClO_4 as the supporting electrolyte. Scan rates are 50 (—), 40 (—), 30 (—), 20 (—) and 10 Vs^{-1} (—). Cathodic currents are up and anodic currents are down with the initial potential set at -0.5 V. The inset shows the dependence of the maximum peak current over the scan rate range 5-50 Vs^{-1} . Where error bars are not visible, errors were determined from at least three independently formed monolayers and are comparable to the size of the symbols.

4.2.3 Adsorption Isotherms

The relationship between the amount of material adsorbed on the electrode surface and the concentration in solution varies with temperature. If surface coverage measurements are measured at a constant temperature the relationship is referred to as an adsorption isotherm. The extent of adsorption is expressed as a surface coverage, Γ , in mol cm^{-2} . As the concentration of the electroactive species in the deposition solution increases there is a concurrent increase in the surface coverage. Cyclic voltammograms for solutions containing 0.2 to 4 μM 1,5-DMAQ with 1M HClO_4 as the supporting electrolyte are illustrated in Figure 3. The surface coverage increases from $1.7 \pm 0.12 \times 10^{-11}$ to $8.5 \pm 0.17 \times 10^{-11}$ mol cm^{-2} over this concentration range. This plot illustrates

clearly that as the concentration of the electroactive species in solution increases there is no significant distortion in the cathodic or anodic peak shapes. This indicates that lateral interactions may not be significant in single component 1,5-DMAQ monolayers. This result contrasts with results in the previous chapter, which detailed the electrochemical response of 1,2,4-AQASH in aqueous solution.²⁷ However, it is important to note that the solutions of 1,5-DMAQ and 1,2,4-AQASH used throughout the experimental of this chapter were 70:30% v/v mixture of water and DMF. Therefore it is possible that the monomolecular films formed are highly solvated, as apposed to monolayers formed from entirely aqueous solutions. The degree of solvation will be investigated further in this chapter through capacitance data and the adsorption isotherms.

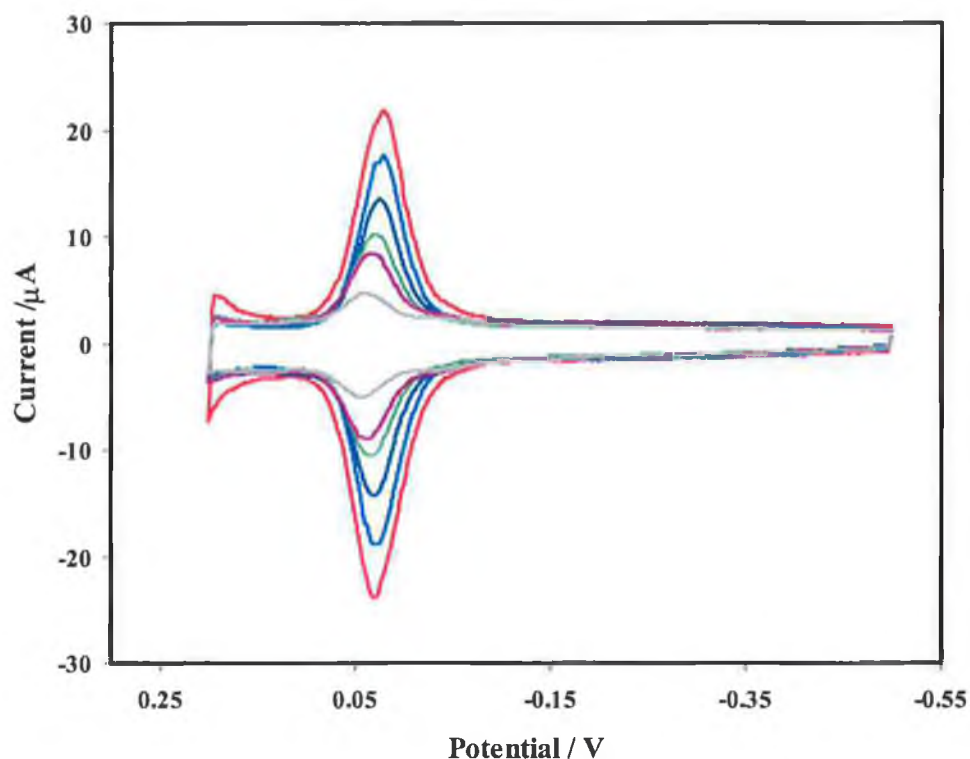


Figure 3. Dependence of the cyclic voltammetry response of a mercury electrode (area = 0.014 cm^2) on the bulk concentration of 1,5-DMAQ in 1.0 M HClO_4 . The pH of the solution is 0.16. The concentrations are 4 (—), 3 (—), 2 (—), 1 (—), 0.5 (—) and 0.2 μM (—). The scan rate is 5 Vs^{-1} . Cathodic currents are up and anodic currents are down, with the initial potential set at -0.5 V .

Two principal adsorption isotherms are the Langmuir and Frumkin isotherms,¹⁸ the theories of which have already been discussed in detail in section 3.2.5 of the previous chapter of this thesis. The adsorption data for 1,5-DMAQ and 1,2,4-AQASH were analysed using both the Langmuir and Frumkin adsorption isotherms as single component monolayers in order to see which provided the best fit to the experimental results.

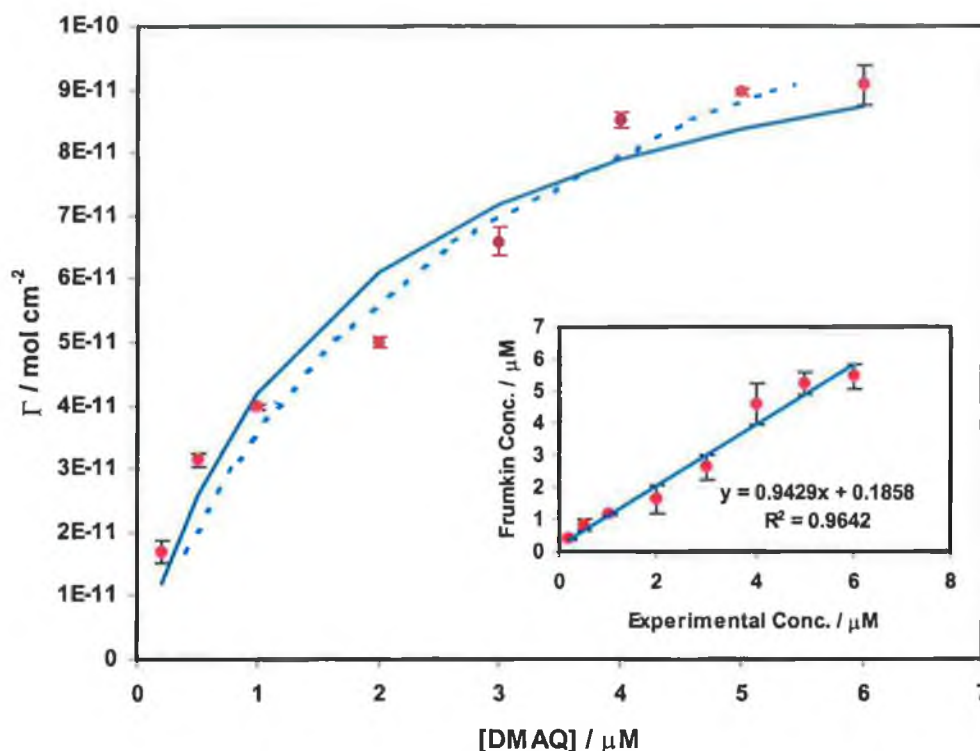


Figure 4. Dependence of the surface coverage on the bulk concentration of 1,5-DMAQ. The solutions were made up in 70:30 % v/v water:DMF and the supporting electrolyte was 1.0 M HClO_4 . The solid and dashed lines represent best fits to the Langmuir and Frumkin adsorption isotherms, respectively. Where error bars are not visible, errors were determined from at least three independently formed monolayers and are comparable to the size of the symbols. The inset shows the correlation between the experimental and theoretical Frumkin concentrations, which were determined using a solver model developed in Microsoft Excel.

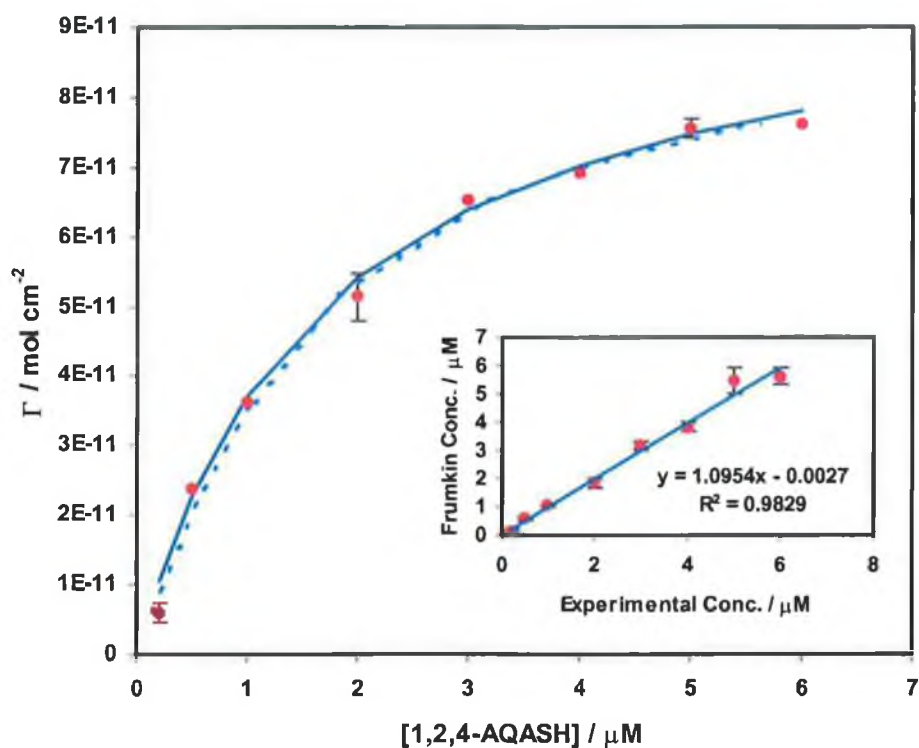


Figure 5. Dependence of the surface coverage on the bulk concentration of 1,2,4-AQASH. The solutions were made up in 70:30 % v/v water:DMF and the supporting electrolyte was 1.0 M HClO₄. The solid and dashed lines represent best fits to the Langmuir and Frumkin adsorption isotherms. Where error bars are not visible, errors were determined from at least three independently formed monolayers and are comparable to the size of the symbols. The inset shows the correlation between the experimental and theoretical Frumkin concentrations, which were determined using a solver model developed in Microsoft Excel.

Table 1 outlines the results obtained for both 1,5-DMAQ and 1,2,4-AQASH films when fit to the both adsorption isotherms outlined above. With reference to this data and the illustrations in Figures 4 and 5 it can be seen that the Frumkin isotherm provides a better fit to the experimental points for the adsorption of 1,5-DMAQ and 1,2,4-AQASH. Interaction parameters of +0.124 and -0.529 were calculated for 1,5-DMAQ and 1,2,4-AQASH respectively. These values correspond to interaction free energies of +0.107 and -0.694 kJ mol⁻¹. This would indicate that small repulsive interactions exist between 1,5-DMAQ molecules when adsorbed on the mercury surface, while somewhat larger attractive interactions exist between 1,2,4-AQASH molecules. In the case of 1,2,4-

AQASH adsorbates these interactions could take the form of hydrogen bonding, as previously outlined in chapter 3.

Table 1. Γ_{sat} and β values for monolayers of 1,5-DMAQ and 1,2,4-AQASH determined from the Langmuir and Frumkin isotherms. The Frumkin interaction parameters, g are also presented for both adsorbates. The conditions under which the experimental data was obtained is as follows; solutions were made up in 70:30 % v/v water:DMF, with 1 M HClO₄ as the supporting electrolyte. These solutions recorded a pH of 0.16.

	Langmuir – Single Component	Frumkin – Single Component
$\Gamma_{\text{SAT, DMAQ}} / \text{mol cm}^{-2}$	$1.11 \pm 0.12 \times 10^{-10}$	$1.43 \pm 0.11 \times 10^{-10}$
$\Gamma_{\text{SAT, AQASH}} / \text{mol cm}^{-2}$	$1.00 \pm 0.09 \times 10^{-10}$	$9.44 \pm 0.10 \times 10^{-11}$
$\beta_{\text{DMAQ}} / \text{M}^{-1}$	$6.08 \pm 0.12 \times 10^5$	$3.44 \pm 0.07 \times 10^5$
$\beta_{\text{AQASH}} / \text{M}^{-1}$	$5.93 \pm 0.17 \times 10^5$	$4.89 \pm 0.14 \times 10^5$
g_{DMAQ}		+ 0.124
g_{AQASH}		- 0.529

Values for the adsorption coefficient have been calculated as $3.44 \pm 0.07 \times 10^5$ and $4.89 \pm 0.14 \times 10^5 \text{ M}^{-1}$ for 1,5-DMAQ and 1,2,4-AQASH respectively. These values indicate that both adsorbates interact strongly with the mercury electrode surface, however 1,2,4-AQASH binds relatively more strongly. It is interesting to note that the adsorption coefficient obtained for the 1,2,4-AQASH monolayer is approximately half that quoted in the previous chapter. This reduction in adsorption strength most likely arises because the strength of the hydrophobic interaction of the organic molecule with the electrode surface decreases when the deposition solution contains 30% DMF. A similar observation was made by Forster and O'Hanlon²⁸ when investigating the adsorption behaviour of 2,7-AQDS on mercury formed from deposition solutions containing 20% DMF.

The saturation coverage obtained using the Frumkin isotherm for 1,2,4-AQASH is $9.44 \pm 0.10 \times 10^{-11} \text{ mol cm}^{-2}$, which is less than the value obtained for monolayers deposited from entirely aqueous solutions, $1.68 \times 10^{-10} \text{ mol cm}^{-2}$. Saturation coverage determined using the Frumkin isotherm for 1,5-DMAQ is $1.43 \pm 0.11 \times 10^{-10} \text{ mol cm}^{-2}$. The limiting coverages obtained from optimized fits to the Frumkin isotherm for 1,2,4-AQASH and 1,5-DMAQ correspond to areas of occupation per molecule of approximately 131 and 87 \AA^2 , respectively.

4.2.4 Interfacial Capacitance

As outlined in Section 1.1 of Chapter 1 adsorption of an electroactive species onto an electrode surface generally causes ions and solvent molecules to be displaced. The extent to which the double layer capacitance decreases upon modification can thus provide information on the packing density of a monolayer. The double layer capacitance of 1,5-DMAQ and 1,2,4-AQASH films was determined independently from cyclic voltammetric data when the deposition solution contains 30 % DMF. This analysis is similar to that carried out in Section 3.2.6 of the previous chapter, when 1,2,4-AQASH deposition solutions were prepared entirely in water. Under these conditions the interfacial capacitance was seen to depend on both the redox state of the adsorbing species and the surface coverage on the electrode surface. The double layer capacitance, C_{dl} changed from $36.9 \pm 0.7 \text{ \mu F cm}^{-2}$ for an unmodified mercury surface to a limiting value of $23.6 \pm 0.5 \text{ \mu F cm}^{-2}$ and $19.7 \pm 0.5 \text{ \mu F cm}^{-2}$ for fully oxidized and reduced monolayers, respectively. The concentration of 1,2,4-AQASH was sufficient to yield saturation surface coverage in these measurements. This result was similar to previous studies carried out by Forster and coworkers^{27,29,30,31} when studying single component anthraquinone monolayers, formed from entirely aqueous solutions.

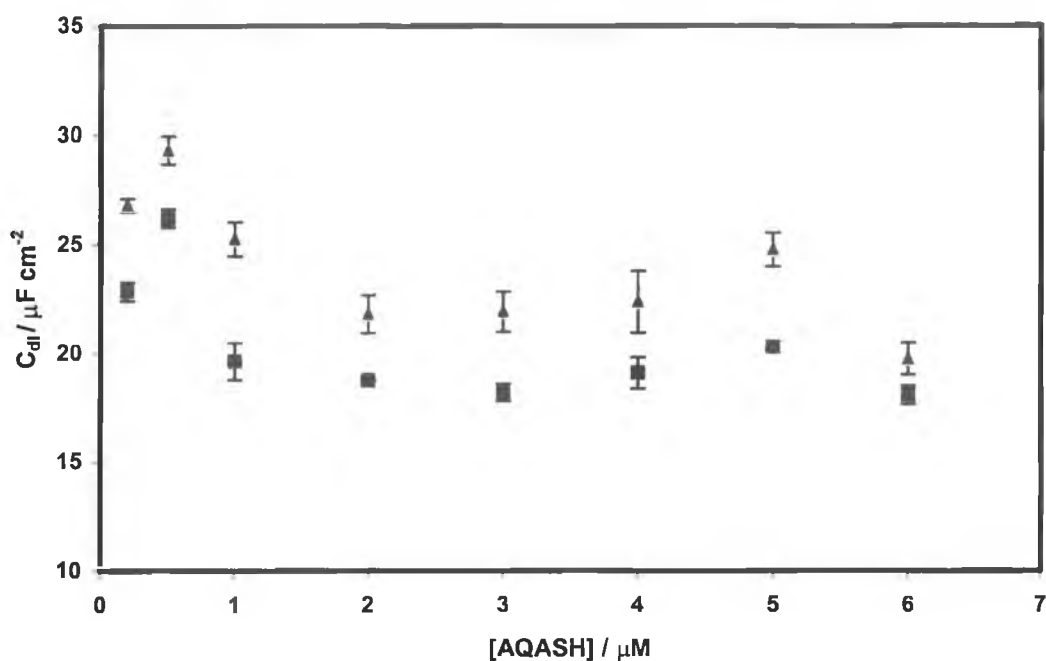


Figure 6. Dependence of the double layer capacitance on the bulk concentration of quinone (\blacktriangle) and hydroquinone (\blacksquare) forms of 1,2,4-AQASH monolayers formed on hanging mercury drop electrodes. The interfacial capacitance was measured at potentials of +0.10 and -0.40 V from cyclic voltammograms run at a scan rate of 5 Vs^{-1} . Solutions were made up in 70:30 % water:DMF with 1 M HClO_4 as the supporting electrolyte.

When the deposition solution contained 30 % DMF the interfacial capacitance was significantly less sensitive to concentration and surface coverage. As illustrated in Figure 6 the interfacial capacitance changed from 26.8 to $19.8 \mu\text{F cm}^{-2}$ as the solution concentration of 1,2,4-AQASH increased from 0.2 to $6 \mu\text{M}$. Measurements were taken when the monolayer was in the fully oxidized state, at a potential of $+0.1$ V. The variation of the capacitance over the same concentration range when the monolayer is in the fully reduced state was from 22.8 to $18.1 \mu\text{F cm}^{-2}$. From these results it is evident that the interfacial capacitance decreases with increasing surface coverage, however the decrease was much less significant than that measured when deposition solutions were made up entirely in aqueous electrolyte. This would suggest that monomolecular films formed from deposition solutions containing 30 % DMF are highly solvated for all surface coverages and the dielectric constant within the layer is similar to that found at an unmodified interface. Analogous observations have been made by Forster and

O'Hanlon²⁸ when studying the adsorption behaviour of 1,4-AQClOH and 2,7-AQDS deposited from deposition solutions containing 20 % DMF.

The interfacial capacitance of 1,5-DMAQ in a deposition solution containing 30 % DMF was also studied. The results presented in Figure 7 show capacitance values measured at potentials of +0.14 V (fully oxidized monolayer) and -0.30 V (fully reduced monolayer). Similar to the result for 1,2,4-AQASH monolayers, the double layer capacitance appears to be independent of surface coverage but dependent on the redox state of the monolayer. A lower capacitance was recorded for reduced monolayers regardless of concentration. This would suggest that fully reduced monolayers pack more densely than fully oxidized monolayers.

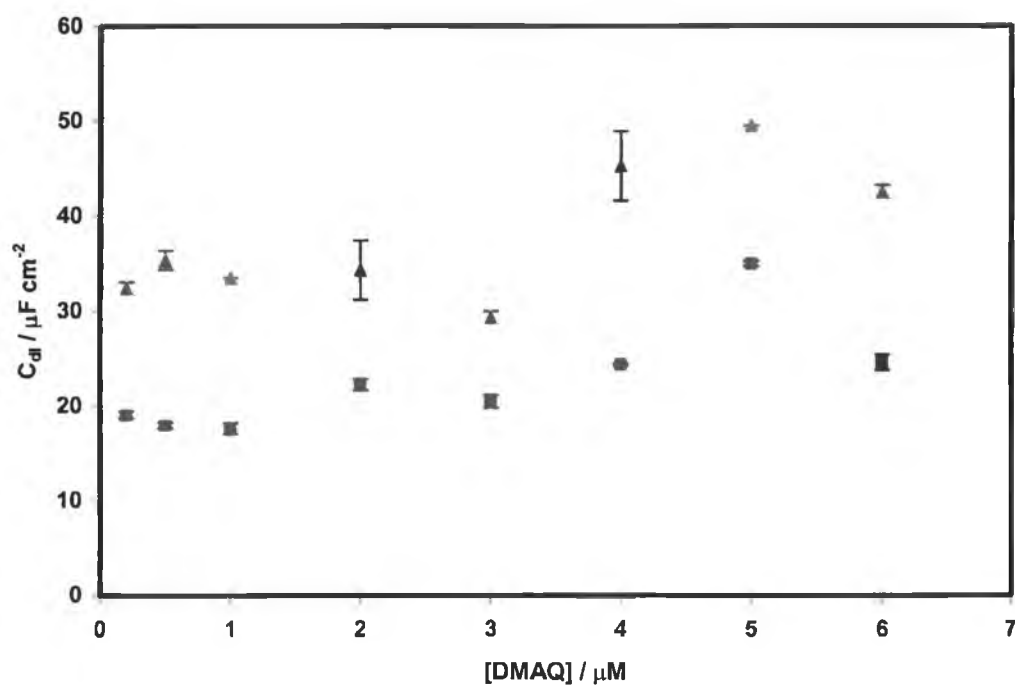


Figure 7. Dependence of the double layer capacitance on the bulk concentration of quinone (\blacktriangle) and hydroquinone (\blacksquare) forms of 1,5-DMAQ monolayers formed on hanging mercury drop electrodes. The interfacial capacitance was measured at potentials of +0.14 and -0.30 V from cyclic voltammograms run at a scan rate of 5 Vs^{-1} . Solutions were made up in 70:30 % water:DMF with 1 M HClO_4 as the supporting electrolyte.

4.2.5 1,5-DMAQ Adsorption Kinetics

The cyclic voltammetric response illustrated in Figure 1 shows the response obtained from a 3 μM solution of 1,5-DMAQ once adsorption has come to equilibrium. The time taken for this equilibrium response to be established depends on the concentration of the adsorbing species in solution. In this section of the chapter the kinetics of adsorption will be investigated for two solution concentrations of anthraquinone. The concentrations used are 2 and 10 μM , which yield intermediate and saturation coverages on the electrode surface, respectively. These two solution concentrations were analysed because the rates of initial adsorption and interconversion are different for solutions of high and low concentration. Figures 8 and 9 show the response obtained from a 2 μM solution over a period of one hour. Initially two peaks are seen in the cyclic voltammetric response at potentials of 0.132 V and 0.046 V. Cyclic voltammograms were recorded in a repetitive run program every nine seconds to monitor the variation of the surface coverage leading to an equilibrium, one-peak response.

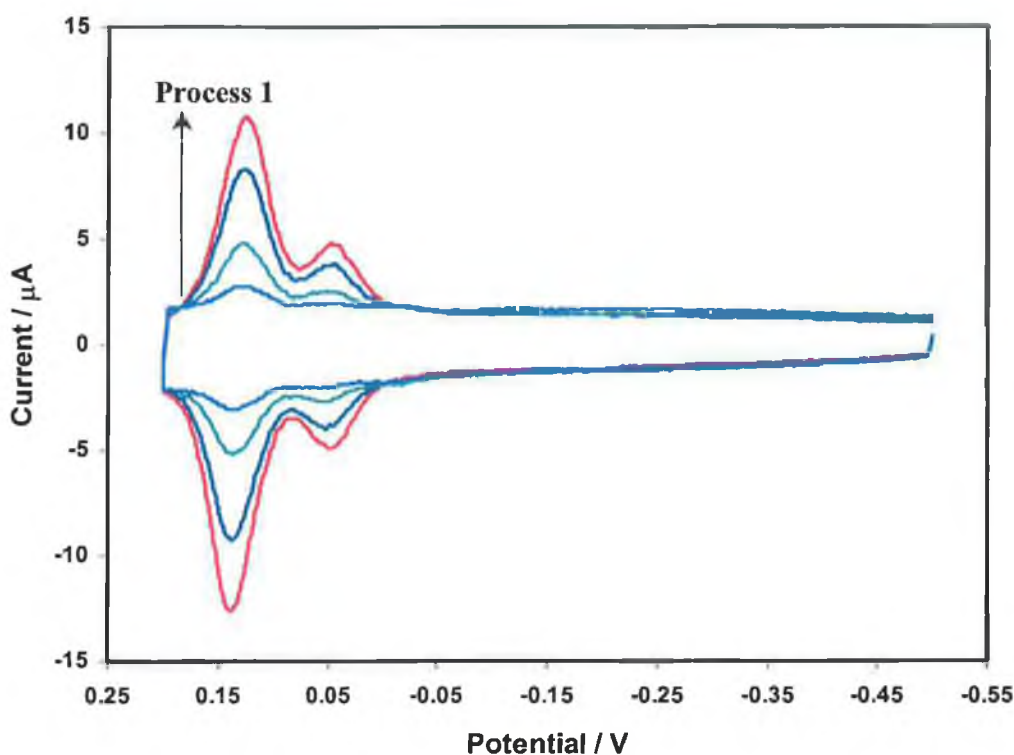


Figure 8. Cyclic voltammetry response of a mercury electrode immersed in a deposition solution containing 2 μM 1,5-DMAQ. The solution is 70:30 % v/v DMF:H₂O containing 1 M HClO₄ as the supporting electrolyte. The scan rate was 5 Vs⁻¹. The potential limits were +0.2 and -0.5 V and the potential was scanned in a positive potential direction. CVs were recorded at times 9 (—), 45 (—), 135 (—) and 306 (—) seconds.

From this analysis the following was noted, the peak at the more positive potential was seen to grow rapidly over the first five minutes approximately to a maximum height. This is shown in Figure 8 above and will be referred to as “Process 1” in the discussion that follows. Subsequent CVs showed a decrease in the peak height until it disappeared from the cyclic voltammograms altogether. This process, which is illustrated in Figure 9 takes place over a longer period of time, in the case of a 2 μM deposition solution displayed here the process takes approximately 1 hour. As the peak at 0.132 V decreased over time, “Process 2A” a simultaneous increase in the peak height at 0.046 V, “Process 2B” was observed. These initial adsorption and interconversion kinetic results were reproducible for other 2 μM solutions of 1,5-DMAQ when monolayers were formed independently on different mercury drops.

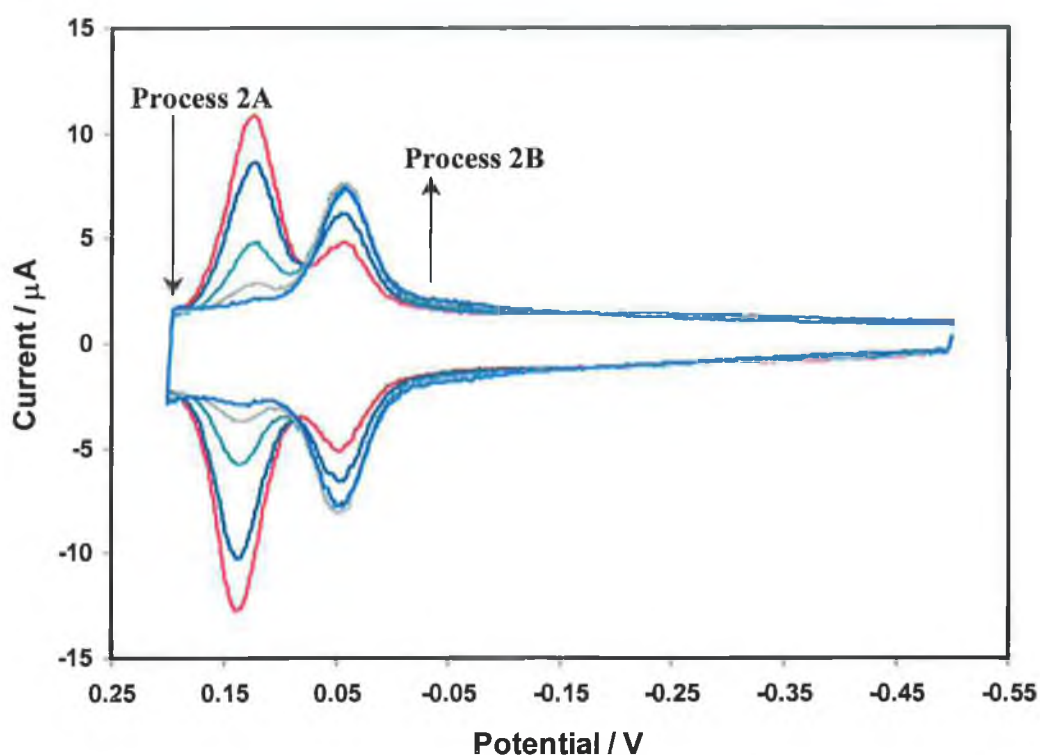


Figure 9. Cyclic voltammety response of a mercury electrode immersed in a deposition solution containing 2 μM 1,5-DMAQ. The solution is 70:30 % v/v DMF:H₂O containing 1 M HClO₄ as the supporting electrolyte. The scan rate was 5 Vs⁻¹. The potential limits were +0.2 and -0.5 V and the potential was scanned in a positive potential direction. CVs were recorded at times 6 (–), 15 (–), 30 (–), 45 (–) and 60 minutes (–).

The results for a 10 μM solution, although not graphically presented here showed the same trend in the data. The peak at the more positive potential, 0.132 V increased over the first two minutes approximately with subsequent loss of the peak at 0.132 V and growth of the peak at 0.046 V taking approximately 4 hours to reach an equilibrium response. In order to gain some understanding of the mechanism of adsorption in these monomolecular films, which leads to equilibrium surface coverage the results for processes 1, 2A and 2B were fit to a number of adsorption models.

In an extensive review carried out by Schreiber³² on the structure and growth of self-assembling monolayers, a discussion of the growth behaviour of self-assembled monolayers from solution was presented. The SAMs reviewed in this paper were largely alkanethiol monolayers, however some similarities were apparent. In the alkanethiol systems it was noted that as the concentration of electroactive species in solution increased the initial growth increased too. This was also seen for the 2 and 10 μM deposition solutions of 1,5-DMAQ. Schreiber also found that the first adsorption step resulted in 80-90% coverage, typically in the time scale of a few minutes. After that the growth rate proceeded at a much slower rate. This can also be seen in the adsorption kinetic data of 1,5-DMAQ, for example the results for a 2 μM solution are presented in Figure 10. This plot shows how the peak current at 0.046 V increases as adsorption proceeds, (Process 2A) while the voltammetric peak at 0.132 V simultaneously decreases (Process 2B). The total current at each time is also shown. From this plot it can be seen that the interconversion proceeds over a period of one hour, however the adsorption process reaches an equilibrium response after approximately 20 minutes. It is also evident from this plot that Process 2A is much faster than Process 2B, as the total surface coverage, (\bullet) decreases over the time period investigated. The mechanism outlined in Section 4.2.5.4 of this chapter proposes an explanation for this process, following a discussion of models that provide the best fit to the experimental data.

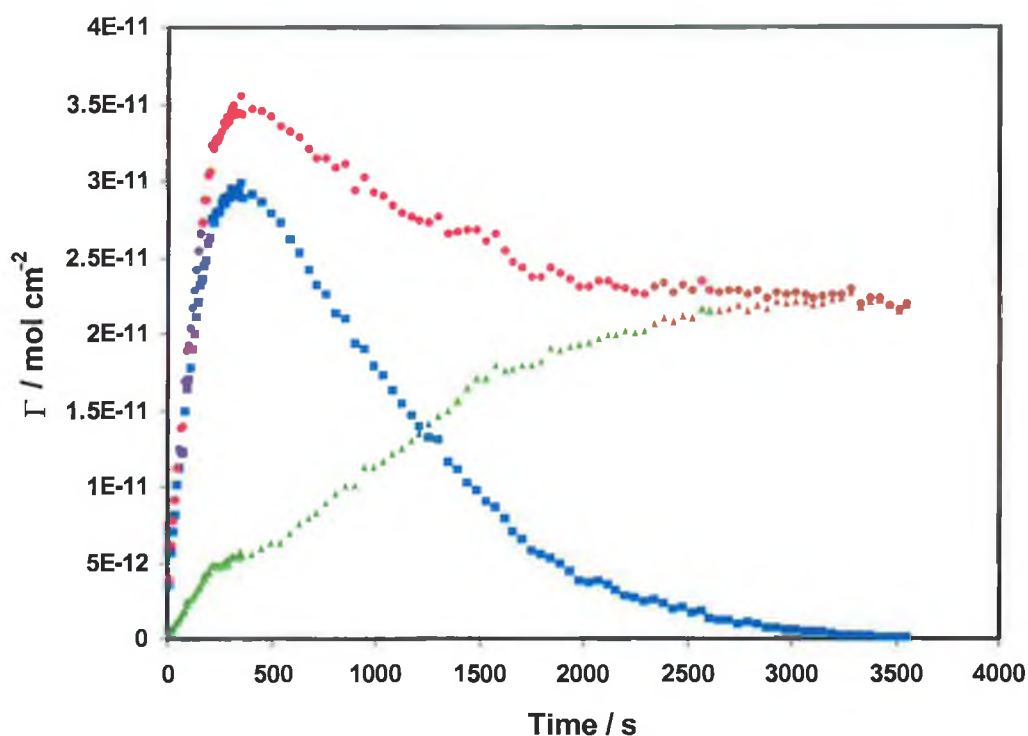


Figure 10. Surface coverage as a function of time for a 2 μM solution of 1,5-DMAQ in 1 M HClO_4 , initial adsorption and subsequent desorption at 0.132 V (\blacksquare), adsorption at 0.046 V (\blacktriangle), and the total surface coverage (\bullet) – sum of desorption and adsorption surface coverages at each time.

4.2.5.1 Initial Growth Kinetics – Process 1

As mentioned previously the voltammetric peak at 0.132 V is seen to increase rapidly in magnitude as the potential is scanned between potential limits of -0.5 and $+0.2$ V. Cyclic voltammograms were recorded every nine seconds and in the case of a 2 μM solution this initial adsorption came to an equilibrium response within five minutes. In the case of the 10 μM solution this initial adsorption step came to equilibrium within two minutes. A kinetic model originally proposed by Hubbard, Silin and Plant¹³ to model the formation of a monolayer of phospholipid from vesicles in solution onto a hydrophobic alkanethiol monolayer was fitted to the experimental data presented here. The model expresses the time-dependent surface concentration in terms of the maximum surface coverage of anthraquinone, the bulk concentration of the adsorbing species, bulk diffusion of the adsorbing species, and a surface reorganization rate constant. Using this model it was possible to deduce the extent to which monolayer

formation was controlled by kinetics (bulk diffusion) or thermodynamics (surface reorganization). The model may be expressed using Equation (1):

$$\Gamma(t) = \Gamma_{\text{mono}} \left[1 - \exp \left[\frac{-kC_0}{\Gamma_{\text{mono}}} \left[\frac{D}{k^2} \left(\exp \left[\frac{k^2 t}{D} \right] \operatorname{erfc} \left[\left(\frac{k^2 t}{D} \right)^{1/2} \right] - 1 \right) + \frac{2}{k} \left(\frac{Dt}{\pi} \right)^{1/2} \right] \right] \right] \quad (1)$$

where Γ_{mono} is the surface coverage associated with a dense monolayer, k is the apparent rate constant (cm s^{-1}), D is the bulk diffusion coefficient of the complex, t is the time in seconds and erfc is the complement of the error function. The apparent rate constant, k , incorporates a number of interfacial processes including the binding itself and surface diffusion. When $k^2/D \gg 1$, corresponding to instantaneous surface binding relative to diffusion, Equation (1) simplifies to the stretched exponential expression.

$$\Gamma(t) = \Gamma_{\text{mono}} \left[1 - \exp \left(\frac{-2C_0}{\Gamma_{\text{mono}}} \left(\frac{Dt}{\pi} \right)^{1/2} \right) \right] \quad (2)$$

However, if surface binding kinetics represent the rate determining step then first order behaviour is observed, as described by Equation (3) and the surface coverage increases exponentially over time.

$$\Gamma(t) = \Gamma_{\text{mono}} \left[1 - \exp \left(\frac{-kC_0 t}{\Gamma_{\text{mono}}} \right) \right] \quad (3)$$

The experimental data has been fit to Equations (2) and (3) using a Solver model in Microsoft Excel by naming the saturation surface coverage, diffusion coefficient and rate constant as variable parameters. The best fit was obtained by minimizing the sum of the squared residuals between the experimental values the values calculated using the equations above. A residual plot for both the diffusion and surface reorganization kinetic models is shown in the inset of Figures 11 and 12. From these plots it can be seen that the residuals of the surface reorganization kinetic model, (\blacksquare), are smaller than the diffusion model, (Δ). This would indicate that the model described using Equation (3) may provide the best fit to the experimental data for both the 2 and 10 μM data. However, diffusion may be important at shorter timescales on the basis of the following calculation. The two concentrations analysed were 2 and 10 μM , which yield equilibrium surface coverages of 4.5×10^{-11} and 1.1×10^{-10} mol cm^{-2} , respectively.

The depletion layer thickness may be determined by calculating the volume of the mercury drop and the volume of anthraquinone solution, which forms the depletion layer. This yields a value for the total volume and hence the outer radius of the sphere. The difference between this value and the radius of the mercury drop yields a value for the thickness of the depletion layer, δ . This value changes from 0.016 to 0.009 cm as the concentration changes from 2 to 10 μM . Assuming linear diffusion of electroactive species towards the electrode surface, the time taken for the diffusion process may be calculated using Equation (4):

$$t = \frac{\delta^2}{\pi D} \quad (4)$$

where δ is the film thickness and D is the diffusion coefficient of the electroactive species in solution. Scan rate dependent cyclic voltammetry of 1,5-DMAQ dissolved in solution indicates that D is $2.00 \times 10^{-6} \text{ cm}^2 \text{ s}^{-1}$. Therefore, the time taken for equilibrium surface coverage to be reached takes 40.7 and 12.9 seconds for the 2 and 10 μM solutions respectively. Repeating the calculation assuming linear diffusion of the anthraquinone to the electrode surface and dividing the concentration on the surface by the concentration in solution, the depletion layer thickness have been calculated as 0.023 and 0.011 for the 2 and 10 μM solutions, respectively. The timescale for the diffusion process decreases from 80.3 to 19.2 seconds. It can be seen from the experimental results in Figures 11 and 12 that it takes between 300 and 80 seconds for a dense monolayer to form, depending on the concentration of 1,5-DMAQ in the deposition solution. Therefore it is possible that the diffusional mass transport to the electrode surface is significant in the initial fast adsorption step, referred to as Process 1 in this chapter. The optimized parameters from the best fits of the experimental data to the diffusion model described in Equation (2) are listed in Tables 2 and 3 of this chapter. The predicted values of 6.22×10^{-5} and 5.71×10^{-5} s for the 2 and 10 μM solutions are larger than the experimentally measured value of $2.00 \times 10^{-6} \text{ cm}^2 \text{ s}^{-1}$. This is reflected in the fits illustrated in Figures 11 and 12, which show deviations between experimental and predicted data points.

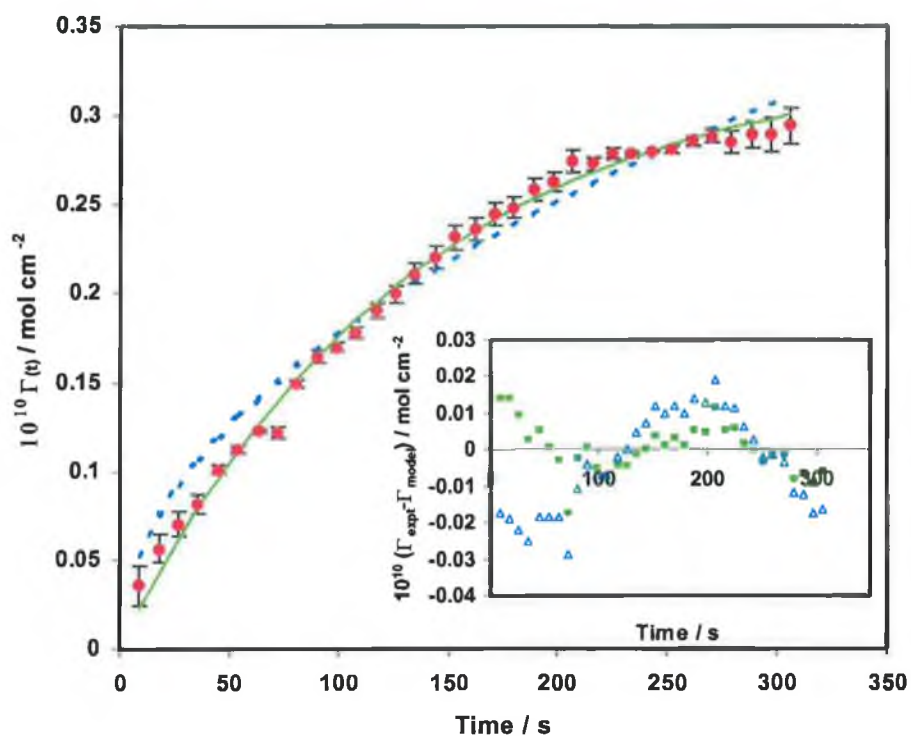


Figure 11. Evolution of the surface coverage of 1,5-DMAQ at a potential of 0.132 V adsorbed on a mercury electrode. The data points are experimental results for a 2 μM solution, the error bars represent data taken from three independently formed monolayers. The solid and dashed lines represent the best fits to the adsorption and diffusion models respectively. The inset shows the residuals for both the adsorption (\blacksquare) and diffusion (\triangle) models.

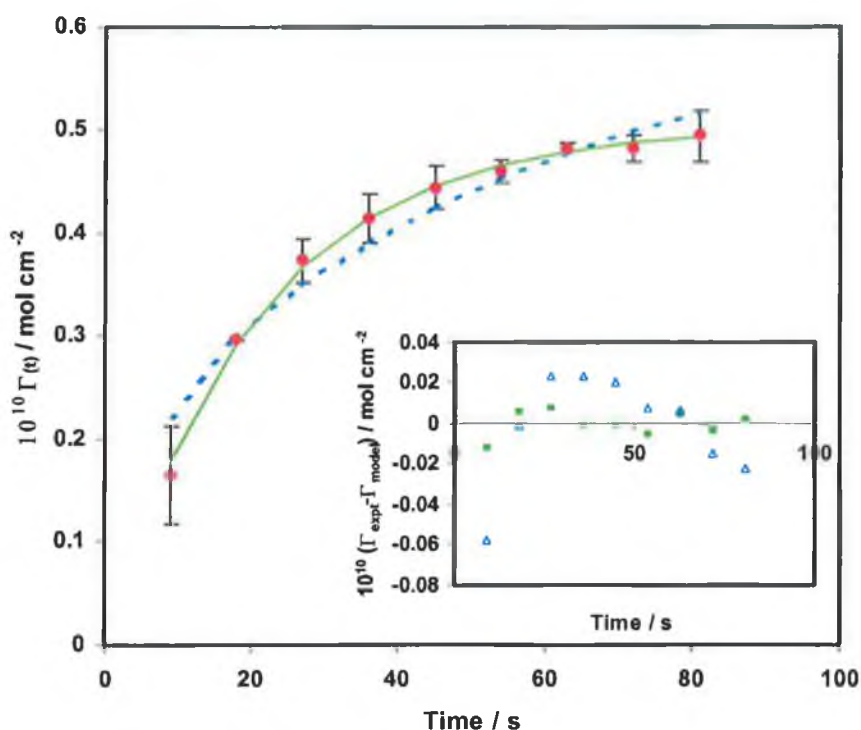


Figure 12. Evolution of the surface coverage of 1,5-DMAQ at a potential of 0.132 V adsorbed on a mercury electrode. The data points are experimental results for a 10 μM solution, the error bars represent data taken from three independently formed monolayers. The solid and dashed lines represent the best fits to the adsorption and diffusion models respectively. The inset shows the residuals for both the adsorption (\blacksquare) and diffusion (\triangle) models.

4.2.5.2 Interconversion Kinetics – Process 2A

Following the initial rapid adsorption of the peak at 0.132 V this peak was seen to decrease in magnitude and a subsequent increase in the peak at 0.046 V proceeded for times of 1-4 hours depending on the solution concentration of 1,5-DMAQ. The decrease in peak current at 0.132 V was fit to first and second order kinetic plots. The results for a 10 μM solution are presented below. The best fit was obtained from first order kinetics as the second order plot gives a curved response. The results for a 2 μM solution were the same, first order kinetics providing a significantly better fit to the data. These results suggest that the desorption process is mechanistically simple, in that the electroactive species in solution has no significant effect on the desorption rate. That 1,5-DMAQ desorption can be modeled using first order kinetics indicates that all

adsorption sites are equivalent, and lateral interaction between adsorbates is small. This is supported by the adsorption isotherm data presented earlier for 1,5-DMAQ as a single component monolayer. The Frumkin isotherm predicted an interaction parameter of +0.124, which implies only small repulsive interactions between adsorbates. The rate constants for the decrease in peak current, (Process 2A) at both concentrations are summarized in Tables 2 and 3, which follows a discussion of the kinetics of adsorption at 0.046 V. Processes 2A and 2B occur simultaneously and represent an interconversion mechanism.

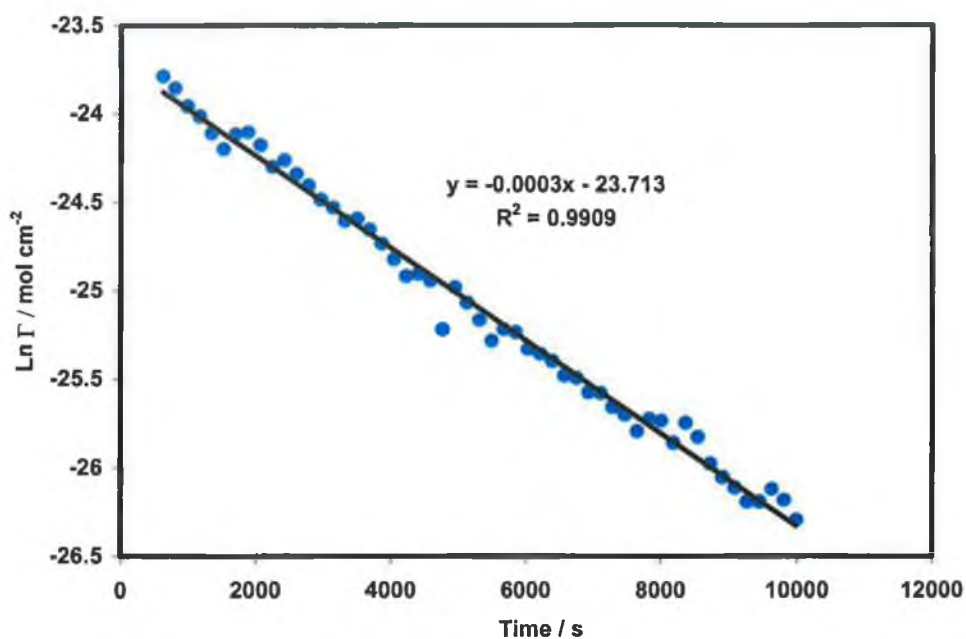


Figure 13. First order kinetic plot for desorption of 1,5-DMAQ at 0.132 V from a mercury electrode, the solution concentration of anthraquinone is 10 μM . The solution was made up in 70:30 % water:DMF with 1 M HClO_4 as the supporting electrolyte.

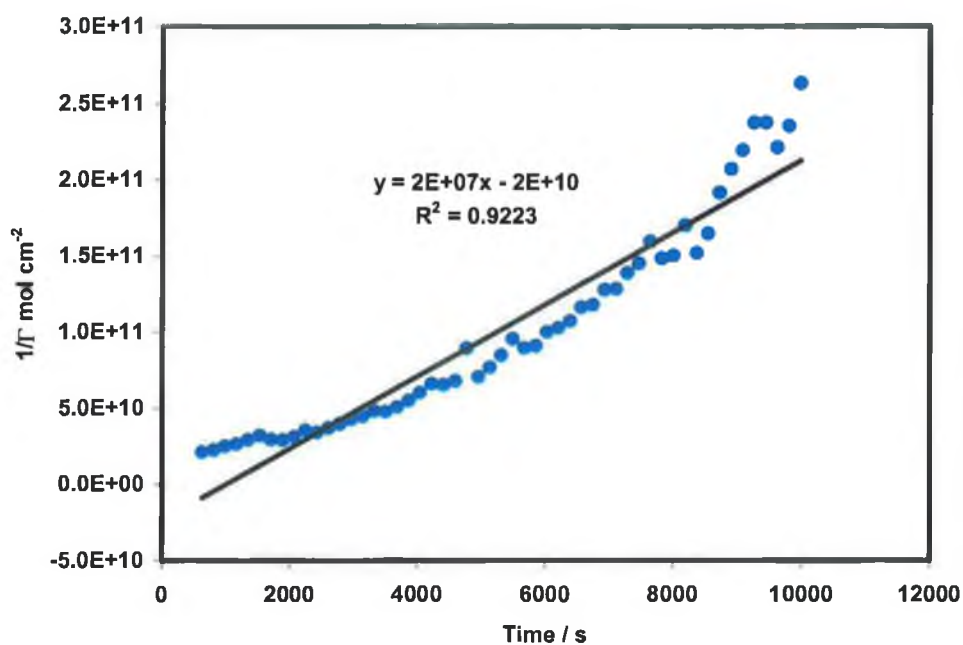


Figure 14. Second order kinetic plot for desorption of 1,5-DMAQ at 0.132 V from a mercury electrode, the solution concentration of anthraquinone is 10 μM . The solution was made up in 70:30 % water:DMF with 1 M HClO_4 as the supporting electrolyte.

4.2.5.3 Growth Kinetics – Process 2B

Similar to the results presented previously growth of the peak at 0.046 V has been fit to the diffusion and surface adsorption and reorganization models. The results for a 10 μM solution are presented in Figure 15. Both models provide a reasonable fit to the experimental points, however as before the adsorption model yields the best fit at all times. The residual plot for the diffusion model shows time dependent structure at shorter times and the optimized parameters obtained from this model are less accurate than those obtained from the adsorption model. As discussed previously diffusion processes would only play a significant role if monolayer formation reached equilibrium at short timescales. The results are the same when both models are fit to experimental data from a 2 μM solution. The optimized rate constants for the adsorption and interconversion processes 1, 2A and 2B are summarised in Tables 2 and 3.

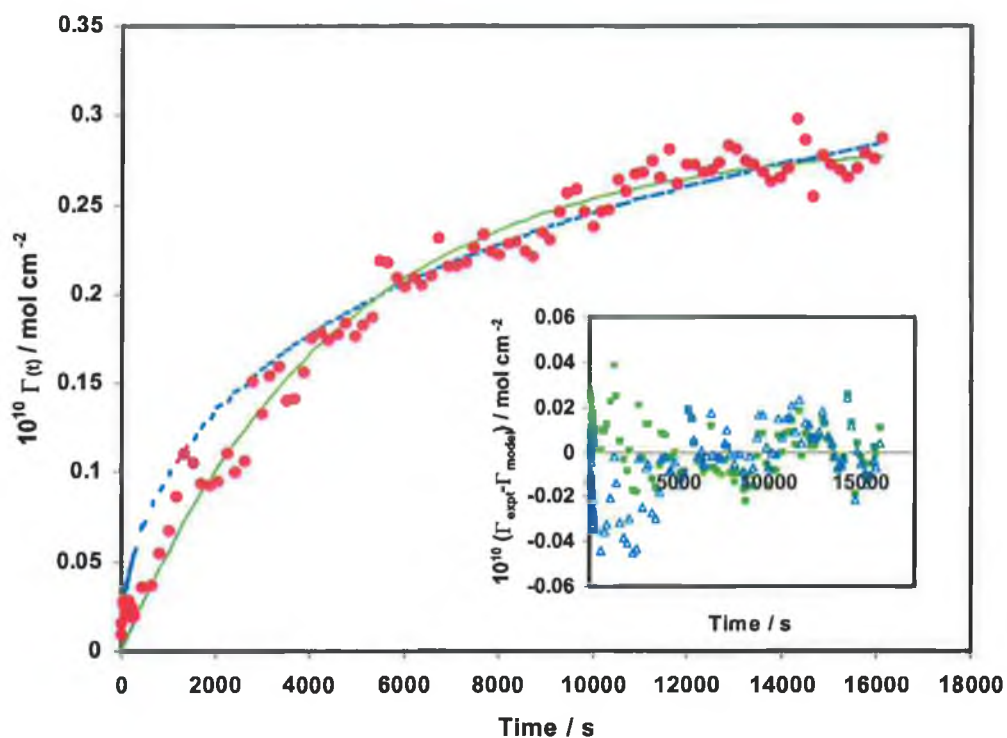


Figure 15. Evolution of the surface coverage of 1,5-DMAQ at a potential of 0.046 V adsorbed on a mercury electrode. The data points are experimental results for a 10 μM solution made up in 70:30 % water:DMF with 1 M HClO_4 as the supporting electrolyte. CVs were recorded starting the potential scan at -0.5 V. The solid and dashed lines represent the best fits to the adsorption and diffusion models respectively. The inset shows the residuals for both the adsorption (\square) and diffusion (Δ) models.

Table 2. Optimised parameters obtained from the surface binding and diffusion models for the adsorption of 1,5-DMAQ on a mercury electrode surface. The concentration of anthraquinone in solution is 2 μM .

	$\Gamma_{SAT} / \text{mol cm}^{-2}$	$k_{SB} / \text{cm s}^{-1}$	$K_{DIFF} / \text{cm s}^{-1}$
Initial Adsorption at 0.132 V Process 1	3.35×10^{-11}	1.25×10^{-3}	6.22×10^{-5}
Interconversion at 0.046 V Process 2A	–	1.50×10^{-3}	–
Adsorption at 0.046 V Process 2B	2.52×10^{-11}	8.64×10^{-5}	3.08×10^{-6}

Table 3. Optimised parameters obtained from the surface binding and diffusion models for the adsorption of 1,5-DMAQ on a mercury electrode surface. The concentration of anthraquinone in solution is 10 μM .

	$\Gamma_{SAT} / \text{mol cm}^{-2}$	$k_{SB} / \text{cm s}^{-1}$	$K_{DIFF} / \text{cm s}^{-1}$
Initial Adsorption at 0.132 V Process 1	5.03×10^{-11}	2.43×10^{-3}	5.71×10^{-5}
Interconversion at 0.046 V Process 2A	–	3.00×10^{-4}	–
Adsorption at 0.046 V Process 2B	3.86×10^{-11}	6.23×10^{-6}	1.00×10^{-7}

4.2.5.4 Mechanism of 1,5-DMAQ Adsorption

A mechanism by which 1,5-DMAQ adsorbs onto the mercury electrode surface to yield an equilibrium response is proposed in this section. The interconversion from a two-peak cyclic voltammetric response to one peak most likely arises from a reorganization of the adsorbates on the electrode surface. To explain the voltammetry presented in this work it is possible that 1,5-DMAQ initially adsorbs in a tilted or perpendicular orientation on the electrode surface. This is reflected in the initial rapid adsorption of the peak at 0.134 V, referred to as Process 1 in this chapter. Either of these conformations would result in less interaction with the electrode surface than would be attained if the anthraquinone adsorbed in a parallel orientation. Therefore, tilted or perpendicularly oriented molecules would be less stable and the molecules would reorient to a parallel conformation, prior to saturation coverage being achieved. This reorientation would result in the 1,5-DMAQ molecule forming a π -interaction with the mercury surface, which would lower the free energy and thus increase the stability of the system. This mechanism is displayed in Figure 16 with the parallel orientation energetically favoured over the perpendicular or tilted orientation by an amount ΔG . The initial adsorption at the more positive potential proceeds at a rate of $1.25 \times 10^{-3} \text{ cm s}^{-1}$ at low solution concentration and increases to $2.43 \times 10^{-3} \text{ cm s}^{-1}$ at high solution concentration. These values are not significantly different and show that the rate of adsorption is similar irrespective of solution concentration. The saturation surface coverage for Process 1 is greater than that obtained for Process 2B. This may be explained, as the saturation surface coverage for perpendicular oriented molecules would be significantly higher than that for a parallel orientation.

Anthraquinone derivatives have been reported to adsorb in a tilted or perpendicular conformation previously by Ramakrishnan and coworkers^{33,34,35} and Taniguchi and coworkers,³⁶ as discussed in Chapters 1 and 3 of this work. However, these studies dealt with the adsorption of anthraquinone derivative molecules onto silver and gold surfaces. Hence, no direct comparison may be made with the experimental work presented in this chapter, as the substrate used in this work was mercury.

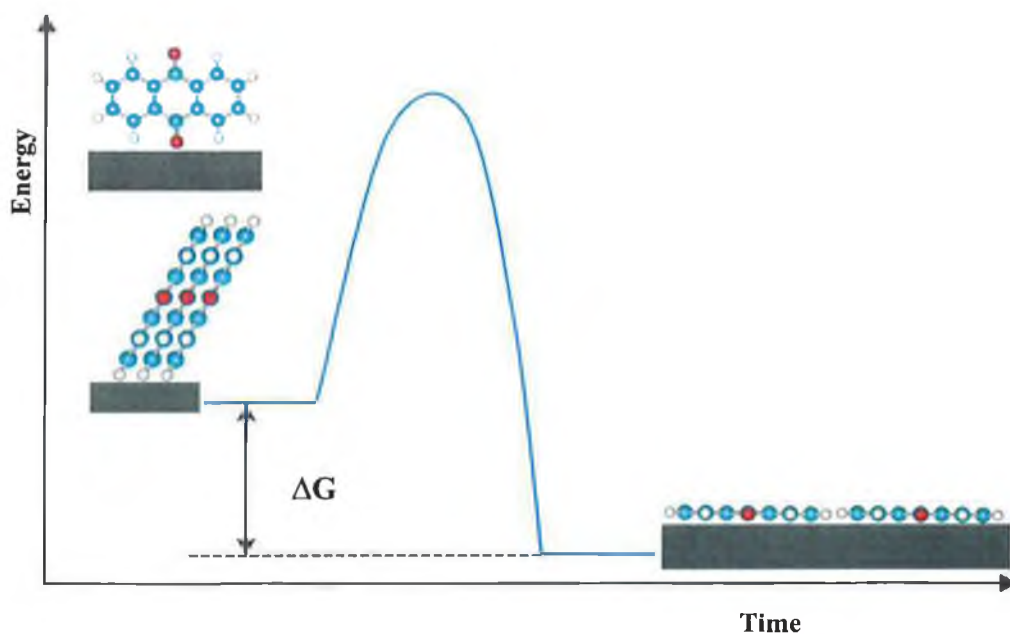


Figure 16. Energy level diagram demonstrating the difference in free energy of 1,5-DMAQ when adsorbed on a mercury electrode surface in three different orientations. The parallel orientation is energetically favoured over the tilted or perpendicular orientation by an amount ΔG .

In support of the mechanism proposed, the decrease of the voltammetric peak at 0.132 V and concurrent growth of the peak at 0.046 V, Processes 2A and B, is due to the tilted or perpendicularly oriented anthraquinone spontaneously reorienting into a parallel conformation. While the decrease in the voltammetric peak at 0.132 V proceeds over a long period of time the increase in the voltammetric response at 0.046 V comes to an equilibrium response faster, as saturation coverage for the parallel orientation is lower. Process 2A proceeds at a rate of $1.5 \times 10^{-3} \text{ cm s}^{-1}$ for a $2 \mu\text{M}$ solution, and decreases to $3.0 \times 10^{-4} \text{ cm s}^{-1}$ for a $10 \mu\text{M}$ solution. Process 2B is slower at high concentration also. One possible reason for these slower rates is that there are a larger number of adsorbates to reorient from tilted or perpendicular to parallel configuration when the solution concentration of 1,5-DMAQ is higher. Therefore, it takes longer for the adsorbates to reorient and the system to reach an equilibrium response.

4.2.6 Two Component Monolayers

Thus far it has been shown that the cyclic voltammetric response for 1,5-DMAQ and 1,2,4-AQASH follow the Frumkin adsorption isotherm when monolayers are formed independently. Also, with reference to Figure 1 the surface coverages obtained from deposition solutions containing 3 μM of both anthraquinones are comparable, i.e., $6.5 \pm 0.31 \times 10^{-11} \text{ mol cm}^{-2}$ for 1,5-DMAQ and $6.7 \pm 0.43 \times 10^{-11} \text{ mol cm}^{-2}$ for 1,2,4-AQASH. The values for the strength of adsorption, calculated from the Frumkin isotherm in the single component monolayers are similar, i.e., $3.44 \pm 0.21 \times 10^5 \text{ M}^{-1}$ and $4.89 \pm 0.24 \times 10^5 \text{ M}^{-1}$ for 1,5-DMAQ and 1,2,4-AQASH, respectively. Therefore, it is reasonable to expect that equimolar mixed solutions of 1,5-DMAQ and 1,2,4-AQASH would yield a monolayer in which the surface coverages of the two anthraquinones would be comparable. However, Figure 17 shows that 1,5-DMAQ is preferentially adsorbed onto the mercury surface when monolayers are formed from a mixed deposition solution. Cyclic voltammograms of a solution containing 0.5 μM 1,5-DMAQ and 5 μM 1,2,4-AQASH result in a sub-monomolecular film, where the surface coverage of 1,5-DMAQ is $1.8 \pm 0.2 \times 10^{-11} \text{ mol cm}^{-2}$ and the surface coverage of 1,2,4-AQASH is $1.7 \pm 0.3 \times 10^{-11} \text{ mol cm}^{-2}$. In order to study the thermodynamics of monolayer formation for mixed monolayers containing these two anthraquinone components a series of mixed deposition solutions was prepared. Analysis of the data allows the extent of interaction in these two component assemblies to be determined. The kinetics of monolayer formation were also modeled.

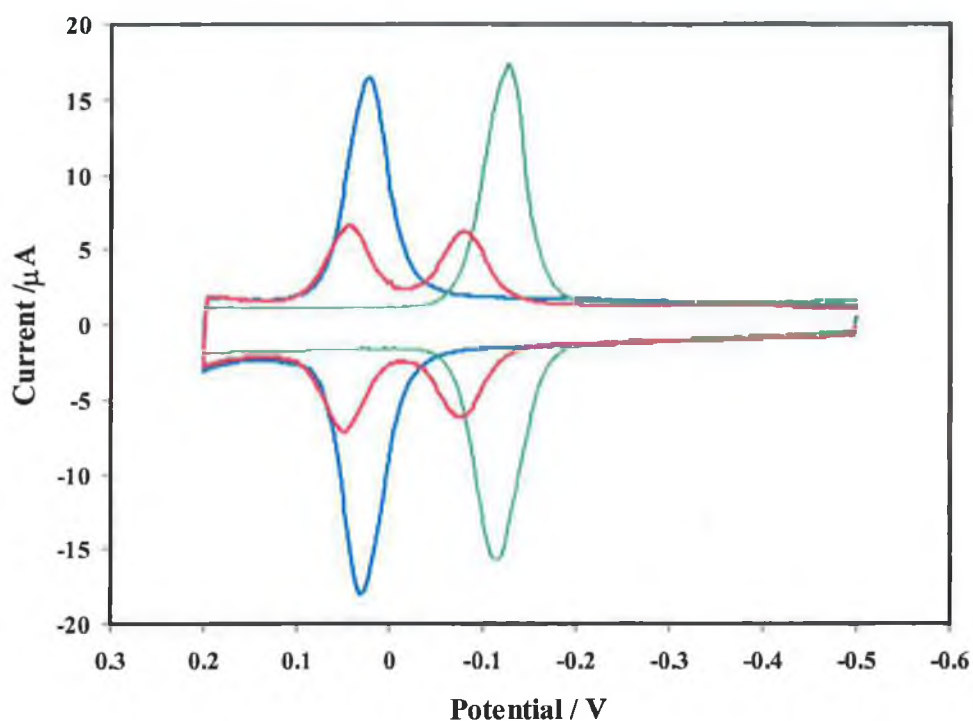


Figure 17. Cyclic voltammogram of a mercury electrode ($A = 0.014 \text{ cm}^2$) immersed in a solution containing $0.5 \text{ } \mu\text{M}$ 1,5-DMAQ and $5 \text{ } \mu\text{M}$ 1,2,4-AQASH (—) overlaid with the response obtained from a $3 \text{ } \mu\text{M}$ solution of 1,5-DMAQ (—) and $3 \text{ } \mu\text{M}$ solution of 1,2,4-AQASH (—). The solutions are 30:70 % v/v DMF:H₂O containing 1.0 M HClO₄ as the supporting electrolyte. The scan rate is 5 Vs^{-1} . Cathodic currents are up and anodic currents are down.

4.2.7 General EC Properties of Two Component Monolayers

Figure 17 displays the cyclic voltammetric response of 1,5-DMAQ and 1,2,4-AQASH when adsorbed on a mercury electrode surface from a mixed deposition solution. This may be compared to the response obtained when monolayers are formed from deposition solutions containing a single adsorbing species. The formal potentials are seen to shift in a positive potential direction when part of a two component system. 1,5-DMAQ shifts by $24 \pm 4 \text{ mV}$, while 1,2,4-AQASH shifts by $47 \pm 2 \text{ mV}$. The positive shift in both cases would indicate that both species are easier to reduce when part of a two component assembly.⁷ This result clearly contrasts with that obtained by Forster and O'Hanlon²⁸ when studying the electrochemistry of 2,7-AQDS and 1,4-AQCIOH as a two component assembly. In this study the formal potential of 1,4-AQCIOH was seen

to shift in a positive potential direction, however the formal potential of 2,7-AQDS shifted to a more negative potential, when part of a two component assembly. This would indicate that these two anthraquinones interacted laterally on the electrode surface through intermolecular hydrogen bonding interactions. 1,4-AQCIOH and 2,7-AQDS act as electron donors and acceptors respectively in this system.

The peak-to-peak separation for 1,5-DMAQ and 1,2,4-AQASH when part of a two component assembly is 5 ± 0.25 mV and 3 ± 0.21 mV, respectively. These values show little variation from the single component results, which were discussed in Section 4.2.1 of this chapter. The voltammetric peak waves exhibit full width at half maximum (FWHM) values of 49.5 ± 1.83 mV for 1,5-DMAQ and 59.0 ± 2.04 mV for 1,2,4-AQASH. These values are both larger than the theoretical value of 45.3 mV for a reaction that involves the transfer of two electrons.^{25,26,37} The larger FWHM values compared to the expectations suggest that destabilising repulsive interactions exist between adsorbates on the electrode surface.

4.2.8 Competitive Adsorption

The adsorption thermodynamic results presented in Section 4.2.3 of this chapter for single component monolayers of 1,5-DMAQ and 1,2,4-AQASH suggest that interactions exist between dissimilar adsorbates on the electrode surface. 1,5-DMAQ molecules undergo small repulsive interactions ($g = +0.124$), while 1,2,4-AQASH molecules undergo attractive interactions ($g = -0.529$). In this section the competitive Frumkin isotherm^{18,38,39} is fit to adsorption data from mixed deposition solutions. This adsorption isotherm allows a determination of the extent of interaction between like molecules and also takes into account the interaction of two different molecules with each other, i.e., the magnitude of interaction between 1,5-DMAQ and 1,2,4-AQASH adsorbates. Equations (5) and (6) describe the competitive adsorption of the two anthraquinone species, i and j , present in solution according to:

$$\beta_i C_i = \frac{\theta_i}{1 - \theta_i - \theta_j} \exp(g_{i,i}\theta_i + g_{i,j}\theta_j) \quad (5)$$

$$\beta_j C_j = \frac{\theta_j}{1 - \theta_j - \theta_i} \exp(g_{j,j}\theta_j + g_{i,j}\theta_i) \quad (6)$$

where i and j are 1,5-DMAQ and 1,2,4-AQASH adsorbates, respectively. The interaction parameters g_{ii} and g_{jj} represent interactions between similar adsorbates, while g_{ij} represents interactions between dissimilar adsorbates. As previously stated, a series of mixed solutions was investigated. Due to the fact that 1,5-DMAQ adsorbs to a much greater extent than 1,2,4-AQASH it was important that the response obtained was representative of a binary system. In order to ensure this, the concentration of 1,2,4-AQASH was always in excess of 1,5-DMAQ and the surface coverage of the minor component was at least 10 % of a dense monolayer. Table 4 contains details of the results obtained from 15 mixed deposition solutions of 1,5-DMAQ and 1,2,4-AQASH. This set of data provides a wide range of concentrations and surface coverages required to give a true representation of the competitive adsorption observed in this two component system.

Table 4. Concentrations of 1,5-DMAQ and 1,2,4-AQASH in mixed monolayer systems with corresponding surface coverages.

DMAQ Conc. / μM	Γ / mol cm^{-2}	AQASH Conc. / μM	Γ / mol cm^{-2}
0.1	3.70×10^{-12}	2.5	1.41×10^{-11}
0.2	8.12×10^{-12}	2.5	1.63×10^{-11}
0.5	1.22×10^{-11}	2.5	1.19×10^{-11}
0.5	1.96×10^{-11}	5	1.67×10^{-11}
0.5	1.60×10^{-11}	7.5	1.03×10^{-11}
0.7	2.16×10^{-11}	20	2.89×10^{-11}
0.8	2.61×10^{-11}	10	2.11×10^{-11}
1	1.89×10^{-11}	5	8.13×10^{-11}
1	2.70×10^{-11}	10	1.02×10^{-11}
1	2.90×10^{-11}	15	1.54×10^{-11}
1	2.57×10^{-11}	20	1.96×10^{-11}
1	2.50×10^{-11}	40	2.36×10^{-11}
2	2.98×10^{-11}	20	1.74×10^{-11}
2.5	5.40×10^{-11}	15	1.15×10^{-11}
3	2.11×10^{-11}	15	1.20×10^{-11}

Table 5. Saturation surface coverages, adsorption coefficients and Frumkin interaction parameters for monolayers of 1,5-DMAQ and 1,2,4-AQASH as single and two component assemblies.

	Frumkin – Single Component	Frumkin – Two Component
$\Gamma_{\text{SAT, DMAQ}} / \text{mol cm}^{-2}$	$1.43 \pm 0.08 \times 10^{-10}$	$1.19 \pm 0.05 \times 10^{-10}$
$\Gamma_{\text{SAT, AQASH}} / \text{mol cm}^{-2}$	$9.44 \pm 0.15 \times 10^{-11}$	$8.89 \pm 0.22 \times 10^{-11}$
$\beta_{\text{DMAQ}} / \text{M}^{-1}$	$3.44 \pm 0.12 \times 10^5$	$3.60 \pm 0.09 \times 10^5$
$\beta_{\text{AQASH}} / \text{M}^{-1}$	$4.89 \pm 0.11 \times 10^5$	$2.72 \pm 0.07 \times 10^4$
g_{DMAQ}	+ 0.124	+ 0.012
g_{AQASH}	- 0.529	+ 0.010
$g_{\text{DMAQ, AQASH}}$		+ 0.441 \pm 0.024

By fitting the data presented in Table 4 to Equations (5) and (6) the theoretical Frumkin concentration of 1,5-DMAQ (C_i) and 1,2,4-AQASH (C_j) may be determined for each experimental concentration, where $\theta_i = \Gamma_i/\Gamma_{\text{sat}}$. A solver model was set up in Microsoft Excel where Γ_{sat} , g_{ii} , g_{jj} , g_{ij} , β_i and β_j were named as variables. This model was run to minimise the sum of square residuals between the experimental concentrations and the values generated using the competitive Frumkin adsorption isotherm. If the model fits the experimental data accurately a plot of the C_{expt} versus C_{theory} for both 1,2,4-AQASH and 1,5-DMAQ should have a slope of 1. Table 5 contains the saturation surface coverages of both anthraquinone derivatives within the two component monolayers and the three interaction parameters as determined from the concentration dependence of the experimental surface coverages using nonlinear optimization techniques. Figure 18 illustrates the correlation between the theoretical surface coverages obtained using these parameters and those measured experimentally. For both anthraquinones, the

theoretical and experimental concentrations agree closely with a correlation coefficient of 0.9944. Hence, the competitive Frumkin isotherm provides a satisfactory fit to the experimental data.

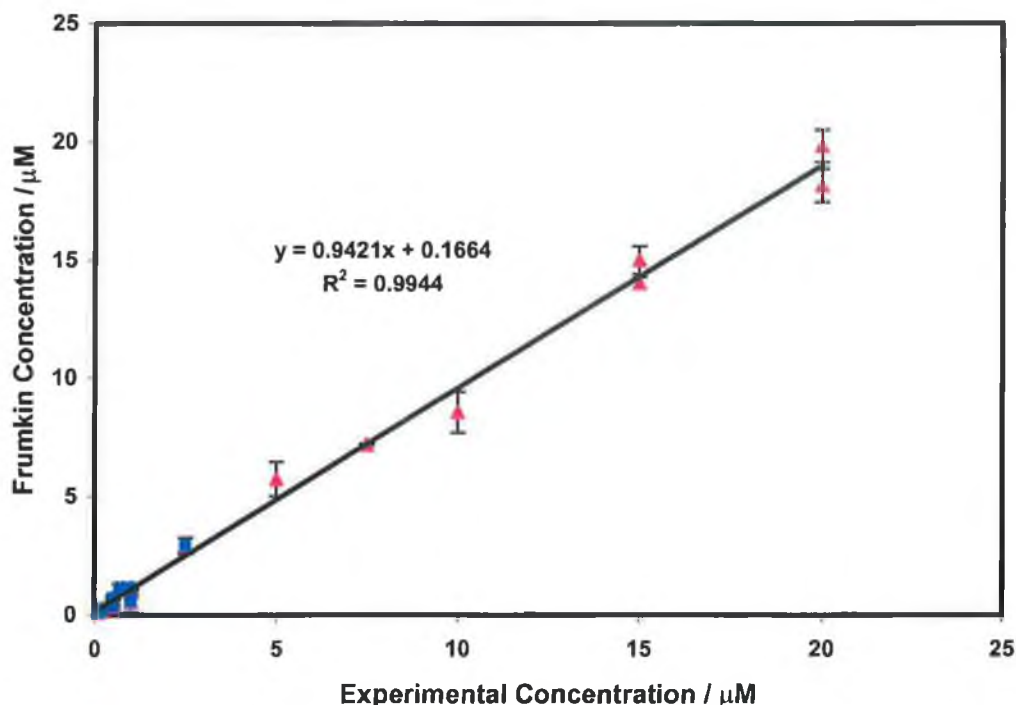


Figure 18. Ability of the competitive Frumkin isotherm to predict the experimental concentrations of 1,5-DMAQ (■) and 1,2,4-AQASH (▲) within two component monolayers.

Table 5, which outlines the difference between single and two component systems yields the following conclusions. In the two component assembly the saturation coverages of both anthraquinones are different to those in single component monolayers. $\Gamma_{\text{sat}, 1,5\text{-DMAQ}}$ decreases from $1.43 \pm 0.08 \times 10^{-10}$ to $1.19 \pm 0.05 \times 10^{-10}$ mol cm^{-2} , while $\Gamma_{\text{sat}, 1,2,4\text{-AQASH}}$ decreases from $9.44 \pm 0.15 \times 10^{-11}$ to $8.89 \pm 0.22 \times 10^{-11}$ mol cm^{-2} on going from single to two component monolayers. When the two anthraquinones adsorb competitively onto the electrode surface, the adsorption coefficient of 1,5-DMAQ increases from $3.44 \pm 0.12 \times 10^5$ to $3.60 \pm 0.09 \times 10^5$ M^{-1} while the adsorption coefficient of 1,2,4-AQASH decreases from 4.89 ± 0.11 to $2.72 \pm 0.07 \times 10^4$ M^{-1} . This confirms the preferential adsorption of 1,5-DMAQ in two component systems. The Frumkin parameters also provide an insight into the nature

and strength of interactions that exist between both like and unlike adsorbates. The interaction parameters describing self interactions, $g_{1,5\text{-DMAQ}} (g_{ii})$ and $g_{\text{AQASH}} (g_{ij})$ are low; 0.012 and 0.010. These interaction parameters correspond to interaction energies of 0.013 and 0.014 kJ mol⁻¹. However, the interaction parameter between unlike molecules, $g_{1,5\text{-DMAQ}, 1,2,4\text{-AQASH}} (g_{ij})$ is $+ 0.441 \pm 0.024$ indicating that significant repulsive interactions¹⁸ exist between 1,5-DMAQ and 1,2,4-AQASH adsorbates. This value corresponds to an interaction energy of 0.443 kJ mol⁻¹. These interactions cannot take the form of hydrogen bonding interactions in this mixed monolayer system as the forces between the adsorbates are repulsive. The interactions may take the form of electrostatic repulsion between adsorbed moieties.

The general electrochemical properties of mixed monolayer systems together with the competitive adsorption isotherm fits can provide information as to the final arrangement of adsorbates in the monomolecular film when equilibrium is reached. Scheme 2 illustrates two possible scenarios, (A) where adsorption results in a random distribution of 1,2,4-AQASH and 1,5-DMAQ molecules, and (B) where 1,2,4-AQASH and 1,5-DMAQ molecules separate into two domains. In the system under investigation in this chapter the mechanism illustrated in Scheme 2(B) describes the data more accurately. The interaction parameters for like adsorbates, g_{ii} and g_{jj} are very small, 0.012 and 0.010, respectively. These interaction parameters are so small that they can be considered to be negligible. The interaction parameter for unlike adsorbates, g_{ij} is +0.441, which implies repulsive interactions between adsorbates. Therefore, the parameter which determines the structure of mixed monolayers is the repulsive interaction between unlike adsorbates. The monolayer will segregate into two domains as illustrated in Scheme 2(B).

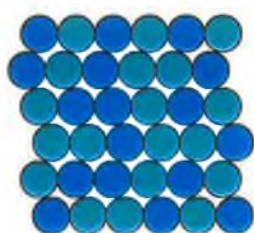
Scheme 2. Schematic illustrating two possible mixed monolayer states that could be obtained after reaching equilibrium. (A) randomly mixed monolayer, and (B) phase separated mixed monolayer.

● = 1,2,4-AQASH

● = 1,5-DMAQ

(A)

(B)



4.2.9 Adsorption Dynamics in Two Component System

When 1,5-DMAQ and 1,2,4-AQASH adsorb onto the mercury electrode surface from a mixed deposition solution, a short period of time is required for an equilibrium response to be established. This adsorption process has been monitored for all the mixed deposition solutions used to model the thermodynamics of adsorption in the previous section of this chapter. The cyclic voltammetry data for a solution containing $1 \mu\text{M}$ 1,5-DMAQ and $15 \mu\text{M}$ 1,2,4-AQASH is displayed in Figure 19. Initially the two components are seen to spontaneously adsorb onto the mercury surface. Following this initial adsorption step the voltammetric peak for 1,5-DMAQ increases in magnitude and the response for 1,2,4-AQASH shows a concurrent decrease. The rate of increase is proportional to the rate of decrease as illustrated in Figure 20.

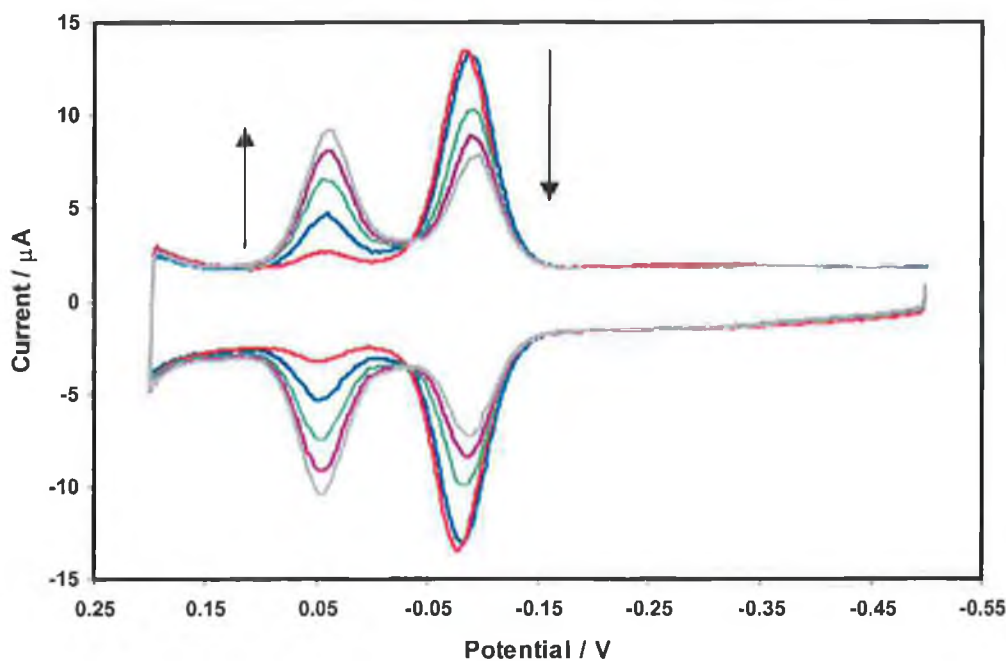


Figure 19. Cyclic voltammetry response of a mercury electrode immersed in a deposition solution containing $1 \mu\text{M}$ 1,5-DMAQ and $15 \mu\text{M}$ 1,2,4-AQASH. Cyclic voltammograms were measured at times of 0 (—), 45 (—), 90 (—), 135 (—) and 180 seconds (—) leading to equilibrium coverage. The arrows show the direction of peaks with successive scans.

It is evident from Figure 19 that the voltammetric curves for 1,5-DMAQ and 1,2,4-AQASH, taken at various stages of the adsorption process have a common crossing point at -0.036 ± 0.003 V. This well defined point is known as an isopotential point and can only occur in a series of current-potential curves at an electrode when the potential scanning program is the same for all experimental run; such is the case here. Bruckenstein et al.⁴⁰ and Wasberg⁴¹ propose that a common intersection point in current-potential curves occurs when the two electroactive species adsorb to a different extent initially. The electrode behaves as if it consists of two independent electrochemical regions. As time proceeds one adsorbate is displaced by the other, but the total surface coverage remains constant at all times. This mechanism explains the experimental data in two component monolayers of 1,5-DMAQ and 1,2,4-AQASH, as illustrated in Figure 20 below. Similar adsorption kinetic behaviour has been reported by Tirado and Abruna,⁷ when studying self assembling monolayers based on transition metal complexes of osmium and ruthenium.

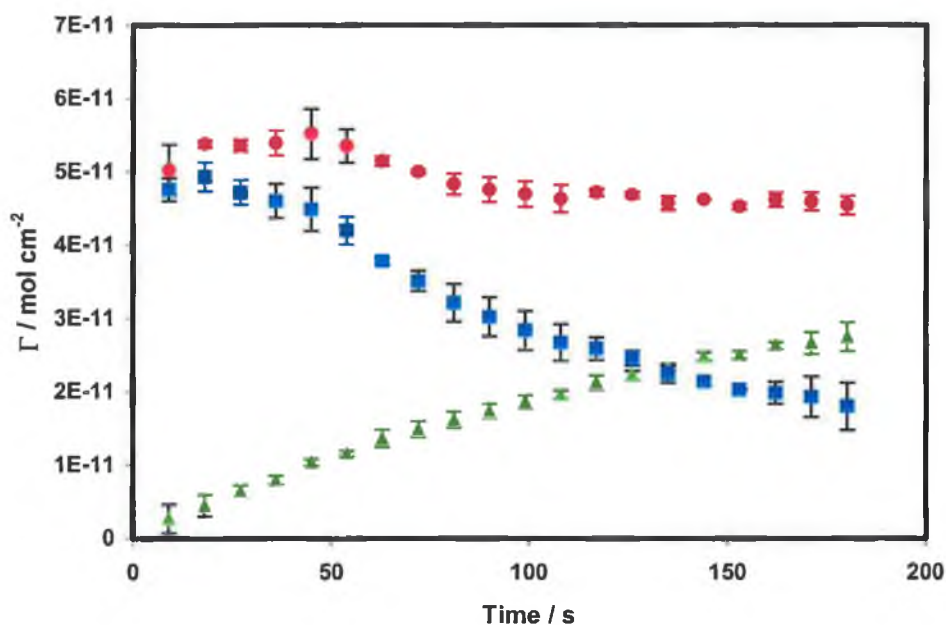


Figure 20. Surface coverage as a function of time for a deposition solution containing $1 \mu\text{M}$ 1,5-DMAQ and $15 \mu\text{M}$ 1,2,4-AQASH, made up in 70:30 % water:DMF containing 1 M HClO_4 as the supporting electrolyte. (■) and (▲) represent the desorption and adsorption of 1,2,4-AQASH and 1,5-DMAQ respectively, and (●) is the sum of the desorption and adsorption surface coverages at each time.

The exchange dynamics presented for the two component assembly have been modeled to determine the rates of adsorption and desorption in this system. The desorption of the voltammetric peak due to 1,2,4-AQASH follows first order kinetics, as illustrated in Figure 21. The rate constant for this desorption process is $6.4 \times 10^{-3} \text{ s}^{-1}$.

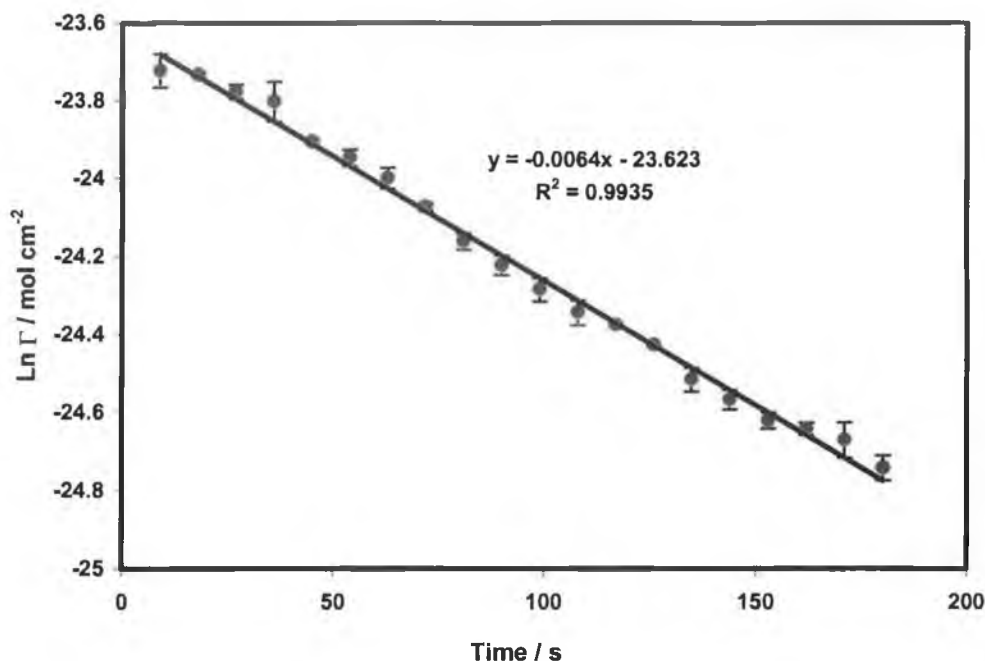


Figure 21. First order kinetic plot for the desorption of 1,2,4-AQASH from a mercury electrode surface. The deposition solution contains $1 \mu\text{M}$ 1,5-DMAQ and $15 \mu\text{M}$ 1,2,4-AQASH. Solutions were prepared in 70:30 % water:DMF with 1.0 M HClO_4 as the supporting electrolyte.

Adsorption of 1,5-DMAQ was fitted using the same model used to explain the adsorption process of 1,5-DMAQ as a single component monolayer. This model accommodates two limiting cases, one where diffusion of the electroactive species is the rate limiting step and the second where adsorption and surface reorientation at the electrode surface is rate limiting. The best fits obtained from both models are presented in Figure 22. The model, which adequately described the experimental data over the time period investigated was the surface reorganisation model. The optimized parameters generated using this model predicted a value of $4.02 \times 10^{-11} \text{ mol cm}^{-2}$ for

saturation coverage of 1,5-DMAQ and a value of $2.53 \times 10^{-3} \text{ cm s}^{-1}$ for the kinetics of surface binding and reorganization.

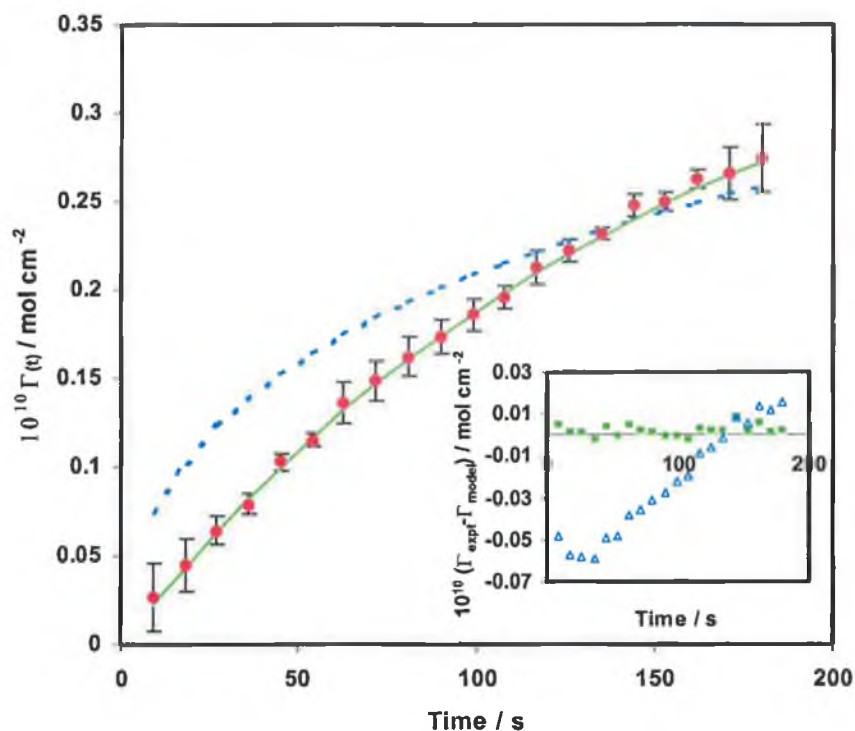


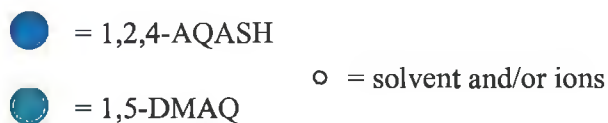
Figure 22. Evolution of the surface coverage of 1,5-DMAQ from a deposition solution containing $1 \mu\text{M}$ 1,5-DMAQ and $15 \mu\text{M}$ 1,2,4-AQASH. Solutions were prepared in 70:30 % water:DMF with 1.0 M HClO_4 as the supporting electrolyte. The data points are experimental results for a 1,5-DMAQ, with error bars representing data taken from three independently formed monolayers. The solid and dashed lines represent the best fits to the adsorption and diffusion models respectively. The inset shows the residuals for both the adsorption (\blacksquare) and diffusion (\triangle) models.

4.2.9.1 Mechanism of Monolayer Formation

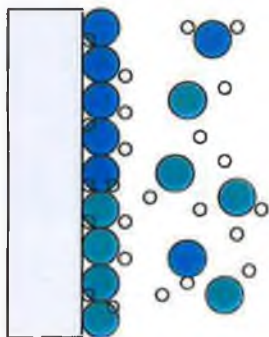
Having investigated the general electrochemical properties of the binary monolayer system and the kinetics, which lead to an equilibrium response a mechanism for the formation of a monomolecular film can be proposed. Scheme 2 proposed the equilibrium structure of mixed monolayers of 1,5-DMAQ and 1,2,4-AQASH. Adsorbates are segregated on the electrode surface with preferential interaction between dissimilar adsorbates, this is reflected in the interaction parameter, g_{ij} , $+0.441 \pm 0.024$, implying repulsive interactions between adsorbates. The mechanism, which leads to equilibrium coverage is displayed in Scheme 3 and proceeds as follows:

1. 1,5-DMAQ and 1,2,4-AQASH spontaneously adsorb onto mercury from a mixed deposition solution and attain maximum surface coverage for the concentration present in solution.
2. As time proceeds 1,2,4-AQASH spontaneously desorbs from the electrode surface at a rate of $6.4 \times 10^{-3} \text{ cm s}^{-1}$. Desorption follows first order kinetics. 1,2,4-AQASH desorbs because this anthraquinone derivative is less strongly bound to the electrode surface than 1,5-DMAQ in a two component assembly. The adsorption coefficients for 1,2,4-AQASH and 1,5-DMAQ are $2.72 \pm 0.07 \times 10^4$ and $3.60 \pm 0.09 \times 10^5$, respectively.
3. As surface sites become available 1,5-DMAQ adsorbs on the electrode surface at a rate of $2.53 \times 10^{-3} \text{ cm s}^{-1}$.
4. It is evident from the results that the rate of desorption is slightly faster than the rate of adsorption. This may be due to species in solution weakly associating with 1,2,4-AQASH on the electrode surface, thus enhancing the rate at which this anthraquinone desorbs from the surface. However, this association between species in solution and adsorbates on the electrode surface would have to be to a very small extent, as the total surface coverage remains constant over the time period analysed. The system is at equilibrium at all times, as illustrated in Figure 20. Desorption kinetics of 1,2,4-AQASH were also accurately modelled by a first order rate law, indicating that electroactive species in solution do not contribute to the desorption mechanism.

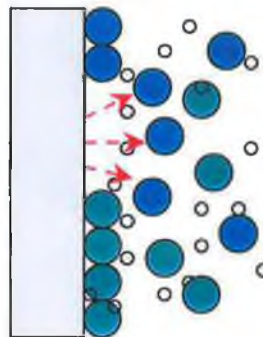
Scheme 3. Proposed mechanism for the desorption of 1,2,4-AQASH and simultaneous adsorption of 1,5-DMAQ onto a mercury electrode surface from a mixed deposition solution. Step (A) is rapid, steps (B) and (C) are transition states which occur simultaneously, thus maintaining Γ constant at all times; step (D) shows the system when equilibrium surface coverage is reached.



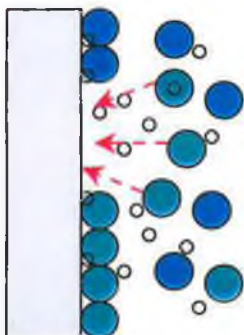
(A) 1,2,4-AQASH and 1,5-DMAQ spontaneously adsorb on mercury.



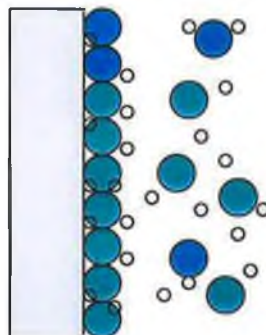
(B) 1,2,4-AQASH spontaneously desorbs.



(C) 1,5-DMAQ adsorbs from solution.



(D) Equilibrium surface coverage of mixed monolayer.



4.3 Conclusions

The first section of this chapter focused on the electrochemical properties of 1,2,4-AQASH, which spontaneously adsorb on the surface of a mercury electrode. Fitting the experimental data to the Langmuir and Frumkin isotherms, as in the previous chapter revealed that the Frumkin isotherm provided a better fit. It is interesting to note the effect of the presence of 30 % DMF in the deposition solution on the adsorption parameters of 1,2,4-AQASH. The adsorption coefficient, β decreases considerably from that observed when adsorption is carried out from deposition solutions made up in distilled water. This decrease is thought to be due to a decrease in the strength of hydrophobic interaction of the organic molecule with the mercury surface in the presence of DMF. In all other aspects the electrochemistry of 1,2,4-AQASH was similar to that reported in Chapter 3.

The adsorption kinetics of 1,5-DMAQ, which leads to an equilibrium surface coverage was looked at in detail in this chapter. The experimental data was fit to a number of models, including 1st and 2nd order, diffusion and adsorption. The change in the cyclic voltammetric response over time is thought to be due to reorganization of adsorbates on the electrode surface. The anthraquinone molecules reorient from a perpendicular or tilted conformation to a parallel conformation. This orientation maximizes the interaction of 1,5-DMAQ molecules with the mercury surface and thus the overall stability of the system.

The latter part of this chapter dealt with the investigation of two component anthraquinone monolayers adsorbed on mercury. The two adsorbates were seen to interact laterally, and this interaction was modeled using the competitive Frumkin isotherm. This allowed a determination of the extent of interaction between similar and dissimilar adsorbates. Co-adsorption was seen to have a significant effect on the strength of adsorption of the two molecules also. 1,5-DMAQ was seen to be preferentially adsorbed from mixed deposition solutions. This result was confirmed by the optimized parameters obtained from the competitive Frumkin isotherm. Also based on the cyclic voltammetric response it is believed that mixed monolayers segregate into two phases, rather than random distribution of adsorbates on the electrode surface.

The kinetics of monolayer formation were modeled. 1,2,4-AQASH spontaneously desorbs from the electrode surface and 1,5-DMAQ adsorbs on the available surface area. The desorption kinetics were modeled by a first order process, while the kinetics of surface binding and reorganization best described the adsorption of 1,5-DMAQ.

4.4 References

1. Soriaga, M.P., Hubbard, A.T., *J. Am. Chem. Soc.*, **1982**, 104, 2735.
2. Soriaga, M.P., Hubbard, A.T., *J. Am. Chem. Soc.*, **1982**, 104, 2742.
3. Soriaga, M.P., Hubbard, A.T., *J. Am. Chem. Soc.*, **1982**, 104, 3937.
4. Soriaga, M.P., Hubbard, A.T., *J. Phys. Chem.*, **1984**, 88, 1089.
5. Soriaga, M.P., Soriaga, E.B., Hubbard, A.T., Benziger, J.B., Pang, K.-W.P., *Inorg. Chem.*, **1985**, 24, 65.
6. Chen, S., Abruna, H.D., *J. Phys. Chem.*, **1995**, 99, 17235.
7. Tirado, J.D., Abruna, H.D., *J. Phys. Chem.*, **1996**, 100, 4556.
8. Forster, R.J., O'Kelly, J.P., *Langmuir*, **2000**.
9. Bretz, R.L., Abruna, H.D., *J. Electroanal. Chem.*, **1996**, 408, 199.
10. Bretz, R.L., Abruna, H.D., *J. Electroanal. Chem.*, **1995**, 388, 123.
11. Kuan, W-H., Lo, S-L., Chang, C.M., Wang, M.K., *Chemosphere*, **2000**, 41, 1741.
12. Ulman, A., Kang, J.F., Shnidman, Y., Liao, R.J., Jordan, R., Choi, G-Y., Zaccaro, J., Myerson, A.,S., Rafailovich, M., Sokolov, J., Fleischer, C., *Reviews in Molecular Biotechnology*, **2000**, 74, 175.
13. Hubbard, J.B., Silin, V., Plant, A.L., *Biophysical Chemistry*, **1998**, 75, 163.
14. Chidsey, C.E.D., Bertozzi, C.R., Putvinski, T.M., Mujsce, A.M., *J. Am. Chem. Soc.*, **1990**, 112, 4301.
15. Chidsey, C.E.D., *Science*, **1991**, 251, 919.
16. Forster, R.J., Faulkner, L.R., *Anal. Chem.*, **1995**, 67, 1232.
17. Forster, R.J., *Langmuir*, **1995**, 11, 2247.
18. Bard, A.J., Faulkner, L.R., *Electrochemical Methods : Fundamentals and Applications, Second Edition*, Wiley, New York, **2001**.
19. Brett, C.M.A.; Brett, A.M.O.; *Electroanalysis*; Oxford Science Publications.
20. Ta, T.C., Kanda, V., McDermott, M.T., *J. Phys. Chem.*, **1999**, 8, 1295.
21. Katz, E., Willner, I., *Langmuir*, **1997**, 13, 3364.
22. Sato, Y., Fujita, M., Mizutani, F., Uosaki, K., *J. of Electroanal. Chem.*, **1996**, 409, 145.
23. Forster, R.J., *The Analyst*, **1996**, 121, 733.
24. He, P., Crooks, R.M., Faulkner, L.R., *J. Phys. Chem.*, **1990**, 94, 1135
25. Wopschall, R. H., Shain, I., *Anal. Chem.*, **1967**, 39, 1514.

26. Laviron, E., *J. Electroanal. Chem.*, **1974**, 52, 395.
27. Forster, R.J., Keyes, T.E., Farrell, M., O'Hanlon, D., *Langmuir*, **2000**, 16, 9871.
28. O'Hanlon, D., Forster, R.J., *Langmuir*, **2000**, 16, 702.
29. O'Kelly, J.P., Forster, R.J., *The Analyst*, **1998**, 123, 1987.
30. Forster, R.J., *J. Electroanal. Chem.*, **1997**, 144, 1165.
31. Forster, R.J., *Anal. Chem.*, **1996**, 68, 3143.
32. Schreiber, F., *Progress in Surface Science*, **2000**, 65, 151.
33. Jayaraj, S.E., Ramakrishnan, V., *Spectrochimica Acta*, **1995**, 51A, 979.
34. Ramaakrishnan, V., Krishnamurthy, Gurunathan, M., Srivatsavoy, V.J.P., *Spectrochimica Acta*, **1990**, 46A, 1615.
35. Umadevi, M., Ramakrishnan, V., *Spectrochimica Acta*, **2002**, in press.
36. Nishiyama, K., Tahara, S., Uchida, Y., Tanoue, S., Taniguchi, I., *J. of Electroanal. Chem.*, **1999**, 478, 83.
37. Brown, A. P. Anson, F. C., *Anal. Chem.* 1977, 49, 1589.
38. Ruthven, D., *Principles of Adsorption and Adsorption Processes*, John Wiley & Sons, **1984**.
39. Adamson, A.W., Gast, A.P., *Physical Chemistry of Surfaces*, John Wiley & Sons, **1997**.
40. Untereker, D.F., Bruckenstein, S., *Anal. Chem.*, **1972**, 6, 1009.
41. Wasberg, M, *J. of Electroanal. Chem.*, **1994**, 379, 541.

Chapter 5

Coupled Proton and Electron Transfer in 1-amino-2-sulphonic- 4-hydroxyanthraquinone Monolayers

“You may be disappointed if you fail, but you are doomed if you don’t try.”

- *Beverly Sills*

5. Introduction

The model chemical system used in this work to study fast heterogeneous electron transfer at a mercury electrode surface is 1-amino, 2-sulphonic, 4-hydroxyanthraquinone. These molecules adsorb on mercury to form tightly bound monolayers,¹ as seen from the parameters calculated using the Frumkin adsorption isotherm in Chapter 3. Both redox forms are stable and the CV response at low pH is that expected for an adsorbed moiety.² Hence, diffusion processes are totally excluded in this system and will not affect the voltammetric response. Another important prerequisite when choosing a system to study electron transfer dynamics is whether the molecules dissolve in water. It is better to perform experiments in acidic aqueous solutions as the solution resistance is decreased. Using aqueous solutions coupled with microelectrodes leads to reduced iR drop and cell time constant.³ When these conditions are fulfilled the fast electron transfer rate constant, expected for adsorbed 1,2,4-AQASH molecules may be measured more accurately.

A significant feature of the electrochemistry of anthraquinone molecules is that proton and electron transfer are coupled. Much research effort has focused on the elucidation of proton and electron transfer rates since the 1950s. Vetter^{4,5} published a number of papers detailing the electrochemistry of p-benzoquinone/hydroquinone adsorbed on a platinum surface. In the 1980s Laviron^{6,7,8,9} published extensive theoretical studies detailing the mechanism of proton coupled electron transfer. These contributions focus on anthraquinone derivatives, which undergo a two electron-two proton redox reaction. A scheme of squares is introduced in these papers, which includes all the intermediates possible in the conversion of an anthraquinone molecule to a hydroquinone structure. This scheme of squares, also known as the “nine-member box scheme” is implemented in this work to elucidate the sequence of electron and proton transfer for 1,2,4-AQASH monolayers in reduction and oxidation directions.

In this chapter, the relative rates of proton and electron transfer are probed over a wide pH range. The potential waveforms used are cyclic voltammetry and chronoamperometry. The experimental data is fit to theoretical models proposed by Butler and Volmer as well as Marcus to elucidate electron transfer rates. These theories have been described in detail in Chapter 1 of this thesis. The apparent heterogeneous

electron transfer rates are then compared with proton transfer rates to determine the rate limiting step at low and high pH. Further experiments are performed to determine the potential and proton concentration dependence of the kinetics of electron transfer. Finally a mechanism for the reduction and oxidation processes at low and high pH is proposed.

5.1 pH Dependence of the CV Response

In order to gain some insight into the rate limiting steps at low and high pH cyclic voltammograms were recorded as the proton concentration in solution was changed. In the experimental procedure a 5 μ M anthraquinone solution was made up in 1 M HClO₄, which recorded an initial pH of -0.02. The pH of this solution was varied by addition of concentrated NaOH. The CV responses in Figure 1 were cycled between positive and negative potential limits until a time independent response was attained. At low pH the voltammetric response is close to ideal, the peak current at any pH increases linearly with scan rate, as expected for an adsorbed moiety.² The ratio of the anodic to cathodic peak current is indistinguishable from unity, indicating that the redox reaction is fully reversible. However at higher pH values the cathodic and anodic peaks broaden, both peaks decrease in magnitude, with the anodic peak decreasing to a greater extent. This would indicate that the redox reaction is less reversible at higher pH. Another notable feature of the CVs is that the formal potential is seen to shift in a negative potential direction up to a pH of 4.11. However, the formal potential of the CVs recorded at higher pH values do not depend on the proton concentration. This pH dependence of the formal potential can be analysed using the Nernst equation^{2,10,11} to gain an insight into the mechanism of the redox reaction of 1,2,4-AQASH.

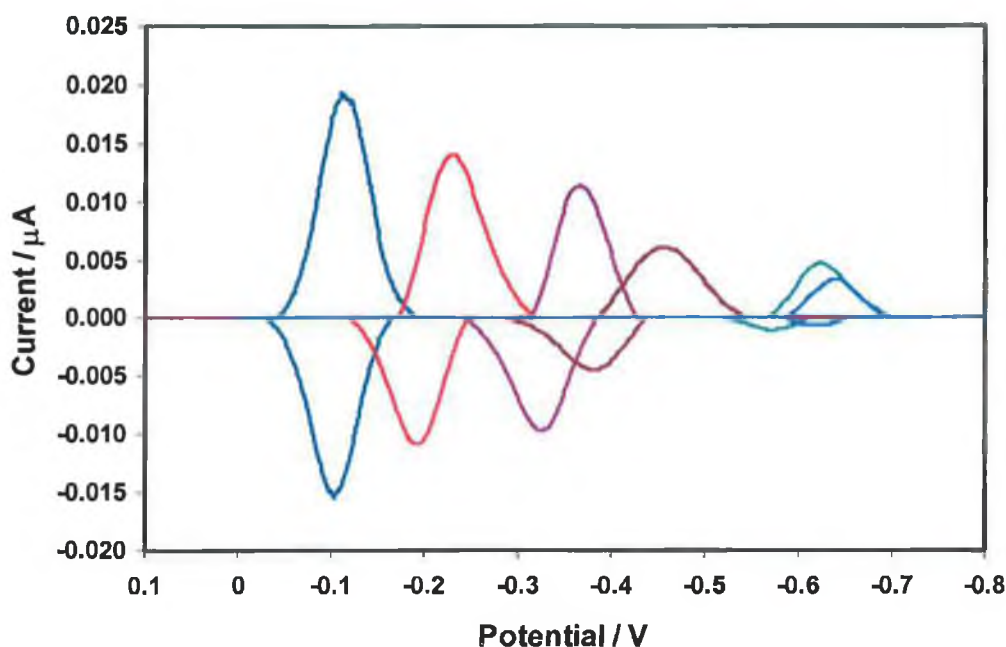


Figure 1. Cyclic voltammograms for a $5\mu\text{m}$ radius mercury electrode immersed in a $5\mu\text{M}$ solution of 1,2,4-AQASH as the pH of the solution was changed using concentrated NaOH. The pH values are, -0.02 (—), 1.49 (—), 3.53 (—), 4.11 (—), 5.93 (—), and 8.22 (—). The initial pH is -0.02 and the scan rate is 5Vs^{-1} , cathodic currents are up and anodic currents are down. The initial potential is 0.1 V.

It has been widely accepted in literature^{8,9,12,13,14,15,16,17} that the mechanism of proton and electron transfer varies with pH. Figure 2 illustrates how the formal peak potential depends on the solution pH. This method of analysis has been reported by a number of research groups,^{12,15,16,17,18} in an attempt to elucidate the redox mechanism of anthraquinone derivatives in oxidation and reduction directions. From this graph it can be seen that the peak potential shifts in a negative potential direction as the solution pH increases with a slope of $61.4 \pm 2.1 \text{ mV}$. This value is indistinguishable from the Nernstian slope of 59 mV pH^{-1} , indicating that over this pH range, quinone, Q, is converted to hydroquinone, H_2Q , by a two electron two proton mechanism. In the pH range 5.71 to 10.22 the slope of the graph is $14 \pm 1.0 \text{ mV}$. The formal potential over this pH range is much less dependent on proton concentration and this would imply that electron transfer is essentially independent of proton transfer at high pH. It is possible that reduction of the monolayer causes depletion of the interfacial proton concentration,

as the availability of protons is significantly reduced at high pH. This would mean that the monolayer exists as a deprotonated hydroquinone when reduced. The redox mechanism is more complicated than at low pH as discussed in Section 5.4.1 of this chapter. This section will also propose a mechanism by which quinone, Q, is reduced to hydroquinone, H₂Q, at low and high pH. The analysis is based on the potential dependence with pH, and the relative rates of proton and electron transfer over the pH range 0-12.

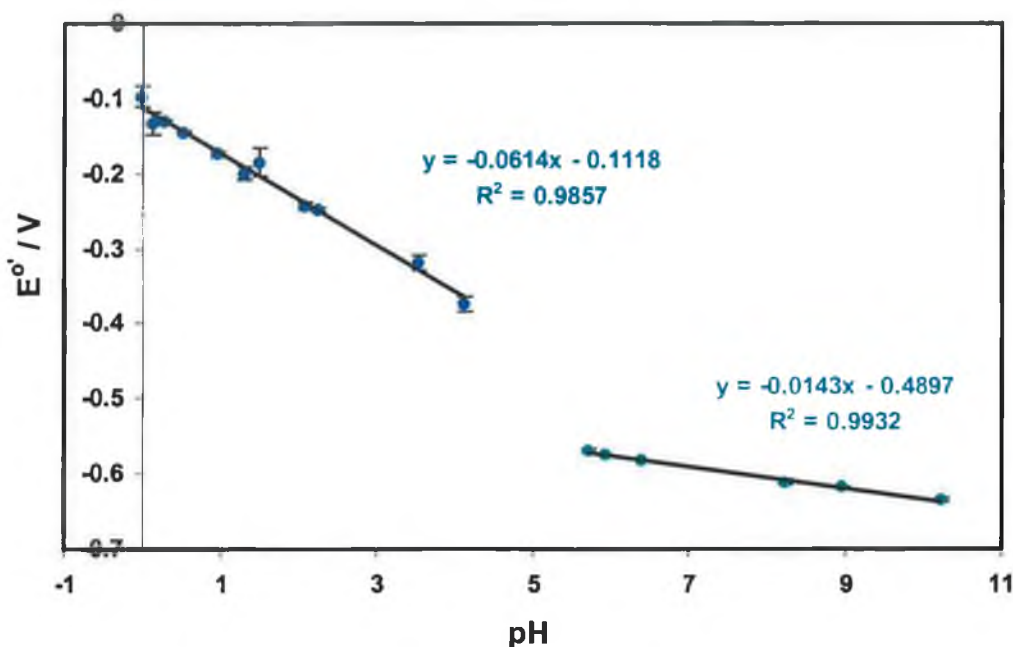


Figure 2. pH dependence of the formal potential. The concentration of 1,2,4-AQASH is 5 μ M with 1 M HClO₄ as the supporting electrolyte. The solution pH was varied from -0.02 to 10.22 using concentrated NaOH. Where error bars are not visible, the error is comparable to the size of the symbol.

5.1.1 Relative Rates of Proton and Electron Transfer

The ultimate objective of this work is to propose a mechanism for the oxidation/reduction reaction of 1,2,4-AQASH. In proposing such a mechanism, the rate of proton transfer relative to the rate of electron transfer has to be considered. This chapter deals with the elucidation of electron transfer rates from experimental data by a number of methods. The rate of proton transfer is approximated here over the pH range 1 to 6. These values are compared with the experimentally determined values for

electron transfer to determine whether proton or electron transfer is the rate limiting step in the redox reaction at low and high pH.

The thickness of the H^+ depletion layer, δ , and thus the time it takes for a proton to diffuse to the electrode surface may be calculated using Equation (1),^{3,12}

$$\delta(t) = \sqrt{\pi Dt} \quad (1)$$

where δ is the depletion layer thickness and D is the proton diffusion coefficient ($9.30 \times 10^{-5} \text{ cm s}^{-1}$).

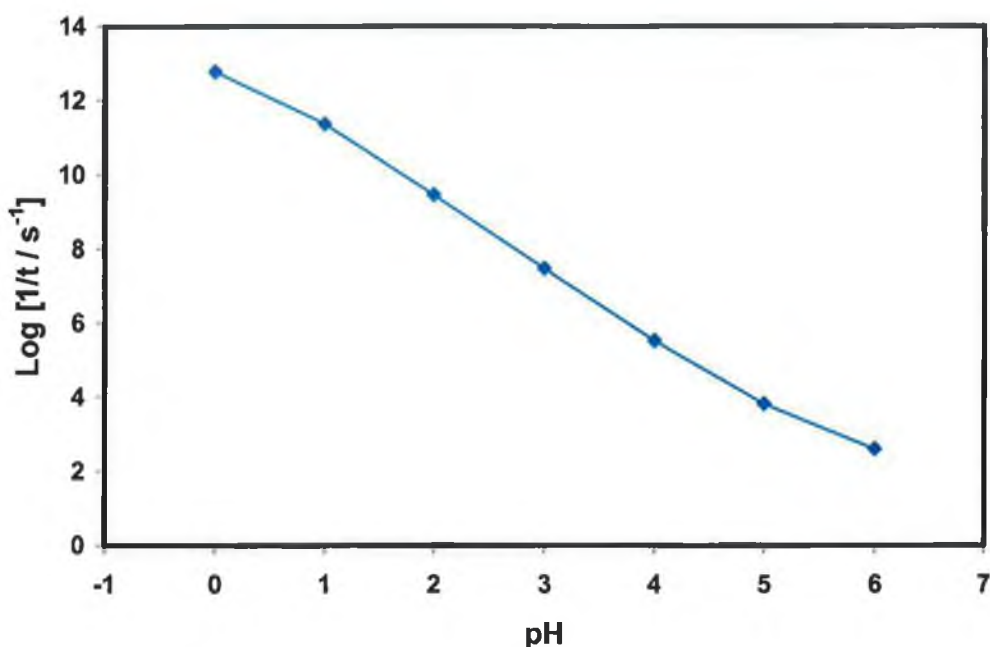


Figure 3. The dependence on the rate of proton transfer on the pH of the solution in the pH range 0-6, the proton transfer rate was calculated as outlined in the text.

The depletion layer thickness increases from $3.56 \times 10^{-8} \text{ cm}$ at pH 1 to $3.17 \times 10^{-6} \text{ cm}$ at pH 3 and further increases to $8.59 \times 10^{-4} \text{ cm}$ at pH 6. From Figure 3 the rate of proton transfer has been approximated as 10^{12} to 10^7 s^{-1} in the pH range 0-3. The proton transfer rate decreases to 10^5 s^{-1} at pH 4 and further decreases to 10^3 s^{-1} at pH 5. This data shows that the rate of proton transfer is very fast at low pH values, the electron transfer rates are in the range 10^5 to 10^4 s^{-1} from pH 0 to 5. Therefore, electron transfer is determined to be the rate limiting step in low pH solution and may be measured

accurately without being effected by proton transfer. Sections 5.2 to 5.4 will present the experimental results obtained in the elucidation of electron transfer rates, primarily in low pH media. In the latter section of the chapter a mechanism detailing the sequence of proton and electron transfer is proposed, based on the experimental results.

5.2 Rapid Scan Rate CV of 1,2,4-AQASH

In potential sweep measurements, when the timescale of the experiment becomes comparable to the rate of heterogeneous electron transfer the cathodic and anodic peaks in a cyclic voltammogram split apart and kinetic information can be obtained.^{19,20} The timescale of an experiment can be changed by varying the scan rate. This method of estimating the heterogeneous electron transfer rate has been implemented in this work to determine the heterogeneous electron transfer rate of 1,2,4-AQASH adsorbed on a mercury microelectrode. The peak-to-peak splitting at high scan rates has been fitted to two models; Laviron, which is based on the Butler Volmer^{21,22} theory of electron transfer, and a recently developed computer based theoretical model based on the Marcus^{23,24,25} theory.

In determining the electron transfer rate for 1,2,4-AQASH adsorbed on a mercury electrode surface the scan rate has been changed from 2 to 4000 Vs^{-1} . The peak-to-peak separation is seen to increase significantly over this scan rate range, scan rates in the interval 80 to 2000 Vs^{-1} are illustrated in Figure 4. CVs were run using a 5 μM solution of 1,2,4-AQASH with 1 M HClO_4 as the supporting electrolyte, this concentration of anthraquinone in solution is known to give saturation coverage. When using cyclic voltammetry data to calculate heterogeneous electron transfer rates an important consideration is the existence of ohmic drop at high scan rates. As the scan rate increases the peak current increases and hence iR drop increases. To counteract this effect mercury microelectrodes were used in this work. The fabrication procedure is outlined in Section 6.1.2 of Chapter 6. The solution resistance measured at micrometer sized electrodes is dramatically larger than that at a macroelectrode, however the currents measured are decreased typically by 6 orders of magnitude.²⁶ Therefore microelectrodes are less affected by iR drop as the scan rate of the experiment is increased.

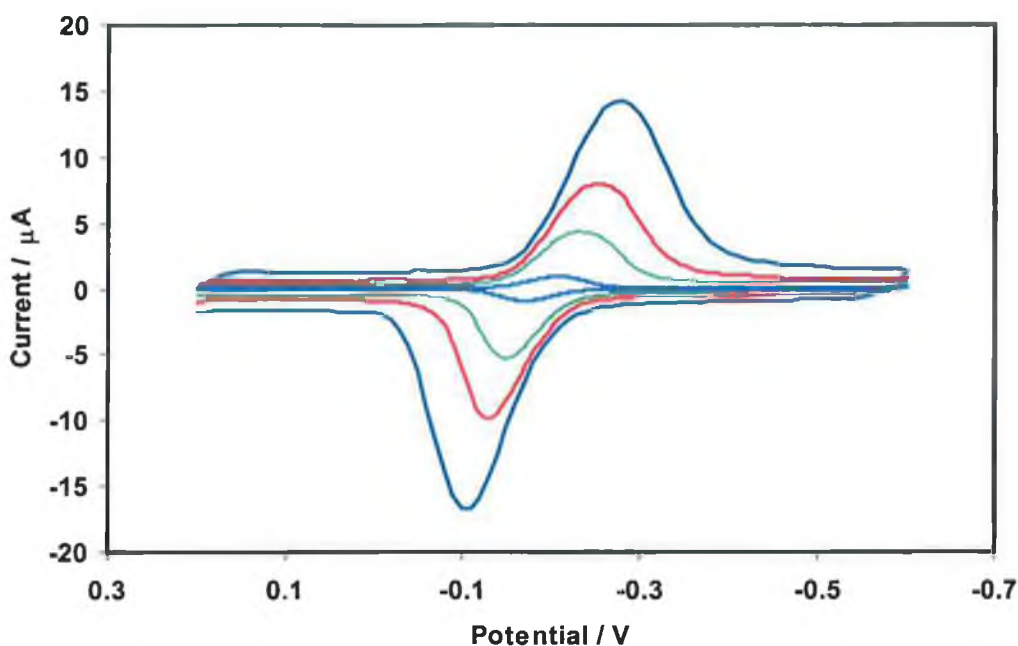


Figure 4. Scan rate dependence of the cyclic voltammetry response of a 5 μm radius mercury electrode immersed in 5 μM solution of 1,2,4-AQASH with 1M HClO_4 as the supporting electrolyte. The potential limits are 0.2 and -0.6 with the initial potential set at 0.2 V. The scan rates are 2000 (—), 800 (—), 500 (—) and 80 Vs^{-1} (—).

Chronoamperometry has been used to calculate the resistance of the mercury microelectrode used to measure the CV responses displayed in Figure 4 above. The resistance has been measured as 1175 Ohms for the 5 μm radius mercury electrode. Using this value and the limiting current from cyclic voltammetry at each scan rate the iR drop can be estimated as the scan rate increases. As seen in Figure 5 iR drop at low scan rates is very low, only 0.580 mV at 100 Vs^{-1} , however it increases to 8.1 mV at 2000 Vs^{-1} and 15.2 mV at 4000 Vs^{-1} . However, when one takes into consideration the peak-to-peak separation at these scan rates it is evident that, while ohmic drop effects introduce some error into the calculations, they have no significant effect on the kinetic parameters calculated from the CV data. The separation between the cathodic and anodic peaks is 43, 160 and 220 mV at scan rates of 100, 2000 and 4000 Vs^{-1} , respectively.

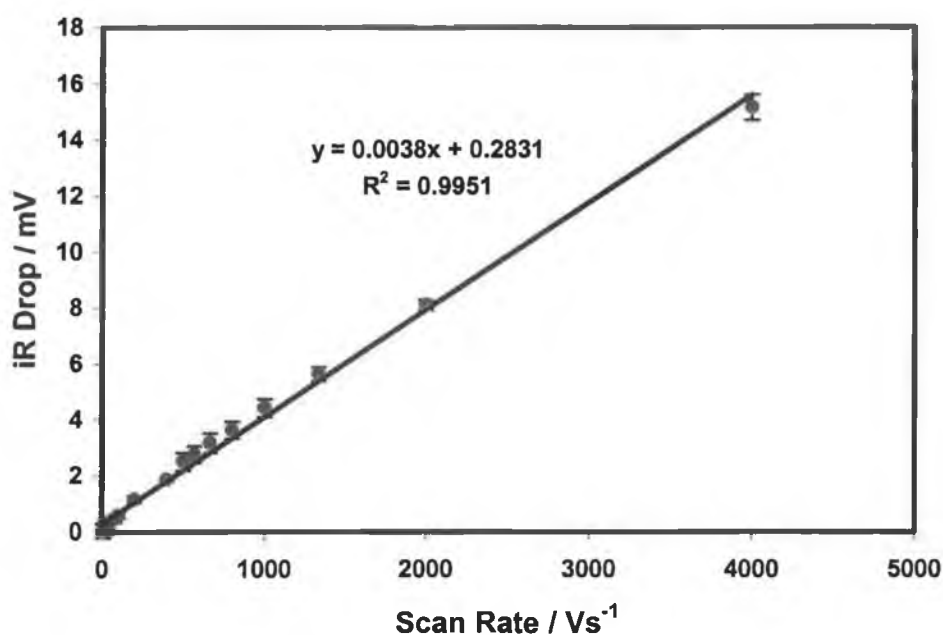


Figure 5. Calculated Ohmic potential drop at a 5 μm radius mercury electrode immersed in a 5 μM solution of 1,2,4-AQASH with 1M HClO_4 as the supporting electrolyte. The scan rate was varied from 2 to 4000 Vs^{-1} . Peak currents obtained from the experimental data in Figure 1 and resistance was obtained from chronoamperometric measurements.

To further probe the reliability of the experimental results obtained by increasing the scan rate in cyclic voltammetric measurements the CH instruments 660A software has been used to simulate CV responses under the same conditions as an experiment. The simulation is based on the Butler Volmer theory of electron transfer and should therefore give the same result as that obtained by fitting experimental CV data to the Laviron formulation outlined in Section 5.2.2. The parameters inputted to simulate the CV response are:

- High and low potential limits, initial potential, scan rate and sensitivity; these parameters were set the same as the experimental values used to generate the CV data fitted to the Laviron formulation and Marcus theory.

- The formal potential of the redox species, obtained from the slow scan CV response, and the expected heterogeneous electron transfer rate constant, obtained from cyclic voltammetry and chronoamperometry measurements.
- The surface coverage of the electroactive species on the electrode surface; the surface coverage for a 5 μM 1,2,4-AQASH solution was used in the simulations as this is known to yield saturation surface coverage, $1.1 \times 10^{-10} \text{ mol cm}^{-2}$.
- The electrode area, obtained from the experimental determination of the mercury electrode area after the deposition process. The electrode area was determined by measuring the faradaic current due to the oxidation and reduction of an electroactive species in solution. The redox probe used in these experiments was 5 μM 1,2,4-AQASH, which has been shown to adsorb on mercury to yield monolayer coverage.

Simulations have been run for a number of scan rates to determine if the experimental data is consistent with Butler Volmer theory. The experimental response at 4000 Vs^{-1} and the predicted response from the simulation are overlaid in Figure 6 for comparison. The separation between the cathodic and anodic peaks in the experimental CV is 220 mV. This compares with a peak-to-peak separation of 206 mV estimated from the simulated CV data. The difference between the experimental and simulated data is 14 mV. This value of 14 mV may be attributed to iR drop, as this would not be predicted by the CH instruments simulated CV. iR drop calculated from chronoamperometry data and the limiting current in CV at a scan rate of 4000 Vs^{-1} was 15.157 mV. Therefore the results from the model are remarkably consistent with the experimental results presented in this chapter thusfar. The experimental CV data adhere to the Butler Volmer theory of electron transfer and are only negligibly affected by ohmic drop effects.

Analysis of the model fit to the experimental data points in Figure 6 shows that a better fit to the cathodic peak potential points is obtained than to the anodic peak potentials. The Butler Volmer theory is designed to find a standard rate constant. It is assumed that the forward and reverse rate constants are equal. However, it would appear from the experimental cyclic voltammogram that the cathodic and anodic rate constants are significantly different. This theory can be tested through chronoamperometric

measurements, as it is possible to measure the cathodic and anodic rate constants separately.

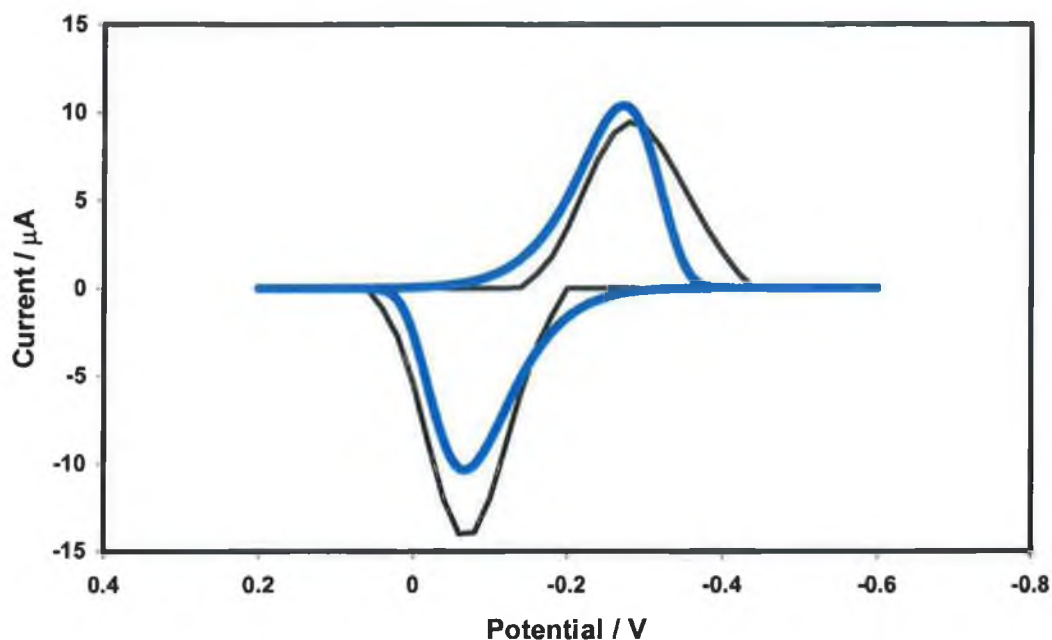


Figure 6. CV response for a 5 μm radius mercury electrode (—) immersed in 5 μM solution of 1,2,4-AQASH with 1M HClO_4 as the supporting electrolyte. The potential limits are 0.2 and -0.6 with the initial potential set at 0.2 V. (---) represents the simulated CV response generated using the CHI 660A software, which is based on the Butler Volmer theory of electron transfer. The scan rate for both CVs is 4000 Vs^{-1} .

5.2.1 Simplex Algorithm Method

A computer based CV simulation model developed by Loughman and Forster²⁷ has been implemented in this work to estimate heterogeneous electron transfer rates. This model differs from the simulation produced using the CHI 600A software as this model is based on the Marcus theory of electron transfer. The simplex algorithm method is also specifically developed to predict electron transfer rates of adsorbed species as opposed to freely diffusing species in solution. Previously published models by Finklea and Hanshaw,²⁸ Chidsey,²⁹ as well as Weber and Creager,³⁰ also based on the Marcus theory allowed the variation of a number of parameters, namely the heterogeneous electron transfer rate constant, k^0 and the reorganization energy, λ . The primary

difference in those models and the model implemented in this work is that a fitting algorithm is incorporated in this simulation allowing the full CV to be modeled.

The algorithm, which was developed by Nelder and Mead³¹ is known as the simplex and was coded into the model by means of a Microsoft Excel macro. A detailed description of the algorithm will not be given here as it is beyond the scope of this work but is available from the PhD thesis presented by Paul Loughman.²⁷ It is sufficient to mention in this work the fitting parameters, which are used to minimize the sum of squares between the experimental and theoretical CV responses. These include k^0 and λ , similar to the parameters used in previously developed models based on the Marcus theory. However, using the simplex algorithm it is possible to vary both of these parameters at the same time, and hence a more accurate estimation of the rate constant is obtained, than would be possible if the parameters were changed one at a time. This method works by minimising the sum of squares of the differences between each point on the theoretical CV and the experimental CV. Therefore, using the full CV curve in the fitting model will allow the experimental curve to influence the result generated by the simplex and thus yield a more accurate estimation of the rate constant.

In the adiabatic model the cathodic rate constant at a given overpotential is given by an integral over energy (ϵ) of three functions.

- (1) The Fermi function for the metal, $n(\epsilon)$
- (2) A Gaussian distribution of energy levels for acceptor states in the monolayer, $D_{Ox}(\epsilon)$.
- (3) A probability factor describing electron tunneling at a given overpotential, $P(\epsilon)$.

$$k_{Ox}(\eta) = A \int_{-\infty}^{\infty} n(\epsilon) D_{Ox}(\epsilon) P(\epsilon) d\epsilon \quad (2)$$

In electron transfer theory the extent of interaction or electronic coupling between the reactant and electrode is described in terms of adiabaticity. When the interaction is strong it is termed adiabatic, and the probability that the reaction will proceed from reactant to product state is high. This has been discussed in more detail in Section 1.2.3.2 of Chapter 1 of this thesis.

The zero point of energy is taken as the Fermi level of the metal at a particular overpotential. The Fermi function describes the distribution of occupied states within the metal and is described by Equation (3):

$$n(\epsilon) = \left(\frac{1}{1 + \exp[(\epsilon - \epsilon_F)/k_B T]} \right) \quad (3)$$

where k_B is the boltzmann constant. The density of states for the adiabatic model is derived from the Marcus theory and can be represented by Equation (4):

$$D_{Ox}(\epsilon) = \exp \left[-\frac{(\epsilon + \eta - \lambda)^2}{4K_B \lambda T} \right] \quad (4)$$

where λ is the reorganization energy. The rate parameter for electron tunneling for the adiabatic model is approximated by Equation (5):

$$P(\epsilon) = \left(\frac{E_B - \epsilon + e\eta}{2} \right) \exp(-\beta d) \quad (5)$$

where E_B is the average barrier height at zero overpotential and d is the electron transfer distance. β is the tunneling constant and is given by Equation (6):

$$\beta = \left(\frac{2[2m]^{1/2}}{\hbar} \right) \left(\frac{E_B - \epsilon + e\eta}{2} \right)^{1/2} \quad (6)$$

where m is the mass of the electron.

In the adiabatic model the anodic rate constant at a given overpotential is obtained by replacing $n(\epsilon)$ by its compliment $1-n(\epsilon)$, and substituting $D_{Ox}(\epsilon)$ with $D_{Red}(\epsilon)$, where $-\lambda$ is replaced with $+\lambda$.

The input parameters to the model are as follows:

- Radius of the microelectrode in μm .
- Temperature in Kelvin.
- Resolution, which is the interval of overpotential used in the calculation of the individual theoretical currents in the simulation.
- The scan rate used to generate the experimental data in Vs^{-1} .
- Overpotential range for the simulation. Simulations are only run for cyclic voltammograms run at fast scan rates where the separation between the cathodic and anodic peak is large. Under these conditions the overpotential range is set over a large scan range.
- Formal potential of the redox species, obtained from the experimental CV data. This parameter is important as it determines the position of the simulated CV response on the potential axis.
- An estimate of the distance of the redox center from the electrode surface. In the case of adsorbed anthraquinone moieties this distance is expected to be quite short and is set between 4 and 5 Å.
- Estimates of the heterogeneous electron transfer rate, k^0 and the reorganization energy, λ . In fitting the experimental data in this work it was preferred to input entirely random values for these two parameters. This ensured a non-biased starting point for the simplex algorithm each time and facilitated testing of the model for the system under investigation in this work. When fitting the experimental data to this model the Simplex was run a number of times for each CV, changing the input parameters for k^0 and λ each time. If the same result was attained from repetitive runs the true minimum was found. Hence, the results were taken to be reliable and correct for the system under investigation.

Rapid scan rate cyclic voltammograms were analysed using the Marcus model, i.e. scan rates in the range 800-4000 Vs^{-1} were modeled. In order to model the experimental CV responses the CVs had to be background corrected, i.e., the capacitive current had to be subtracted from the current response. The model has been extensively tested²⁷ to probe the effect of background charging current in experimental cyclic voltammograms. From these tests it was concluded that the value for the heterogeneous electron transfer rate constant, k^0 was not particularly sensitive to the background current. However, the reorganization energy, λ was estimated more accurately when background current was subtracted from the CVs. Figure 7 shows the CV model fits at scan rates from 800 to 4000 Vs^{-1} . The optimized parameters predicted by the model are presented in Table 1.

In order to test the ability of the CV fitting model described in this section to approximate heterogeneous electron transfer rate constants it has been fit to experimental data over a range of scan rates. The system under investigation here is 1,2,4-AQASH adsorbing on a mercury electrode surface. These molecules are spontaneously adsorbed on mercury and are approximately 4-5 Å from the electrode surface. Therefore, it is expected that the rate constants will be fast in comparison to those determined for alkanethiol systems or osmium complexes. Both of these adsorbates are held further from the electrode surface, approximately 15 to 20 Å,^{32,33} resulting in slower electron transfer rates, in the range 10^3 s^{-1} .^{29,33,34,35}

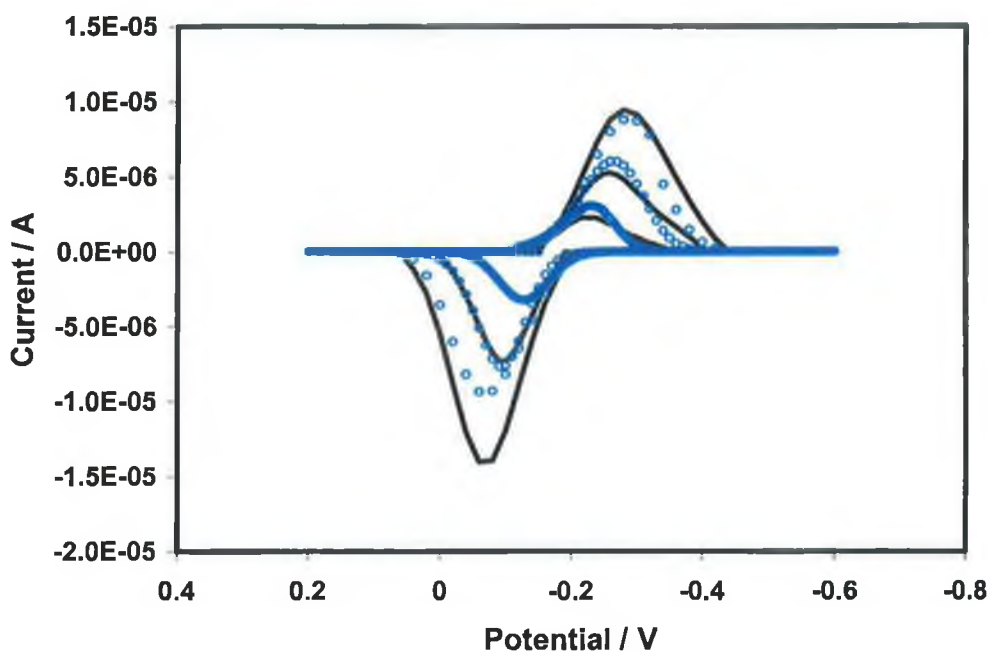


Figure 7. Cyclic voltammograms showing the adsorbed monolayer response from a $5\mu\text{M}$ solution of 1,2,4-AQASH at scan rates of 800, 2000 and 4000 Vs^{-1} . The solid lines denote experimental data, while (.....) denotes the best theoretical response generated using the adiabatic electron transfer model for the cathodic and anodic branches.

Table 1. Table ?. Optimised parameters for k° and λ obtained from the simplex algorithm electron transfer model at various scan rates.

<i>Scan Rate / Vs⁻¹</i>	<i>k^o_{ET} / s⁻¹</i>	<i>λ_{os} / kJ mol⁻¹</i>
800	9.37×10^3	17.9
1000	8.74×10^3	24.4
1333	9.97×10^3	23.9
2000	4.31×10^3	10.4
4000	3.01×10^3	15.6

When evaluating the ability of the CV model to determine heterogeneous electron transfer rates a number of points are significant. Firstly, as outlined earlier at low scan rates, (below 600 Vs⁻¹), the CV response shows negligible peak-to-peak splitting and the CVs contain no kinetic information. The model generates no theoretical results as expected. However at scan rates of 800 Vs⁻¹ and above the model is capable of predicting values for k^0 and λ . The model fits illustrated in Figure 7 at the lower scan rates would appear to approximate the experimental data quite well, the peak potentials and full width at half maximum of the experimental CVs are accurately traced by the model data. However, at a scan rate of 4000 Vs⁻¹ the simplex algorithm is not capable of providing a good fit for the anodic branch of the CV. The same trend is seen in the optimized parameters obtained from the model presented in Table 1. At scan rates up to 1333 V there is little variation between the rate constants, however the values

obtained for scan rates of 2000 Vs⁻¹ and above are seen to deviate. This should not happen if the CV model is capable of approximating the rate constant accurately; the rate constant should be the same at all scan rates. The CV model is designed to find a value for the standard heterogeneous electron transfer rate constant, similar to the CH Instruments Butler Volmer fits presented in an earlier section of this chapter. If the forward and reverse rate constants are different the Marcus model does not predict different apparent rate constants. An evaluation of the results obtained from the cyclic voltammetry and chronoamperometry measurements to calculate electron transfer rates is discussed in detail in Section 5.4.

A theoretical value for the outer sphere reorganization energy has been calculated using Equation (7). This outer sphere component refers to solvent reorganization effects.

$$\lambda_{os} = \frac{\Delta E^2}{8\pi\epsilon_0} \left(\frac{1}{r} - \frac{1}{R_e} \right) \left(\frac{1}{\epsilon_{opt}} - \frac{1}{\epsilon_s} \right) \quad (7)$$

where e is the absolute electronic charge, 1.602×10^{-19} C, r is radius of the anthraquinone molecule, 4Å, R_e is the reactant image distance, ϵ_{opt} is the optical dielectric constant of water, 5.5, and ϵ_s is the static dielectric constant, 78.5. As in previous calculations the reactant image distance has been neglected for electrochemical reactions, i.e., $R_e \rightarrow \infty$.^{32,35} Equation (7) yields a value of 56 kJ mol⁻¹ for the outer sphere reorganization energy. The values generated by the model for the total

reorganization energy, λ_{total} were seen to be consistent at low scan rates, in the range 17.9 to 23.9 kJ mol⁻¹. However, at a scan rate of 2000 Vs⁻¹, λ_{total} decreases to 10.4 kJ mol⁻¹ and increases to 15.6 kJ mol⁻¹ at a scan rate of 4000 Vs⁻¹. Values for the total reorganization energies predicted by the Simplex algorithm model deviate considerably from the theoretical value for outer sphere reorganisation determined from the Marcus theory. It is thought that the CV model is capable of predicting λ_{total} over a limited scan rate range. The actual outer sphere reorganization does not exceed 56 kJ mol⁻¹ and according to the CV model is less. Therefore the total reorganization in this system is dominated by outer sphere reorganization, inner sphere reorganization is not significant. Unfortunately no experimental electron transfer studies, which involve fitting experimental data to the Marcus theory have been published for anthraquinone derivatives. Therefore a literature comparison of the outer sphere reorganization determined for 1,2,4-AQASH in this work is not possible. However potential dependent chronoamperometry measurements have been carried out in this work and are presented in Section 5.3.1 of this chapter. Reorganisation energies are determined for the oxidation and reduction reactions from best fits of the data to the Butler Volmer theory of electron transfer.

Outer sphere reorganization energies in the range 43.45 to 67.61 kJ mol⁻¹ have been reported previously for ferrocene alkanethiols^{29,36,37,38} with the reorganisation energy increasing with increasing chain length. Forster and Faulkner³² have reported outer sphere reorganisation energies for [Os(bpy)₂Cl(pNp)]⁺ monolayers, where bpy is 2,2'-bipyridyl and pNp is either 1,2-bis(4-pyridyl)-ethane, or 4,4'-trimethylenedipyridine equal to 25.5 kJ mol⁻¹, by fitting experimental data to the Marcus theory. In a study carried out by Forster and O'Kelly³⁹ investigating the pH dependent electron transfer dynamics of [Os(bpy)₂(p3p)2]²⁺, where bpy is 2,2'-bipyridyl and p3p is 4,4'-trimethylenedipyridine, the rate of electron transfer is seen to depend on pH. The reorganisation energy at pH 5.05 is 100 kJ mol⁻¹, which decreases to 68 and 56 kJ mol⁻¹, at pH values of 3.10 and 1.07, respectively. At high pH inner sphere reorganization contributes significantly to the total reorganization energy, however at low pH the reorganisation energy is dominated by λ_{os} . The reorganization energy for dense monolayers of [Os(bpy)₂py(p3p)]²⁺, where bpy is 2,2'-bipyridyl, py is pyridine, and p3p is 4,4'-trimethylenedipyridine has been calculated⁴⁰ to be 56 kJ mol⁻¹, using the theoretical Marcus equation. This value corresponds to the value from experimental

data and so the total reorganisation is dominated by outer sphere reorganisation for this complex also.

5.2.2 Laviron Method

Having concluded that iR drop has no significant effect on the CV response measured using a micrometer sized electrode the experimental data was fit to the Laviron^{19,41} formulation. The mathematical expression for the determination of the rate constant, k is expressed in Equation (8):

$$k = \frac{\alpha n F v_c}{RT} = \frac{(1 - \alpha) n F v_a}{RT} \quad (8)$$

where α is the transfer coefficient, n is the number of electrons transferred in the redox reaction, v is the scan rate of the experiment and R, T and F have their usual meaning. This method of estimating heterogeneous electron transfer rate constants is rapid but not as accurate as chronoamperometry measurements presented below. This is due to a number of factors; firstly it is assumed that the transfer coefficient, α , is equal to 0.5 in the Laviron method. This assumption may or may not be true for the anthraquinone under investigation here. Tafel plots constructed using chronoamperometry data allow a determination of α_a and α_c , these results are presented later in this chapter.

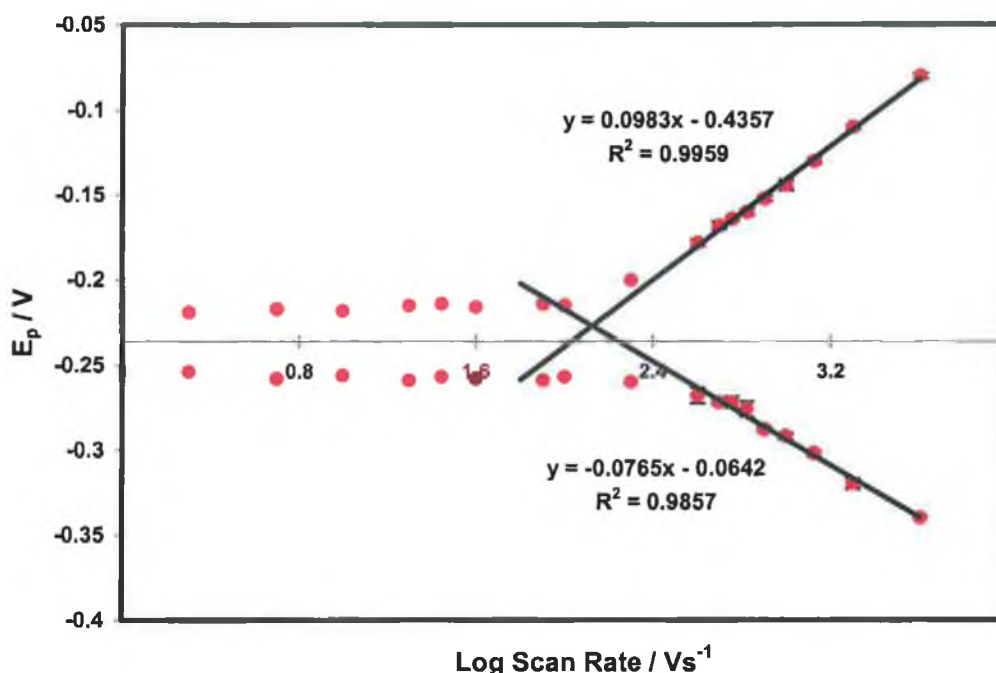


Figure 8. Laviron model for the determination of the heterogeneous electron transfer rate constant for 1,2,4-AQASH adsorbed on a 5 μm radius mercury electrode. The concentration of the AQ in solution was 5 μM , which yielded saturation coverage. The supporting electrolyte was 1 M HClO_4 and the pH of the solution was -0.25 .

The scan rate range investigated in the data fit to the Laviron method is 2–4000 Vs^{-1} . It can be seen from Figure 8 that the peak potentials vary very little until high scan rates are applied to the system. At scan rates above 200 Vs^{-1} significant peak-to-peak separation can be seen and these points have been linearised. The formal potential for 1,2,4-AQASH in acidic media is -0.236 V. The lines through the cathodic and anodic points intersect the x-axis and these are the scan rates used to estimate the forward and reverse rate constants. In the set of results illustrated in Figure 8 the lines intersect at values of 2 and 2.25, the antilog of these numbers is 100 and 177.83 Vs^{-1} , respectively. These values can be substituted into Equation (8) to calculate a value for the rate constants, which in this case works out to be 3.9×10^3 and 6.9×10^3 s^{-1} for the cathodic and anodic processes respectively. This evaluation however is not very accurate, as the constant peak separation of approx. 40 mV at scan rates up to 200 Vs^{-1} is not due to the kinetics of electron transfer. Therefore, the analysis method was modified by subtracting the peak-to-peak separation at low scan rates from the separation at high

scan rates. The results are illustrated in Figure 9. The line through the cathodic and anodic points intersect the x-axis at 2.25 and 2.52. The antilog of these numbers is 177.82 and 331.13 Vs^{-1} . The cathodic and anodic rate constants were calculated as $6.9 \times 10^3 \pm 1.1$ and $1.3 \times 10^4 \pm 1.0 \text{ s}^{-1}$, respectively. These values show an increase from those calculated using the data in Figure 8, however they are still lower than the rate constants determined using the CV simulation model based on the Marcus theory and the values determined from chronoamperometry.

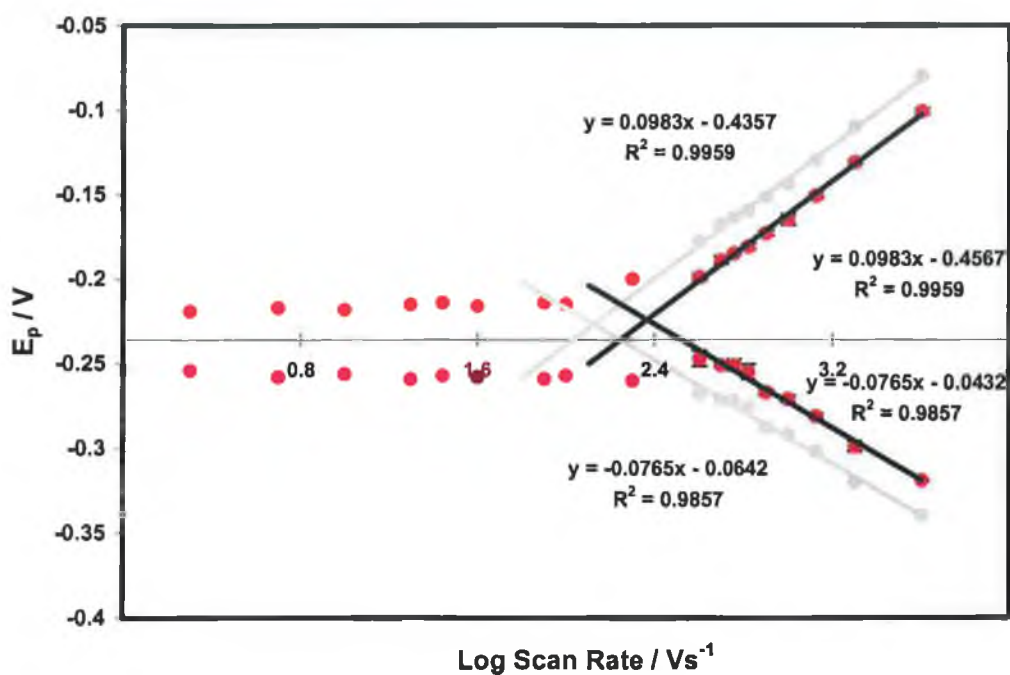


Figure 9. Laviron model for the determination of the heterogeneous electron transfer rate constant for 1,2,4-AQASH adsorbed on a 5 μm radius mercury electrode. The supporting electrolyte was 1 M HClO_4 and the pH of the solution was -0.25 . The peak separations at high scan rates have been corrected to correct for iR drop effects.

5.3 Chronoamperometric Measurements

Chronoamperometry conducted on a microsecond timescale has been used to probe the rate of heterogeneous electron transfer, k , across the metal/monolayer interface. This high-speed technique allows for a more accurate determination of the heterogeneous electron transfer rate than that obtainable from cyclic voltammetric measurements. This is due to the fact that capacitive and faradaic currents are separated in this potential step technique on a time domain. This is not the case in cyclic voltammetry measurements, as outlined in the previous section. Cyclic voltammograms have to be background corrected to elucidate kinetic data and the method by which this is done will inevitably determine the reliability of the rate constant calculated. At high scan rates the capacitive current is quite large and it can be difficult to extract the faradaic current from the net current response accurately.

Chronoamperometry involves stepping the potential from an initial potential value to a final value, as described in Section 1.6.2 of Chapter 1. Following a potential step which steps over the formal potential of the electroactive species a double exponential decay is observed. This is due to the fact that double layer charging of the electrode and the faradaic processes from the electroactive species have different decay rates.^{2,42} The decay rate of the charging process is exponential and faster, while the faradaic current decreases with the square root of time.³ The rate at which the charging current decays depends on the size of the electrode, the specific double layer capacitance and the solution conductivity. In the experiments conducted in this section microelectrodes were used and measurements were carried out in highly conductive solutions. This combination results in a significant reduction in the cell time constant and ohmic drop effects, as both current and solution resistance are minimised.

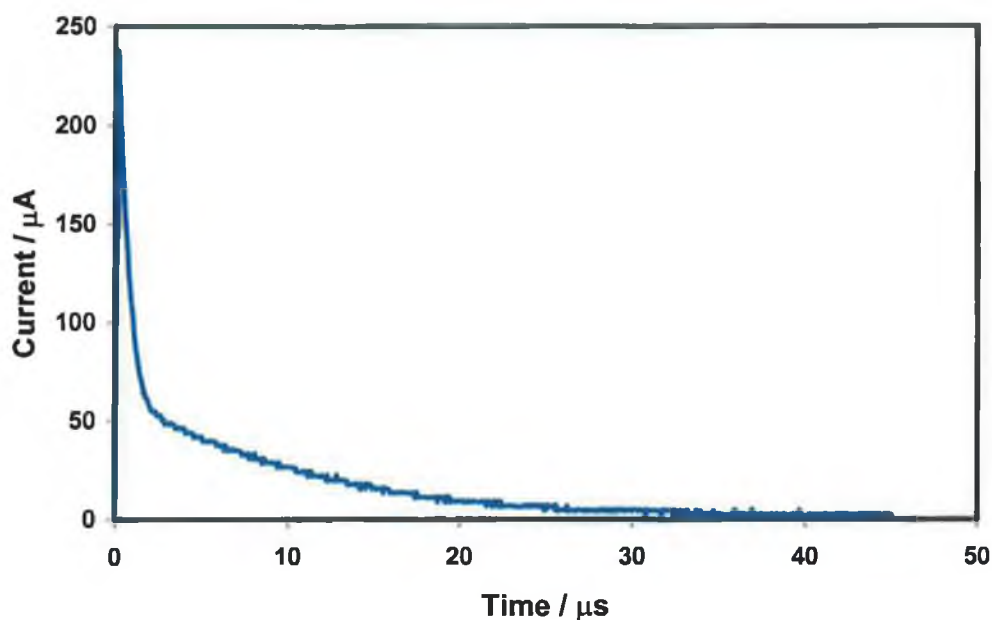


Figure 10. Current response for a 5 μm radius mercury microelectrode immersed in a 5 μM solution of 1,2,4-AQASH following a potential step from +129 to -307 mV. The supporting electrolyte is 1.0 M HClO_4 and the pH of the solution is 0.14.

Figure 10 illustrates the response of a 5 μm radius mercury electrode immersed in a 5 μM solution of 1,2,4-AQASH in acidic media. The potential was stepped from +129 to -307 mV. The formal potential of 1,2,4-AQASH equals -180 mV and thus the overpotential applied in this step was 127 mV. This figure shows that the current initially decays rapidly due to double layer charging, followed by a region where the current response decays more slowly, corresponding to faradaic current flow. The response time of this electrode can be obtained by analysing the capacitive current according to Equation (9):^{2,43}

$$i_c(t) = \left(\frac{\Delta E}{R} \right) \exp\left(\frac{-t}{RC_{dl}} \right) \quad (9)$$

where ΔE is the amplitude of the potential step in the chronoamperometry experiment. By plotting $\ln i(t)$ vs t the cell time constant and resistance can be calculated from the slope and intercept of the graph respectively. In this experiment the response time of the electrode has been calculated to be 1.14 μs . Meaningful kinetic data can be obtained

at 5-10 times the RC time constant and thus faradaic responses have been probed at longer times in the semilog plot. The faradaic response decays according to Equation (10):^{29,44}

$$i_f(t) = kQ\exp(-kt) \quad (10)$$

where k is the apparent rate constant for the overall reaction at a particular overpotential and Q is the charge passed in the redox switching. The heterogeneous electron transfer rate constant for 1,2,4-AQASH at low pH has been calculated from the slope of the semilog plot as $9.6 \pm 1.1 \times 10^4 \text{ s}^{-1}$.

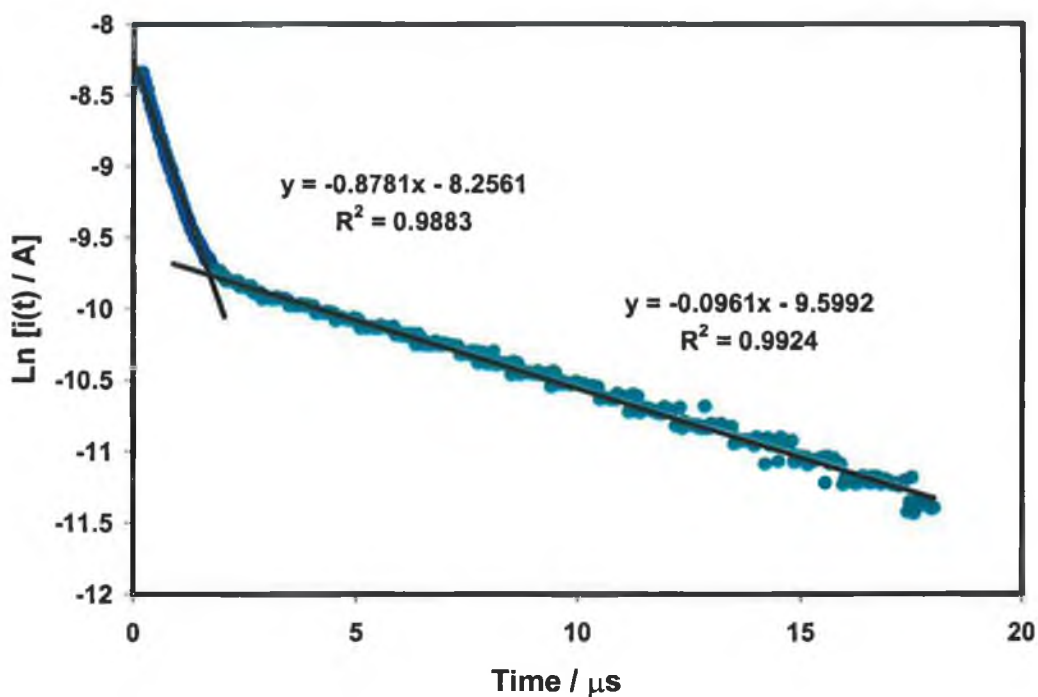


Figure 11. Semilog plot of the current response for a 5 μm radius mercury microelectrode immersed in a 5 μM solution of 1,2,4-AQASH, which yields monolayer coverage. The potential was stepped from +129 to -307 mV, overpotential, η equals 127 mV. The supporting electrolyte is 1.0 M HClO_4 and the pH of the solution is 0.14.

5.3.1 Potential Dependence of Reduction / Oxidation Rates

The potential dependences for the reduction and oxidation kinetics of 1,2,4-AQASH have been investigated by stepping the electrode potential to different overpotentials. In amperometric measurements, an increased potential step relative to the formal potential increases the free driving force for the reaction and causes increased reaction rates to be observed.² As previously explained, the reaction rates are determined from an exponential decay of the current following a potential step, which changes the redox state of the electroactive species. Current time transients for applied overpotentials ranging from 62 to 427 mV are displayed in Figure 12. The corresponding semilog plots for the Faradaic reaction are illustrated in Figure 13, and the heterogeneous electron transfer rates have been calculated from the slopes of these lines.

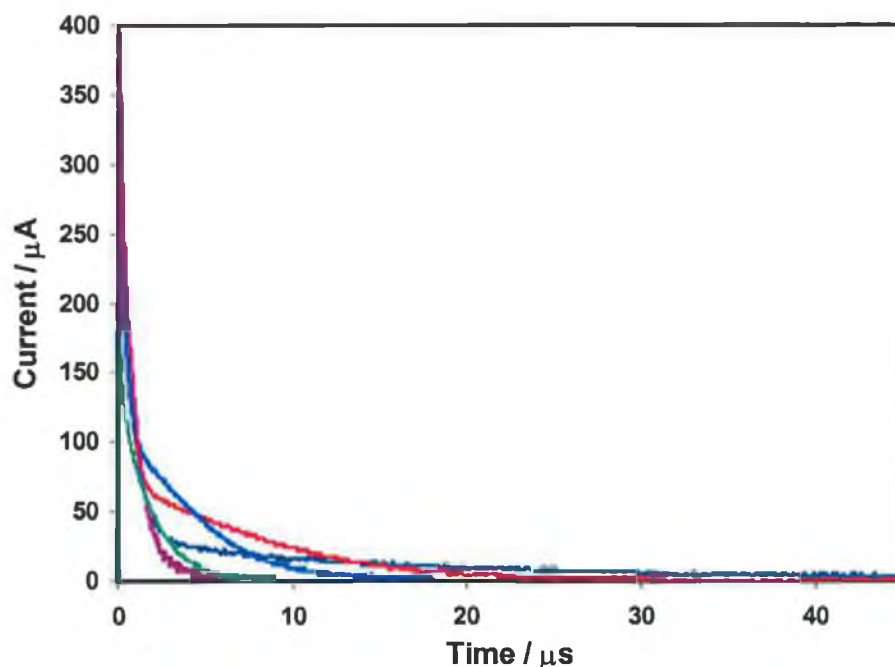


Figure 12. Current responses for a 5 μm mercury microelectrode immersed in a 5 μM solution of 1,2,4-AQASH following potential steps where the overpotentials are 62 (—), 149 (—), 220 (—), 340 (—), and 427 mV (—), respectively.

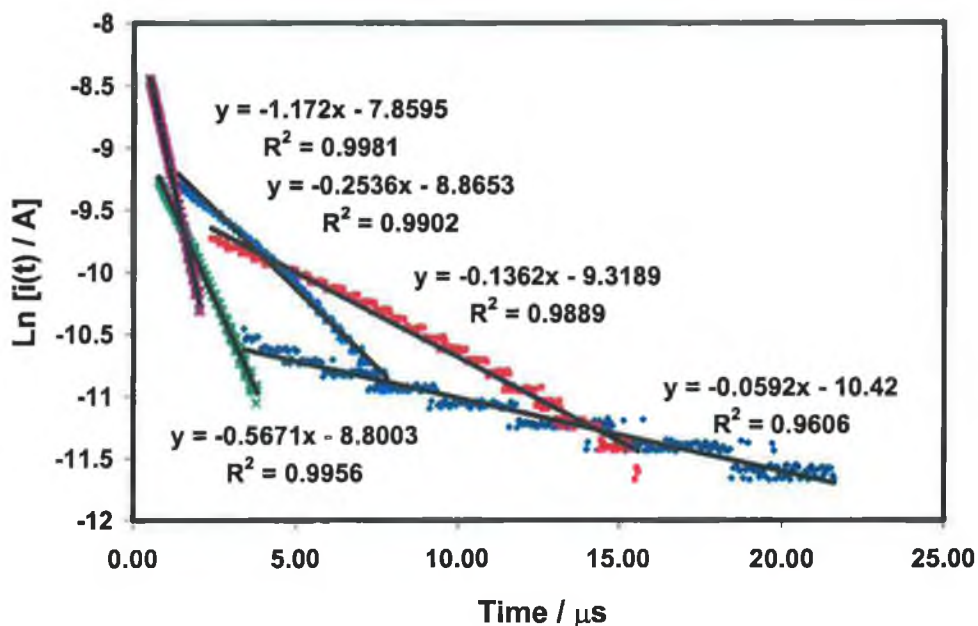


Figure 13. Effect of the various overpotentials on the $\text{Ln } i(t)$ plots for a spontaneously adsorbed 1,2,4-AQASH monolayer. The concentration of AQ is $5 \mu\text{M}$, which yields monolayer coverage. The supporting electrolyte is 1.0 M HClO_4 . Overpotentials of 62 (—), 149 (—), 220 (—), 340 (—), and 427 mV (—) were applied to the system.

Figures 12 and 13 show that there are substantial differences in the magnitude of the currents observed as the overpotential is increased. It is also evident that the timescale over which the faradaic current decays to zero decreases dramatically as the magnitude of the overpotential is increased. Heterogeneous electron transfer rates obtained from faradaic data are only meaningful at 5-10 times the response time of the electrode.⁴⁵ Therefore, it was necessary when carrying out these measurements to use a microelectrode with a fast response time. In this way capacitive and faradaic currents were well separated on the time domain and more accurate analysis of the data was made possible.

The Butler Volmer theory of electron transfer models the potential dependence of the reaction rates according to Equations (11) and (12). These equations have been introduced in Section 1.2.2 of Chapter 1 of this document.

$$k_f = k^{\circ} \exp\left(\frac{-\alpha n F (E - E^{\circ})}{RT}\right) \quad (11)$$

$$k_b = k^{\circ} \exp\left(\frac{(1 - \alpha) n F (E - E^{\circ})}{RT}\right) \quad (12)$$

where k° in Equations (11) and (12) is the standard rate of heterogeneous electron transfer, i.e., at the formal potential where the driving force is zero. The forward reaction refers to a reduction process and the reverse reaction refers to an oxidation process. Taking the natural logarithm of the both sides of these equations leads to a set of equations known as the Tafel equations:

$$\text{Ln}k_f = \text{Ln}k^{\circ} - \frac{\alpha n F \eta}{RT} \quad (13)$$

$$\text{Ln}k_b = \text{Ln}k^{\circ} - \frac{\alpha n F \eta}{RT} \quad (14)$$

where η is the overpotential and is defined as the difference between the applied potential and the formal potential of the redox species. Plotting the potential dependent data according to the Tafel equations yields straight line plots for reduction and oxidation steps. A value for the forward and reverse rate constants can be calculated from the intercepts of the straight lines in Figure 14, respectively. The experimental results presented were attained at pH 0.14, and the overpotential was changed from 149 to 427 mV in the reduction direction and from 116 to 528 mV in the oxidation direction.

The apparent rate constant for reduction is 4.61×10^4 and for oxidation is $8.71 \times 10^4 \text{ s}^{-1}$. These values confirm the rapid nature of electron transfer for these adsorbed moieties, as expected, as the molecules are adsorbed just 4-5 Å from the electrode surface. However it is evident from this result that the rate of the forward reaction (reduction) exceeds that of the back reaction (oxidation). This observation has been reported previously by Forster and Faulkner³² in the elucidation of heterogeneous electron transfer rates in monolayers of osmium polypyridyl complexes. In this study the difference in electron transfer rates has been attributed to pairing effects, which causes the formal potential in cyclic voltammetry and chronoamperometry to differ. Ion pairing cannot explain the difference in electron transfer rates observed in this work, as

both the oxidized and reduced forms of 1,2,4-AQASH are uncharged. However if the fast timescale in chronoamperometry could cause the formal potential of the oxidized and reduced anthraquinone to differ this would explain the difference in the apparent rate constants determined.

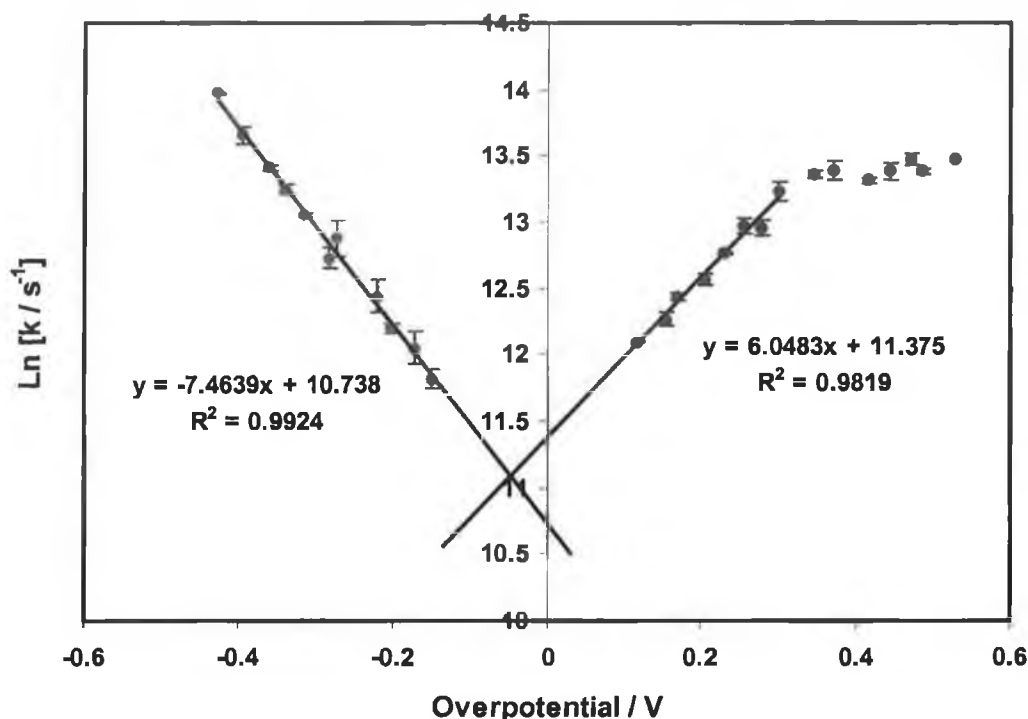


Figure 14. Dependence of the $\text{Ln } k$ on the overpotential for a spontaneously adsorbed 1,2,4-AQASH monolayer. The concentration of AQ is $5 \mu\text{M}$, which yields monolayer surface coverage. The supporting electrolyte is 1 M HClO_4 . Data was collected using a $5 \mu\text{m}$ radius mercury microelectrode.

Forster and coworkers^{44,46,47,48} have published a number of electron transfer rate studies focusing on analogous anthraquinone derivatives adsorbed on mercury. The heterogeneous electron transfer rate constant for 2,6-AQDS monolayers is more than 50 times larger than that for 1,5-AQDS monolayers.^{3,44,49} This large difference in electron transfer rates was attributed to different film structures, and in particular extents of hydrogen bonding for these two systems. This is supported by other electrochemical^{50,51} and scanning probe microscopy studies⁵² of 2,6- and 1,5-AQDS, which conclude that 2,6-AQDS intermolecularly hydrogen bonds when adsorbed on mercury while 1,5-AQDS does not. By comparing the electron transfer rates of 1,2,4-

AQASH with those of 2,6-AQDS and 1,5-AQDS, an idea of the presence and extent of hydrogen bonding in 1,2,4-AQASH monolayers can be obtained. The rate of electron transfer in 2,6-AQDS films is $6.7 \times 10^4 \text{ s}^{-1}$, which is 62 times faster than for 1,5-AQDS monolayers, $1.08 \times 10^3 \text{ s}^{-1}$. The electron transfer rate for 1,2,4-AQASH is $6.66 \times 10^4 \text{ s}^{-1}$, when the cathodic and anodic rate constants are averaged. This rate constant is equal to that quoted for 2,6-AQDS. Hence, it can be concluded from these results that 1,2,4-AQASH adsorbates undergo intermolecular hydrogen bonding, similar to 2,6-AQDS. This supports the conclusions drawn from the spiked CV data in Chapter 3 of this thesis also. Heterogeneous electron transfer rates for AQ monolayers, which do not hydrogen bond are considerably lower, values such as 8.5×10^2 and 9.9×10^3 have been reported for 2-OHAQ⁴⁷ and 2-AQCA⁴⁸ monolayers, respectively.

The transfer coefficients for reduction and oxidation were calculated from the slopes of the lines in the Tafel plot. Under these low pH conditions the slopes for monolayer reduction and oxidation were 7.46 and 6.05 V^{-1} respectively. If $n = 2$, then $\alpha_c = 0.096$ and $\alpha_a = 0.078$. The sum of the transfer coefficients is far from the value of unity predicted by the Butler Volmer theory of electron transfer. At this pH it is expected that the redox reaction involves the transfer of two electrons. One explanation for the extremely low transfer coefficients is that the reorganization energy is very low in this system. The Butler Volmer model does not account for the situation where the reorganization energy becomes comparable to the activation energy for the reaction. If the reorganization energy were extremely low the entire data set presented in Figure 14 would lie in the Marcus inverted region discussed earlier and the slope of the graph would decrease significantly leading to a low transfer coefficient. However, analysis of the data and the discussion that follows shows that the reorganization energy is not that low. Therefore the result is inconclusive and has not been reported before in the literature for systems of this kind.

Another significant feature of the Tafel plot is that the apparent rate constant for reduction becomes independent of potential from an overpotential of 0.3 V and above for the oxidation reaction. This can be explained through the Marcus inverted region, which predicts that the rate constant becomes independent of overpotential when the activation energy becomes comparable to the reorganization energy. The reorganization energy has been approximated from the overpotential as 28 kJ mol^{-1} . This value for the

total reorganization energy is in reasonable agreement with the values determined from the simplex algorithm model presented earlier. Values in the range 17 to 23 kJ mol⁻¹ were reported. However it is interesting to note that the reduction rate constants remain dependent on the applied overpotential at least up to an overpotential of 0.43 V. The reorganization energy in this case would have to be 43 kJ mol⁻¹ or greater, as it is not known from these results the overpotential at which the apparent rate constant becomes independent of potential. From these results the following can be concluded; the oxidation reaction has a lower reorganization energy than the reduction reaction. The oxidation reaction involves conversion from a C-OH to a C=O. Reduction involves conversion from a C=O to a C-OH, thus requiring the uptake of protons from solution. This may explain why the total reorganization energy is higher on the reduction side.

5.4 pH Dependence of the Reaction Rates

Throughout the literature survey and experimental chapters of this thesis repeated reference has been made to the fact that anthraquinone molecules undergo coupled proton and electron transfer redox reactions.^{4,5,6,7,18,53} Experiments were carried out varying the solution pH to investigate the dependence of the reduction and oxidation kinetics on the proton concentration. The experimental techniques and analysis of data were the same as those presented above. Standard heterogeneous electron transfer rates were attained from cyclic voltammograms using the Marcus model, and chronoamperometric measurements were analysed to attain rate constants also. A comparison and analysis of the reliability of the results from the different methods is discussed in this section.

Cyclic voltammograms at high scan rates have been fit to the Marcus model developed by Loughman and Forster.²⁷ The pH range investigated was from -0.54 to +2.83. The rate of electron transfer is seen to decrease as the solution pH is increased. Representative CVs for the pH range investigated are illustrated in Figure 15. The optimized rate constants from the model at scan rates of 2000 and 4000 Vs⁻¹ are presented in Table 2.

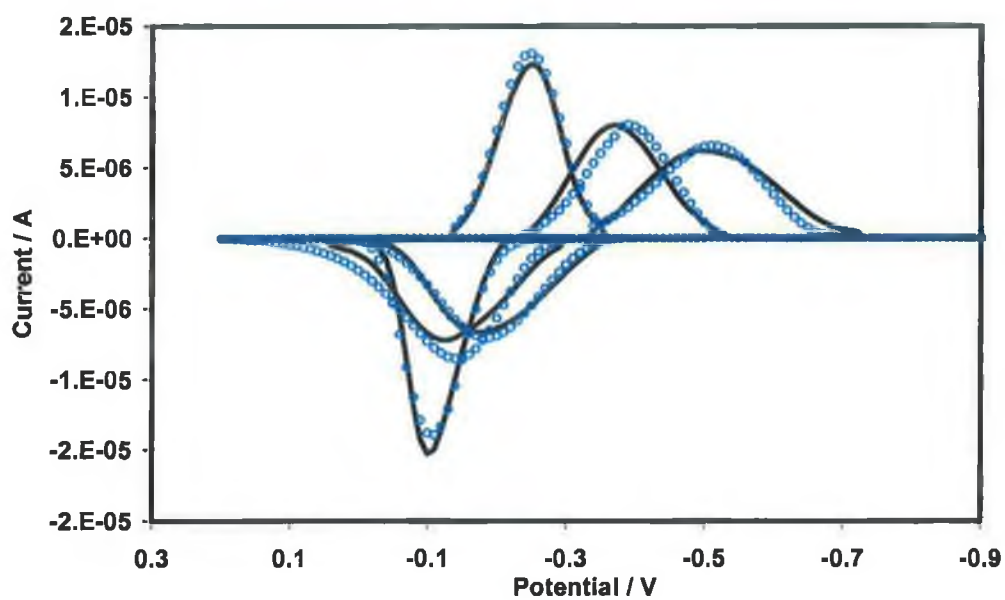


Figure 15. Cyclic voltammograms of 1,2,4-AQASH at a scan rate of 2000 Vs^{-1} . The solid lines denote experimental data at pH values of -0.54 , $+0.49$ and $+2.26$ from left to right. (•••) denotes the best theoretical response generated using the adiabatic electron transfer model for the cathodic and anodic branches.

Table 2. Heterogeneous electron transfer rates for 1,2,4-AQASH monolayers; the rate constants at scan rates of 2000 and 4000 Vs^{-1} were generated from the CV model based on the Marcus theory. The initial solution was made up in 1 M $HClO_4$ and recorded a pH of -0.54 . The pH of this solution was varied by adding concentrated NaOH.

<i>pH</i>	$k_{app}^o / s^{-1} @ 2000 Vs^{-1}$	$k_{app}^o / s^{-1} @ 4000 Vs^{-1}$	<i>Average</i> k_{app}^o / s^{-1}
-0.54	$1.20 \times 10^4 \pm 1.56$	$1.50 \times 10^4 \pm 1.94$	$1.35 \times 10^4 \pm 1.75$
-0.25	$6.50 \times 10^3 \pm 1.02$	$5.50 \times 10^3 \pm 1.19$	$6.00 \times 10^3 \pm 1.10$
+0.49	$4.40 \times 10^3 \pm 1.07$	$3.70 \times 10^3 \pm 1.18$	$4.05 \times 10^3 \pm 1.12$
+1.03	$2.40 \times 10^3 \pm 1.52$	$2.30 \times 10^3 \pm 1.41$	$2.35 \times 10^3 \pm 1.47$
+1.49	$2.31 \times 10^3 \pm 1.27$	$1.90 \times 10^3 \pm 1.32$	$2.11 \times 10^3 \pm 1.29$
+1.75	$1.90 \times 10^3 \pm 1.36$	$1.40 \times 10^3 \pm 1.56$	$1.65 \times 10^3 \pm 1.45$
+2.26	$2.52 \times 10^3 \pm 1.24$	$2.20 \times 10^3 \pm 1.33$	$2.36 \times 10^3 \pm 1.28$
+2.83	$2.30 \times 10^3 \pm 1.48$	$1.9 \times 10^3 \pm 1.58$	$2.10 \times 10^3 \pm 1.53$

Consistent with the chronoamperometry data presented in Section 5.3.1, Tafel plots have been constructed for pH values in the range -0.54 to 2.49 . Figure 16 shows that for both oxidation and reduction $\ln k$ depends linearly on the overpotential, η , at least for overpotentials up to 350 mV. The heterogeneous electron transfer rate constants for oxidation and reduction have been calculated from the intercepts of the semilog plots and are summarized in Table 3.

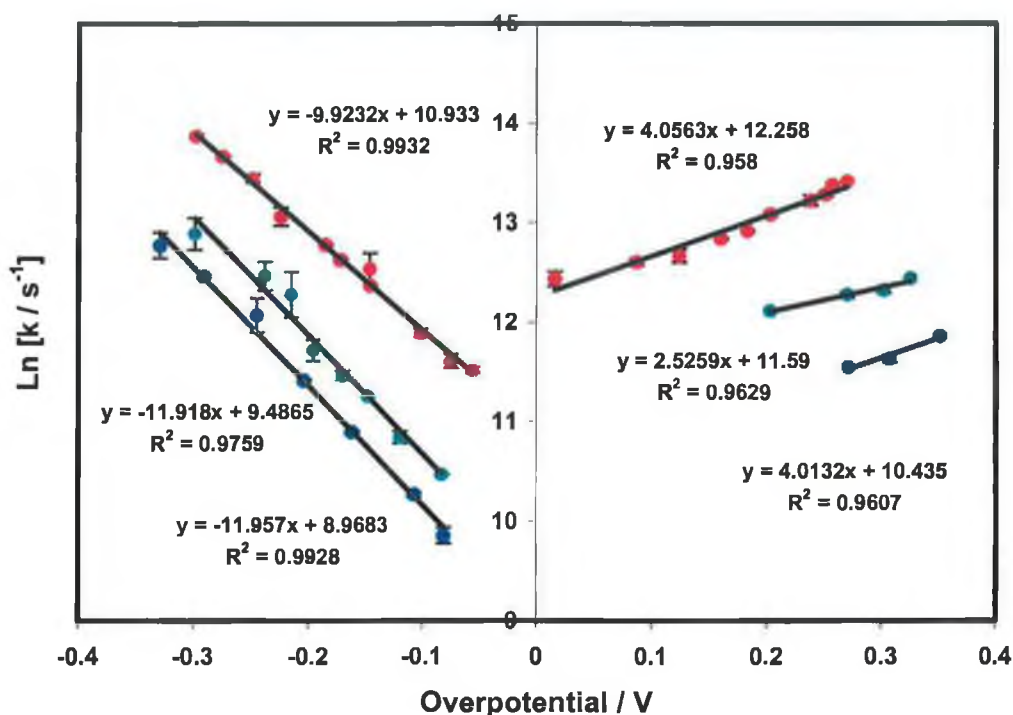


Figure 16. Dependence of the $\ln k$ on the overpotential for a spontaneously adsorbed 1,2,4-AQASH monolayer. The pH values are -0.54 (i), 0.45 (i) and 2.14 (i). Supporting electrolyte is 1M HClO_4 and the pH was varied by addition of concentrated NaOH. Data was collected using a $5\mu\text{m}$ radius mercury microelectrode.

Table 3. Heterogeneous electron transfer rate constants for 1,2,4-AQASH monolayers; apparent rate constants for oxidation and reduction reactions were determined from chronoamperometry data fitted to the Butler Volmer model.

<i>pH</i>	<i>k_{app} / s⁻¹ Reduction</i>	<i>k_{app} / s⁻¹ Oxidation</i>
-0.5	5.60 x 10 ⁴ ± 1.05	2.11 x 10 ⁵ ± 1.06
0.45	1.32 x 10 ⁴ ± 1.16	1.08 x 10 ⁵ ± 1.10
0.96	2.24 x 10 ⁴ ± 1.03	5.97 x 10 ⁴ ± 1.07
1.57	9.96 x 10 ³ ± 1.01	4.28 x 10 ⁴ ± 1.09
2.14	7.85 x 10 ³ ± 1.11	3.40 x 10 ⁴ ± 1.29
2.49	7.69 x 10 ³ ± 1.12	4.28 x 10 ⁴ ± 1.09

Analysis of the methods used to estimate the pH dependent rate constants presented in this section shows that the values estimated from chronoamperometric measurements are more reliable than those calculated using cyclic voltammetry. In the cyclic voltammetry model based on the Marcus theory it is only possible to calculate a value for the standard heterogeneous electron transfer rate constant, k^0 . The model does not take into account the possibility that the forward and reverse reactions may precede at different rates. At a pH of -0.5 the CV model generates a value of $1.35 \times 10^4 \pm 1.75 \text{ s}^{-1}$ for the standard electron transfer rate constant.

Using chronoamperometry it is possible to determine the rate of the oxidative and reductive reaction separately. For example at a pH of -0.5 the rate of reduction is $5.60 \times 10^4 \pm 1.05 \text{ s}^{-1}$ and the rate of oxidation is $2.11 \times 10^5 \pm 1.06 \text{ s}^{-1}$. Both of these values are greater than those calculated using cyclic voltammetry ($1.35 \times 10^4 \pm 1.75 \text{ s}^{-1}$). This result is representative of the results calculated over the pH range investigated. The rate constants attained from the cyclic voltammetric model are consistently lower than those

calculated using chronoamperometry. The same trend was seen in the rate constants calculated using the Laviron formulation. This method of calculating the rate constant is based on the potential of the cathodic and anodic peaks in cyclic voltammograms. The rate constants calculated using the Laviron method show little variation over the pH range investigated, therefore the results have not been included in this section.

5.4.1 Surface Reaction Kinetics

A brief comparison of the results obtained from the Butler Volmer and Marcus theories is presented here. The reaction rate may be determined by analysis of the data using Equation (15).⁵⁴

$$k = A[H^+]^x \quad (15)$$

where k is the rate of the reaction, x is the order of the reaction and $[H^+]$ is the proton concentration. By plotting $\text{Log } k$ vs $\text{Log } [H^+]$ a value for the order of the reaction can be obtained from the slope of the graph. The pH range investigated is from -0.54 to $+2.49$, and within this range the redox reaction involves the transfer of two electrons, as determined from the potential dependent pH data. From the results presented in the plot below it is evident that regardless of the technique used to calculate the rate constants the order of the reaction is 0.3 . This value compares with a value of 0.8 reported by Xu³ in the investigation of the order of reaction of 2,6-AQDS. The range of pH's analysed in this study was from 0 to 1 . Xu has concluded from these results that protonation is involved in the rate limiting step for both the reduction and oxidation reactions. From the results presented in Section 5.1.1 of this Chapter it has been concluded that the rate of proton transfer greatly exceeds the rate of electron transfer. However, the observation of a slope of 0.3 in Figure 17 suggests that electron transfer is not entirely independent of proton transfer over this pH range.

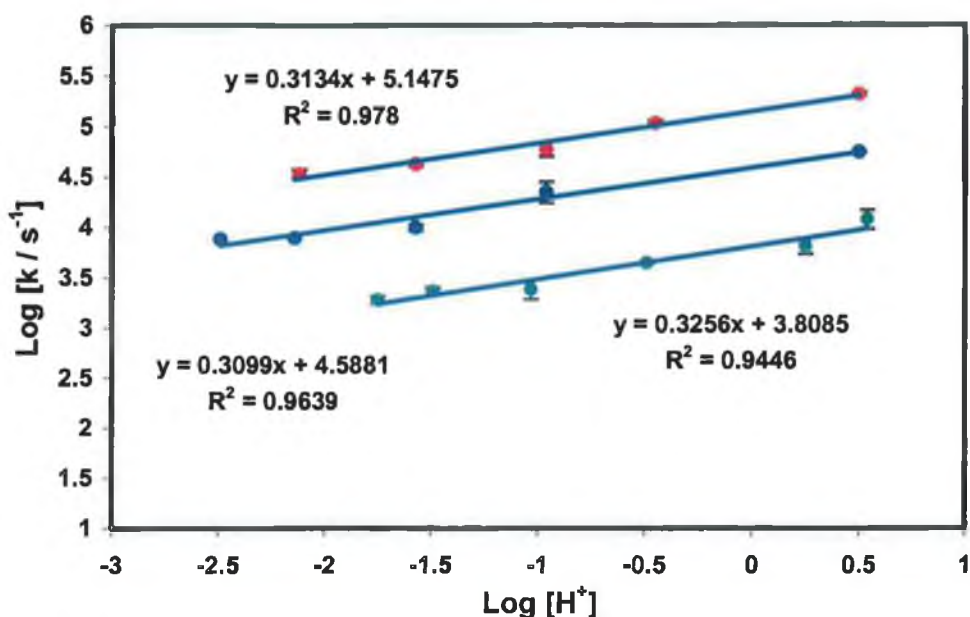
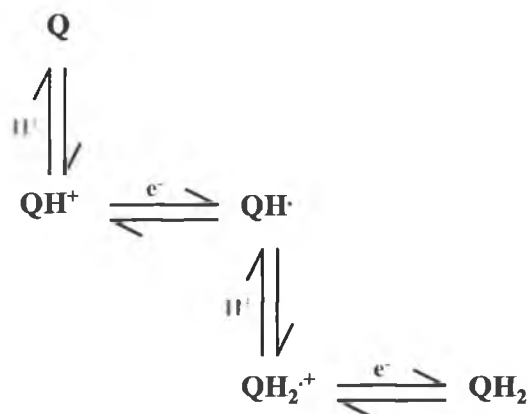


Figure 17. Rate constants as a function of the concentration of HClO_4 . Data collected using a $5\mu\text{M}$ 1,2,4-AQASH solution in 1M HClO_4 , the pH was varied using concentrated NaOH . (■) denotes values determined from the adiabatic electron transfer model presented in Table 3 above; (●) and (■) denote values from chronoamperometric measurements in reduction and oxidation directions respectively, standard rate constants were determined from the Butler Volmer theory of electron transfer at each pH.

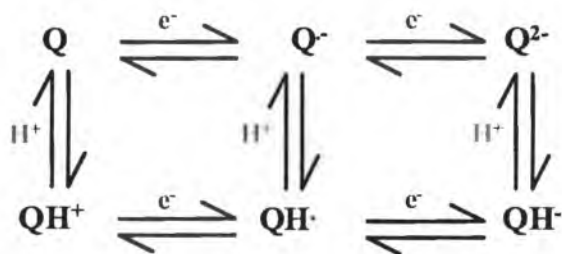
With these kinetic results, and knowledge of the pK_a values for the functional groups in this molecule the mechanism of proton and electron transfer at low pH can be proposed. The experimental results from this chapter show that the rate of proton transfer greatly exceeds the rate of electron transfer at least up to pH 5. This suggests that electron transfer is the rate limiting step in low pH media. The most likely intermediates in the scheme of squares for 1,2,4-AQASH are displayed in Scheme 1. The other intermediates in the nine-member box scheme can be ignored at low pH as the pK_a s for QH_2^{2+} and Q^{2-} are at 9.85 and 11.40, respectively,⁹ and therefore, cannot be involved in the redox mechanism at low pH. The mechanism is H^+e^- for the reduction step and e^-H^+ for the oxidation step.

Scheme 1. Possible intermediates in the 9-member box scheme for oxidation and reduction of anthraquinone at low pH.



At high pH the mechanism of reduction and oxidation is more complicated and more difficult to determine experimentally. From the potential-pH data it appears that electron transfer is independent of proton transfer. However, the rate constants for electron transfer have not been probed as the CV response becomes ill-defined at high pH values. Previous publications^{3,12} focusing on elucidating the redox mechanism of anthraquinone derivatives propose that the reaction proceeds by $e^-H^+e^-H^+$. From the analysis of the experimental data presented in Section 5.1 of this chapter it has been concluded that the reduced form of the anthraquinone is the deprotonated hydroquinone, QH^- , at high pH. Therefore, the reduction reaction could only involve the intermediates illustrated in Scheme 2 below. The anthraquinone/hydroquinone conversion thus involves two electrons and one proton and the possible mechanisms are $e^-H^+e^-$, $e^-e^-H^+$ or $H^+H^+e^-$. However, further details of the redox mechanism at high pH are not obtainable from the experimental results presented in this chapter.

Scheme 2. Possible intermediates in the 9-member box scheme for oxidation and reduction of anthraquinone at high pH.



5.5 Conclusions

It is evident from the literature survey presented in chapter 1 of this thesis that there is significant interest in the elucidation of the mechanism of proton and electron transfer in anthraquinone derivative molecules. While Vetter^{4,5} and Laviron^{6,7,8,9} have presented extensive publications detailing the theory of coupled proton and electron transfer less work has focused on experimental studies.

The experimental work presented in this chapter detailed a number of methods by which heterogeneous electron transfer rate constants can be measured. Fast scan rate cyclic voltammetry of 1,2,4-AQASH spontaneously adsorbed on a mercury surface was measured. At high scan rates the peak-to-peak potential separation was principally due to the kinetics of electron transfer. The results were fit to the Laviron Formulation,⁴¹ which is based on the Butler Volmer theory of electron transfer. Cyclic voltammograms that were run at scan rates of 800 Vs⁻¹ and above were fit to a CV simulation model that was developed by Loughman and Forster.²⁷ This model was based on the Marcus theory of electron transfer. One significant feature of this analysis was that values for the reorganization energy could be approximated. Values in the range 17 to 23 kJ mol⁻¹ were predicted for the total reorganization energy. No publication has dealt so far with fitting experimental data related to anthraquinone derivatives to the Marcus theory. A value of 56 kJ mol⁻¹ was calculated using the theoretical Marcus model. Therefore, it can be concluded that the reorganisation energy in this system is mainly due to outer sphere reorganization.

Chronoamperometry measurements were carried out to determine the rate of heterogeneous electron transfer. The data was fit to the Butler Volmer theory of electron transfer. This method of analysis allowed the measurement of the forward and reverse rate constants and revealed that there was a significant difference between the rate of the oxidative and reductive reactions. From potential dependent chronoamperometry data at low pH a value for the reorganization energy in the oxidation reaction was determined to be approximately 28 kJ mol⁻¹. The total reorganization energy for the reduction reaction was predicted to be at least 43 kJ mol⁻¹. Electron transfer rates were probed in detail from pH values of 0 to 5. These proton concentration dependent experiments allowed an estimation of the sequence of proton and electron transfer in oxidation and reduction directions at low and high pH.

5.6 References

1. Forster, R.J., Keyes, T.E., Farrell, M., O'Hanlon, D., *Langmuir*, **2000**, 16, 9871.
2. Bard, A.J., Faulkner, L.R., *Electrochemical Methods : Fundamentals and Applications, Second Edition*, Wiley, New York, **2001**, Chapter 1.
3. Xu, C., *Thesis, University of Illinois at Urbana-Champaign*, **1992**, Chapter 1.
4. Vetter, K.J., *Z. Electrochem.*, **1952**, 56, 797.
5. Vetter, K.J., *Electrochemical Kinetics, Academic Press, New York*, **1967**.
6. Laviron, E., *J. Electroanal. Chem.*, **1981**, 124, 9.
7. Laviron, E., *J. Electroanal. Chem.*, **1981**, 130, 23.
8. Laviron, E., *J. Electroanal. Chem.*, **1983**, 146, 15.
9. Laviron, E., *J. Electroanal. Chem.*, **1984**, 164, 213.
10. Walczak, M.M., Dryer, D.A., Jacobson, D.D., Foss, M.G., Flynn, N.T., *J. of Chem. Educ.*, **1997**, 74, 1195.
11. Brett, C.M.A., Oliveira-Brett, A.M., *Electrochemistry: Principles, Methods and Applications*, Oxford Science Publications, Oxford, **1993**.
12. Forster, R.J., O'Kelly, J.P., *J. of Electroanal. Chem.*, **2001**, 498, 127.
13. O'Kelly, J.P., Forster, R.J., *The Analyst*, **1998**, 123, 1987.
14. Thorp, H.H., *Journal of Chemical Education*, **1992**, 69, 250.
15. Sato, Y., Fujita, M., Mizutani, F., Uosaki, K., *J. of Electroanal. Chem.*, **1996**, 409, 145.
16. Eggins, B.R., Chambers, J.Q., *Chem. Commun.*, **1969**, 232.
17. Eggins, B.R., Chambers, J.Q., *J. Electrochem. Soc.*, **1970**, 117, 186.
18. Bailey, S.I., Ritchie, I.M., *Electrochim. Acta*, **1985**, 30, 3.
19. Laviron, E., *J. Electroanal. Chem.*, **1974**, 52, 395.
20. Brown, A.P., Anson, F.C., *Anal. Chem.*, **1977**, 49, 1589.
21. Butler, J.A., *Trans Faraday Soc.*, **1924**, 19, 729.
22. Erdey, Gruz, T., Volmer, M.Z., *Physik. Chem.*, **1930**, 150A, 203.
23. Marcus, R.A., *J. Chem. Phys.*, **1956**, 24, 4966.
24. Marcus, R.A., *J. Chem. Phys.*, **1965**, 43, 679.
25. Marcus, R.A., *Ann. Rev. Phys. Chem.*, **1964**, 15, 155.
26. Forster, R. J., *Chemical Society Reviews*, **1994**, 289.
27. Loughman, J.P., Ph.D. Thesis, *Voltammetry of Adsorbed Monolayers : Computer Simulation and Experiment*, **2001**.

28. Finklea, H.O., Hanshew, D.D., *J. Am. Chem. Soc.*, **1992**, 114, 3173.
29. Chidsey, C.E.D., *Science*, **1991**, 251, 919.
30. Weber, K., Creager, S.E., *Anal. Chem.*, **1994**, 66, 3164.
31. Nelder, Mead, *Computer J.*, **1965**, 79, 308.
32. Forster, R.J., Faulkner, L.R., *J. Am. Chem. Soc.*, **1994**, 116, 5444.
33. Forster, R.J., Figgemeier, E., Loughman, P., Lees, A., Hjelm, J., Vos, J.G., *Langmuir*, **2000**, 16, 7871.
34. Forster, R.J., Loughman, P., Keyes, T.E., *J. Am. Chem. Soc.*, **2000**.
35. Forster, R.J., Faulkner, L.R., *J. Am. Chem. Soc.*, **1994**, 116, 5453.
36. Finklea, H.O., Hanshew, D.D., *J. Am. Chem. Soc.*, **1992**, 114, 3173.
37. Finklea, H.O., Ravenscroft, M., Snider, D.A., *Langmuir*, **1993**, 9, 223.
38. Chidsey, C.E.D., Bertozzi, C.R., Putvinski, T.M., Mujisce, A.M., *J. Am. Chem. Soc.*, **1990**, 112, 4301.
39. Forster, R.J., O'Kelly, J.P., *J. Phys. Chem.*, **1996**, 100, 3695
40. Forster, R.J., *Inorg. Chem.*, **1996**, 35, 3394.
41. Laviron, E., *J. Electroanal. Chem.*, **1979**, 101, 19.
42. Brett, C.M.A., Oliveira-Brett, A.M., *Electrochemistry: Principles, Methods and Applications*, Oxford Science Publications, Oxford, **1993**.
43. Wightman, R.M., Wipf, D.O., *Electroanal. Chem.*, Vol 15., Marcel Dekker, New York, **1989**.
44. Forster, R.J., *Langmuir*, **1995**, 11, 2247.
45. Wightman, R.M., *Anal. Chem.*, **1981**, 53, 1125A.
46. Forster, R.J., *Analyst*, **1996**, 121, 733.
47. Forster, R.J., *Anal. Chem.*, **1996**, 68, 3143.
48. Forster, R.J., *J. Electrochem. Soc.*, **1997**, 144, 1165.
49. Berg, H., *Naturwissenschaften*, **1961**, 48, 714.
50. He, P., Crooks, R.M., Faulkner, L.R., *J. Phys. Chem.*, **1990**, 94, 1135.
51. Zhang, J., Anson, F.C., *J. Electroanal. Chem.*, **1992**, 331, 945.
52. Ta, T.C., Kanda, V., McDermott, M.T., *J. Phys. Chem.*, **1999**, 8, 1295.
53. Chambers, J.Q., *Chemistry of Quinonoid Compounds, Vol.2*, **1988**, 719.
54. Christian, G.D., *Analytical Chemistry, Fifth Edition*, Wiley and Sons Inc., **1994**.

Chapter 6

Nanodes – New Dimensions of Space and Time in Electroanalysis

“A will finds a way.”

- *Orison Sweet Marden*

6. Introduction

The fabrication of nanometer sized electrode tips is important for a number of applications, particularly various types of microscopies such as scanning tunneling microscopy (STM) and scanning electrochemical microscopy (SECM). Spatial resolution increases dramatically as the size of the scanning tip is decreased. As a result, much research effort has focused on the development of fabrication techniques to produce small tips displaying ideal electrochemical responses. The principal method utilized in literature to make nanometer dimension tips for application in STM has been etching procedures.^{1,2,3,4,5,6,7,8} This technique yields geometrically sharp tips, however one characteristic of the tip shape makes these tips less useful than the ones fabricated using a micropipette puller. When electrodes are electrochemically sharpened the height-to-radius ratio of the tip cannot be varied over a wide range causing the electrode radius to increase significantly as the electrode is polished.

This chapter outlines a method of fabricating micrometer to nanometer-sized electrodes using an argon ion based micropipette puller from Sutter Instrument Company. This method has been used previously by a number of research groups in the fabrication of nanoelectrodes, including Katemann and Schuhmann,⁹ Unwin et al.,¹⁰ Wong and Xu,¹¹ Shao and Mirkin,¹² Lewis et al.,¹³ Kim, Scarnlis and Ewing,¹⁴ and Wightman and Kelly.¹⁵ Some details of the procedures carried out in these studies and results obtained have already been discussed in section 1.7.4 of Chapter 1 of this document. Using a micropipette puller it is possible to fabricate nanoelectrodes, which have a long taper where the platinum wire is of nanometer dimension. However success requires careful selection of the parameters of the micropipette puller program and the materials used in the fabrication procedure. In the development of the fabrication technique platinum wire of two different grades, hard drawn and annealed were used. The glass capillaries used were aluminosilicate, borosilicate and quartz of various inner and outer diameters. The electrodes produced during different stages of the development of the method have been characterized using a number of techniques such as optical microscopy, scanning electron microscopy and cyclic voltammetry.

The earlier sections of this chapter focus on the fabrication of micrometer sized mercury electrodes of hemispherical geometry on platinum disk electrodes. These electrodes

have been used in the experimental work presented in Chapter 5 to measure fast heterogeneous electron transfer rate constants. Experiments, which deal with the deposition of mercury onto platinum nanoelectrodes will be discussed in the latter part of this chapter.

6.1 Fabrication of Mercury Microelectrodes

Mercury electrodes have been implemented extensively in many electrochemical research areas due to a number of significant features unique to this electrode material. These features have already been highlighted in section 1.7.4.1 of Chapter 1 of this work. For the purpose of the work presented in this thesis it is significant to note that mercury has a large negative potential window for electrochemical studies and also serves as an atomically flat surface for the adsorption of electroactive species from solution. Mercury microelectrodes were necessary in this study to measure fast heterogeneous electron transfer rates as presented in the previous chapter. Anthraquinone molecules are adsorbed parallel to the electrode surface at a distance of approximately 4-5 Å. As the electrode size is made smaller the response time decreases and the measurement of fast electron transfer rates is made possible. The procedure for the fabrication of hemispherical mercury electrodes of various sizes is described in this chapter. A variety of metals have been used as substrates for mercury deposition, these include platinum,^{16,17,18,19,20} iridium^{21,22} and carbon fiber^{23,24} microelectrodes. Platinum electrodes of radius between 5 and 12.5 μm have been used in this work.

The fabrication procedure for these electrodes is outlined briefly here but is explained in more detail by O'Hanlon,²⁵ Faulkner²⁶ and Xu.²⁷ Firstly, the soft glass tubing, which forms the body of the electrode was cut into pieces 10-15 cm long. These glass pieces were soaked overnight in dilute nitric acid to remove any dirt or grease, which may adhere to the inside of the glass. When the glass was removed it was rinsed thoroughly with Milli-Q water, acetone and again with Milli-Q water. The glass was then dried in an oven for 30 minutes. The dried lengths of glass were heated in the center using a Bunsen flame and the center section was drawn apart once it became soft enough. Once the glass cooled down the glass was snapped in the middle to form two tapered ends.

At this stage a piece of micrometer sized platinum wire about 1 cm in length was cut. The wire was held with a tweezers, washed in acetone and dried. An aluminium wire of

approximate length 4 cm was cut and bent in a zig-zag pattern. This wire was wound around the copper wire and soldered in place. The cleaned micrometer sized platinum wire was wound around the other end of the aluminium wire and soldered to make an electrical connection. This wire assembly was inserted into the glass tubing, as illustrated in Figure 1. The glass was then sealed around the micrometer sized wire by applying a vacuum to the open end of the glass tubing. Finally the open end of the glass capillary was covered with a plastic cap, which was secured in place using araldite epoxy resin. Mercury can then be deposited on the platinum surface to produce a micrometer sized mercury electrode. For the deposition procedure to be successful the platinum surface must be clean. This was ensured by electrochemical cleaning and polishing of the platinum surface, as outlined in the following section.

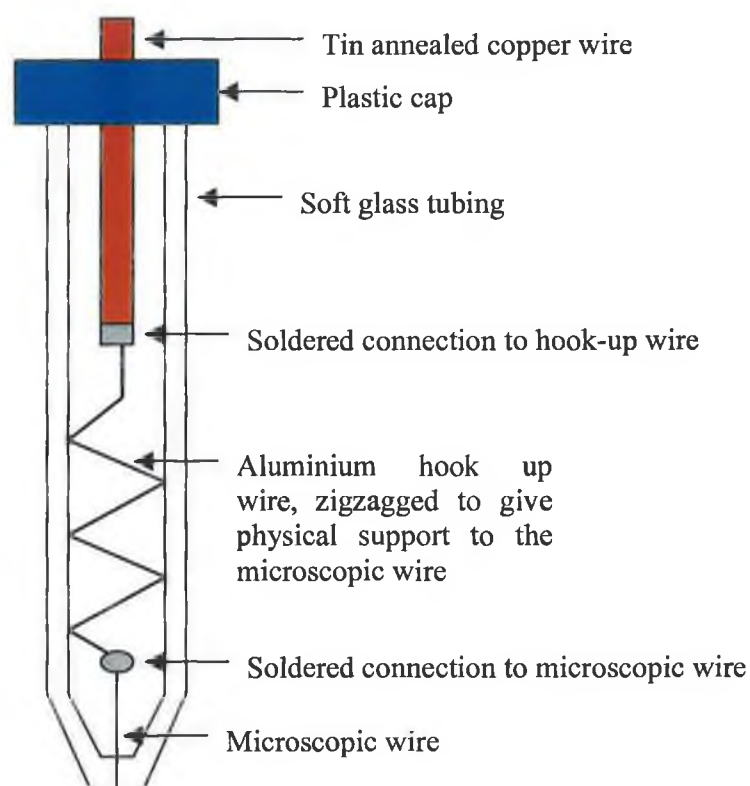


Figure 1. Schematic illustrating the cross section of a micrometer sized platinum electrode.

6.1.1 Microelectrode Preparation

Electrodes were polished on polishing cloths obtained from Struers, Denmark. Alumina was placed on the cloth and mixed with a small amount of Milli-Q water to form a paste. The electrode was held at a 90° angle to the polishing cloth and rotated in a figure of eight approximately 50 times. The electrode was then placed on another part of the polishing cloth and the procedure repeated to ensure uniform polishing of the entire surface. At this stage, the electrode was rinsed with Milli-Q water, sonicated to ensure the removal of all alumina particles from the surface and rinsed with Milli-Q water once more. A cyclic voltammogram was run in a suitable electrolytic solution to see the capacitive current response. The electrolyte used was 0.1 M LiClO₄, and CVs were run at a scan rate of 0.2 Vs⁻¹. A typical CV response at this stage of the polishing procedure is shown in Figure 2.

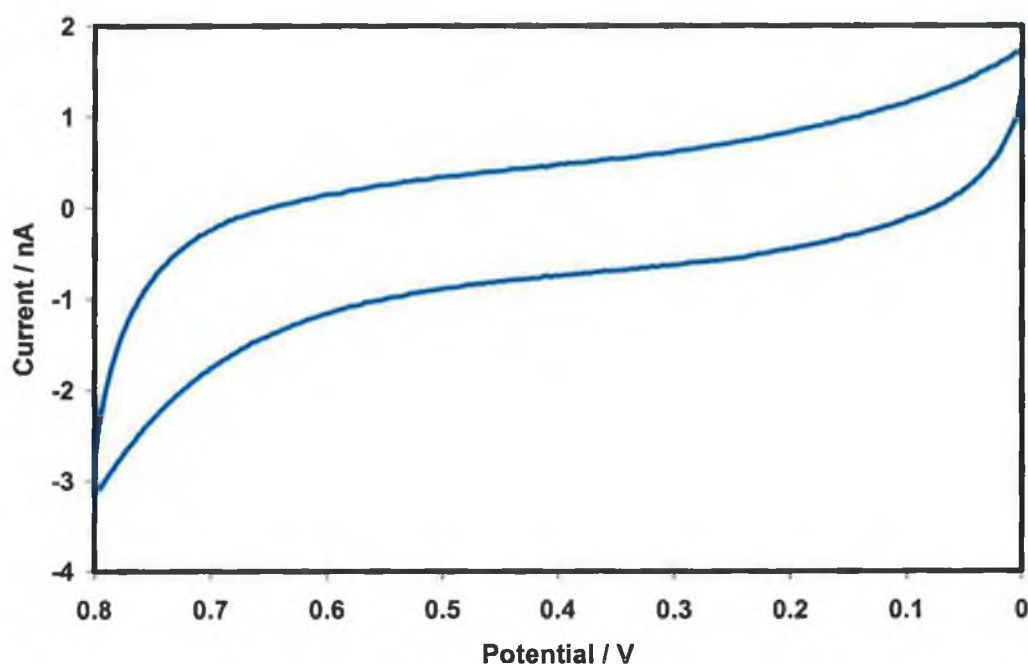


Figure 2. Background cyclic voltammogram for a 12.5 μm radius platinum electrode in 0.1 M LiClO₄ following polishing with 0.3 μm alumina particles. The scan rate is 0.2 Vs⁻¹. The potential limits are 0 and 0.8 V with the initial potential set at 0 V.

The polishing procedure described above was repeated, successively decreasing the size of the alumina particles to 5, 1 and 0.3 μm . Background CVs were run in 0.1 M LiClO₄ solution between particle sizes to monitor the progress of the cleaning process. As the alumina particle size was decreased the background capacitive response should become more stable. An unchanging flat capacitance indicates that the electrode is free of adsorbed electroactive impurities, whereas a sloped background indicates that there is high resistance flowing between the electrode and electrolytic solution. Figure 3 shows improvement of the CV response as the polishing procedure progresses.

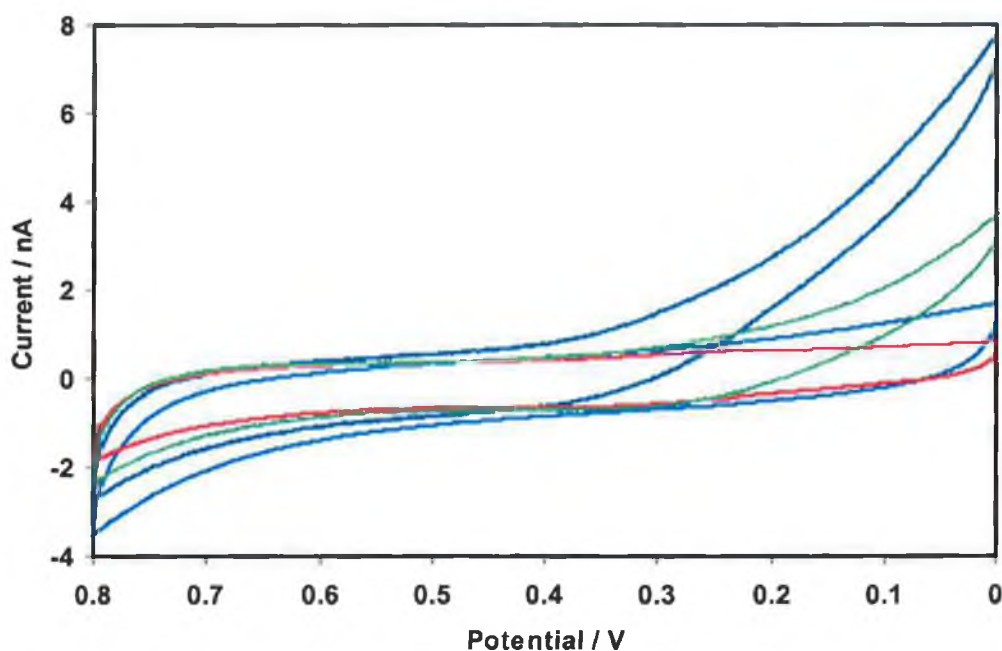


Figure 3. Cyclic voltammetric response of a 12.5 μm radius platinum electrode immersed in 0.1 M LiClO₄ following polishing with 5 ($-$), 1 ($-$), and 0.3 μm ($-$) ($-$) alumina particles. The scan rate is 0.2 Vs^{-1} and the initial potential is 0 V.

Platinum electrodes were electrochemically cleaned by cycling in 1 M H₂SO₄. The CVs were run between potential limits of 1.4 and -0.25 V and the CV response is shown in Figure 4. The peaks in the cyclic voltammogram are due to the oxidation and reduction of platinum at the surface of the electrode and oxidation and reduction of hydrogen at the adsorbed electrode surface. The peaks are labeled in Figure 4 and are designated as follows;²⁸

O_a – formation of adsorbed oxygen and platinum oxide layers.

O_c – reduction of oxide layers.

H_a – oxidation of adsorbed hydrogen.

H_c – reduction of adsorbed hydrogen.

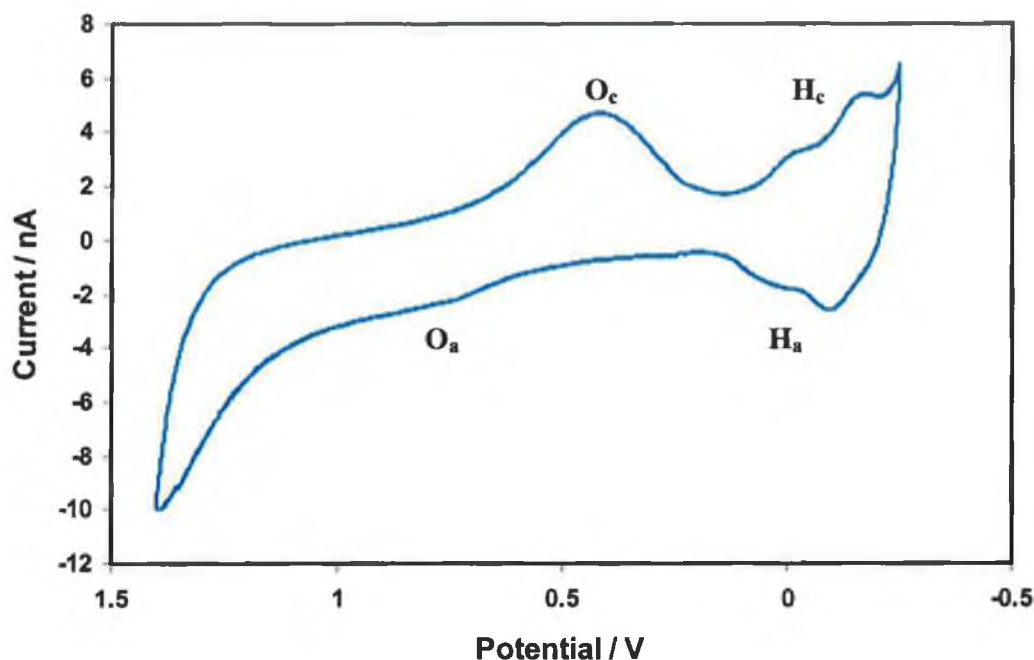


Figure 4. Cyclic voltammogram showing the electrochemical response of a 5 μm radius platinum microelectrode immersed in 1 M H_2SO_4 . The scan rate is 0.1 V s^{-1} . The potential limits are 1.4 and -0.25 V . The initial potential is -0.25 V .

The area under the oxygen peak can be used to calculate the surface roughness, which is important to evaluate the cleanliness of the platinum surface of the electrodes and this is described in a later section. The charge under the voltammetric peak for hydrogen adsorption can be integrated to provide a value for the electrochemical area of the electrode. This is described in Section 6.3.3.1 of this chapter to provide an estimate of the size of the electrodes produced.

6.1.2 Mercury Deposition and Determination of Electrode Area

Once the platinum surface has been electrochemically cleaned mercury deposition was carried out. The deposition solution contained 5.7 mM mercury (I) nitrate dihydrate (Aldrich) made up in 1 M KNO_3 and 0.5% HNO_3 . The technique used for deposition was bulk electrolysis with coulometry^{29,30} using a CH Instruments 660 potentiostat with the deposition potential set at -0.2 V. These parameters were deemed suitable for deposition of mercury onto the platinum surface to form a hemispherical drop. These conditions also gave the most reproducible method of making micrometer-sized mercury electrodes. When deposition was carried out at potentials other than -0.2 V the deposition process was slower, increasing the time taken to form a hemispherical drop on the platinum microelectrode surface. Following a deposition time of 200 s the electrode is removed from the mercury deposition solution, rinsed and placed in a solution containing 5 μM 1-amino, 2-sulphonic, 4-hydroxyanthraquinone. The faradaic current, which results from the oxidation and reduction of the electroactive species can be used to determine the area of the hemispherical mercury drop deposited. This is possible due to the fact that the mercury surface is atomically smooth and so the real and geometric areas of the electrode are identical. Hence, a method, which relates the faradaic current to the electrode area can be used to calculate the area. Methods used to evaluate the area of platinum nanoelectrodes are presented in the following section of this chapter.

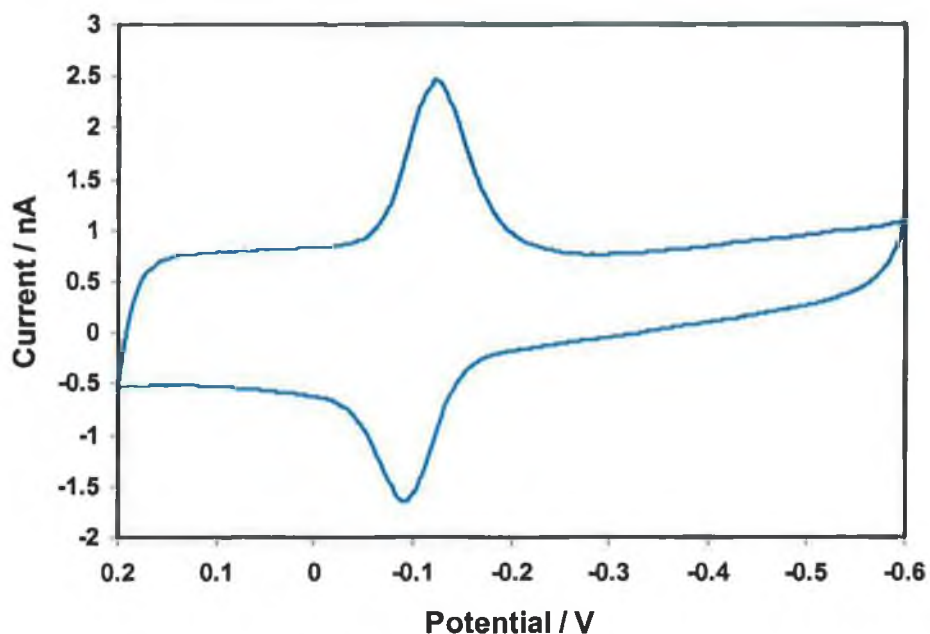


Figure 5. Cyclic voltammogram for a 5 μm radius platinum electrode after deposition of mercury for 200 s. The electrolytic solution contains 5 μM 1,2,4-AQASH and 1 M HClO_4 as the supporting electrolyte. The scan rate is 5 Vs^{-1} and the initial potential is set at 0.2 V.

The size of the mercury electrode can be calculated from the CV response in Figure 5 by using Equation (1),

$$A = \frac{Q}{\Gamma nF} \quad (1)$$

where A is the area of the electrode, Q is the charge passed in the redox reaction, Γ is the surface coverage of the electroactive species on the electrode surface, n is the number of electrons transferred and F is Faradays constant. When using this equation it has been assumed that a 5 μM solution of 1,2,4-AQASH yields monolayer coverage, i.e., $1.1 \times 10^{-10} \text{ mol cm}^{-2}$. This assumption is reasonable given the electrochemical properties of 1,2,4-AQASH detailed in Chapter 3 of this thesis. Once a CV has been recorded, the electrode was rinsed and placed in the mercury deposition solution for a further 200 s. The electrode area was then measured the same way as detailed above using a 5 μM 1,2,4-AQASH solution. This three-step procedure of deposition,

measurement of the electrode area and rinsing was repeated in order to determine a relationship between the deposition time and the surface area. The CVs at deposition times from 200 to 2200 s are illustrated in Figure 6.

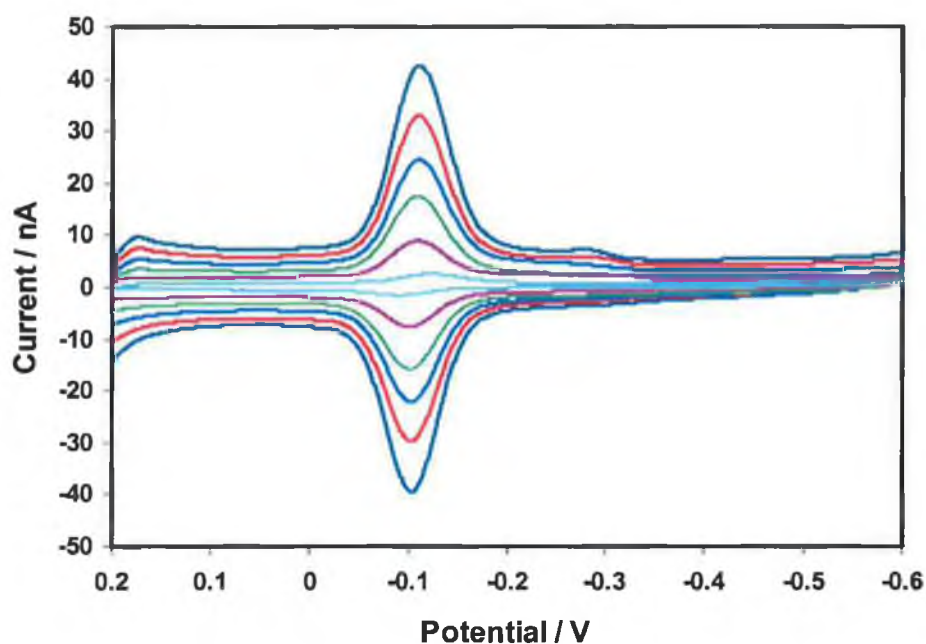


Figure 6. Cyclic voltammograms of 1,2,4-AQASH on a mercury electrode after mercury deposition from mercury (I) nitrate dihydrate for times of 200 (—), 600 (—), 1000 (—), 1400 (—), 1800 (—) and 2200 (—) seconds. The scan rate is 5 Vs^{-1} and the potential limits are 0.2 and -0.6 V . The initial potential is 0.2 V.

The surface coverage at each deposition time has been calculated and the results are graphed in Figure 7. A linear relationship results up to a deposition time of 2400 s. The radius of the hemispherical Hg electrode a deposition time of 2400s is $24 \mu\text{m}$ and further deposition caused the Hg drop to become unstable and drop off the platinum surface. Smaller drops were seen to be stable on the platinum surface for longer periods of time but careful handling is necessary when carrying out experiments.

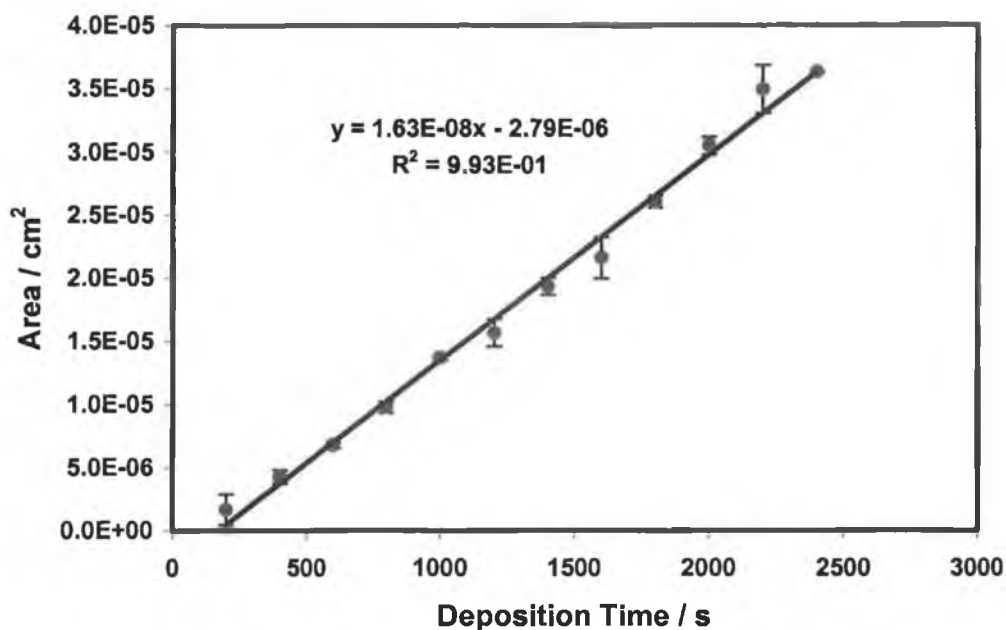


Figure 7. Relationship between the deposition time and the area of the mercury electrode produced. The deposition solution contained 5.7 mM mercury (I) nitrate dihydrate made up in 1 M KNO₃ and 0.5 % HNO₃. The deposition potential was set at -0.2 V.

6.2 Construction of Nanoelectrodes

This section describes a method of producing micrometer to nanometer-sized electrodes using a P-2000 micropipette puller from Sutter Instruments. The materials used in the fabrication of the nanodes in this work were platinum wire with a diameter of 25 μm – hard temper obtained from Goodfellow and quartz glass capillaries obtained from Hilgenberg GmbH, Malsfeld, Germany. The capillaries were 100 mm long with an outer diameter of 0.9 mm and an inner diameter of 0.3 mm leading to a wall thickness of 0.3 mm. Quartz and borosilicate and aluminosilicate capillaries obtained from Sutter Instrument Co. with varying inner and outer diameters were used initially but these capillaries proved unsuitable for fabrication of nanometer-sized electrodes due to a number of reasons. Firstly borosilicate and aluminosilicate glasses have a lower melting point than quartz and so the glass capillaries melted at a lower temperature in the laser puller and the heat was not transferred to the platinum wire to soften it. Also,

capillaries of larger inner diameter than 0.3 mm were unsuitable as this prevented transfer of heat from the insulating glass to the platinum wire before the pulling step.

The micropipette puller implemented in the construction of the platinum nanoelectrodes is illustrated in Figure 8 below. This instrument contains five parameters, which can be varied to produce an electrode of nanometer size. These parameters are:

1. **Heat** – output power of the laser, depending on the type of material used as the insulator different heat settings are required to melt the glass.
2. **Filament** – scanning pattern of the laser beam, which determines the length of the capillary heated.
3. **Velocity** – the velocity at which the puller bars, containing the glass-wire assembly move away when the hard pull is executed.
4. **Delay** – controls the timing of the activation of the hard pull relative to the deactivation of the laser, the shorter the delay the longer the taper and the smaller the tip diameter.
5. **Pull** – controls the force of the hard pull, which determines the length of the taper and the size of the tip produced.

Figure 8 illustrates the components of the micropipette puller and shows the experimental setup, which was used to fabricate nanoelectrodes in this work. The micropipette puller clamps the capillary containing the platinum wire in place at both ends, as illustrated below. Both ends of the capillary are then attached to silicon tubing which serves to evacuate the glass capillary during the fabrication process to form an electrode with the platinum wire located exactly in the center of the glass capillary. The fabrication procedure is described in detail in the following section of this chapter.

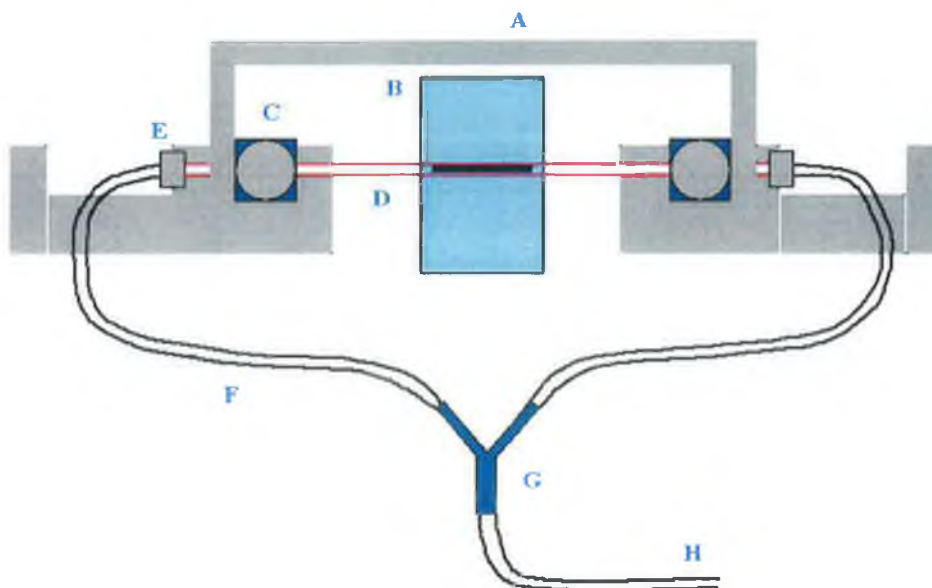


Figure 8. Micropipette puller, (A) metal clamp to prevent the hard pull during the first heating process, (B) laser beam and retro mirror, (C) capillary fixing screws, (D) quartz glass capillary with inserted platinum wire, (E) puller bars, (F) silicon tube connecting to glass capillary to allow its evacuation, (G), Y-connector and (H) silicon tube connection to the vacuum pump.

The five parameters listed above for the micropipette puller have been varied systematically to obtain a set of parameters, which melts the glass body and the platinum wire simultaneously, that can then be drawn to produce a nanoelectrode. The most reproducible results were obtained when the hard pull took between 4 and 6 seconds. Longer times produced electrodes with uneven taper lengths. If the pull takes less than 4 seconds the platinum wire was frequently heated too fast and was not drawn with the capillary once the hard pull was executed, as shown in the microscope images in Figure 9 (A) and (B). A Nikon ECLIPSE ME600D Microscope at 10X magnification was used to image the electrodes and the images were captured using a Nikon Coolpix 950 digital camera.

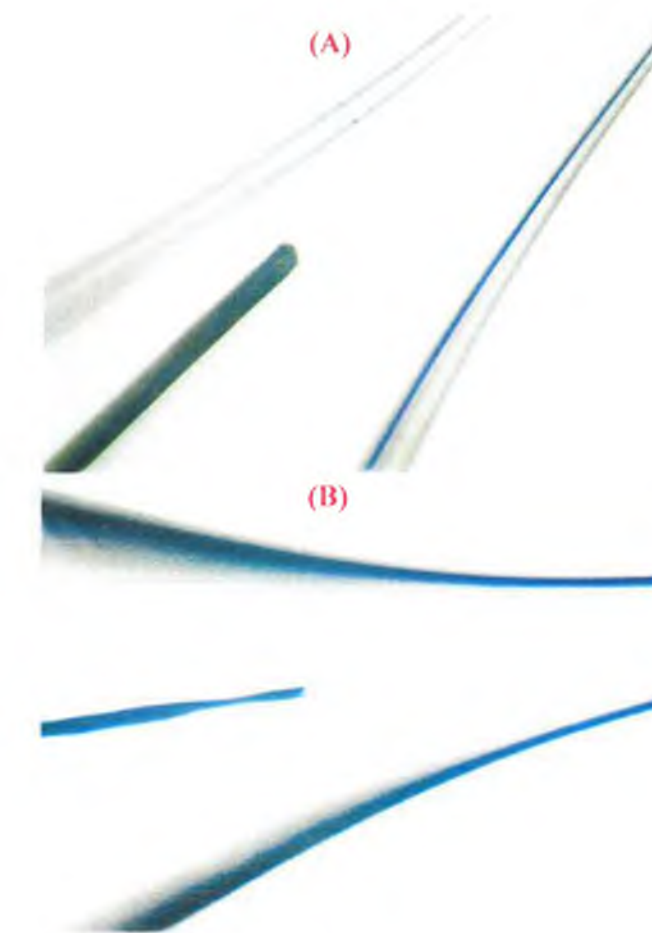


Figure 9. Optical microscope images of electrodes after the pulling process, the parameters in the pulling program were, (A) Heat – 750, Filament – 4, Velocity – 55, Delay – 120 and Pull – 150 and (B) Heat – 550, Filament – 4, Velocity – 55, Delay – 70 and Pull – 150.

6.2.1 Fabrication Process

A stepwise description of the fabrication process is shown in Figure 10. A piece of 25 μm platinum wire 15 to 20 mm long is cut from the reel and placed using a tweezers into the quartz capillary, Figure 10(A). This is placed in the midpoint of the capillary length and the glass-wire assembly is then placed in the laser puller using the fixing screws. Silicon tubing is connected to the ends of the capillary and the vacuum is switched on to evacuate the capillary prior to the first heating step. In order to fabricate a nanoelectrode using the micropipette puller, it is essential that the quartz melts around the platinum wire, and then the heat is transferred to the platinum wire. In a conventional experiment, the laser puller applies a constant pulling force on the glass

capillary in order to detect the viscosity of the glass during heating and the hard pull initiates once a sufficiently low viscosity is attained. This automatic pulling of the glass has to be stopped when fabricating nanoelectrodes so a two-step heating process has been implemented. During the first heating step a clamp is placed on the assembly to prevent the pulling bars from separating. This ensures that the platinum wire is heated and softened sufficiently to be pulled to smaller dimensions during the second heating step.

The parameters in the first heating program are: Heat – 775, Filament – 5, Velocity – 100, Delay – 120 and Pull – 1. The laser puller and stop watch are switched on simultaneously. After 40 seconds of heating the laser puller program is stopped for 20 seconds and then restarted for a further 40 seconds. This was done to prevent the laser from overheating and the procedure was repeated five times to ensure that the platinum wire was sealed inside the quartz glass capillary, Figure 10(B). The clamp was removed and the second heating program: Heat – 600, Filament – 2, Velocity – 130, Delay – 150 and Pull – 220 was activated as soon as possible to prevent the glass wire assembly from cooling down. The second program takes between 4 and 6 seconds to produce two platinum nanoelectrodes sealed in glass, Figure 10(C). The platinum wire inside the glass capillary is connected to a copper wire using a two component silver filled epoxy glue and left to dry in an oven for two hours, Figure 10(D). The electrodes are then polished as outlined in the following section until electrical contact is made, Figure 10(E).

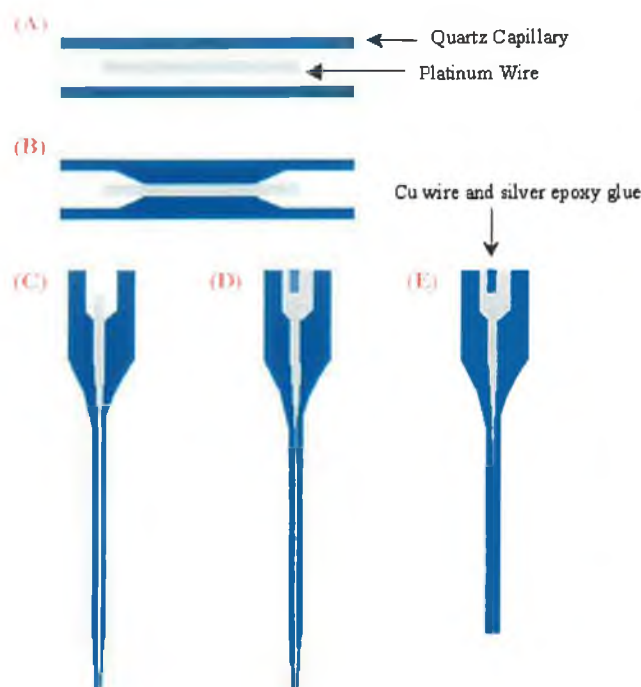


Figure 10. Step-by-step summary of the microelectrode fabrication process, (A) insertion of the Pt-wire into the glass capillary, (B) cylindrical melting of the quartz glass to invoke contact between the glass and Pt-wire, also ensuring positioning of the Pt-wire in the center of the glass capillary, (C) simultaneous pulling of the quartz glass capillary and Pt-wire, (D) contacting of the Pt-wire by means of a copper wire and a silver filled epoxy glue and, (E) polishing of the microelectrode.

6.2.2 Polishing Procedure

To polish nanoelectrodes the procedure developed by Katemann and Schuhmann⁹ was implemented. The nanoelectrode was placed in cylindrical brass holder and secured in place using a soft silicon tube and a fixing screw, Figure 11. The brass holder was rotated at a speed of 5000 rpm and slowly lowered down onto the surface of the polishing plate using manual micropositioning elements. Old computer hard disks were used as the polishing platform, due to the flatness of the surface. Polishing is performed on a soft polishing cloth in a 50 nm particle size alumina paste. The length of time polishing influences the size of the nanoelectrode produced and frequently a few seconds of polishing is sufficient to form electrical contact. Cyclic voltammograms were run at intervals during the polishing procedure to check if electrical contact had

been made. Careful and slow polishing is required to fabricate electrodes in the small nanometer range.

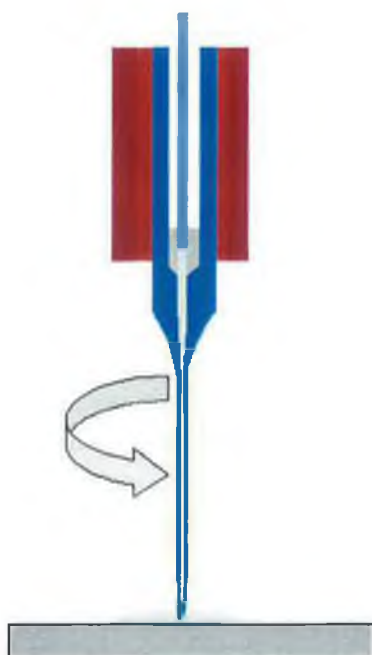


Figure 11. Schematic representation of the setup for nanoelectrode polishing.

6.3 Characterisation of Nanoelectrodes

In an effort to characterize these nanometer electrodes a number of techniques have been implemented. Optical microscopy images provide a rapid and simple way of visualizing the electrode after the pulling process to see if the wire has been drawn to smaller dimensions. Scanning electron microscopy provides some information. However, the information obtainable from this technique is limited when looking at structures of such small dimensions insulated in quartz. The most informative method of characterization used in this work was cyclic voltammetry. The quality of the seal could be tested and an estimate of the electrode area and geometry was obtained from the measurements. A brief summary of the results from all three methods is outlined in the following sub-sections.

6.3.1 Optical Microscopy

In the initial stages of this work much experimental time was spent developing a program, which would produce a nanometer size electrode. Hence, a rapid characterization technique was necessary to determine the probable success of each experiment after the pulling step. A Nikon ECLIPSE ME600D Microscope with a mercury lamp as the light source was used to image the nanoelectrode assemblies. Images were captured using a Nikon Coolpix 950 digital camera. Figure 9 in Section 6.2 of this chapter shows an image of a nanode after the pulling process. As is evident from this image, the parameters in the pulling program were not compatible with the quartz capillaries and platinum wire to fabricate a nanoelectrode. Such electrodes were discarded immediately. This method of characterization was much faster than characterization by SEM or cyclic voltammetry and so saved time in the development of the fabrication process.

Once the parameters in the pulling program were refined to produce a nanoelectrode, optical microscopy was used to visualize the electrodes. The fabrication process has been explained in Section 6.2.1 above with each step displayed in Figure 10. The images in Figure 12 below suggest that nanodes were formed as expected. The first heating step produces a 25 μm platinum wire sealed in quartz glass, Figure 12(A), this assembly is pulled from micrometer to nanometer dimensions in the second heating step, Figure 12(B) and (C). Figure 12(B) shows clearly that the wire has been softened sufficiently in the second heating step and is pulled with the glass to smaller dimensions.

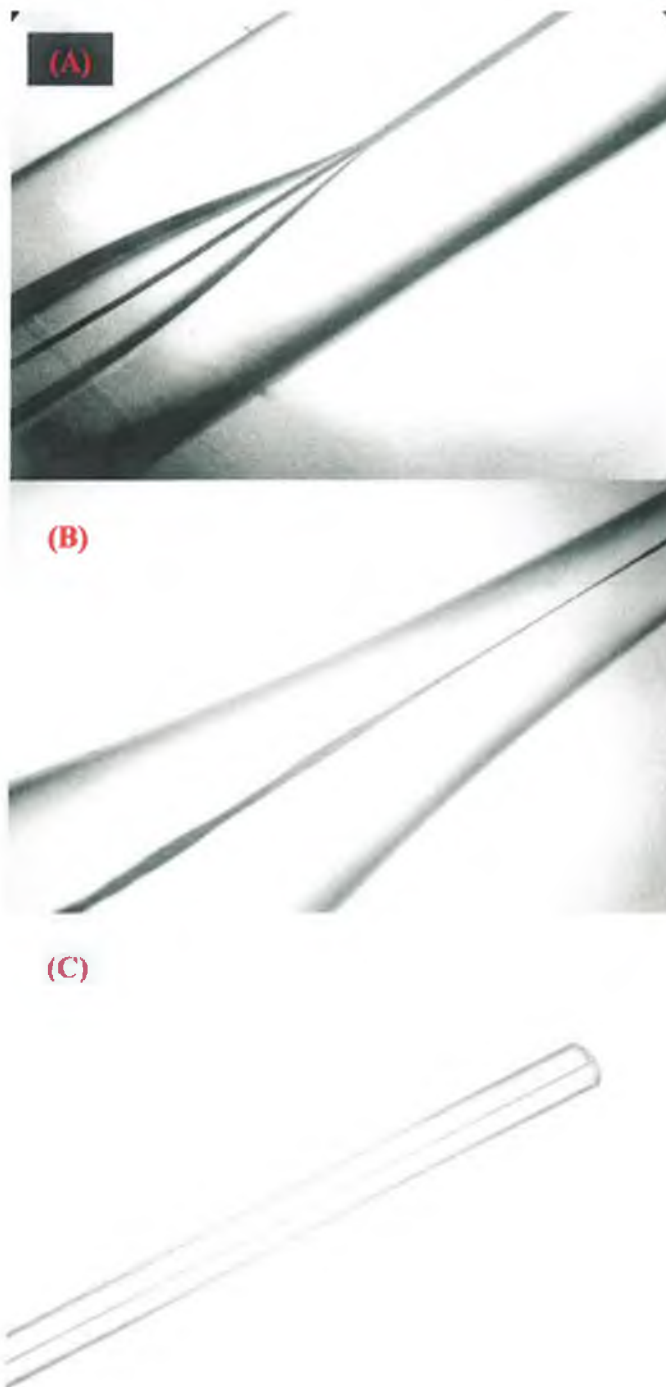


Figure 12. Optical microscope images of an electrode after the two step pulling process. (A) step 1 – a tight seal has formed between the 25 μm platinum wire and the quartz glass capillary and (B) step 2 – the platinum wire is drawn with the quartz glass capillary to form a nanometer sized electrode. (C) shows the tip of a nanoelectrode.

6.3.2 Scanning Electron Microscopy

Scanning electron microscopy has been used extensively in the characterization of nanometer-sized electrodes. A Hitachi S3000N Scanning Electron Microscope was used to obtain the SEM images presented in this section. Scanning electron microscopy is a useful technique to characterize electrodes of micrometer dimensions as discussed in Section 1.7.6 of Chapter 1. Wightman and Kelly¹⁵ have successfully imaged carbon fiber electrodes of 10 μm radius to determine the geometry of the electrode after the fabrication and polishing steps. This publication claims that the quality of the seal between the carbon fiber and glass capillary may be seen from SEM images also. However, as illustrated in this work, this is only possible if the electrode radius is 20 μm or greater.

Figure 13 (A) and (B) show SEM images of micrometer sized platinum electrodes, which were taken during the development of the pulling program. These images show that the materials and pulling parameters used were unsuitable for fabrication of an electrode of small dimensions. The materials used for fabrication were borosilicate capillaries with an outer diameter of 1 mm and inner diameter of 0.75 mm (Sutter Instrument Co.) and hard temper platinum wire. The platinum wire wasn't drawn to a smaller dimension in the pulling process and a good seal between the wire and capillary was not produced. This could be due to a number of factors but is primarily due to the fact that the heat setting was too low to soften the platinum wire and borosilicate glass simultaneously before the hard pull. It is also evident from the SEM images that the borosilicate glass is uneven at the tip and this indicates that the hard pull took place too early effectively breaking the capillaries apart.

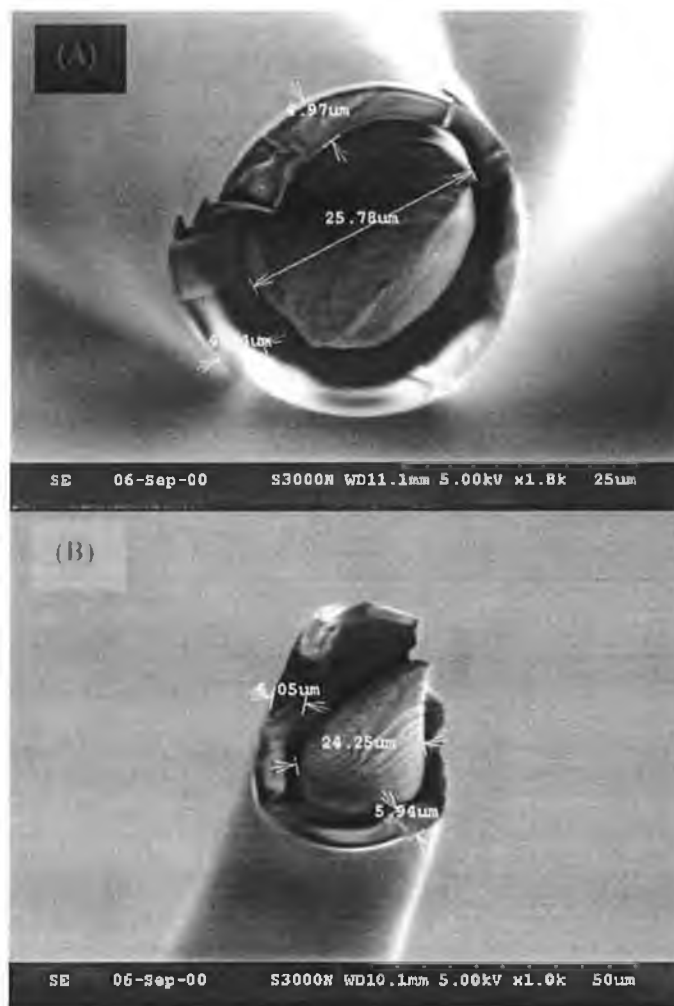


Figure 13. Scanning electron micrographs of micrometer-sized tips after the pulling process. The scale, magnification and accelerating voltage of images (A) and (B) are shown on the individual images.

The SEM images of nanoelectrodes provide much less characterization information due to the ultrasmall size of the electrodes imaged. Figure 14 shows a nanoelectrode after the pulling process. The image shows clearly that the quartz glass and platinum wire are pulled to very small dimensions by the micropipette puller. The length of the taper can be measured in SEM. However, attempts to image the tip of the nanoelectrode were unsuccessful because charging from the glass insulator caused the image to drift and a fine focus on the electrode tip could not be achieved. Figures 15 (A), (B) and (C) show typically the quality of images obtained when focusing on the electrode tip.



Figure 14. Scanning electron micrograph of a nanoelectrode which has been fabricated using the P-2000 Micropipette Puller from Sutter Instruments. The scale, magnification and accelerating voltage are displayed on the image.

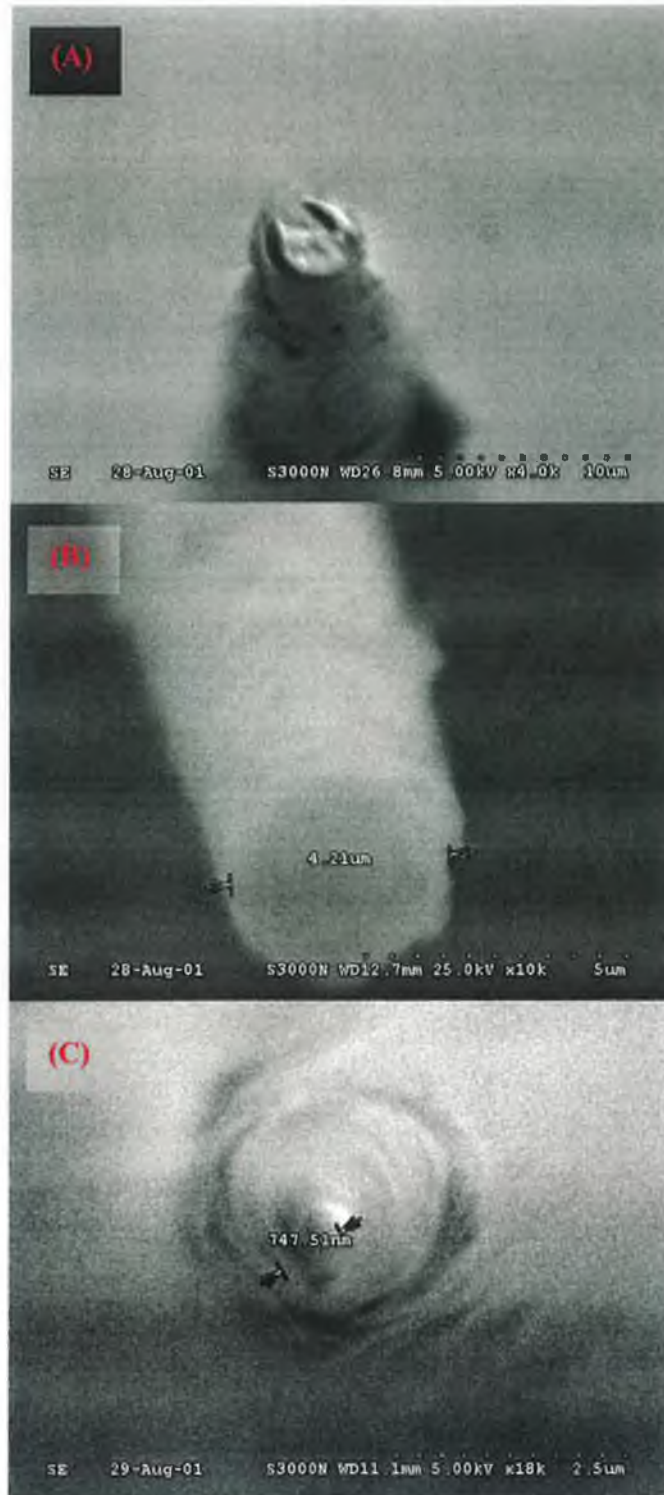


Figure 15. Scanning electron micrographs of submicrometer-sized tips after the pulling and polishing processes. The scale, magnification and accelerating voltage of images (A), (B) and (C) are shown on the individual images.

6.3.3 Cyclic Voltammetry

The most comprehensive and informative technique used in this work to characterize nanometer-sized electrodes was cyclic voltammetry. An estimate of the size of the electroactive area of the nanoelectrodes was also obtained from the limiting steady state current of the cyclic voltammogram. After the polishing procedure the nanoelectrodes were cycled in 1 M and 0.1 M H₂SO₄ to electrochemically clean the electrodes and determine the surface roughness of the platinum surface, assuming the geometry of the electrode is disk shaped.

6.3.3.1 Determination of the Electrochemical Area

The cyclic voltammogram in Figure 16 represents the response of a nanoelectrode which has been cycled in 1 M H₂SO₄. This procedure is an effective method of cleaning the platinum surface. As the potential is swept from -0.25 to 1.4 V an oxide film forms on the platinum surface, which triggers desorption of adventitious impurities. This oxide layer is reduced on the cathodic branch leaving a clean platinum surface.³¹ The sequence of cycles should end with a negative step and the electrode is ready for use in an experiment.

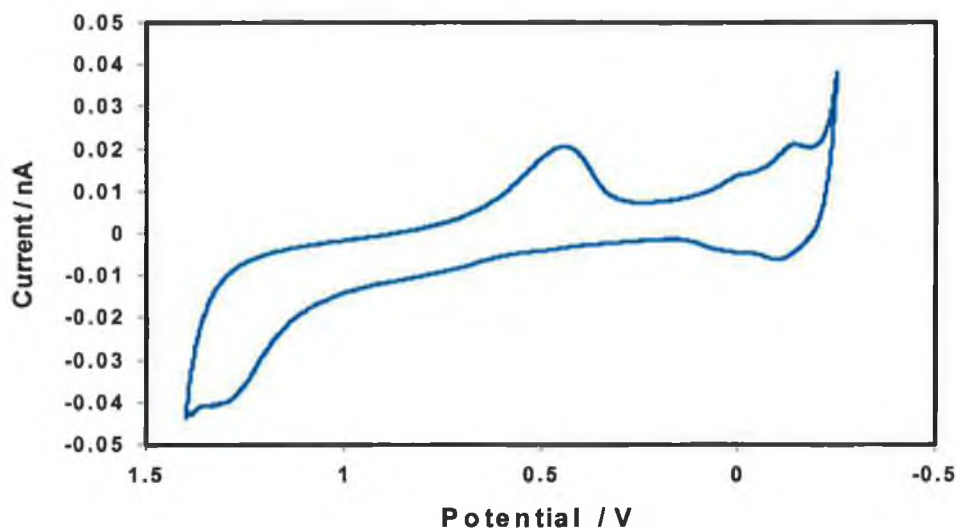


Figure 16. Cyclic voltammogram showing the electrochemical response of a nanometer-sized platinum electrode immersed in 1 M H₂SO₄. The scan rate is 0.05 Vs⁻¹. The potential limits are -0.25 V and 1.4 V with the initial potential set at -0.25 V.

Hydrogen adsorption and oxide formation are two methods, which can be used to determine the electrochemical area of an electrode. The method used in this work is oxide formation. This technique is based on the assumption that oxygen forms a monoatomic layer on the platinum surface. Each metal atom is thought to be bound to a single oxygen atom. The charge under the voltammetric peak for oxide desorption can be related to the electrochemical area using Equations (2) and (3),

$$Q_o = 2eN_A\Gamma_oA \quad (2)$$

where N_A is Avogadro's constant, Γ_o is the surface concentration of atomic oxygen, assumed to be equal to the surface density of metal atoms. The reference charge Q_o^s is calculated from the number of metal atoms per unit surface area so that,

$$A = \frac{Q_o}{Q_o^s} \quad (3)$$

A value for Q_o of $420 \mu\text{C cm}^{-2}$ has been accepted for polycrystalline platinum.^{32,33} The peak for oxide reduction on platinum is at a potential of approximately 0.45 V.

6.3.3.2 Determination of the Geometric Area

In the characterization of nanoelectrodes it was assumed that the electroactive area is disk shaped. This assumption may or may not be justified as is evident from the cyclic voltammetry data presented in this section but a reasonable approximation of the nanode area is nevertheless easily obtained using this method. The electroactive area can be calculated from the diffusion limited steady state current using Equation (4).

$$i_{lim} = 4nFDCr \quad (4)$$

where i_{lim} is the limiting current, n is the number of electrons in the redox reaction, F is Faraday's constant, D is the diffusion coefficient of the electroactive species, C is the concentration and r is the radius of the electrode. Cyclic voltammograms were run in a solution containing 5 mM $\text{Ru}(\text{NH}_3)_6^{3+}$ containing 0.1 M KCl as the supporting electrolyte. The diffusion coefficient for this redox species has been experimentally determined as $5.4 \pm 0.08 \times 10^{-6} \text{ cm}^2 \text{ s}^{-1}$. The cyclic voltammetry response for a number of electrodes produced is illustrated in Figure 17. The CV responses are seen to be

sigmoidal at low scan rates. The sigmoidal response indicates that the electrodes produced are of very small dimensions and that a good seal has formed between the nanometer sized platinum wire and the quartz glass. The limiting currents measured are in the low nanoampere range and the voltammograms remain sigmoidal for scan rates up to a few volts per second. This response agrees with the theoretical predictions outlined in Section 1.7.2.1 of Chapter 1 of this thesis for hemispherical diffusion of electroactive species to the electrode surface.

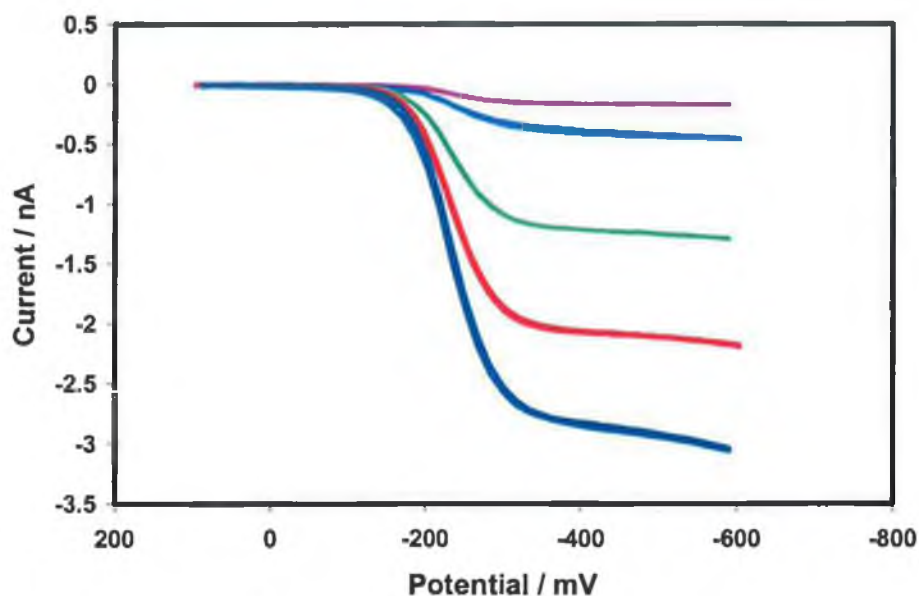


Figure 17. Steady state cyclic voltammetry responses for a range of electrodes produced in 5 mM $[\text{Ru}(\text{NH}_3)_6]^{3+}$ containing 0.1 M KCl as the supporting electrolyte. The scan rate was 1000 mV s^{-1} and the initial potential was 100 mV. The radius of the electrodes have been calculated as: 158 nm (—), 391 nm (—), 1170 nm (—), 1972 nm (—) and 2741 nm (—) using Equation 4.

The surface roughness of the platinum surface can then be calculated by dividing the electrochemical area by the geometric area of the electrode. Values in the range 2-3 are acceptable for surface roughness but values below 2 are preferable. The surface roughness values for a number of the nanoelectrodes fabricated are presented in Table 1.

Table 1. Electrochemical, Geometric Areas and Surface roughness values determined for a number of micro- and nanoelectodes fabricated. The radii of the electrodes have been determined from the steady state limiting current using Equation (4). The electrochemical and geometric areas have been calculated as detailed in the text above.

Radius / nm	Electrochemical Area / cm²	Geometric Area / cm²	Surface Roughness
158	1.46×10^{-9}	7.84×10^{-10}	1.9
391	6.64×10^{-9}	4.80×10^{-9}	1.4
1170	5.79×10^{-8}	4.30×10^{-8}	1.3
1972	2.54×10^{-7}	1.22×10^{-7}	2.1
2741	3.69×10^{-7}	2.36×10^{-7}	1.6

6.4 Ultramicroelectrode Geometries

A scan rate dependent study was carried out to estimate the geometry of the ultramicroelectrodes produced. As the scan rate of the experiment is increased linear diffusion predominates and a conversion from a sigmoidal CV response to a peak shaped CV response is observed. The scan rate dependent response for an electrode with a radius of $3.12\ \mu\text{m}$ is presented in Figure 18. The range of scan rates investigated was from $0.1\ \text{Vs}^{-1}$ to $50\ \text{Vs}^{-1}$.

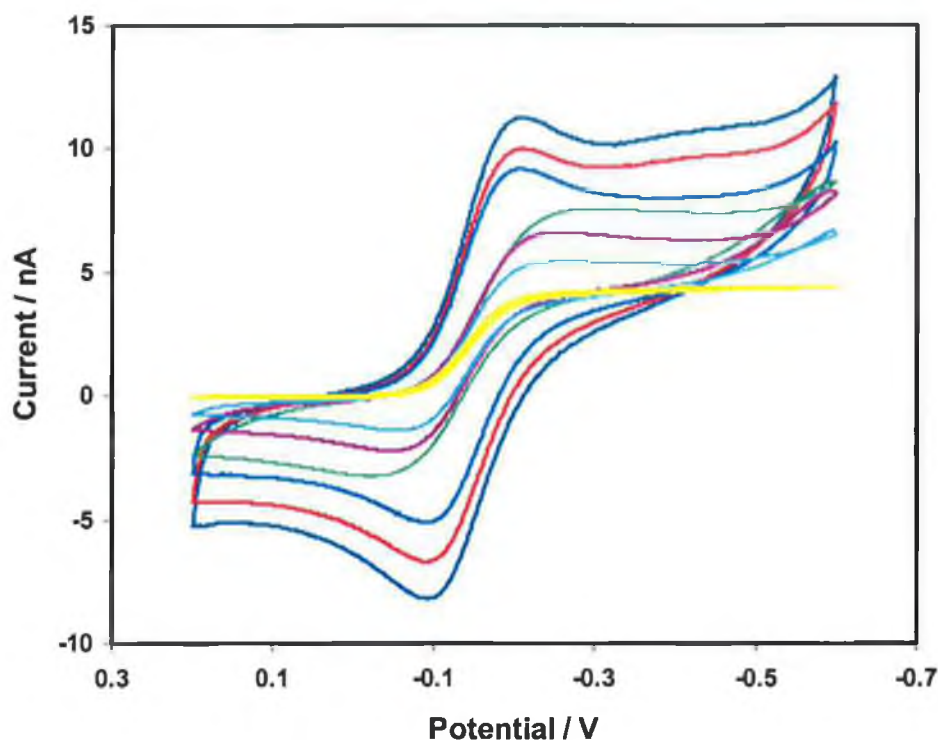


Figure 18. Cyclic voltammety response for a $3.12\ \mu\text{m}$ platinum electrode immersed in a solution of $5\ \text{mM}\ [\text{Ru}(\text{NH}_3)_6]^{3+}$ containing $0.1\ \text{M}\ \text{KCl}$ as the supporting electrolyte. The scan rates are $0.1\ (\text{---})$, $5\ (\text{---})$, $10\ (\text{---})$, $20\ (\text{---})$, $30\ (\text{---})$, $40\ (\text{---})$ and $50\ \text{Vs}^{-1}\ (\text{---})$.

The close to ideal CV response for micrometer sized electrodes contrasts with the rather less well behaved response obtained when using a nanoelectrode. The voltammetric response obtained when increasing the scan rate is illustrated in Figure 19 below. The currents obtained in these CVs are lower than those obtained when using a micrometer sized tip, this can be seen by comparing the data in Figure 18 with that in Figure 19. At

low scan rates, from 0.1 to approximately 1 V s^{-1} a sigmoidal response is obtained, however as the scan rate is increased a conversion to a peak shaped response is not seen. In contrast, as the scan rate increases the capacitive current is seen to increase. This could be due to a number of reasons, firstly the electrode geometry may not be disk shaped but lagooned as discussed previously in Section 1.7.5 of Chapter 1. A number of publications have been concerned with the elucidation of the electrochemical response of lagooned shaped microelectrodes. Mirkin and coworkers,³⁴ Baranski³⁵ and Oldham³⁶ believe that a lagooned-shaped electrode will show large charging currents and be slow to reach a steady state response. This is due to the fact that the true geometric area of these electrodes is larger than that calculated from the steady state CV response. However, this is not the case for the nanodes characterized here. The currents measured even at high scan rates, i.e. at 40 Vs^{-1} are only a few nanoamperes.

The second possible explanation for the cyclic voltammetric response displayed in Figure 19 is that the faradaic response is swamped by the capacitive response at higher scan rates. As the electrode radius decreases stray capacitance caused by the leads and electrical connections increase. However, this is unlikely to have caused the non-ideal cyclic voltammetry response observed for the electrodes presented here, as the electrochemical leads connected to the nanoelectrodes were kept as short as possible for all measurements. The nanodes fabricated using the micropipette puller were also characterized thoroughly in this work and were determined to have a good tight seal between the platinum wire and the quartz glass capillary after the pulling process.

The third possible explanation for the CV response displayed in Figure 19 is that the scan rate range investigated is too limited to observe significant effects from linear diffusion. It may be necessary to go to higher scan rates to observe a peak shaped CV response for electrodes of such small dimensions. Using the Randles Sevcik Equation it is possible to calculate the theoretical current as the scan rate increases. At a scan rate of 5 Vs^{-1} the ratio of steady state to transient current is 0.9, this value increases to 7.3 at a scan rate of 40 Vs^{-1} . The same calculations were carried out for the experimental data generated using a $3.12 \mu\text{m}$ electrode presented in Figure 18 above. At a scan rate of 5 Vs^{-1} the ratio of steady state to transient current is 3.2, this value increases to 25.5 at a scan rate of 40 Vs^{-1} . It is evident from observation of the CVs in Figure 18 that a CV response dominated by linear diffusion is obtained only at a scan rate of 40 V s^{-1} and

above. Therefore the ratio of steady state to transient current must be 25 or greater to observe a true linear diffusion response. This result is also confirmed in Figure 20 below. It is possible that diffusive behaviour would be observed for the 757 nm platinum electrode if the scan rate were increased further. Theoretical calculations predict that this scan rate would have to be a few hundred volts per second before lateral diffusion has a significant effect on the cyclic voltammetric response.

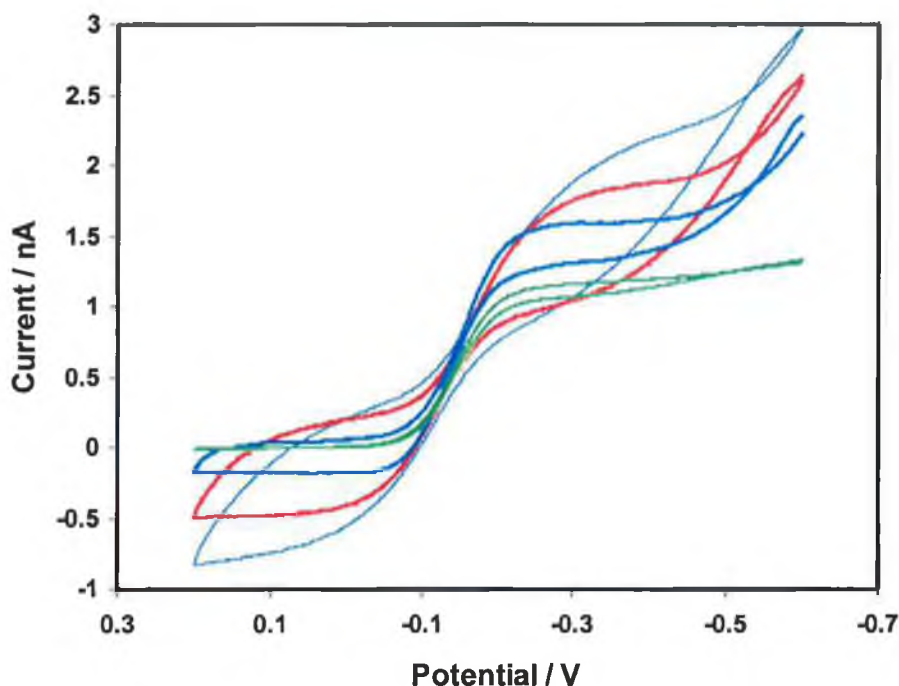


Figure 19. Cyclic voltammetry response for a 757 nm platinum electrode immersed in a solution of 5 mM $[\text{Ru}(\text{NH}_3)_6]^{3+}$ containing 0.1 M KCl as the supporting electrolyte. The scan rates are 0.1 (—), 5 (---), 20 (—), and 40 Vs^{-1} (—).

By plotting the maximum current measured from the CV response at each scan rate versus the log of scan rate it is possible to observe when the current is dominated by radial diffusion and lateral diffusion of electroactive species towards the electrode surface.³⁷ In the case of the micrometer sized electrode scan rates above 5 Vs^{-1} are dominated by linear diffusion. However, when measuring the scan rate dependence of a nanometer sized electrode it is not clear that the current response is ever controlled by linear diffusion of species towards the electrode surface, at least for the range of scan rates investigated in this study. The results for both size of electrode are illustrated in Figure 20.

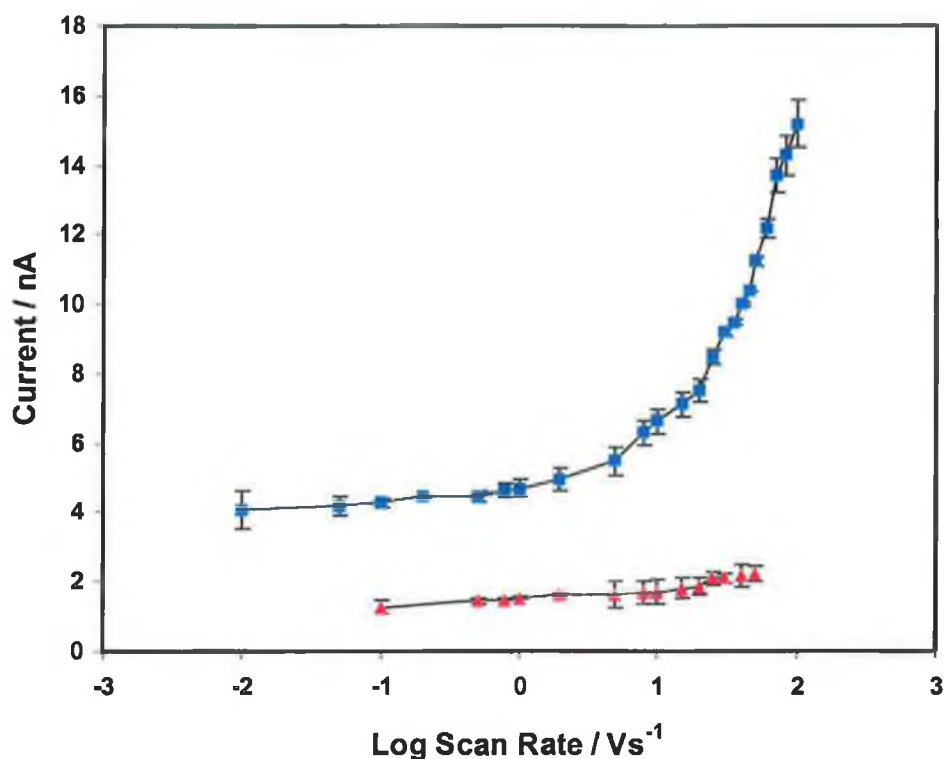


Figure 20. Dependence of the maximum peak current on the scan rate for a 3.120 μm platinum electrode (\blacksquare) and a 757 nm electrode (\blacktriangle). The range of scan rates measured was from 0.01 to 100 V s^{-1} for the microelectrode and 0.1 to 50 V s^{-1} for the nanoelectrode.

6.5 Mercury Nanoelectrodes

The fabrication of micrometer sized mercury electrodes on platinum disk electrodes has been described in Section 6.1 of this chapter. Here a description of the experimental efforts to deposit mercury onto nanometer-sized electrodes is presented. The procedure was less successful due to the fact that some of the the nanometer-sized electrodes produced were not a perfect disk shape but had a different geometry, possibly lagooned. Analysis of the experimental results obtained showed that it was more difficult to deposit mercury on electrodes of this geometry, this is thought to be due to the fact that the platinum wire is recessed into the glass body, thus preventing the formation of a nucleation site.

Figure 21 shows the results obtained when mercury deposition was carried out on a 3.12 μm platinum electrode. Deposition was carried out in a solution containing 5.7 mM

mercury (I) nitrate dihydrate (Aldrich) made up in 1 M KNO_3 and 0.5 % HNO_3 . The technique used was bulk electrolysis with coulometry using a CH Instruments 440 potentiostat with the deposition potential set at -0.2 V. These conditions were the same as those used to deposit a mercury drop onto the platinum microelectrodes discussed earlier in this chapter. The deposition process was carried out for 80 s and the total charge passed was 8.43×10^{-7} C.

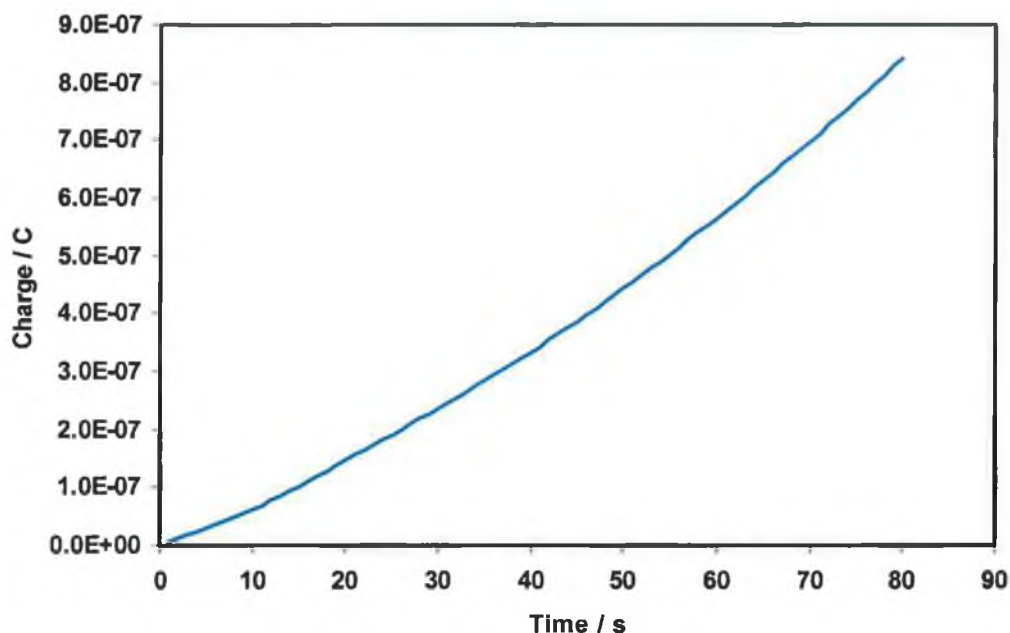


Figure 21. Charge vs time relationship obtained from depositing mercury onto a platinum electrode of radius $3.12 \mu\text{m}$. The deposition solution contained 5.7 mM mercury (I) nitrate dihydrate (Aldrich) made up in 1 M KNO_3 and 0.5% HNO_3 . Deposition was carried out at a potential of -0.2 V.

Following this deposition process the electrode was removed from the mercury deposition solution and placed in a $5 \mu\text{M}$ 1,2,4-AQASH solution, containing 1 M HClO_4 as the supporting electrolyte. This anthraquinone spontaneously adsorbs onto the surface of mercury but does not adsorb onto platinum. Therefore the presence of a faradaic response proves that mercury has deposited onto the surface of the ultrasmall platinum electrode. The result of this experiment is illustrated in Figure 22 below. It is evident from the analysis of this CV that the redox wave is present at a potential of approximately -0.10 V.

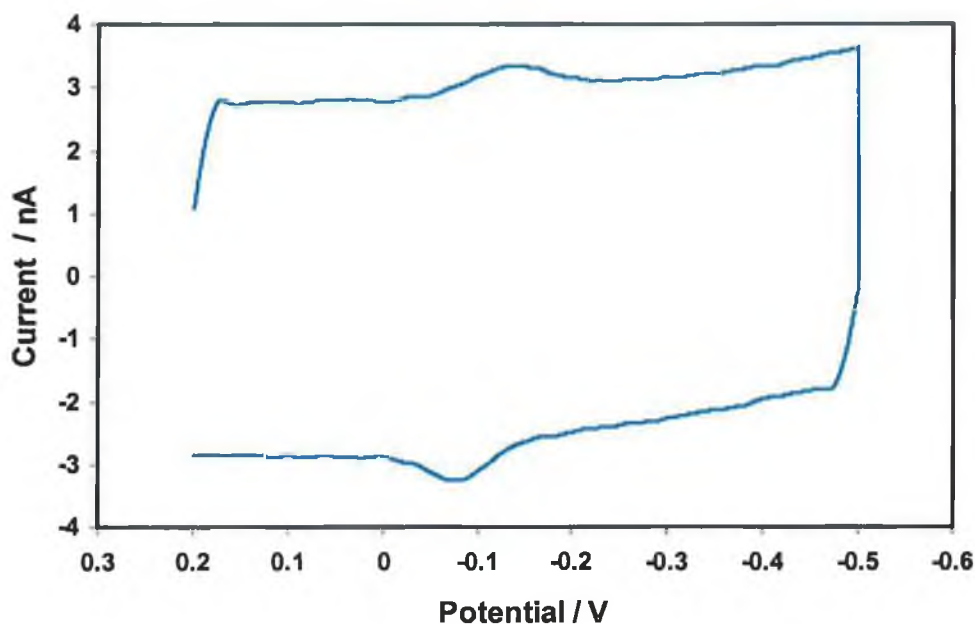


Figure 22. Cyclic voltammogram for a 3.12 μm radius platinum electrode following deposition of mercury for 80 s. The electrolytic solution contains 5 μM 1,2,4-AQASH with 1 M HClO_4 as the supporting electrolyte. The scan rate was 5 Vs^{-1} and the initial potential was 0.2 V.

The charge under this voltammetric wave has been integrated by background correcting the CV to calculate the size of the mercury drop deposited. The background corrected CV is presented in Figure 23. The area was calculated by substituting the charge measured into Equation (1), with the same assumptions as outlined in Section 6.1.2 of this chapter. The area of the hemispherical drop in this case was $3.98 \times 10^{-7} \text{ cm}^2$, yielding a value of 2.51 μm for the radius. This electrode area is significantly smaller than any other produced in this work.

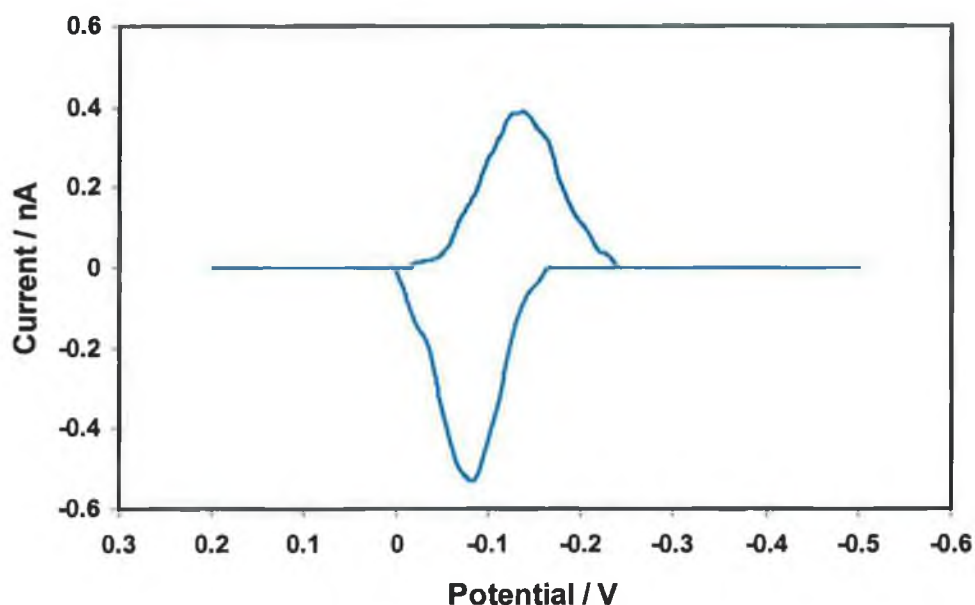


Figure 23. Background corrected cyclic voltammogram for a 3.12 μm radius platinum electrode following deposition of mercury for 80 s. The electrolytic solution contains 5 μM 1,2,4-AQASH with 1 M HClO_4 as the supporting electrolyte. The scan rate was 5 Vs^{-1} and the initial potential was 0.2 V.

Another significant feature of the cyclic voltammogram in Figure 22 is the extremely large contribution from the capacitive current. The capacitive current measured at a potential of 0.1 V is $5.63 \times 10^{-9} \text{ C}$. This results in a capacitance of $5.62 \times 10^{-10} \text{ F}$. The double layer capacitance for a mercury macroelectrode of size 0.0134 cm^2 modified with an oxidized monolayer of 1,2,4-AQASH has been calculated as $15.0 \pm 0.9 \mu\text{F cm}^{-2}$. Hence the theoretical capacitance for the small mercury electrode produced here is $5.97 \times 10^{-12} \text{ F}$. From this calculation it is evident that there is an excess capacitance of $5.56 \times 10^{-10} \text{ F}$, which cannot be attributed to interfacial processes. Capacitance at nanometer-sized electrodes has been discussed in the literature review presented in Chapter 1 of this thesis and suggests that excess capacitance originates from the experimental setup or the nanodes themselves. This is referred to as stray capacitance. The contribution to the stray capacitance from the potentiostat and leads has been minimized in this work by using cables of minimum length. It is thought that the major contribution is due to the design of the nanoelectrodes. A small imperfection in the seal between the insulating glass and the platinum wire would allow solution leakage, which would cause the capacitance to increase significantly. This has been discussed in a publication by

Menon and Martin,³⁸ where cyclic voltammograms were recorded prior to and after sealing the nanoelectrode tip. Faulkner and coworkers²⁶ as well as Wightman³⁹ have attributed large stray capacitive currents to the electrode design also. When silver epoxy or mercury is used to make the electrical connection between the microwire and the larger hook up wire large RC cell time constants result. This is due the electronically conducting / mercury / glass insulator / ionically conducting solution junctions causing a large stray capacitance. RC cell time constants have not been measured in this work for the nanometer-sized electrodes as the currents produced were too low to measure. However it is expected that the cell time constants would not be smaller than those measured at a micrometer sized electrode due to the significant contribution from stray capacitance. The cell time constants may even be larger than those measured at microelectrodes as a result.

6.6 Conclusions

This chapter described in detail a method of fabricating micro- and nanoelectrodes using a micropipette puller. This fabrication procedure has a number of advantages, the most obvious of which is the rapid nature of the process, thus enabling the production of nanoelectrodes in a short time period. The success of the fabrication procedure is high once the parameters of the pulling program chosen are compatible with the materials used for fabrication. This work described the fabrication of ultrasmall electrodes using quartz glass capillaries and hard temper platinum wire. Other materials could possibly be used for fabrication of ultrasmall probes but the parameters used in the pulling program would have to be modified.

These electrodes may be used for a number of applications among which the measurement of fast heterogeneous electron transfer rates as described in the previous chapter. According to existing theory the smaller the electrode radius is the faster the response time. Attempts to measure the RC time constants of nanoelectrodes produced in this work were unsuccessful as the current produced by the nanodes were too low to measure. However it is thought that significantly faster response times would not be achieved, as the stray capacitance would prevent a decrease in the cell time constant.

6.7 References

1. Bourque, H., Leblanc, R.M., *Rev. Sci. Instrum.*, **1995**, 66, 2695.
2. Zhang, B., Wang, E., *Electrochimica Acta*, **1994**, 39, 103.
3. Lee, C.L., Miller, C.J., Bard, A.J., *Anal. Chem.*, **1991**, 63, 78.
4. Melmed, A.J., *J. Vac. Sci. Technol. B*, **1991**, 9, 601.
5. Ibe, J.P., Bey, P.P., Brandow, S.L., Brizzolara, R.A., Burnham, N.A., DiLella, D.P., Lee, K.P., Marrian, C.R.K., Colton, R.J., *J. Vac. Sci. Technol. A*, **1990**, 8, 3570.
6. Penner, R.M., Heben, M.J., Lewis, N.S., *Anal. Chem.*, **1989**, 61, 1630.
7. Nagahara, L.A., Thundat, T., Lindsay, S.M., *Rev. Sci. Instrum.*, **1989**, 60, 3128.
8. Kawagoe, K.T., Jankowski, J.A., Wightman, R.M., *Anal. Chem.*, **1991**, 63, 1589.
9. Katemann, B.B., Schuhmann, W., *Electroanal.*, **2002**, 14, 22.
10. Slevin, C.J., Gray, N.J., Macpherson, J.V., Webb, M.A., Unwin, P.R., *Electrochem. Commun.*, **1999**, 1, 282.
11. Wong, D.K.Y., Xu, L.Y.F., *Anal. Chem.*, **1995**, 67, 4086.
12. Shao, Y., Mirkin, M.V., Fish, G., Kokotov, S., Palanker, D., Lewis, A., *Anal. Chem.*, **1997**, 69, 1627.
13. Fish, G., Bouevitch, O., Kokotov, S., Lieberman, K., Palanker, D., Turovets, I., Lewis, A., *Rev. Sci. Instrum.*, **1994**, 66, 3300.
14. Kim, Y.T., Scarnulis, D.M., Ewing, A.G., *Anal. Chem.*, **1986**, 58, 1782.
15. Kelly, R.S., Wightman, R.M., *Anal. Chim. Acta*, **1986**, 187, 79.
16. Baldo, M.A., Daniele, S., Bragato, C., Mazzocchin, G.A., *Anal. Chim. Acta*, **2002**, 464, 217.
17. Abdelsalam, M.E., Denuault, G., Daniele, S., *Anal. Chim. Acta*, **2002**, 452, 65.
18. Daniele, S., Bragato, C., Argese, E., *Electrochem. Comm.*, **2002**, 2, 399.
19. Baldo, M.A., Daniele, S., Mazzocchin, G.A., *Electrochim. Acta*, **1996**, 41, 811.
20. Wehmeyer, K.R., Wightman, R.M., *Anal. Chem.*, **1985**, 57, 1989.
21. Silva, P.R.M., El Khakani, M.A., Chaker, M., Champagne, G.Y., Chevalet, J., Gastonguay, L., Lacasse, R., Ladouceur, *Anal. Chim. Acta*, **1999**, 385, 249.
22. Golas, J., Galus, Z., Osteryoung, J., *Anal. Chem.*, **1987**, 59, 389.
23. Golas, J., Osteryoung, J., *Anal. Chim. Acta*, **1986**, 181, 211.
24. Golas, J., Osteryoung, J., *Anal. Chim. Acta*, **1986**, 186, 1.

25. O'Hanlon, D.P., Ph.D. Thesis, *Spontaneously Adsorbed Monolayers : Anthraquinones and Osmium Polypyridyl Complexes as Molecular Building Blocks*, 1999.
26. Faulkner, L.R., Walsh, M.R., Xu, C., *Contemporary Electranalytical Chemistry*, Plenum Press:New York, 1990.
27. Xu, C., Ph.D. Thesis, University of Illinois at Urbana-Champaign, 1992.
28. Lambrechts, M., Sansen, W., *Biosensor: Microelectrochemical Devices*, Institute of Physics Publishing, Chapter 2.
29. Baldo, M.A., Daniele, S., Mazzocchin, G.A., *Electrochimica Acta*, 1996, 41, 811.
30. Daniele, S., Bragato, C., Argese, E., *Electrochemistry Communications* 2, 2000, 2, 399.
31. Faulkner, L.R., *Physical Methods in Modern Chemical Analysis, Vol. 3*, Academic Press, 1983, 230.
32. Michri, A., Pshchenichnikov, A.G., Burshtein, R. Kh., *Elektrokhimiya*, 1972, 8, 364.
33. Burshtein, K., *Elektrokhimiya*, 1967, 3, 349.
34. Shao, Y., Mirkin, M.V., Fish, G., Kokotov, S., Palanker, D., Lewis, A., *Anal. Chem.*, 1997, 69, 1627.
35. Baranski, A.S., *J. Electroanal. Chem.*, 1991, 307, 287.
36. Oldham, K.B., *Anal. Chem.*, 1992, 64, 646.
37. Wehmeyer, K.R., Deakin, M.R., Wightman, R.M., *Anal. Chem.*, 1985, 57, 1913.
38. Menon, V.P., Martin, C.R., *Anal. Chem.*, 1995, 67, 1920.
39. Wipf, D.O., Michael, A.C., Wightman, R.M., *J. Electroanal. Chem.*, 1989, 15, 269.

Chapter 7

Conclusions and Future Work

“When you make the finding yourself - even if you’re the last person on Earth to see the light – you’ll never forget it.”

- *Carl Sagan*

7. Conclusions

As is evident from the title of this thesis that the work presented has focused on two principal areas, which are important in the area of electrochemical research today. These areas are the modification of an electrode surface with spontaneously adsorbed monolayers, which provide an ideal platform for the study of electron transfer reactions, and the development of a technique to fabricate nanometer sized electrodes. Chapter 1 provided a description of the electrical double layer. An understanding of the unmodified electrode/electrolyte interface is important in the study of processes such as voltammetric analysis, electrodeposition and metal corrosion. In Chapters 3 and 4 capacitance measurements have been carried out at an unmodified interface. This was then compared to capacitance measurements when the electrode surface was modified with sub-monolayer to monolayer coverages of two anthraquinone derivatives; 1-amino, 2-sulphonic, 4-hydroxyanthraquinone (1,2,4-AQASH) and 1,5-dimethoxyanthraquinone (1,5-DMAQ). It has been observed that the double layer capacitance decreases significantly when the mercury electrode surface is modified. The extent to which the capacitance decreases can be used to predict the packing density of the monolayers. A lower interfacial capacitance is indicative of a close packed assembly, as ions and solvent molecules are blocked from the interface. In both investigations it has been concluded that the reduced (hydroquinone) form of 1,2,4-AQASH and 1,5-DMAQ form tighter packed monolayers than the oxidized (quinone) form.

The other results presented in Chapters 3 and 4 provide a detailed investigation of the thermodynamics and kinetics of adsorption in anthraquinone systems. Quinonoid molecules form tightly bound adsorbate layers on mercury, are stable in both redox forms and exhibit nearly ideal electrochemical responses in low pH electrolyte solutions. Initial experiments probed the electrochemistry of 1,2,4-AQASH. The dependence of the surface coverage, as determined by integrating the area under the voltammetric wave on the bulk concentration was best described using the Frumkin adsorption isotherm in which both quinone and hydroquinone forms were stabilized. A spike appeared in the anodic branch of the cyclic voltammograms and this was attributed to lateral hydrogen bonding interactions, when the intersite separation between adsorbates was 3 Å or less. The mechanism of monolayer formation is uncomplicated when 1,2,4-AQASH adsorbs on mercury. An equilibrium CV response

was attained on a sub-second timescale. The molecules adsorb parallel to the electrode surface, this has been confirmed through Raman spectroscopy measurements. The second anthraquinone derivative under investigation, 1,5-DMAQ was studied to model the adsorption dynamics leading to equilibrium surface coverage on the electrode surface. Depending on the concentration of 1,5-DMAQ in the deposition solution the time taken for an equilibrium CV response to establish varied. The experimental data was fit to a number of models, including 1st and 2nd order, diffusion and adsorption. The change in the cyclic voltammetric response over time was thought to be due to reorganization of adsorbates on the electrode surface. 1,5-DMAQ initially adsorbs in a perpendicular orientation with a smaller area of occupation per molecule and hence a higher surface coverage before reorienting into a coplanar configuration with a lower surface coverage. This parallel orientation results in a more stable structure with a higher electron density. This work is the first to deal with adsorption and desorption dynamics of an anthraquinone derivative molecule on a mercury surface.

The electrochemical properties of two component anthraquinone monolayers was investigated in Chapter 4 by coadsorption of 1,2,4-AQASH and 1,5-DMAQ on mercury. The formal potentials of the two molecules were separated by approximately 70 mV on the potential axis and so cyclic voltammetry could be used to investigate the properties of these mixed monolayers. The thermodynamics and kinetics of adsorption have been modeled to determine the mode of adsorption and structure of the mixed monolayer, when equilibrium surface coverage is reached. Coadsorption was seen to have a significant effect on the strength of adsorption of the two molecules. 1,5-DMAQ was preferentially adsorbed from mixed deposition solutions. Based on the cyclic voltammetric response it is believed that mixed monolayers are composed of discrete and separated phases rather than being randomly distributed. The competitive Frumkin isotherm predicts that there is preferential adsorption between dissimilar adsorbates. The kinetics of monolayer formation was modeled. 1,2,4-AQASH spontaneously desorbs from the electrode surface and 1,5-DMAQ adsorbs on the available surface area. Desorption kinetics were modeled by a first order process, while the kinetics of surface binding and reorganization best described the adsorption of 1,5-DMAQ. Diffusion of the electroactive species towards the electrode surface was not rate limiting.

Another topic to be investigated in the experimental work of this thesis was the rate of heterogeneous electron transfer in monolayers of 1,2,4-AQASH. The redox reaction of this anthraquinone proceeds by the transfer of two electrons coupled to the uptake of two protons from solution. Coupled electron and proton transfer reactions are important in areas such as catalysis, molecular electronics and biological systems. Fast electrochemical measurements were performed to probe this fast electron transfer step and these results were presented in Chapter 5. Rate constants have been determined for the oxidation and reduction reactions by fitting the experimental data to the Butler Volmer and Marcus theories of electron transfer, the basic concepts of these models were outlined in Chapter 1. In low pH solution the rate of proton transfer exceeds the rate of electron transfer and a mechanism for the oxidation and reduction reaction has been proposed. Oxidation proceeds by $e^-H^+e^-H^+$ and reduction proceeds by $H^+e^-H^+e^-$. However the mechanism at high pH is less well understood. The conclusion from the experimental results presented in this work is that the redox reaction involves the transfer of 2 electrons and one proton, leading to a mechanism which proceeds by $e^-H^+e^-$, $e^-e^-H^+$ or $H^+H^+e^-$. Further experimental studies will need to be carried out to elucidate the mechanism of proton and electron transfer in the redox reaction of these quinone molecules.

In order to measure the fast electron transfer rates described above ultrasmall mercury electrodes were necessary. Every electrochemical measurement has a lower timescale limit that is imposed by the RC cell time constant. As the size of an electrode decreases the response time decreases also. This is important, as it is only at times of 5-10 RC that meaningful kinetic data can be measured. In this work mercury microelectrodes were fabricated by first constructing platinum microelectrodes. Deposition of mercury on the electrochemically cleaned platinum surface was performed to produce a hemispherical drop. This work led to the fabrication of nanometer-sized electrodes using a microelectrode puller and this work was presented in Chapter 6 of this document. The nanometer sized electrodes were characterized using techniques such as cyclic voltammetry, optical microscopy and scanning electron microscopy to determine the quality of the seal between the glass and the wire. The fabrication procedure has been optimized to produce nanoelectrodes which display good voltammetric properties. Deposition of mercury onto these nanometer sized platinum electrodes was carried out. This was achieved with varying degrees of success, depending on the geometry of the

nanoelectrode produced from the pulling procedure. Cyclic voltammograms of an adsorbed redox probe reveal that there is significant contribution from stray capacitance, which is thought to be due to the design of the electrodes. Future experiments could focus on modification of the fabrication procedure, to produce nanoelectrodes with an electrical connection that causes less stray capacitance. One important application of these nanometer-sized electrodes is in Scanning Electrochemical Microscopy. This technique records microscopic images of surfaces and provides information on the conducting nature of the substrate. Imaging resolution is limited by the tip radius, so substantial improvements in resolution would be obtained by using electrodes of nanometer dimensions.

In conclusion, the work presented in this thesis provides new insights into the kinetics and thermodynamics of anthraquinone adsorption, nanoelectrode fabrication and characterisation and the elucidation of the energetics and dynamics of coupled proton and electron transfer. However, much more work is still to be done in this area, and the possibilities for further experimental research work are vast.

Appendix 1

Abbreviations and Symbols

Standard Abbreviations

[AQ]	Anthraquinone
[1,2,4-AQASH]	1-amino, 2-sulphonic, 4-hydroxyanthraquinone
[1,5-DMAQ]	1,5-dimethoxyanthraquinone
bpy	bipyridine
CV	cyclic voltammetry
DMF	N, N-dimethylformamide
FWHM	full width at half maximum
HClO ₄	perchloric acid
LiClO ₄	lithium perchlorate
p0p	4,4'-dipyridyl
p2p	1,2-bis(4-pyridyl)ethane
p3p	4,4'-trimethylenedipyridine
py	pyridine
Q	quinone
Q ₂ H	hydroquinone
SAM	self assembled monolayer
SECM	scanning electrochemical microscopy
SEM	scanning electron microscopy
SFM	scanning force microscopy
STM	scanning tunnelling microscopy
UME	ultramicroelectrode

Symbols

A	area	cm ²
C	capacitance	F
C _{dl}	double layer capacitance	μF cm ²
D	diffusion coefficient	cm ² s ⁻¹
e	charge on an electron	C
E _f	final potential	V
E _i	initial potential	V
E _{max}	maximum potential	V
E _{min}	minimum potential	V
E _p	peak potential	V
E _{pa}	anodic peak potential	V
E _{pc}	cathodic peak potential	V
E _F	Fermi energy	eV
ΔG _{ads}	Free energy of adsorption	J mol ⁻¹
ΔE _{p1/2}	E _{pa} – E _{pc} in CV	V
ΔS _{rc} ^o	reaction entropy	J mol ⁻¹ K ⁻¹
F	Faraday constant: charge on one mole of electrons	C
g	coefficient in the Frumkin isotherm	-
i _{pa}	anodic peak current	A
i _{pc}	cathodic peak current	A
i _{ss}	steady state current	A
k _B	Boltzmann constant	J K ⁻¹
k ^o	standard heterogeneous electron transfer rate constant	cm s ⁻¹
n	number of electrons involved in overall reaction	-
Q	charge passed in electrolysis	C
r	electrode radius	cm
R	gas constant	J K ⁻¹ mol ⁻¹
	<i>or</i> resistance	Ω

Greek Symbols

α	transfer coefficient	-
β	absorption coefficient	M^{-1}
η	overpotential, $E - E_{eq}$	V, mV
δ	diffusion layer thickness	cm
Γ	surface coverage	$molcm^{-2}$
κ_{el}	electronic transmission coefficient	-
λ	total reorganisation energy	$KJ mol^{-1}$
λ_{is}	inner sphere reorganisation energy	$KJ mol^{-1}$
λ_{os}	outer sphere reorganisation energy	$KJ mol^{-1}$
ϵ_0	permittivity of free space	$F cm^{-1}$
ϵ_{op}	optical dielectric constant of solvent	-
ϵ_s	static dielectric constant of solvent	-
ν	potential scan rate	$V s^{-1}$

Appendix 2

Publications

Impact of Hydrogen Bonding on the Redox Properties of 1-Amino-2-sulfonic-4-hydroxyanthraquinone Monolayers

Robert J. Forster,^{*,†} Tia E. Keyes,[†] Mary Farrell,[†] and Dominic O'Hanlon[†]

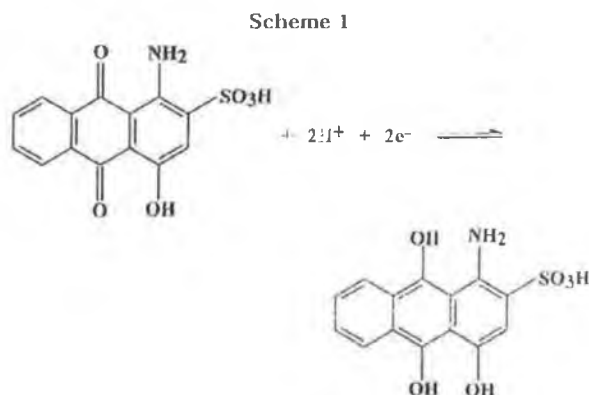
School of Chemical Sciences, National Center for Sensor Research, Dublin City University, Dublin 9, Ireland, and School of Chemistry, Dublin Institute of Technology, Dublin 4, Ireland

Received April 11, 2000. In Final Form: July 26, 2000

Monolayers of 1-amino-2-sulfonic-4-hydroxyanthraquinone, 1,2,4-AQASH, have been formed on mercury electrodes by spontaneous adsorption. Films were deposited from solutions containing either quinone or hydroquinone forms where the bulk concentration, C_B , was between 0.1 and 5 μM . These films have been used as model systems to probe the effect of intersite separation and redox composition on hydrogen bonding interactions in two-dimensions. Both resonance Raman spectroscopy and surface coverage data indicate that at the open-circuit potential the adsorbates are coplanar with the electrode surface. For surface coverages, Γ , less than approximately $1.4 \times 10^{-10} \text{ mol cm}^{-2}$ ($C_B \leq 1.5 \mu\text{M}$) monolayers formed from the quinone exhibit close to ideal voltammetric responses with a peak-to-peak splitting of 17 mV being observed. Also, the full widths at half-maximum are 53 and 63 mV for the cathodic and anodic branches, respectively. Capacitance data reveal that the adsorbates interact only very weakly within fully oxidized or reduced films. The free energy of adsorption is larger for the quinone ($-35.3 \pm 0.2 \text{ kJ mol}^{-1}$) than for the hydroquinone ($-33.5 \pm 0.3 \text{ kJ mol}^{-1}$) monolayer. In contrast to fully oxidized or reduced monolayers, the dependence of the surface coverage as determined from the area under the voltammetric peak, i.e., where the film is of mixed redox composition, on the bulk concentration is best modeled by the Frumkin adsorption isotherm. The interaction parameters, g , are negative for monolayers formed from both quinone (-0.29 ± 0.05) and hydroquinone (-1.78 ± 0.22) forms indicating stabilizing lateral interactions. Where the intersite separation is less than approximately 3 Å, i.e., when Γ exceeds $1.4 \times 10^{-10} \text{ mol cm}^{-2}$, the anodic branch of the voltammogram becomes distorted and a current spike is observed. These data are interpreted in terms of lateral hydrogen bonding between the carbonyl and hydroxy moieties when the film is in a quinhydrone form.

Introduction

Self-assembled monolayers represent a facile, flexible approach to rationally controlling the chemical composition and structure of surfaces.¹ In particular, monolayers composed of functionalized alkanethiols can form monolayers that are highly ordered on the molecular length scale.² The formation of these ordered assemblies depends on two distinct interactions: first, chemisorption onto the surface based on the high affinity of sulfur for the metal surface, e.g., the Au-S bond strength³ is of the order of 160 kJ mol^{-1} ; second, stabilizing lateral van der Waals interactions between the adsorbates. These lateral interactions are weak, and ordered monolayers are typically obtained only for long chain (more than 10 methylenes) systems. Our interest is in developing systems which exhibit strong spontaneous adsorption but have stronger lateral interactions, such as hydrogen bonding, to drive the formation of ordered assemblies using smaller molecules.⁴⁻⁶ In solution, molecules can undergo translational motion in three-dimensions and hydrogen bond strengths are of the order of 20 kJ mol^{-1} . However, in the case of monolayers, there is a reduction in the dimen-



sionality of the system and the local microenvironment of the molecule may be dramatically different from that found in solution.⁷ For example, we recently reported⁸ on single- and two-component monolayers of anthraquinone-2,7-disulfonic acid and 1-chloro-4-hydroxyanthraquinone. In stark contrast to the behavior observed in solution, in essentially *aqueous* solution these monolayers exhibited intermolecular hydrogen bonding in which the 2,7-AQDS and 1,4-AQCIOH adsorbates acted as electron acceptors and donors, respectively.

Here, we report on spontaneously adsorbed monolayers of 1-amino-2-sulfonic-4-hydroxyanthraquinone, 1,2,4-AQASH (Scheme 1), on mercury electrodes. These anthraquinones are attractive building blocks for supramolecular assemblies because the functional groups present,

* To whom correspondence should be addressed.

[†] Dublin City University.

[†] Dublin Institute of Technology.

(1) Finklea, H. O. In *Encyclopedia of Analytical Chemistry*; Meyers, Robert, A., Ed.; John Wiley and Sons Ltd.: Chichester, 2000.

(2) Ulman, A. *Characterization of Organic Thin Films: Materials Characterization Series—Surfaces, Interfaces, Thin Films*; Butterworth-Heinemann: Stoneham, MA, 1995.

(3) Nuzzo, R. G.; Dubois, L. H.; Allara, D. L. *J. Am. Chem. Soc.* **1990**, *112*, 558.

(4) Forster, R. J. *Anal. Chem.* **1996**, *68*, 3143.

(5) Forster, R. J. *J. Electrochem. Soc.* **1997**, *144*, 1165.

(6) O'Kelly, J. P.; Forster, R. J. *Analyst* **1998**, *123*, 1987.

(7) Ariga, K.; Kunitake, T. *Acc. Chem. Res.* **1998**, *31*, 371.

(8) O'Hanlon, D.; Forster, R. J. *Langmuir* **2000**, *16*, 702.

i.e., amino, sulfonic, and hydroxy groups, are capable of undergoing intramolecular hydrogen bonding. Moreover, one might anticipate that these interactions would depend on the redox composition of the film since the carbonyl oxygen of the oxidized quinone, Q, acts as an electron acceptor while the hydroxy group of the reduced hydroquinone, H₂Q, acts as an electron donor. Monolayers can be attractive model systems for probing the distance dependence of lateral interactions since, in theory, the intersite separation can be controlled simply by varying the surface coverage. However, this approach is useful only if partial monolayers consist of randomly distributed adsorbates rather than islands in which close packing occurs. To address this issue, we have probed the dependence of the peak potentials on the surface coverage and found that at low coverages the adsorbates interact only weakly. A second potential difficulty in using anthraquinones as building blocks is that adsorption is reversible and the surface coverage may depend on the applied potential. Therefore, we have used measurements of the interfacial capacitance to probe the strength of lateral interactions within films that contain only quinone or hydroquinone forms of 1,2,4-AQASH. Moreover, we have used cyclic voltammetry to investigate intermolecular interactions within films of mixed redox composition. For monolayers formed using the oxidized quinone species, significant distortion and a current spike on the anodic branch are found when the bulk concentration exceeds approximately 1.5 μM . In contrast, for hydroquinone monolayers a current spike is observed only when the bulk concentration exceeds approximately 20 μM . The dependence of the surface coverage as determined by integrating the area under the voltammetric wave on the bulk concentration is best described by the Frumkin adsorption isotherm in which both quinone and hydroquinone forms are stabilized. This behavior is interpreted in terms of the effects of relatively stronger quinone adsorption and the distance dependence of two-dimensional hydrogen bonding between quinone and hydroquinone forms.

Experimental Section

Apparatus. Cyclic voltammetry was performed using a CH instruments model 660 electrochemical workstation, a PAR EG&G model 270 hanging mercury electrode, and a conventional three electrode cell. Potentials were measured against a potassium chloride saturated silver/silver chloride (Ag/AgCl) reference electrode. A large area ($\approx 2 \text{ cm}^2$) platinum flag was used as the auxiliary electrode. All solutions containing 1,2,4-AQASH were thoroughly degassed by purging with nitrogen which was maintained over the solution during all measurements. The area of the mercury electrode was determined using the density of pure mercury (13.546 g cm^{-3}) by dispensing, collecting, drying, and weighing 100 drops of mercury. An electrochemical area of $0.0140 \pm 0.0007 \text{ cm}^2$ was obtained. This area was also confirmed by recording cyclic voltammograms under steady state and linear diffusion conditions using $[\text{Ru}(\text{NH}_3)_6]^{2+}$ as a solution phase probe.

Raman spectroscopy was conducted on a Dilor Jobinyvon Spex Labram. The exciting 140 mW argon ion laser (514.5 nm), attenuated to 70 mW, was focused through a custom made electrochemical cell onto either the solution or the mercury electrode surface using a 10 \times objective lens. The beam diameter when focused is approximately 3 μm producing approximately 10^6 W cm^{-2} at the sample. Focusing was confirmed by using a CCD camera in imaging mode. A spectral resolution of 1.5 cm^{-1} per pixel was achieved using a grating of 1800 lines/mm.

Materials and Procedures. 1 Amino 2-sulfonic 4-hydroxyanthraquinone (1,2,4-AQASH) was obtained from BASF and used as received. Solutions were prepared using Milli-Q purified water, and unless stated otherwise, the supporting electrolyte was 1.0 M HClO₄. Spontaneously adsorbed monolayers were formed

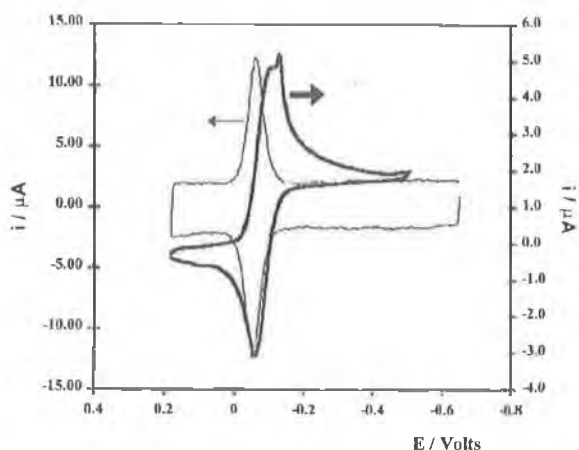


Figure 1. Cyclic voltammograms for a hanging mercury drop electrode immersed in a 1 μM (light line) or 5 mM (dark line) solution of 1,2,4-AQASH dissolved in 1.0 M HClO₄, where the scan rates are 5 and 0.05 V s^{-1} , respectively. The potential scan was started at the negative limit. Anodic currents are down, cathodic currents are up.

by allowing the anthraquinone at micromole per liter concentrations to adsorb onto the mercury electrode surface from electrolytic solutions. At high concentration, dense monolayers were typically formed within a few tens of milliseconds. At concentrations where sub-monolayer coverage was attained, repetitive cyclic voltammetry was performed until the peak current became independent of time. Transferring the modified surfaces into blank electrolyte caused the monolayer to rapidly desorb; i.e., adsorption is reversible in this system. Therefore, all experiments were performed with micromolar concentrations of the anthraquinone in solution.

Results and Discussion

General Electrochemical Properties. Figure 1 shows a cyclic voltammogram recorded at 5 V s^{-1} for a mercury electrode immersed in a 1.0 μM solution of 1-amino-2-sulfonic-4-hydroxyanthraquinone (1,2,4-AQASH) where the supporting electrolyte is 1.0 M HClO₄. The response observed is consistent with that expected for a redox-active species immobilized on an electrode surface. For example, Gaussian peak shapes are observed whose shape is independent of scan rate, ν , and the peak height scales linearly with scan rate up to at least 50 V s^{-1} . The coverage obtained from the background-corrected charge under the voltammetric waves is $(6.8 \pm 0.1) \times 10^{-11} \text{ mol cm}^{-2}$. This behavior contrasts with the diffusive tails and $\nu^{1/2}$ dependence of the peak current associated with freely diffusing species.^{9,10} That the voltammetric response for an adsorbed species increases as ν rather than $\nu^{1/2}$ means that current response is dominated by the adsorbed reactant at high scan rates. For example, given that the diffusion coefficient of 1,2,4-AQASH is $(5.6 \pm 0.8) \times 10^{-6} \text{ cm}^2 \text{ s}^{-1}$ in solution, at a scan rate of 5 V s^{-1} the solution phase reactant contributes less than 0.3% to the total current observed in Figure 1.

Under these conditions of low surface coverage ($\Gamma < 1.00 \times 10^{-10} \text{ mol cm}^{-2}$), a ΔE_p of $17 \pm 2 \text{ mV}$ as well as full width at half-maximum (fwhm) of 53 ± 3 and $63 \pm 8 \text{ mV}$ are observed for the cathodic and anodic branches, respectively. While both ΔE_p and fwhm are somewhat larger than the theoretical values^{11,12} of 0 and 45.3 mV, respectively, the voltammetric response is consistent with

(9) Bard, A. J.; Faulkner, L. R. *Electrochemical Methods: Fundamentals and Applications*; Wiley: New York, 1980.

(10) Wopschall, R. H.; Shain, I. *Anal. Chem.* **1967**, *39*, 1514.

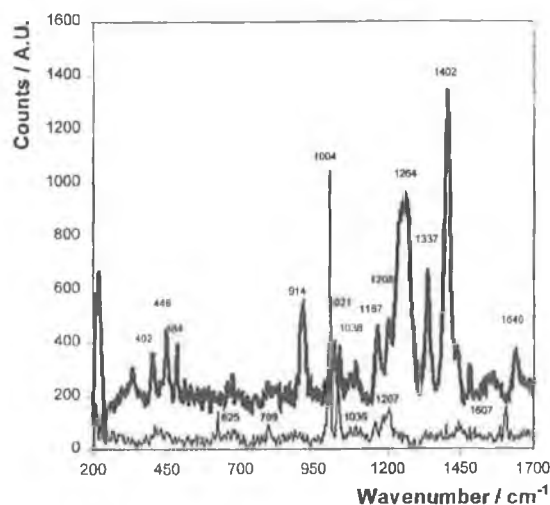


Figure 2. Resonance Raman spectra for 1,2,4-AQASH dissolved in 1.0 M HClO₄ where the bulk concentration is 100 μ M (light line) and for an adsorbed monolayer on a mercury electrode at the open circuit potential (dark line). In both cases an Ar⁺ laser (514.5 nm) was used for excitation.

that expected for an ideal redox reaction involving the transfer of two electrons to an adsorbed species.^{13–15}

The thick line of Figure 1 shows the cyclic voltammogram obtained for solution phase 1,2,4-AQASH. These data reveal that the formal potentials are -96 and -58 mV for the solution phase and adsorbed species, respectively. That E° shifts in a positive potential direction upon surface confinement indicates that 1,2,4-AQASH is harder to oxidize when adsorbed and has a lower electron density.

Raman Spectra of 1,2,4-AQSH Monolayers and in Solution. Figure 2 shows Raman spectra for 1,2,4-AQASH both as a monolayer on a mercury electrode at the open circuit potential ($+0.10 \pm 0.05$ V) and in solution. Given that the λ_{max} of 1,2,4-AQASH is 526 nm, the excitation source, i.e., an Ar⁺ laser at 514.5 nm, is preresonant with the visible $n-\pi^*$ transition of 1,2,4-AQASH. In these Raman experiments, the bulk concentration is 100 μ M, which is sufficiently high to form a dense monolayer *vide supra*. The Raman spectrum for the monolayer is significantly different from that found for solution-phase 1,2,4-AQASH most likely because interactions of the adsorbate with the surface alter the symmetry, and hence the vibrational selection rules, of the system. At the open circuit potential the monolayer is oxidized and a band at 1640 cm^{-1} corresponding to the C=O stretching is observed.¹⁶ This mode is shifted to higher energy by approximately 30 cm^{-1} on adsorption, indicating a strengthening of the C=O bond. Since any additional electron density would occupy antibonding orbitals, this result is consistent with the formal potential data presented earlier which indicated that the electron density on the anthraquinone decreases when it is adsorbed.¹⁷ Significantly, while the solution phase species exhibits a strong aromatic ring breathing mode at 1004 cm^{-1} , this mode is greatly diminished in the monolayer spectrum. The ratio of the intensity of the ring-breathing mode

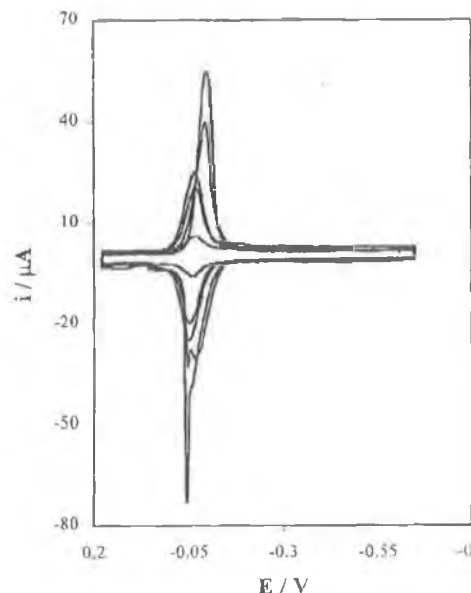


Figure 3. Dependence of the cyclic voltammetric response of a hanging drop mercury electrode on the bulk concentration of 1,2,4-AQASH in 1.0 M HClO₄. The concentrations are (from top to bottom) 3, 1.5, 1, 0.5, and 0.1 μ M. The initial potential is $+0.180$ V. The scan rate is 5 V s⁻¹.

relative to the C=O stretch ($I_{\text{ring}}/I_{\text{C=O}}$), is approximately 1.2 in the monolayer compared to approximately 7.7 for the quinone in bulk electrolyte solution. That the ring-breathing mode is suppressed relative to the C=O stretch in the monolayer suggests that the quinone is adsorbed coplanar with the electrode surface. This result contrasts with investigations of sulfonated anthraquinones on silver and gold where the ratios were approximately 2.0 and 0.3 for the monolayer and powder, respectively, indicating that the adsorbate is approximately perpendicular to the surface on solid electrodes.^{18,19}

Lateral Interactions. Figure 3 illustrates the voltammetric responses obtained as the bulk concentration, C_B , of 1,2,4-AQASH is systematically varied from 0.1 to 3.0 μ M. The increasing area under the voltammogram indicates that the surface coverage increases from approximately 0.4 to 1.5 $\times 10^{10}$ mol cm^{-2} over this concentration range. Also, when the bulk concentration exceeds approximately 1.5 μ M, a current spike is observed on the anodic branch. Current spikes have been previously reported by Anson,¹⁷ McDermott²⁰ and Faulkner,²¹ all of whom examined disulfonated anthraquinones. They performed investigations on mercury and graphite electrodes and all suggest that the spike is due to changes within the adsorbed monolayer through hydrogen bonding interactions. In particular, Faulkner²¹ suggests the possibility of condensation from a gaslike collection of isolated species to a liquid or solid hydrogen-bonded network. Given its structure, 1,2,4-AQASH ought to be capable of intermolecular hydrogen bonding, e.g., between the carbonyl and hydroxy functionalities of the oxidized and reduced forms.

Monolayers represent attractive model systems for understanding the distance dependence of two-dimen-

- (11) Laviron, E. *J. Electroanal. Chem.* **1974**, *52*, 395.
 (12) Brown, A. P.; Anson, F. C. *Anal. Chem.* **1977**, *49*, 1589.
 (13) Forster, R. J. *Analyst* **1996**, *121*, 733.
 (14) Forster, R. J. *Electrochem. Soc. Proc.* **1996**, *96*, 65.
 (15) Forster, R. J. *Langmuir* **1995**, *11*, 2247.
 (16) Colthup, N. B. *Introduction to Infrared and Raman Spectroscopy*; Academic Press: Boston, MA, **1987**.
 (17) Zhang, J.; Anson, F. C. *J. Electroanal. Chem.* **1992**, *331*, 945.

- (18) Nishiyama, K.; Tahara, S.; Uchida, Y.; Tanoue, S.; Taniguchi, I. *J. Electroanal. Chem.* **1999**, *478*, 83.
 (19) Sang Woo, H.; Tai Hwan, H.; Chang Hwan, K.; Kwan, K. *Langmuir* **1998**, *14*, 6113.
 (20) Truong, C. T.; Kanda, V.; McDermott, M. T. *J. Phys. Chem.* **1999**, *103*, 1295.
 (21) He, P.; Crooks, R. M.; Faulkner, L. R. *J. Phys. Chem.* **1990**, *94*, 1135.

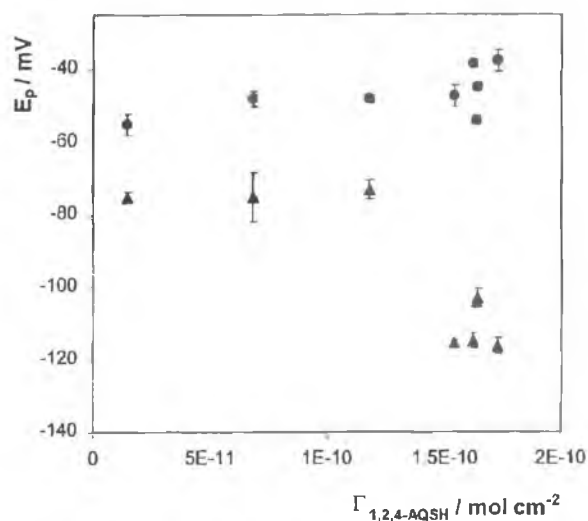


Figure 4. Dependence of the anodic (●) and cathodic (▲) peak potentials on the surface coverage of 1,2,4-AQASH. The monolayers were formed from the oxidized, quinone, form of the compound at +0.18 V. The supporting electrolyte is 1.0 M HClO₄.

sional interactions since the intersite separation can, in theory, be controlled by changing the surface coverage. However, this approach is useful only if incomplete monolayers consist of randomly dispersed adsorbates, rather than a small number of islands within which the adsorbates are closely packed. The peak potentials can provide a useful insight into this issue.

Figure 4 illustrates the dependence of the anodic and cathodic peak potentials, E_{pa} and E_{pc} , on the surface coverage of 1,2,4-AQASH for films assembled from the quinone form at a potential of +0.180 V. For surface coverages between approximately 0.1 and 1.2×10^{-10} mol cm⁻², both the anodic and cathodic peak potentials are insensitive to the surface coverage suggesting that at low surface coverages the films exist as a random array of adsorbates. While the presence of the current spike on the anodic branch makes it difficult to determine an exact value for E_{pa} , Figure 4 suggests that the anodic peak potential shifts abruptly in a positive potential direction when the surface coverage exceeds approximately 1.5×10^{-10} mol cm⁻².

Adsorption Isotherms. The equilibrium surface coverage depends on the bulk concentration of the anthraquinone. To obtain the adsorption isotherm,^{9,22} the surface coverages at equilibrium were determined by integrating the background-corrected cyclic voltammograms. Figure 5 illustrates the dependence of the surface coverage, Γ , on the bulk concentration of 1,2,4-AQASH for both reduced and oxidized forms, i.e., where the monolayers were formed at initial potentials of -0.600 or +0.180 V. In this way, a limited insight into the effect of changing the redox state of the adsorbate on the thermodynamics of adsorption can be obtained.

The peak potential data presented in Figure 4 indicate that adsorbates interact with one another, at least at high surface coverages. The Frumkin adsorption isotherm accounts for lateral interactions by modeling the free energy of adsorption as an exponential function of the surface coverage^{9,11,22}

$$\beta C_i = \frac{\theta_i}{1 - \theta_i} \exp(g\theta_i) \quad (1)$$

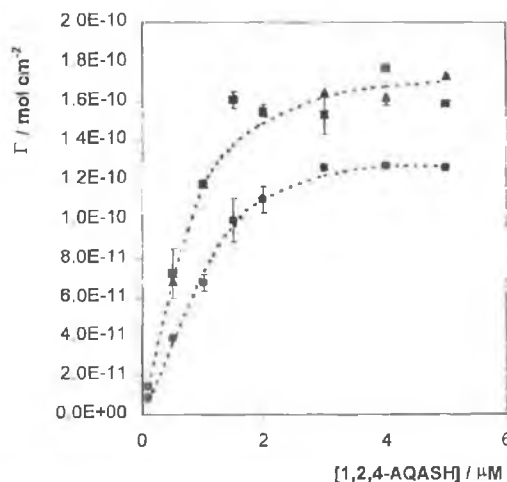


Figure 5. Dependence of the surface coverage on the bulk concentration of the quinone (▲ and ■ denote the areas under the anodic and cathodic peaks, respectively) and hydroquinone (● denotes both anodic and cathodic data) forms of 1,2,4-AQASH. The supporting electrolyte is 1.0 M HClO₄. The dashed lines represent the best fits to the Frumkin adsorption isotherm. Where errors bars are not visible, errors determined from at least three independently formed monolayers are comparable to the size of the symbols.

Table 1. Saturation Coverages, Adsorption Coefficients, and Frumkin Interaction Parameters for 1,2,4-AQASH Monolayers Assembled from Both Oxidized, Q, and Reduced, H₂Q, Species

	quinone	hydroquinone
$10^{-10}\Gamma/\text{mol cm}^{-2}$	1.94 ± 0.13	1.4 ± 0.1
β/M^{-1}	$(1.27 \pm 0.11) \times 10^6$	$(0.56 \pm 0.05) \times 10^6$
$\Delta C/kJ \text{ mol}^{-1}$	-34.8 ± 0.8	-32.1 ± 1.6
g	-0.29 ± 0.05	-1.78 ± 0.22

where $\theta_i = \Gamma_i/\Gamma_{\text{sat}}$, Γ_i is the coverage of 1,2,4-AQASH in mol cm⁻² at a bulk concentration C_i , Γ_{sat} is the saturation coverage obtained at high bulk concentrations, and β is the adsorption coefficient. Attractive interactions are indicated by $g < 0$ and repulsive interactions by $g > 0$.

Figure 5 shows that the optimized Frumkin isotherm provides a satisfactory fit to the experimental surface coverages for monolayers assembled from both reduced and oxidized forms. Moreover, a good correlation ($R^2 > 0.99$) is observed between the experimental bulk concentrations of 1,2,4-AQASH and those predicted by the Frumkin model. Table 1 contains the best-fit parameters. The only significant deviation from Frumkin-type behavior is observed for monolayers assembled from the oxidized form where the bulk concentration is 1.5 μM . This is the lowest concentration for which a current spike is observed. That the experimental data can be accurately modeled according to the Frumkin isotherm indicates the lateral interactions exist in films of mixed redox composition. Significantly, the interaction parameters are negative for both oxidized (-0.29 ± 0.05) and reduced (-1.78 ± 0.22) monolayers indicating that both species, Q and H₂Q, are more stable in a monolayer of mixed redox composition. However, the observation that the two parameters are numerically different from one another suggests that adsorbate-solution interactions, which will be sensitive to the redox composition of the solution, may influence the magnitude of the interaction parameters. These interaction parameters correspond to a free energy of

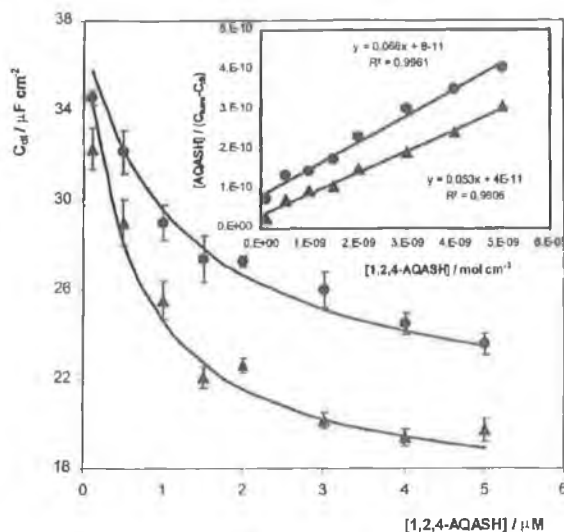


Figure 6. Dependence of the double-layer capacitance on the bulk concentration of the quinone (●) and hydroquinone (▲) forms of 1,2,4-AQASH monolayers formed on hanging mercury electrodes. The interfacial capacitance was determined using scan rate dependent cyclic voltammetry at potentials of +0.180 and -0.400 V. The supporting electrolyte is 1.0 M HClO₄. The inset shows the best-fit linearized Langmuir isotherm.

approximately -0.37 ± 0.05 and -2.2 ± 0.1 kJ mol⁻¹, for films assembled from quinone and hydroquinones forms, respectively. This stabilization most likely involves hydrogen bonding between the carbonyl and hydroxy functionalities present in the oxidized and reduced forms of 1,2,4-AQASH.

The free energy of adsorption, ΔG^* , can be determined from the adsorption coefficient in conjunction with eq 2.

$$\beta = \exp(-\Delta G^*/RT) \quad (2)$$

The free energies of adsorption are -34.8 ± 0.21 and -32.1 ± 1.6 kJ mol⁻¹ for monolayers assembled from Q and H₂Q, respectively. Thus, in common with previous reports on related systems,^{4-6,8,21} the adsorbates are strongly bound to the electrode surface. However, these data suggest that monolayers formed using Q are relatively more stable.

The saturation surface coverages observed for Q and H₂Q are (1.9 ± 0.1) and $(1.4 \pm 0.1) \times 10^{-10}$ mol cm⁻² corresponding to areas occupied per molecule of approximately 86 and 120 Å², respectively. These occupation areas are both larger than the value 70 Å² predicted by energy minimized molecular modeling for a nonsolvated adsorbate. However, they are significantly larger than those associated with edge-on adsorption²³ of anthraquinones where the area per molecule is typically less than 35 Å². Therefore, consistent with the resonance Raman experiments discussed above, these isotherm data suggest coplanar adsorption. A difficulty in trying to use Faradaic data to determine surface coverages is that if Γ changes continuously in response to the applied potential, then the Faradaic charge may not reflect the actual coverages of Q and H₂Q. Therefore, we have probed the dependence of the monolayer capacitance on the bulk concentration of both oxidized and reduced forms.

Effect of Potential on Adsorption Thermodynamics. Figure 6 illustrates how the interfacial capacitance as measured at +0.180 and -0.400 V changes as the bulk

concentration of 1,2,4-AQASH is systematically varied from 0.1 to 5 μM , where the supporting electrolyte is 1.0 M HClO₄. For a modified interface, the total double layer capacitance, C_{dl} , depends on both the capacitance of the film, C_{film} , and the diffuse layer, C_{dl} , as described by eq 3.

$$C_{dl}^{-1} = C_{film}^{-1} + C_{dl}^{-1} \quad (3)$$

As the concentration of the supporting electrolyte is increased, the double layer is compressed causing the diffuse layer capacitance to increase.⁹ For supporting electrolyte concentrations less than 0.6 M HClO₄ the double layer capacitance increases before becoming independent of the electrolyte concentration, i.e., in 1.0 M HClO₄ the diffuse layer capacitance is sufficiently large so that the total capacitance becomes dominated by the film capacitance. Figure 6 shows that C_{dl} changes from approximately 37 $\mu\text{F cm}^{-2}$ for a clean unmodified mercury surface to values of approximately 24 and 20 $\mu\text{F cm}^{-2}$ for oxidized and reduced monolayers, respectively, at high bulk concentrations.

The dependence of the interfacial capacitance on the surface coverage can be described by the parallel capacitor model originally proposed by Delahay and co-workers.²⁴ The double-layer capacitance for incomplete monolayers is represented by an equivalent circuit containing the two parallel capacitances describing the contributions from the modified and bare regions of the electrode surface. For this model, the total double layer capacitance, C_{dl} is given by

$$C_{dl} = C_{mono} + (C_{bare} - C_{mono})(1 - \theta) \quad (4)$$

where C_{bare} and C_{mono} are the double-layer capacitances of a bare and densely coated electrodes, respectively, and θ is the fractional surface coverage.

This parallel capacitor model allows the linearized Langmuir isotherm to be expressed according to eq 5.

$$\frac{C_1}{C_{bare} - C_{dl}} = \frac{1}{C_{mono}} C_1 + \frac{1}{C_{mono}\beta} \quad (5)$$

Hence, the interfacial capacitance corresponding to a dense monolayer on the electrode surface together with the adsorption coefficient can be determined from the slope and intercept of a plot of $C_1/(C_{bare} - C_{dl})$ vs C_1 . The solid lines of Figure 6 shows that close agreement is achieved between the best fit provided by the parallel capacitor model and the experimental data for both oxidized and reduced films. Moreover, the inset of Figure 6 shows that plots of $C_1/(C_{bare} - C_{dl})$ vs C_1 are linear indicating that the Langmuir isotherm provides an appropriate description of adsorption of fully oxidized and reduced films. The absence of lateral interactions contrasts sharply with the Faradaic data presented earlier which could only be accurately modeled by the Frumkin adsorption isotherm because of strong lateral interactions when both Q and H₂Q coexist on the surface.

As shown in Table 2, the best fits to the experimental data are obtained where the dense monolayer capacitances, C_{mono} , are 19.2 ± 0.9 and 17.0 ± 1.1 $\mu\text{F cm}^{-2}$ for fully oxidized and reduced monolayers, respectively. That the capacitance is slightly lower for the reduced films suggests that the packing density may be higher in the fully reduced monolayers. This limiting capacitance can be used to provide an insight into the local microenvi-

(23) Soriaga, M. P.; Hubbard, A. T. *J. Am. Chem. Soc.* **1982**, *104*, 2735.

(24) Delahay, P.; Trachtenberg, L. *J. Am. Chem. Soc.* **1957**, *79*, 2355

Table 2. Limiting Interfacial Capacitances and Adsorption Coefficients for 1,2,4-AQASH Monolayers Assembled from Both Oxidized, Q, and Reduced, H₂Q, Species^a

	quinone	hydroquinone
$C_{\text{mono}}/\mu\text{F cm}^{-2}$	19.2 ± 0.9	17.0 ± 1.1
β/M^{-1}	$(1.53 \pm 0.11) \times 10^6$	$(0.77 \pm 0.07) \times 10^6$
$\Delta G/kJ \text{ mol}^{-1}$	-35.3 ± 0.2	-33.5 ± 0.3

^a Parameters determined from the dependence of the interfacial capacitance on the bulk concentration fitted to a Langmuir adsorption isotherm.

ronment within a dense monolayer. For example, that the E' shifts by 38 mV upon surface confinement might suggest that the local microenvironment, e.g., the dielectric constant, is significantly different within the film.

The dielectric constant of the monolayer can be estimated from C_{mono} using eq 6

$$C_{\text{mono}} = \epsilon_0 \epsilon_{\text{film}} / d \quad (6)$$

where ϵ_0 is the permittivity of free space, ϵ_{film} is the film dielectric constant, and d is the monolayer thickness. The film thickness is taken as 4 Å, i.e., the interplane separation as taken from energy-minimized molecular modeling of crystalline 1,2,4-AQASH. Consistent with the formation of an organic film and displacement of water and anions from the interface, the dielectric constants are approximately 8.7 and 7.7 for reduced and oxidized monolayers, respectively. Therefore, changes in the local microenvironment as well as partial discharge upon adsorption are responsible for the shift in formal potential upon surface confinement.

A significant advantage of using capacitance data to probe monolayer formation is that adsorption coefficients can be determined for both oxidation states. The values obtained for the Q and H₂Q forms are (1.53 ± 0.11) and $(0.77 \pm 0.07) \times 10^6 \text{ M}^{-1}$, respectively, indicating that despite its lower saturation coverage the oxidized form of 1,2,4-AQASH adsorbs relatively more strongly to the electrode surface.

Origin of the Current Spike. That the dependence of the interfacial capacitance on the bulk concentration can be accurately modeled using the Langmuir adsorption isotherm indicates that lateral interactions are weak in fully oxidized and reduced films irrespective of the surface coverage. Figure 3 shows that the voltammetry for films assembled from oxidized 1,2,4-AQASH is close to ideal for surface coverages less than approximately $1.4 \times 10^{-10} \text{ mol cm}^{-2}$. Moreover, the anodic peak potential is independent of Γ for this range of surface coverages. These observations suggest that for surface coverages in this range the monolayers exist as weakly interacting, randomly dispersed adsorbates. Energy minimized molecular modeling indicates that the area of an unsolvated molecule is approximately 70 \AA^2 ($\approx 6.6 \times 10.8 \text{ \AA}$). Therefore, for surface coverages $< 1.4 \times 10^{-10} \text{ mol cm}^{-2}$ the average area occupied per molecule will be more than 120 \AA^2 leading to an intersite separation of at least 3 Å. This intersite separation is too large to allow efficient intermolecular hydrogen bonding between the carbonyl and hydroxy functional groups that exist in the quinhydrone films.

In contrast, when the bulk concentration is such that the surface coverage is greater than $1.6 \times 10^{-10} \text{ mol cm}^{-2}$, the intersite separation will be less than 2.4 Å, allowing hydrogen bonding interactions between the -C=O and -OH groups that coexist in films of mixed redox composition. These lateral interactions mean that Faradaic data of the type presented in Figure 5 can only be accurately

Table 3. pK_a Values for the Functional Groups within 1,2,4-AQASH As Determined Using Solution-Phase UV-Visible Spectroscopy^a

couple	pK_a
$\text{-SO}_3\text{H}/\text{SO}_3^-$	3.2
$\text{-NH}_4^+/\text{NH}_3$	5.2
$\text{-OH}/\text{O}^-$ (4-position)	7.4
$\text{H}_2\text{Q}/\text{HQ}^-$	9.6
$\text{HQ}^-/\text{Q}^{2-}$	11.6

^a The between-run error on the pK_a values is typically 0.2 pH units.

modeled using the Frumkin isotherm. Significantly, the capacitance data provide an important insight into why the voltammetric spike is not observed at the same bulk concentration for monolayers assembled from Q and H₂Q. Tables 1 and 2 as well as Figures 5 and 6 indicate that the free energy of adsorption is significantly larger for the oxidized adsorbate. Therefore, a higher bulk concentration of H₂Q is required to create films in which the intersite separation is reduced to the point where efficient intermolecular hydrogen bonding can occur. For the range of bulk concentrations presented in Figures 5 or 6, the surface coverage of H₂Q is always less than approximately $1.2 \times 10^{-10} \text{ mol cm}^{-2}$; i.e., the intersite separation always exceeds 4.4 Å. Experimentally, we find that current spikes are observed for monolayers assembled from H₂Q only for bulk concentrations in excess of approximately 20 μM .

Proton Dependence of 1,2,4-AQASH Monolayer Electrochemistry. The pH of the supporting electrolyte will directly influence the extent of protonation of the amino, sulfonic acid, and hydroxy moieties. Moreover, under very basic conditions the electrochemistry will become independent of pH with the quinone being reduced in a two-electron reaction to the quinolate dianion, Q^{2-} . To probe the acid/base chemistry of 1,2,4-AQASH, we have investigated the effect of changing the solution pH on the $\pi-\pi^*$ transition of the compound. The pK_a s for the sulfonic acid, amine, and hydroxy functional groups were determined by fitting the change in the absorbance measured at 260 nm to the Henderson-Haselbalch equation using nonlinear optimization procedures.²⁵ All changes were confirmed to be reversible by first increasing and then decreasing the solution pH using concentrated NaOH and HClO₄, respectively. The pK_a data are summarized in Table 3. These data reveal that the pK_a s are widely spread from 3.2 ± 0.2 , corresponding to the protonation/deprotonation reaction of the sulfonic acid group to 11.6 ± 0.2 for the $\text{HQ}^-/\text{Q}^{2-}$ reaction of the hydroquinone. Thus, in principle it ought to be possible to probe the effect of protonation at distinct sites on the overall stability of the monolayer.

Figure 7 illustrates the effect of changing the solution pH on the cyclic voltammograms observed for dense quinone monolayers ($\Gamma = 1.8 \times 10^{-10} \text{ mol cm}^{-2}$) where a current spike is observed. For $1.0 \leq \text{pH} \leq 4.2$, E' shifts linearly in a negative potential direction with increasing electrolyte pH with a slope of $63 \pm 4 \text{ mV/decade}$. The same behavior is observed for incomplete monolayers where the current spike is absent and the electrochemical properties are close to ideal. Given that these data are not corrected for liquid junction potentials, this experimental value agrees with the 59 mV pH^{-1} value expected for a redox reaction involving the transfer of equal numbers of electrons and protons. Thus, intramolecular proton transfer from the protonated sulfonic acid or ammonium moiety

(25) Dean, J. A. *Handbook of Organic Chemistry*; McGraw-Hill: New York, 1987.

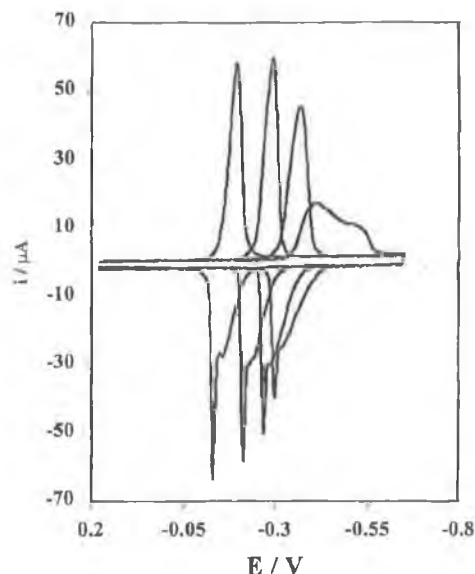


Figure 7. Cyclic voltammograms of a mercury electrode immersed in a $5 \mu\text{M}$ solution of 1,2,4-AQASH as the pH of the electrolyte solution is varied. From left to right, the pH of the solution is 1.03, 2.20, 3.15, and 4.10. The scan rate is 5 V s^{-1} and the supporting electrolyte is 1.0 M HClO_4 titrated directly in the electrochemical cell with concentrated NaOH.

to the reduced quinone is not important over this pH range and the coupled proton transfer occurs from solution. As the solution pH increases, the voltammetry becomes less well defined and at a pH of approximately 4, two distinct peaks are observed on the cathodic branch. The total charge under these two peaks is indistinguishable from that observed under the single peak found at low pH suggesting that the redox transformation does not involve one-electron reductions to the radical anion 1,2,4-AQASH $^{\cdot-}$ and to the quinolate dianion. In contrast, it appears that the two peaks arise because the concentration of both H_3O^+ and OH^- ions is significantly less than that of the quinone. Specifically, for solution pH values greater than approximately 4.0, the proton concentration allows only a fraction of the quinone be reduced to the protonated hydroquinone giving rise to the first set of peaks at an E^{oc} dictated by the bulk pH of the solution.²⁶ However, because electron and proton transfer are coupled in this system, electrolysis is accompanied by a significant change in the interfacial pH. Thus, a second set of peaks is observed as

the remainder of the quinone is reduced to the deprotonated form of the hydroquinone.²⁷

A significant feature of this system is that spontaneously adsorbed monolayers do not form at solution pHs above 4.2. Notwithstanding the low dielectric constant of the monolayer that is likely to increase the apparent $\text{p}K_{\text{a}}$ s, on the basis of the spectroscopic data, this behavior is probably associated with significant deprotonation of the sulfonic acid moiety. Deprotonation of the sulfonic acid will make the compound neutral (quaternary ammonium plus conjugate base of the acid) which becomes significantly more soluble in the medium that contains 30% DMF. Future experiments will address this issue by forming monolayers in solutions in which the organic content is systematically varied.

Conclusions

Monolayers of 1-amino-2-sulfonic-4-hydroxyanthraquinone have been formed in both oxidized and reduced forms by spontaneous adsorption from aqueous solutions. These two-dimensional supramolecular assemblies have been used to probe the effect of changing the intersite separation and the redox composition of the monolayer on the extent of lateral hydrogen bonding. Monolayers formed from the hydroquinone, H_2Q , exhibit nearly ideal electrochemistry at low surface coverages. In contrast, for monolayers assembled from the quinone form of the compound, when the intersite separation is of the order of 3 \AA the adsorbates interact strongly and a current spike is observed. In contrast, capacitance data reveal that adsorbates within fully oxidized or reduced films do not interact strongly irrespective of the surface coverage.

The spontaneous formation of a monolayer is driven by a large negative free energy of adsorption which is approximately -32 kJ mol^{-1} and does not depend strongly on the oxidation state of the adsorbate. While very much weaker than this strong physisorption process, lateral hydrogen bonding interactions within quinhydrone films are of the order of -2 kJ mol^{-1} even when the films are in contact with an essentially aqueous medium. Significantly, in contrast to traditional alkanethiol monolayers these lateral interactions can be modulated by changing the redox composition of the film or the solution.

Acknowledgment. Funding from Enterprise Ireland, the Irish Science and Technology Agency, under Strategic Research Grant ST/98/414, is gratefully acknowledged. We appreciate the insightful comments of the referees in reviewing this paper.

LA000546Z

(26) Forster, R. J.; O'Kelly, J. P. *J. Electroanal. Chem.*, in press.

(27) Bailey, S. I.; Ritchie, I. M. *Electrochim. Acta* **1985**, *1*, 3.